ULTRASONIC DETERMINATION OF SURFACE RESIDUAL STRESSES

By

EWA K. SZYMANSKI, B.ENG.

A Thesis

Submitted to the School of Graduate Studies

In Partial Fulfilment of the Requirements

for the Degree

Master of Engineering

McMaster University

MASTER OF ENGINEERING (2003) McMaster University

(Materials Science and Engineering) Hamilton, Ontario

TITLE: Ultrasonic Determination of Surface Residual Stresses.

AUTHOR: Ewa K. Szymanski, B.Eng. (McMaster University)

SUPERVISOR: Professor P.S. Nicholson

NUMBER OF PAGES: xxvii, 254

ABSTRACT

The velocity of an ultrasonic wave in a material is affected by the stresses due to the Acoustoelastic Effect. The present work utilizes this phenomenon to study surface, residual-stresses that result on machining. Two types of surface wave are used: Rayleigh (R_w) and longitudinal, critically refracted (L_{cr}).

Sound velocity may also change due to grain scattering, surface roughness and grain texture. The present work attempts to determine each contribution to exclusively identify the change of velocity due to stress. The problem is studied systematically by choosing increasingly complex materials i.e. Glass (Corning 9604) - no grains, no texture; Crystallized Glass (Corning 9606) – grains but no texture; Single Crystal Magnesium – all texture; Polycrystalline Titanium – grains and texture.

Glass, glass-ceramic and titanium were machined to introduce surface stress and the R_w and L_{cr} velocities measured before and after stress relief. The velocity changes were converted to stress via appropriate Acoustoelastic Coefficients. The relative values agreed well with the XRD-determined stresses, the former results being consistently lower than the latter. This is expected as ultrasound penetrates deeper and thus samples more material. Annealed specimens identified the surface roughness contribution to the changes of ultrasonic velocity.

Experiments illustrated that the change of velocity due to stress (maximum observed 0.52%) is small, relative to the other contributions: surface roughness contributes $\leq$ 8%,

texture ≤ 2.4%, and grain scattering ≤ 0.6%. This result underscores the importance of considering all material conditions when using ultrasound to quantify surface residual-stresses. Several techniques to exclusively identify the change of velocity due to stress are presented.

ACKNOWLEDGEMENTS

I would like to express my appreciation to all those who assisted me with this project and who made my time spent at McMaster enjoyable:

Dr Nicholson for making it all possible and providing a stimulating working environment;

Dr Patel for being always there when his expertise in ultrasound was needed; for his help with the experimental work and long, informative discussions in which he freely supplied knowledge and advice;

Ena Nicholson just for being such a wonderful person – a friend to laugh with or cry - and her efforts in preparing this document;

Dr Niewczas and Dr Dabkowski for their help and invaluable advice;

Dr Danielson from Corning Inc. for kindly providing the samples;

Chris Butcher and Jim Garrett for sharing their broad expertise in materials preparation and for having a solution to every problem;

Andy Duft for being the only person in North America agreeing to cut my Mg crystal; for organizing the great bike trips and being such a good friend;

Andrzej Borowiec, Steve Koprich, Jim Britten and Wen-He Gong for their assistance with this project;

Everyone in the Ceramics Group: Yoko, Reshma, Yahua, Nanda, Waleed and Hansoo for their company, friendship and support;

Most importantly, my parents and brother Daniel for their encouragement and support through all the years of my education, and Mariusz for his love and understanding.

The author wishes to especially acknowledge the support of Pratt and Whitney Canada, specifically David Craig and David Thomas. P& W C strongly supported the project.

The Natural Science and Engineering Research Council are thanked for their financial award. Without the latter, the study would not exist.

TABLE OF CONTENTS

LIST OF TABLES

LIST OF FIGURES

Chapter 1

INTRODUCTION

An ultrasonic wave propagating through a solid body can measure properties and property alterations in a zone near the surface and throughout the volume. Because the penetration depth of surface waves is inversely proportional to ultrasonic frequency, tests can search different depths by varying frequency. Ultrasonic waves, being mechanical vibrations, are especially suited to detect elastic anomalies and measure physical properties. The most important advantage of the ultrasonic technique is that the test object is undamaged by the test, i.e. non-destructively evaluated.

The well-established applications of ultrasound in materials evaluation include flaw detection, thickness measurement (corrosion detection), interface-inspection and surface analysis. Sound reflections are analyzed in the time (or frequency) domain. Parameters most often considered are signal amplitude and time-of-flight. The purpose of the present work is to develop a method for determining surface residual stresses in titanium, following machining. Ultrasound is used, as stress produces changes in the sound velocity. Velocity however, is also modified by grain-size, grain-texture and surface roughness, thus these effects must be determined to identify exclusively sound velocity changes due to the mechanically-induced, residual surface-stresses.

Titanium is evaluated via a synergetic approach. Hot-pressed titanium (~75 μm particle size), plate-shaped specimens were synthesized with minimum texture.

Commercial, cold-rolled titanium plates were used to study the influence of grain-texture and grain size on ultrasonic velocity. Samples were then systematically machined to different surface roughnesses and the ultrasonic analysis repeated. Subsequent annealing removed residual stresses and the exclusive surface topography influence was studied. The change in surface-wave velocity was measured after each treatment step to isolate, by difference, the exclusive influence of stress.

To obtain an understanding of the change-of-sonic-velocity phenomena, three projects were undertaken on model materials. Glass (Cordierite glass-precursor -- silica-alumina-magnesia) was acquired from Corning (Code 9604) and characterized. It was then crystallized (Code 9606) and characterized again. This facilitated identification of the grain presence effect on sound velocity, i.e. difference between the amorphous and crystallized material. Then specimen surfaces were grooved with a laser (fine), and dice-saw (coarse). The influence of grain presence, surface-roughness and stress on sonic velocity was thus tracked and the magnitude of influence of each defined.

Mg is a reasonable model for Ti as the Young's Modulus / density ratio (the main concern in ultrasonics) is similar to Ti. Magnesium has one stable phase, thus avoids the phase-change complication encountered in Ti. Single crystal Mg allowed identification of the change of sound velocity in different crystallographic directions.

Chapter 2

LITERATURE REVIEW

Part A: Theory of Ultrasound and Ultrasonic Equipment

2.1 Elastic Wave Propagation in a Bulk Solid

Acoustic nondestructive evaluation uses mechanical stress waves. "Ultrasound" implies frequencies > 20 kHz (Figure 2-1, Stephens (1975)), although most commercial ultrasonic testing employs 1 to 25 MHz. The sonic waves of greatest concern are pulses of energy. The solid medium can be imagined as individual particles kept in position by elastic forces (Figure 2-2). As a mechanical wave propagates therein, discrete particles oscillate sinusoidally and, if the oscillations are initiated on the left, the elastic forces transmit vibrational energy from plane-one-particles to plane-two, then plane-three etc. Thus the motion induced by the sound requires time to transmit and the given plane reached, lags in phase behind that first excited by one half oscillation (Krautkramer et al 1983).

Figure 2-3 shows one type of elastic wave encountered in solids and liquids. It is an instantaneous 'snapshot' of a compressional (longitudinal, 1-D) wave traveling from left

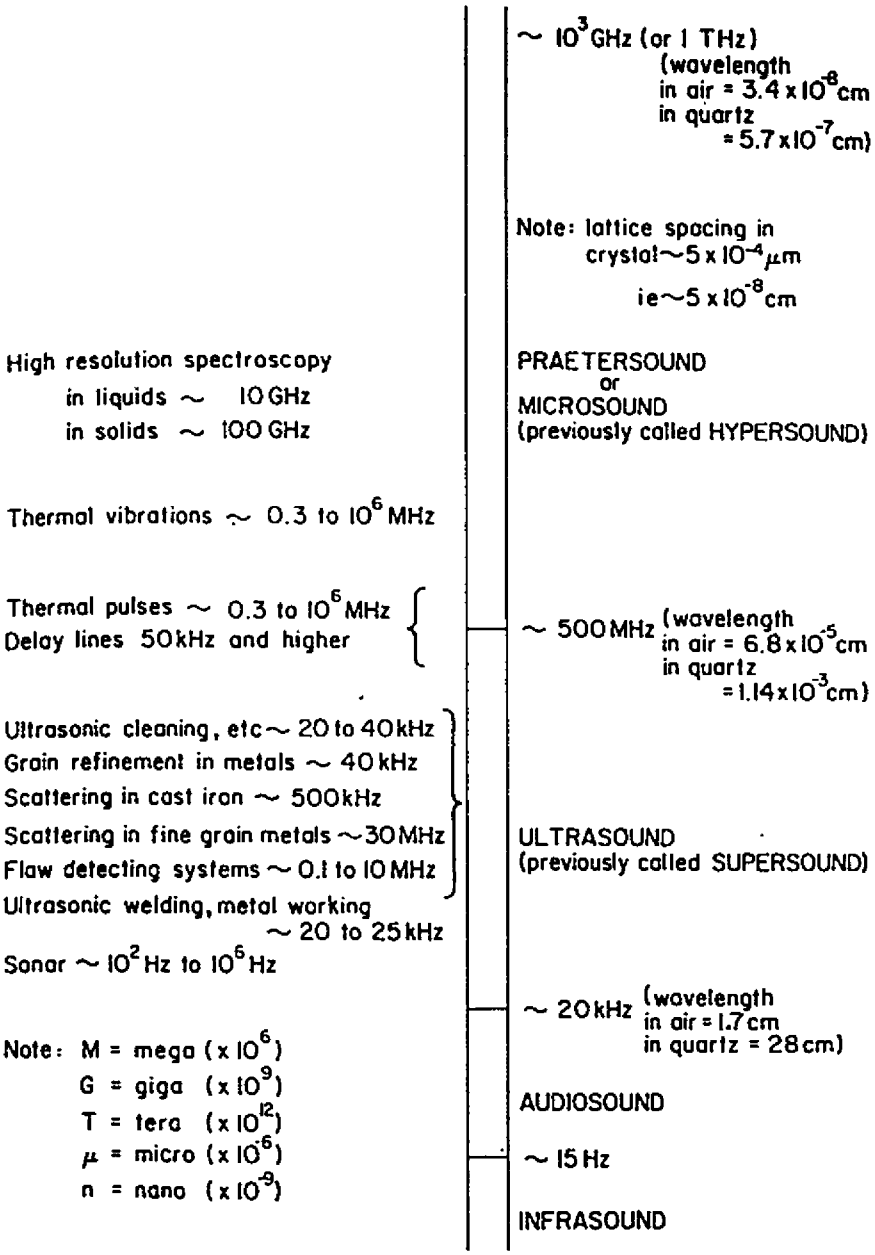

Figure 2-1: Acoustic frequency scale (Stephens 1975)

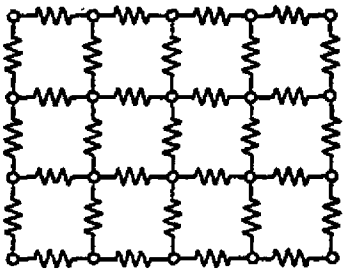

Figure 2-2: Model of an elastic body (Krautkramer et al 1983)

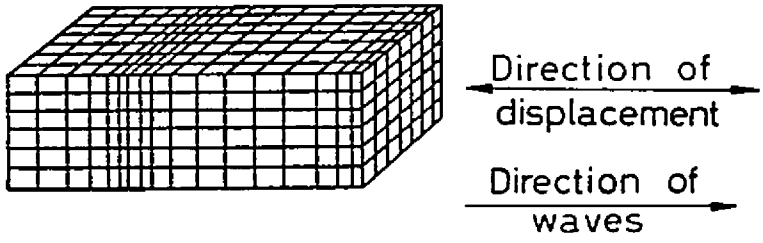

Figure 2-3: Longitudinal wave (Filipczynski et al 1966)

to right (Filipczynski et al 1966). The particles of the medium move forward and backward in the line of wave travel. Compression "zones" alternate with "rarified" ones. These zones travel at a constant velocity. The particles remain in place but oscillate about their rest positions. The above description assumes a homogeneous, isotropic material (Cracknell 1980). The longitudinal-wave-mode can be excited by placing a diaphragm in contact with the particles on the left side (Figure 2-3), and electrically inducing oscillation therein (Krautkramer et al 1983).

Transverse (shear) waves (as opposed to the longitudinal waves) involve particle motion perpendicular to the sound propagation direction. This wave-mode is only observed in solids, as liquids cannot support shear. Figure 2-4 shows an instantaneous

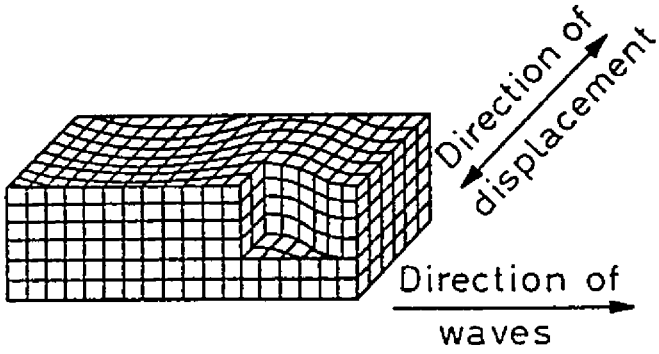

Figure 2-4: Transverse wave (Filipczynski et al 1966)

picture of the particle displacement involved. Wave excitation starts on the left-most plane and the "elastic springs" between particles transmit the disturbance to the right. Periodic shear force moves the particles back and forth sinusoidally (Filipczynski et al 1966). The velocity of the shear wave is approximately half the longitudinal one, in the same material (Cracknell 1980).

Both longitudinal and shear waves are "bulk" waves and exist in this form only when remote from boundaries.

2.2 Wave Parameters that describe a Sonic Wave

The particle displacement (u) from its equilibrium position, when it is in simple harmonic motion, is a function of the equilibrium position (x) and time (t) (Cracknell 1980):

$$u(x,t) = a\sin\left(\frac{2\pi t}{T} - \frac{2\pi x}{\lambda}\right) \quad (1)$$

The amplitude 'a' of the wave is the maximum value of the displacement and the wavelength 'λ' is the distance between two planes of particles vibrating in phase (i.e., two compression zones). 'T' is the period of the oscillation and describes the time required for one complete cycle of a particle's motion (one "wavelength"). The frequency of oscillation 'υ' is defined as:

$$\upsilon = \frac{1}{T} \quad (2)$$

and is related to the angular frequency, 'ω', via:

$$\omega = 2\pi\upsilon \quad (3)$$

During a single period of particle motion, the traveling wave advances one wavelength (λ), thus the speed of sound is:

$$c = \frac{\lambda}{T} \quad (4)$$

The plane (or spherical) wave sound pressure, 'P', and particle amplitude 'a' (maximum displacement from the rest position) are related by (Krautkramer et al 1983):

$$P = W\omega a \quad (5)$$

where W=ρc is the Acoustic Impedance. The intensity of the sound wave is related to 'P' via Equation 6:

$$I = \frac{1}{2}\frac{P^2}{W} = \frac{1}{2}W\omega^2 a^2 \quad (6)$$

The intensity is thus proportional to the square of the particle displacement amplitude. All these relationships apply to longitudinal and transverse waves.

2.3 The Dynamics of a Sound Wave moving in a Solid

The sound waves employed to study material properties are pulses of energy. This section considers the origins of these pulses and their characteristics using the simple, one-dimensional, plane wave equation for longitudinal waves (Bray et al 1989).

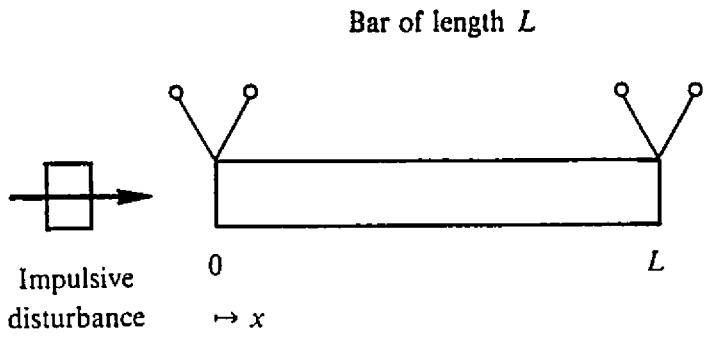

Figure 2-5: Long bar of arbitrary cross section (Bray et al 1989)

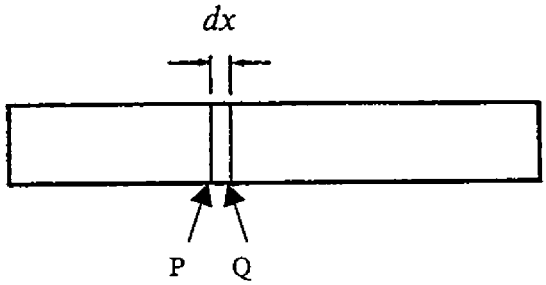

Figure 2-6: A small element, PQ, of equilibrium length, dx, along the bar (Bray 1989)

It is assumed the wave propagates along a bar of cross-section area 'A', length 'L' and Young's modulus 'E'. The bar is suspended on frictionless supports (Figure 2-5). A small element, PQ, of equilibrium length, dx, is defined along the bar (Figure 2-6). The

left end of the bar is struck with an impulse (i.e. a piezoelectric transducer or a hammer tap). The left face "moves" and, after some time, 't', the right face moves, i.e. the disturbance reaches the end of the bar. Such motion implies elastic deformation has occurred.

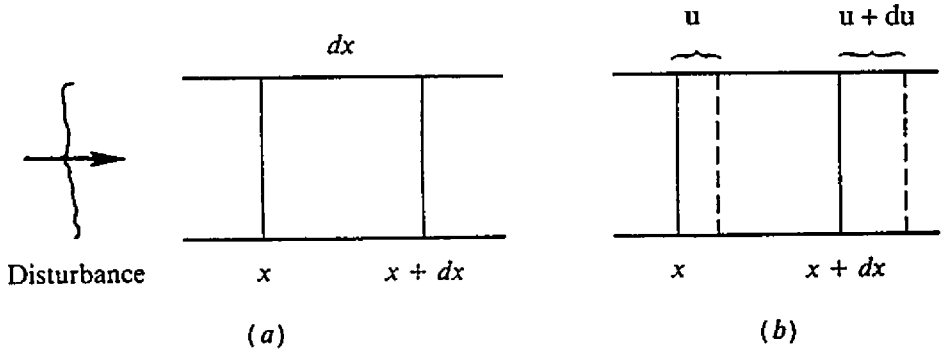

Figure 2.7: (a) Undisturbed element. (b) Disturbed element.(Bray et al 1989).

Figure 2.7 is a magnification of the element PQ of Figure 2-6: a) just before the disturbance reaches it and b), during passage of the perturbation. The instantaneous displacements of the ends of the element are 'u' and 'u+du' respectively. Thus 'u' is a function of 'x' and 't', i.e.:

$$u = u(x,t) \quad (7)$$

If small displacements are assumed, a Taylor series expansion can be used for the displacement, i.e.:

$$u + du = u + \frac{\partial u}{\partial x} dx + H.O.T. \quad (8)$$

If the higher-order terms (H.O.T.) are neglected and the change of element length (Δl) is:

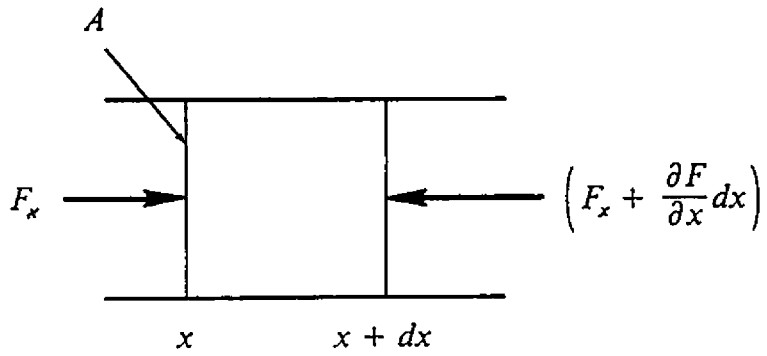

Figure 2-8: Forces on the element during passage of a disturbance (Bray et al 1989)

$$\Delta l = (u + du) - u = du = \frac{\partial u}{\partial x}dx \quad (9)$$

The incremental strain of PQ is:

$$\Delta\varepsilon = \frac{\Delta l}{dx} = \frac{\left(\frac{\partial u}{\partial x}\right)dx}{dx} = \frac{\partial u}{\partial x} \quad (10)$$

Forces must act on the element on deformation. The former are shown schematically in Figure 2-8. If at some instant of time, a force 'F_x' acts on the left face, a reactive force acts on the opposite face: $F_x + \frac{\partial F}{\partial x}dx$, due to elasticity. The difference is:

$$dF_x = \left(F_x + \frac{\partial F_x}{\partial x}dx\right) - F_x = \frac{\partial F_x}{\partial x}dx \quad (11)$$

Now, Young's Modulus for uniaxial deformation is:

$$E = \frac{\Delta\sigma}{\Delta\varepsilon} \quad (12)$$

and this can define the local relationship between the stress at given point in the bar and the strain thereat ($\Delta\sigma$ - incremental stress; $\Delta\varepsilon$ - incremental strain; E – Young's modulus). The incremental stress on face P, is:

$$\Delta\sigma = \frac{F_x}{A} \quad (13)$$

where 'A' is the cross-section of the face. Combining Equation 13 with 10 and 12 gives:

$$E = \frac{\frac{F_x}{A}}{\frac{\partial u}{\partial x}} \quad (14)$$

and, solving for F_x:

$$F_x = AE\frac{\partial u}{\partial x} \quad (15)$$

Taking the partial derivative of Equation 15 and substituting into Equation 11, gives an expression for the net force on the element, involving the elastic properties, i.e.:

$$dF_x = AE\frac{\partial^2 u}{\partial x^2}dx \quad (16)$$

The displacement suffered in the bar is time-dependent so the dynamic nature of the propagating wave is introduced via Newton's Second Law, i.e.:

$$dF_x = ma \quad (17)$$

where, 'm', is the mass of element PQ, and 'a' the instantaneous acceleration of the particles in a face. Since mass is (density x volume):

$$m = \rho(Adx) \quad (18)$$

where 'ρ' is the density. Acceleration is:

$$a = \frac{\partial^2 u}{\partial t^2} \quad (19)$$

thus Equation 17 becomes:

$$dF_x = \rho A \frac{\partial^2 u}{\partial t^2} dx \quad (20)$$

Equations 16 and 20, when equated, yield the general one-dimensional equation for propagation of waves in a solid:

$$\frac{\partial^2 u}{\partial t^2} = C_l^2 \frac{\partial^2 u}{\partial x^2} \quad (21)$$

where 'C_l' is the velocity of the propagating disturbance, i.e. the speed of the sound wave (Bray et al 1989).

Solutions of this 1-D wave equation are (Kinsler et al 2000):

$$u(x,t) = a\exp[i(\omega t - kx)] \quad (22)$$

and

$$u(x,t) = a\exp[i(\omega t + kx)] \quad (23)$$

where 'a', is the wave amplitude and 'k' the "wave vector". This latter is related to wavelength via:

$$k = \frac{2\pi}{\lambda} \quad (24)$$

Generalization to three dimensions gives (Kinsler et al 2000):

$$\frac{\partial^2 u}{\partial x^2} + \frac{\partial^2 u}{\partial y^2} + \frac{\partial^2 u}{\partial z^2} = \frac{1}{C^2}\frac{\partial^2 u}{\partial t^2} \quad (25)$$

Now, the speed of sound in a material depends on the elastic properties and density (Cracknell 1980):

$$C = \sqrt{\left(\frac{\varepsilon}{\rho}\right)} \quad (26)$$

The modulus 'ε' is now a function of the type of the sound wave. The situation is simple for a one-dimensional (plane) wave; e.g.: for a rod (uni-dimensional), the $\varepsilon \equiv E$ (Young's Modulus), if the wave is compressional, i.e.:

$$C_l = \sqrt{\left(\frac{E}{\rho}\right)} \quad (27)$$

When $\varepsilon \equiv G$ (the shear modulus), i.e. the sonic wave is a shear wave:

$$C_t = \sqrt{\left(\frac{G}{\rho}\right)} \quad (28)$$

Ultrasonic examination usually involves propagation of bulk waves in a three-dimensional solid. The Poisson's Ratio effect must now be considered, i.e., a purely longitudinal disturbance produces deformation in both the longitudinal and lateral direction. Thus, expressions for bulk-longitudinal (C_1) and bulk shear (C_2) waves are:

$$C_1 = \sqrt{\left(\frac{\lambda + 2\mu}{\rho}\right)} \quad (29)$$

and

$$C_2 = \sqrt{\left(\frac{\mu}{\rho}\right)} \quad (30)$$

where 'λ' and 'μ' are the Elastic (Lame) Constants (Bray et al 1989).

The actual (dynamic) Elastic Modulus, 'E', can be calculated from the wave velocities, i.e.:

$$E = \frac{\mu(3\lambda + 2\mu)}{\lambda + \mu} \quad (31)$$

Similarly, the Poisson's Ratio 'υ' and bulk modulus 'k' follow:

$$\upsilon = \frac{\lambda}{2(\mu + \lambda)} \quad (32)$$

$$k = \frac{3\lambda + 2\mu}{3} \quad (33)$$

Algebraic manipulation of Equations 29 through 33, gives expressions in terms of the longitudinal and shear bulk velocities:

$$E = \frac{\rho C_2^2 \left[3\left(\frac{C_1}{C_2}\right)^2 - 4 \right]}{\left(\frac{C_1}{C_2}\right)^2 - 1} \quad (34)$$

$$\upsilon = \frac{\left(\frac{C_1}{C_2}\right)^2 - 2}{2\left[\left(\frac{C_1}{C_2}\right)^2 - 1\right]} \quad (35)$$

$$k = \rho C_2^2 \left[\left(\frac{C_1}{C_2}\right)^2 - \frac{4}{3} \right] \quad (36)$$

These relationships facilitate an uncomplicated experimental determination of the elastic properties of a material (Bray 1989).

2.4 The Attenuation and Scattering of Ultrasound

As ultrasonic energy propagates through a medium, the intensity of the wave diminishes as most energy converts to thermal energy via absorption. Secondary energy loss is due to particle "scattering" of it (Payne 1994).

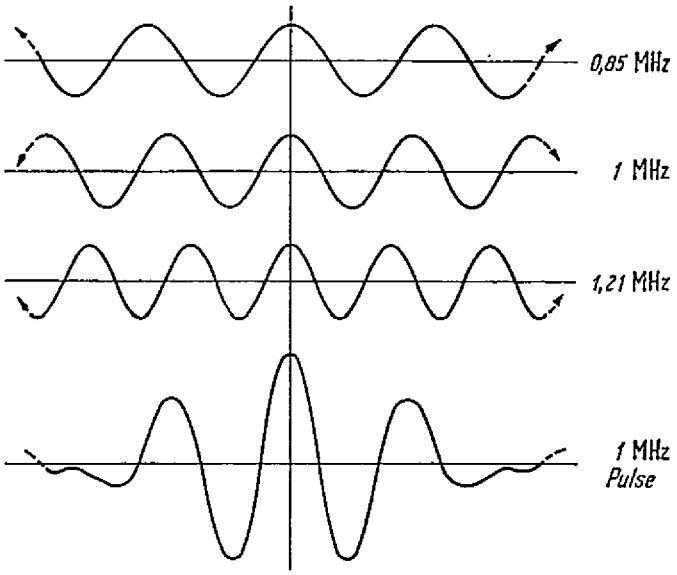

Figure 2-9: Synthesis of a 1MHz pulse composed of purely sinusoidal partial waves of 0.85, 1 and 1.21 MHz (Krautkramer et al 1983)

2.5 Analysis of a Pulse of Ultrasound

A sonic pulse is a limited wave train formed by superposition of purely sinusoidal particle waves of slightly different frequencies - Figure 2-9 (Krautkramer et al 1983).

The width of the pulse depends on the width of frequency range. Figure 2-10 shows pulses of different width and the corresponding resonance curves. In general, the further

the frequencies of the partial waves are displaced from the mean, the narrower is the resulting pulse (Krautkramer et al 1983).

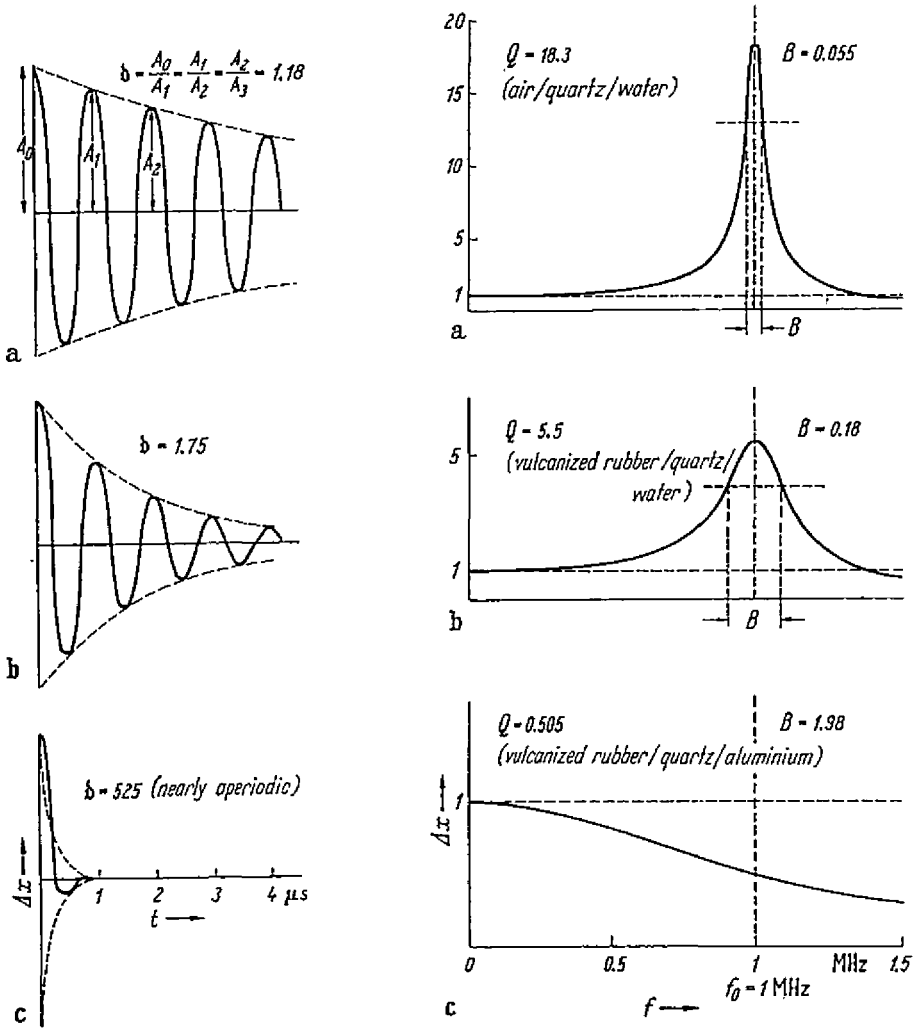

Figure 2.10: Decay of oscillations at different damping coefficients (δ) and the corresponding resonance curves of a 'thickness oscillator (Krautkramer et al 1983)

An originally narrow pulse may be "broadened" if the partial waves have different velocities. This is called "dispersion"(Bray 1989).

2.6 Surface Ultrasonic Waves

The purpose of the present study is to determine the stresses remnant in surfaces after machining. Consequently, surface sound waves must be used. There are many modes of surface wave and the two employed herein are the Rayleigh wave (R_w) and the critically refracted Longitudinal wave (L_{cr}). Each is sensitive to different aspects of material morphology.

2.6.1 Ultrasonic, Surface Sound-Wave Generation

To generate a surface sound wave, a specific angle is required between the incident wave and the surface normal. The liquid/ solid interface is apropo the present work. Water is the coupling medium between the transducers and solid samples.

Figure 2-11 shows reflection and transmission of a plane wave obliquely incident on the planar boundary between two materials with different characteristic impedances. If this was water/ solid interface, a reflected longitudinal wave would be emitted at angle θ_r, and a transmitted longitudinal wave and shear wave at angles $\theta_{t,\,longitudinal}$ and $\theta_{t,\,shear}$, respectively. The relationship between the angle-of-the-incident-wave-in-water and the resulting angle-of-propagation-inside-the-material, is given by the Snell's law (Kinsler et al 2000), i.e.:

$$\frac{\sin\theta_{i,water}}{\sin\theta_{t,solid}} = \frac{C_{water}}{C_{solid}} \quad (37)$$

where θ - the angle between the surface normal and propagation direction of a wave and C - wave velocity. Since the velocities of longitudinal and shear waves are different (the former twice the latter), the angles of refraction are different.

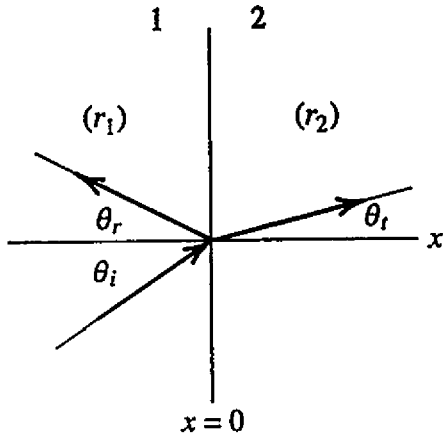

Figure 2-11: Reflection and transmission of a plane wave obliquely incident on a planar boundary between two materials with different characteristic impedances (Kinsler et al 2000).

To demonstrate the creation of a surface wave, consider a water/ aluminum interface - Figure 2-12 (Krautkramer et al 1983). At small angles-of-incidence, a longitudinal wave enters the solid at small angles as per Snell's Law. The acoustic pressure and angle increase rapidly with increasing angle of incidence. Concurrently, a weak transverse wave forms with maximum value at 20° in the solid. Finally, when the incidence angle reaches 13.56° (this angle characteristic of Al / H_2O), the refracted angle for the longitudinal wave = 90°, i.e.: the wave propagates along the surface. This is the so-

called critical-angle-longitudinal-wave (L_{cr}). Beyond this angle, the longitudinal wave disappears. Immediately however, a stronger transverse wave forms and, as the angle of

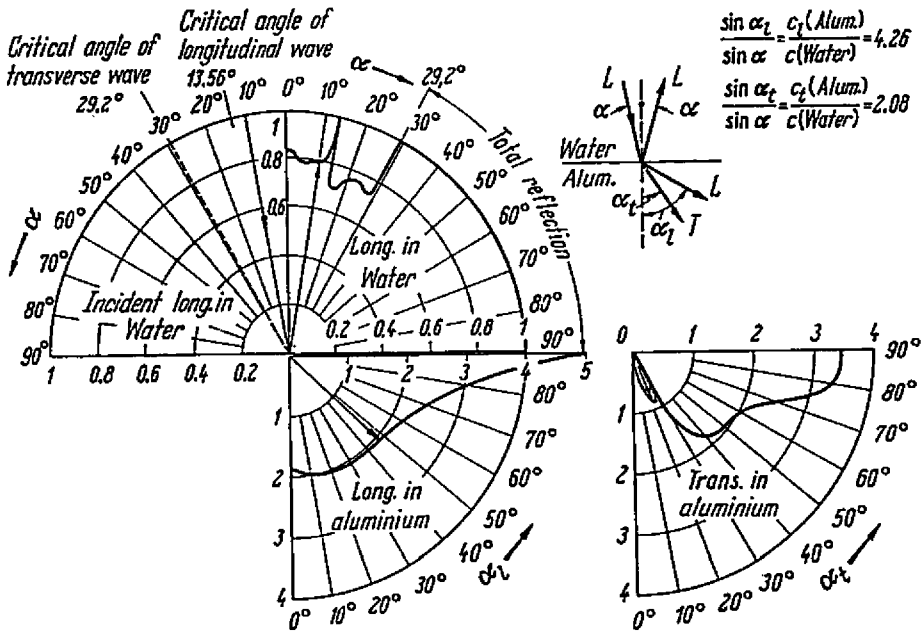

Figure 2-12: Interface water/ aluminum (Krautkramer et al 1983)

incidence increases, the refraction angle increases (Snell's law). Finally, this transverse wave travels along the surface (90°) when the incidence angle approaches 29.2°. This is the "second-critical-angle". Above this angle, the incident longitudinal wave completely reflects from the interface and no wave is detected in the aluminum (Krautkramer et al 1983).

2.6.2 The Rayleigh Wave

The Rayleigh wave (R_w) exists only on a surface. It can be considered a linear combination of shear and longitudinal solutions of the wave equation, the relative

amplitudes of which satisfy the zero-stress, boundary conditions. R_w decays exponentially with material depth. Since there is no loss of energy due to radiation to the bulk, R_w propagates long distances without intensity loss. R_w travels at ≈ 93% the shear wave velocity and ≈ 50% the L_{cr} wave value- the exact value depends on the Poisson's Ratio, ν (Thompson et al 1995). The latter slowness renders R_w more sensitive to grain size and surface roughness, as for the same frequency the wavelength is shorter. Because the R_w is geometrically bound and travels only along the material surface, it propagates

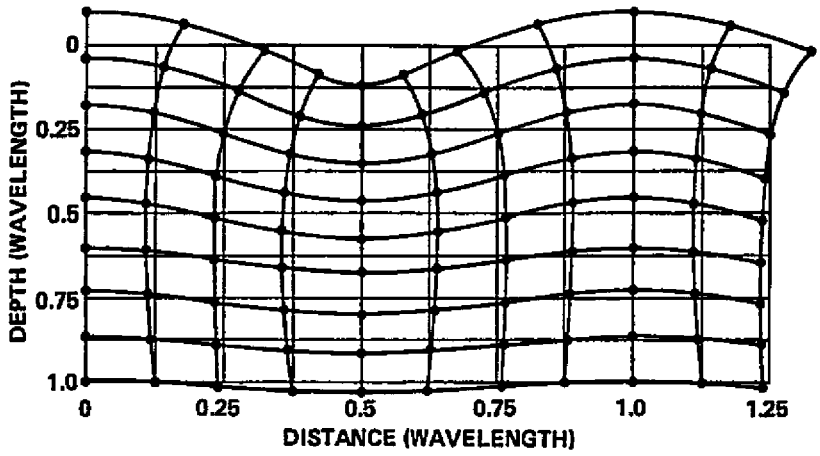

Figure 2-13: A cross section of the particle displacements in a Rayleigh wave traveling along the surface of an isotropic solid (Hickernell 1999)

along curved surfaces and over unusual geometry difficult to probe with other ultrasonic waves (Lindgren et al 1998). Rayleigh waves are also non-dispersive, i.e.: the velocity of R_w is independent of frequency (Lindgren et al 1994).

Figure 2-13 shows a cross-section of particle displacement caused by R_w in an isotropic solid. The surface displacements are elliptical with a strong shear component perpendicular to the propagation direction and compression-extension along the surface

in the propagation direction (Hickernell 1999). Thus R_w is polarized. This renders its velocity sensitive to "texture" in the material.

Because R_w suffers exponential decay with depth, a large fraction of its energy is confined to a wavelength from the surface (Hirao et al 1981). Hence it is advantageous to measure residual stress gradients in a material (the depth-of-penetration is: $d \approx \lambda = V_{Rw}/f$, where 'f' is the frequency). R_w velocity is determined by the average material properties over depth of penetration. Assuming the stress-free Elastic Constants do not vary with depth, examination of the R_w velocity frequency dependence can yield information vis a vis stress gradients (Lindgren et al 1998)- Figure 2-14.

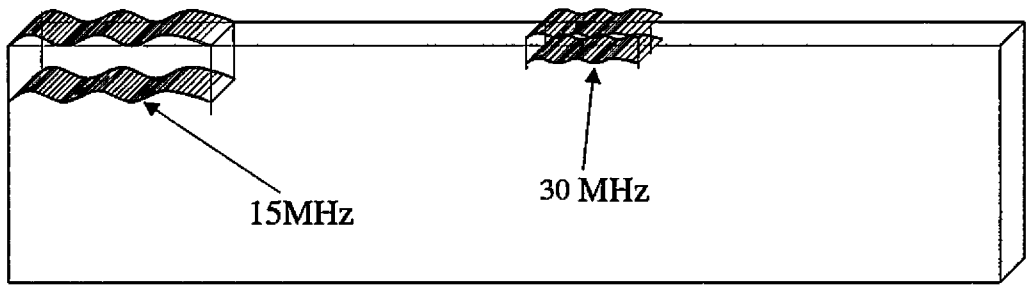

Figure 2-14: R_w penetration depth dependence on frequency.

2.6.3 The Ultrasonic Longitudinal, Critically-Refracted Wave (L_{cr})

The incidence angle of a longitudinal wave on a solid surface can be adjusted to result in a longitudinal wave propagating just beneath the surface (L_{cr} = longitudinal, critically-refracted wave). This wave travels at a speed ≈ the bulk longitudinal wave speed (Thompson et al 1995).

The particle displacements involved in the L_{cr} wave propagation are the same as the bulk longitudinal wave, i.e.; compression zones alternate with rarified ones. The L_{cr} velocity is sensitive to surface stress changes in the material and will be discussed in the following sections.

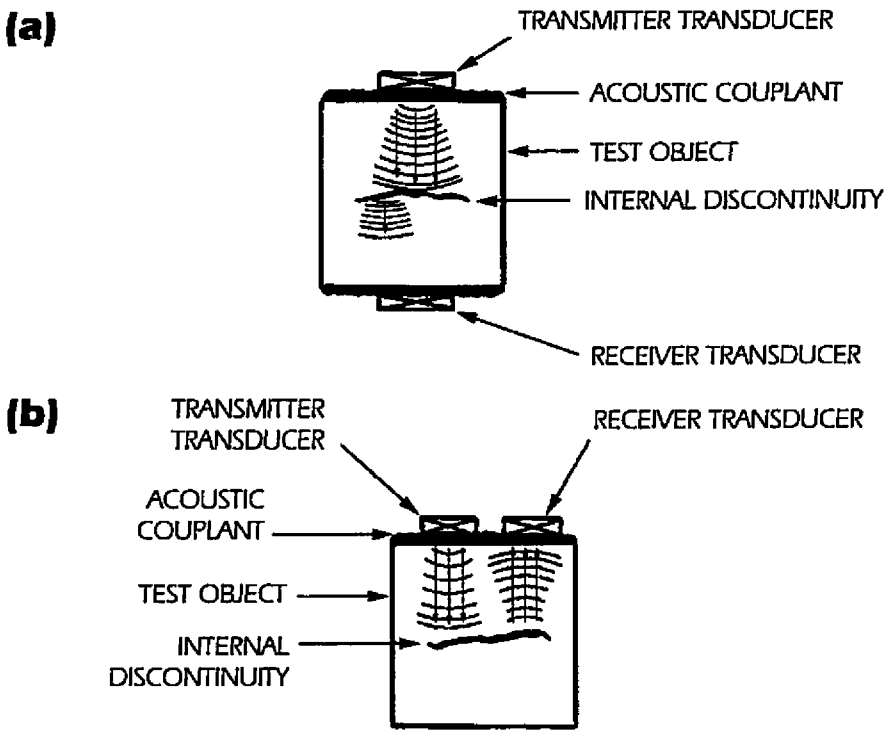

Figure 2-15: Basic ultrasonic testing methods: (a) the through-transmission mode; (b) the reflection mode(Birks et al 1996)

2.7 Ultrasonic Instrumentation – Pulse-Echo Inspection

As compared to earlier instrumentation, the solid-state electronics used in present equipment offer considerable improvement vis a vis reduced power and size (Bray 1989).

However, the fundamental principles of operation of the key components of a typical ultrasonic circuit have not changed.

Advances in numerical analysis have benefited ultrasonic inspection techniques. The ability of computers to retrieve, store, analyze and report vast amounts of data generated by ultrasonic tests has increased the number of applications as well as reduced the uncertainty of results (Bray 1989).

This section describes the basic principles of operation of a typical ultrasonic inspection instrument.

Ultrasonic inspection is performed in a through-transmission or reflection mode. In the former, a beam of ultrasonic energy is directed into the test object and the energy transmitted there-through measured - Figure 2-15 (a). In the latter, waves are launched by a transmitting transducer, propagate through a region of the material, reflect from a discontinuity therein, to be detected by a receiving transducer - Figure 2-15 (b) (Birks et al 1996). The reflection technique is termed 'pulse-echo' if the same transducer is used for excitation and detection, or a 'pitch-catch' if two transducers are used (Figure 2-16 (a) and (b), respectively (Thompson et al 1995)). The present work employed the pulse-echo method.

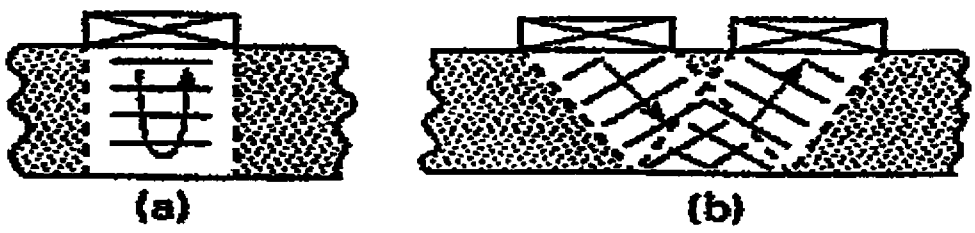

Figure 2-16: The reflection techniques: (a) pulse-echo; (b) pitch-catch (Thompson et al 1995).

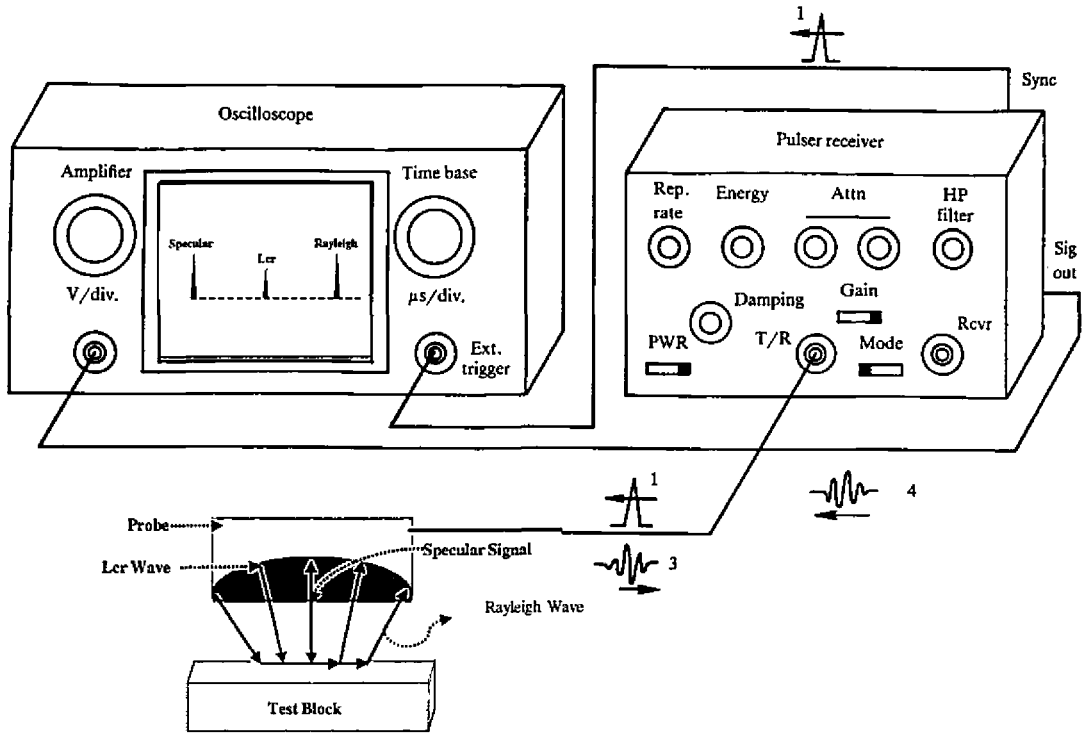

Figure 2-17: Typical laboratory setup for ultrasonic pulse-echo inspection (Bray et al, 1989, figure modified for the focused-probe conditions).

Figure 2-17 shows the equipment arrangement for focused-transducer, pulse-echo inspection (Bray et al 1989, modified). The pulser and receiver are in the same unit and are connected to an oscilloscope.

The oscilloscope defines an A-scan ultrasonic system (Birks et al 1996). The horizontal-axis tracks elapsed time (from left to right) and the vertical axis, the signal amplitude.

The pulser starts the inspection. A brief electric pulse of sine waves is applied to the ultrasonic transducer. The latter generates an ultrasonic vibration (Bray 1989). The time-base generator excites the instant the ultrasonic pulse leaves the transducer and

causes a spot to move, left to right horizontally across the oscilloscope screen with constant velocity. A horizontal line (the time base) appears on the screen (Birks et al 1996). The "main-bang" (the initial echo on the left of the screen in Figure 2-17) indicates the high-voltage spike striking the probe. The latter produces a short train of elastic waves, which transmit the coupling medium (water) and enter the test object (Bray et al 1989).

Once the voltage spike occurs, the pulser switches to an open, non-conducting, electrical circuit and the receiving circuit awaits the return signal to strike the transducer (Bray et al 1989). A percentage of the sound waves traveling the couplant are reflected from the object surface, and, on return to the transducer, transform to electrical pulses which are fed to the receiver. The peak corresponding to this reflection is the first to appear on the time axis of the oscilloscope, after the "main-bang". A portion of sound-wave energy enters the sample and if no defects are present, a "back-echo" signal results from reflection at the back of the sample (Birks et al 1996).

The oscillation of the probe is governed by a tuned, LC circuit. Timing circuits measure the intervals between transmission of the initial pulse and reception from the surface of and within, the test object. The pulse repetition rate is adjustable so reverberations within the test object completely decay between the sonic pulses. The latter may vary between 60Hz and 10kHz (Selfridge 1985).

Since the test object would normally support a constant sound velocity, the time read from the oscilloscope base line can be directly used to calculate the distance (or depth) traveled by the sound before reflection. The first back-surface echo from the surface

reflection, for example, occurs after time, $t = 2\frac{d}{C}$, where 'd' is the distance traveled and 'C' the wave velocity in the material (Bray 1989).

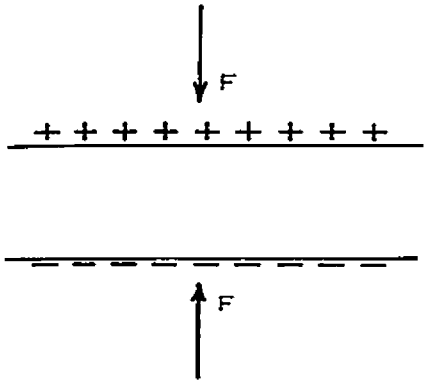

Figure 2-18: A piezoelectric material under pressure (Cracknell1980)

2.8 The Generation and Reception of Ultrasonic Waves: Transducers

2.8.1 The Piezoelectric Effect

Ultrasonic testing requires high frequency (≥ 5 MHz). Such cannot be generated by mechanical oscillators, thus electrical oscillations of the required frequency are generated and converted to mechanical oscillations (stress-waves). Similarly, the returning mechanical oscillations convert back to electrical oscillations. Active components capable of such interconverting are termed "transducers". The electromechanical conversion uses the property of "piezoelectricity" (Papadakis et al 1999).

When a piezoelectric material is deformed by external pressure, an electric charge is produced, positive on one side, negative on the other - Figure 2-18 (Cracknell 1980). An electrostatic potential difference is thus produced between the surfaces and an electrostatic field is created within the material. Brothers Curie discovered this effect in

quartz in 1880. One year later the reverse phenomenon was observed, i.e.: the same material placed between two electrodes distorts if an electric potential is applied (Krautkramer et al 1983). If the piezoelectric is a thin disk, the change of thickness, 't', of the disk is proportional to the electric field. The disk physically contracts or expands, depending on the field polarity, (Figure 2-19). Increased field strength causes further contraction (or expansion) and, conversely, the reduction relaxes the stress (Bray 1989).

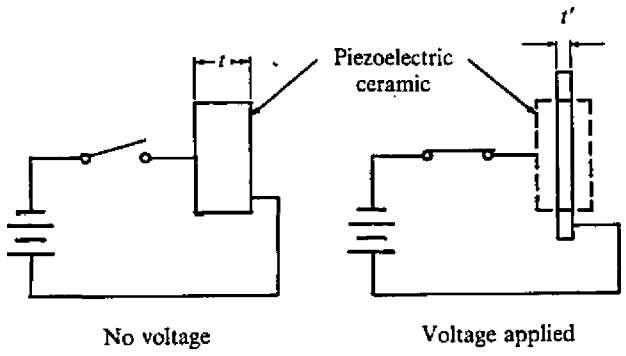

Figure 2-19: The piezoelectric effect (Bray et al, 1989)

Piezoelectricity is associated with the arrangement of atoms within a crystal. The piezoelectric behavior of a given crystal depends on the internal symmetry (the single crystal structure should not have a center of symmetry) and the orientation of the crystal slice relative to its crystallographic axes (Krautkramer et al 1983). Thus the useful cuts (and directions) in a crystal are specified for production of longitudinal and shear waves. Longitudinal plates vibrate with particle motion in the thickness direction to generate longitudinal waves that propagate normal to the crystal major faces. Shear configured plates vibrate with particle motion in a direction in the plane of major faces and generate

shear waves that propagate normal to the major crystallographic faces. The lateral dimensions of such plates must be many wavelengths to produce ultrasonic beams. A detailed description of piezoelectricity is included in Mattiat (1971), Krautkramer et al (1983), and Meeker (1996).

A number of materials exhibit piezoelectricity. Most common are quartz and ceramics such as barium titanate ($BaTiO_3$), lead zirconate titanate (PZT), and lead metaniobate (PMN) (Bray 1989).

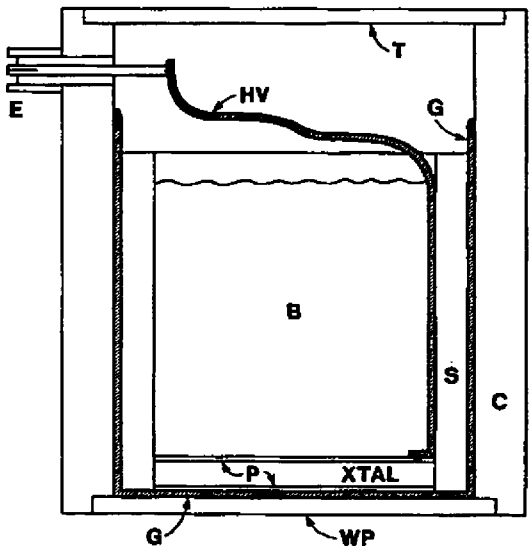

Figure 2-20: A typical ultrasonic probe: XTAL = piezoelectric element, P = plating, WP = wear plate, G = ground strap, B = backing, S = insulating shields, C = case, T = top cover, HV = high voltage lead, E = electrical connector (Papadakis et al 1999)

2.8.2 Piezoelectric Transducers – The Construction Thereof

The construction process of a piezoelectric transducer is shown in Figure 2-20 (Papadakis et al 1999). It consists of electrical connections, a case, a protective element (termed the wear plate or wave guide), a damping element (backing to absorb energy directed into the transducer) and the piezoelectric element.

A schematic of the conditions for contact-testing is shown in Figure 2-21, where "load-material" is the test object (Bray et al 1989). The thickness of the wear-plate is adjusted such that it is "invisible" to the propagating sound wave (100% transmission), i.e., its thickness is $\lambda/4$ (λ - sound wavelength) (Kinsler et al 2000).

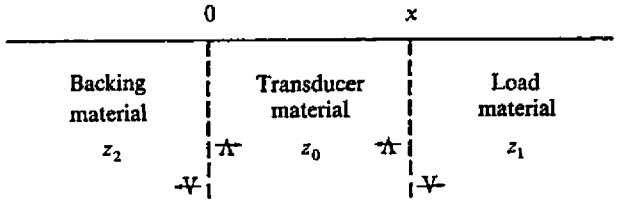

Figure 2-21: Material impedances for ultrasonic probes (Bray et al 1989)

The acoustic impedance of the materials (z_0, z_1, z_2) is determined from the density, 'ρ', and dilatational wave velocity in the material, 'C_1' (Kinsler et al 2000), i.e.:

$$z = \rho C_1 \quad (38)$$

When a transducer is excited by an electrical spike, impulses of opposite sign are excited at each interface (spikes on each side of the interfaces in Figure 2-21). As vibrations generated, the sound waves therefrom travel back and forth within the piezoelectric and, each time a wave strikes a boundary, the amplitude and phase of the

reflected and transmitted waves are governed by the relative impedance of the two materials at the boundary. The Reflection Coefficients at the boundaries are:

$$R_x = \frac{z_0 - z_1}{z_0 + z_1} \quad (39), \quad R_0 = \frac{z_0 - z_2}{z_0 + z_2} \quad (40)$$

where R_x - Reflection Coefficient at the transducer-load interface; R_0 – the Reflection Coefficient at the transducer-backing material interface, and z - the involved Acoustic Impedances.

The Transmission Coefficients are:

$$T_x = \frac{2z_1}{z_0 + z_1} \quad (41), \quad T_0 = \frac{2z_2}{z_0 + z_2} \quad (42)$$

The Acoustic Impedances of several materials are listed in Tables 2-1 and 2-2. Strong reflections occur for load (or backing) material impedances that are different from the transducer impedance. Maximum energy transfer occurs when boundary impedances are equal, i.e.; zero reflection (Bray 1989).

Table 2-1: Typical values for elastic constants and wave speeds for engineering materials (Bray et al 1989)

	English Units								
Material	E†‡ lb / in²	λ† lb / in²	μ† lb / in²	ρ§ lb / in³	C_l†§ in / s	C_1§ in / s	C_t§ in / s	C_2§ in / s	$z = \rho C_1$§ 10^3 (lbm m / s)
Steel	29.6×10^6	16×10^6	11.6×10^6	0.28	204,000	232,000	127,000	127,000	65
Stainless steel 3XX	28.7×10^6	"	11.0×10^6	0.28	"	228,000	"	123,000	65
Copper	15.8×10^6	13.6×10^6	6.4×10^6	0.32	144,000	185,000	89,000	89,000	59
Aluminum	10.3×10^6	8.0×10^6	3.7×10^6	0.10	200,000	249,000	123,000	123,000	25
Plexiglas	0.49×10^6	"	"	0.04	"	107,000	56,000	56,000	4.3
Rubber (soft)	28.6×10^3	0.14×10^6	1.1×10^3	0.03	1,811	58,000	"	"	1.7
Rubber (vulcan.)	"	"	"	0.04	"	91,000	"	"	3.6
Fused quartz‡	10.4×10^6	"	4.5×10^6	0.10	209,000	219,000	138,000	138,000	22
Polyester‡	0.4×10^6	"	"	"	"	"	"	"	"
60% G, 40% PE (9)‡	6.1×10^6	"	"	"	"	"	"	"	"
Polyethylene (10)¶	$(0.06–0.19) \times 10^6$	"	"	"	"	"	"	"	"
Water	"	"	"	0.04	"	58,000	"	"	2.3

Table 2-2: Typical Acoustic Impedances for transducer materials (Bray et al 1989)

Material	$z \times 10^6$ kg / (m^2 s)
Piezoelectric materials	
Quartz [27]	15.2
BaTi (barium titanate) [31]	31.2
PZT (lead zirconate titanate) [27]	33.0
PMN (lead metaniobate) [27]	20.5
LSH (hydrated lithium sulfate) [27]	11.2
PVDF (polyvinyl film) [27]	4.1
Mounting and backing materials	
Araldit casting resin [10]	2.8–3.7
Casting resin [18]	5.2
Tungsten/epoxy (200 : 100) [18]	9.4

The value of Acoustic Impedance dictates the transducer backing material (Krautkramer 1983). The latter limits duration of the element vibration, i.e.: it creates a pulse. Considering a briefly-excited piezoelectric plate, oscillating freely, its sinusoidal oscillation will not remain constant as it constantly loses energy, i.e., oscillation is reduced by internal friction and, more significantly, sound energy transmitted to the mounting and the ambient material. This energy loss leads to the oscillation damping, so the amplitude decreases by the factor 'δ' (the "damping coefficient") from one oscillation to the next (Figure 2-10) (Krautkramer 1983) . Thus, the shorter the pulse, the stronger the damping required. Increased damping is achieved by increasing the sound energy transmitted to the backing. To maximize the transmittance (Equation 42), the backing material must be selected with highest impedance value.

Another function of the backing element is to absorb sonic waves that enter it, so avoiding any interfering echoes. The damping body also provides mechanical support for

the thin piezoelectric, so it does not deform when the transducer element is pressed onto the material. Preferred backing materials are curable, synthetic-resins or rubber, that incorporate other powder admixtures (Krautkramer 1983). A tungsten/epoxy mixture is commonly employed as backing. The Acoustic Impedance is adjusted by varying the tungsten level (Silk 1984).

2.8.3 Piezoelectric Polymer Transducers

Many polymeric materials exhibit piezoelectric behaviour. Early piezoelectric polymers did not receive much attention until the work of Fukada (1964), who discovered that rolled films of polypeptides and numerous other polymers develop surface charges when stressed. Kawai (1969) demonstrated a strong piezoelectric effect in PVDF (polyvinylidenedifloride) and it became the leading piezoelectric polymer. Since then, this material has enjoyed widespread use in the ultrasonic industry due to its flexibility, low cost, low noise and an acoustic impedance much lower than piezoelectric ceramics. PVDF transducers are widely used in hydrophones and broad-band sources, BBS (Bar-Cohen et al 1996).

Figure 2-22 shows the cross-section of a large-aperture, low-frequency, BBS-transducer (Papadakis 1999). A layer of PVDF is bonded to an acoustically-matched backing of a filled epoxy. It is not difficult to synthesize such a material with impedance in the 4 to 5 MRayl range, required to match the PVDF elements.

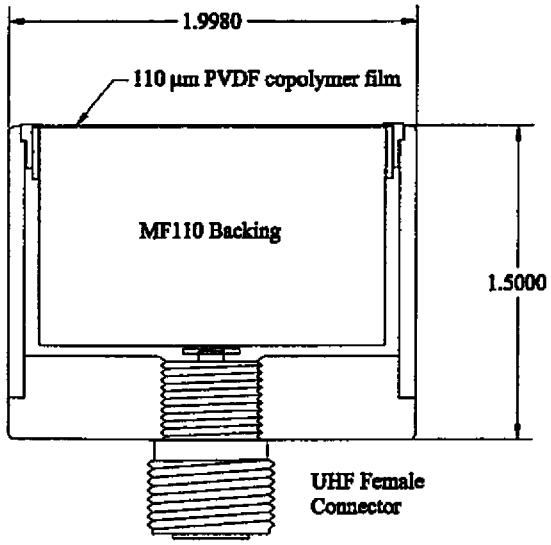

Figure 2-22: A cross-section of a large-aperture, low frequency, broad-band-transducer (Papadakis et al 1999)

2.8.4 A Pulsed Ultrasonic Circuit for Broadband Signals

Figure 2-23 shows the electric circuit for pulsed, ultrasonic waves (Bray 1989). The piezoelectric plate is represented by its electrical capacitance, C_0. A high voltage electrical spike, U_s, strikes the piezoelectric ceramic causing it to oscillate. In the ideal case, the resulting oscillation will be at the resonant frequency, i.e.:

$$f_{re} = \frac{1}{2\pi\sqrt{LC_0}} \quad (43)$$

where 'f_{re}' is the Electrical Resonant frequency and 'L' the inductance of the electrical coil.

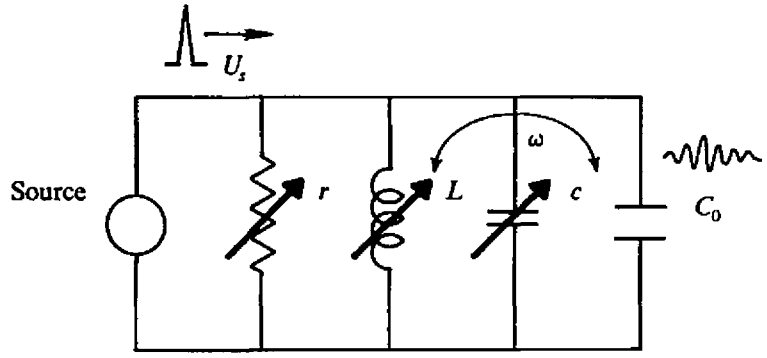

Figure 2-23: Basic, ultrasonic pulser-receiver circuit (Bray et al 1989)

A piezoelectric transducer also has a mechanical, resonant-frequency determined by:

$$f_{rm} = \frac{1}{2\pi}\sqrt{\frac{s}{m}} \quad (44)$$

where 's' is the mechanical stiffness of the transducer material and 'm' the mass. For optimum transducer performance, $f_{re} = f_{rm}$. The 's', 'm' and 'C_0' are constant for a particular transducer, thus tuning is achieved by varying the inductance 'L'. The electrical damping and hence, the pulse length, can be adjusted via a variable resistance, 'r' (Bray 1989).

The magnitude and shape of the initial electrical pulse significantly influences the acoustic signal generated. Triangular, square-wave and more-specialized initial pulse shapes are available. Typical voltages for commercial pulsers are, ≈ 300-500V (Posakony 1985).

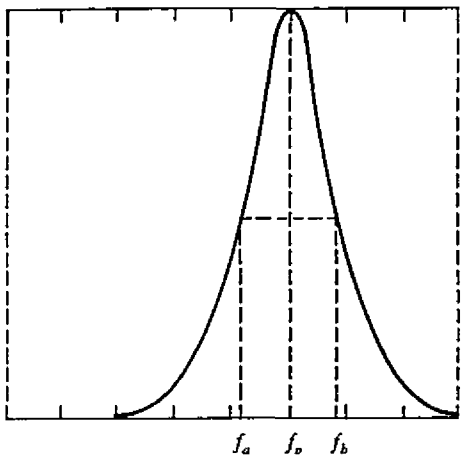

Figure 2-24: Spectrum power curve for ultrasonic transducers (Bray et al 1989)

2.8.5 The Characteristics of an Ultrasonic Transducer

Commercial ultrasonic transducers have many frequencies, diameters, and damping characteristics. As described earlier, the frequency bandwidth, and consequently, the pulse length of an ultrasonic transducer signal, is a measure of its inherent damping characteristics. The bandwidth increases as the pulse shortens (Krautkramer 1983). Bandwidth, 'B', is $B = f_b - f_a$ (Figure 2-24), where f_a and f_b are the frequency locations for the half-power points of the power spectrum (Bray 1989).

The spectrum curve for most ultrasonic probes is skewed rather than Gaussian (Figure 2-25). A measure of the skew is another parameter important for evaluation of transducer performance. The "skewness" is:

$$f_{sk} = \frac{f_p - f_a}{f_b - f_p} \quad (45)$$

where f_p is the peak-power frequency. Ideal probe performance is a normal spectrum curve, i.e., $f_{sk} = 1$ and f_p = central frequency (Bray 1989).

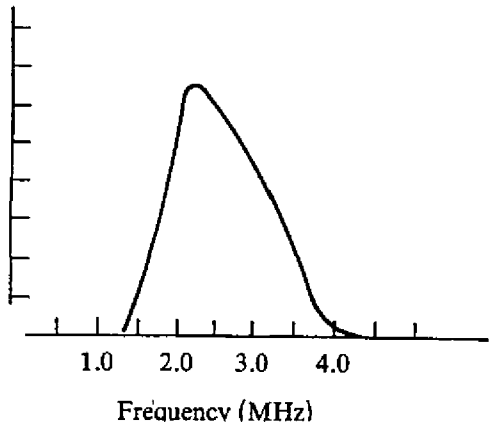

Figure 2-25: A typical skewed spectrum for a nominal 5MHz probe in contact with an aluminum block (Bray et al 1989)

Narrow bandwidth transducers have a sharp spectrum peak, thus require close tuning of the inductance coils and piezoelectric capacitance, to obtain optimum peak performance. On the other hand, broad-band transducers are 'flatter' across the peak and, therefore, are excited and respond over a wider range of frequency. Close tuning of the inductance and capacitance does not significantly influence performance (Bray 1989).

The total test bandwidth is not necessarily the transducer bandwidth, as the latter is influenced by all elements of the ultrasonic test, i.e., (1) the transmitter pulse, (2) the cable, (3) the transducer, (4) the coupling medium, (5) the material, (6) the amplifier, and (8) the digitizer (Payne 1994).

Selection of bandwidth is essential for certain tests. Narrow-bandwidth transducers are used for highly-sensitive testing. Broad-band transducers are used for high-resolution testing (Shung 1996).

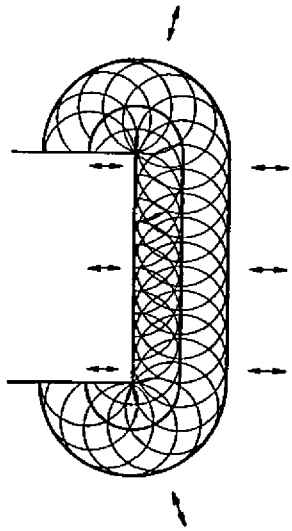

Figure 2-26: Construction of wave surfaces from elementary waves according to Huygens (Krautkramer et al 1983)

2.8.6 The Radiation Characteristics of an Ultrasonic Transducer

This section begins with the beam characteristics for a flat plate, piezoelectric transducer of a thin circular element in direct contact with an infinite medium. This, though complex, is the simplest field pattern to analyze Derivation involves the solution of a three-dimensional geometrical problem (Payne 1994).

The continuous wave transducer transmits the same phase and amplitude as its own longitudinal (or transverse motion) to the particles of the contiguous material. Spherical elementary waves form plane wave surfaces, according to Huygens' principle, in the centre zone of the oscillating plate - Figure 2-26 (Krautkramer et al 1983). An annular

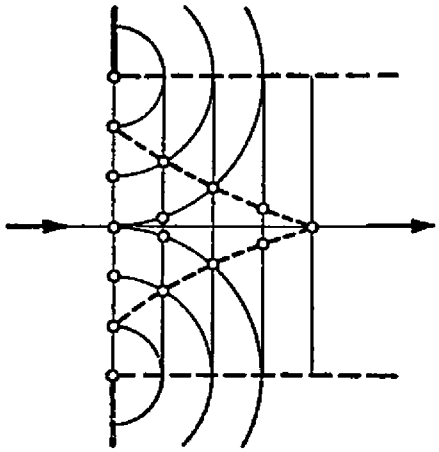

Figure 2-27: The interference structure of the sound field behind a diaphragm (according to the Huygens' principle) (Krautkramer et al 1983)

wave is produced at the edge and, superposition thereof on the plane wave (Figure 2-27), produces a field of maxima and minima of acoustic pressure in the "near-field", immediately adjacent to the probe. Beyond the "near-field" to the transducer, is a region where sonic pressure decays smoothly with distance from the probe. This smooth zone is termed the "far field" of the transducer. Figure 2-28 illustrates the sonic pressure fluctuation along a transducer's normal axis (Krautkramer et al 1983).

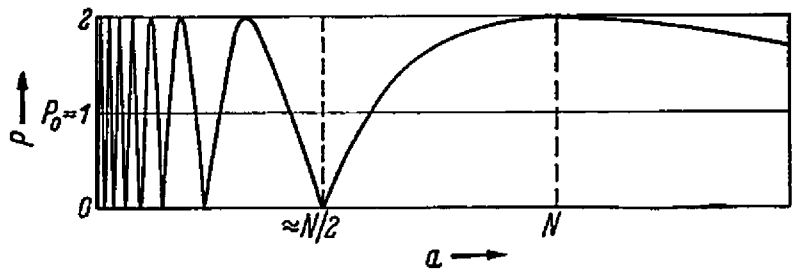

Figure 2-28: The acoustic pressure on the axis of a plane, circular radiator, N – near field (Krautkramer et al 1983)

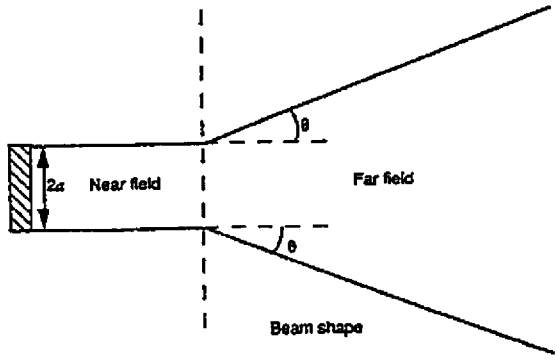

Figure 2-29: Beam divergence in the far-field of a circular piston source (Wells 1977)

Figure 2-29 is the corresponding beam divergence (Wells 1977). The "near-field" is the distance from the transducer's surface to the last maximum pressure point and is related to the probe diameter 'd' and radiation wavelength, 'λ', i.e. (Krautkramer et al 1983);

$$N = \frac{d^2 - \lambda^2}{4\lambda} \quad (46)$$

Hence, if the ratio of diameter to wavelength is large, a sharply defined and far-extending beam with a long near zone, results. It is crucial that inspection not be conducted within the "near-field" of the transducer.

Figure 2-30 shows a typical main-energy lobe beam (isobaric) from a circular piston radiator. Parameters of interest herein are the acoustic pressure, 'P', at some location, 'p', in the field of energy emitted by a circular element of diameter, 'd'. The element is assumed excited at a single frequency 'ω'. The coordinates of 'p' are 'r', the distance from the center of the element and, 'Φ/2', the angle from the center axis of the element. The time 't' is included since the emitted pressure exists as a traveling wave (Bray 1989).

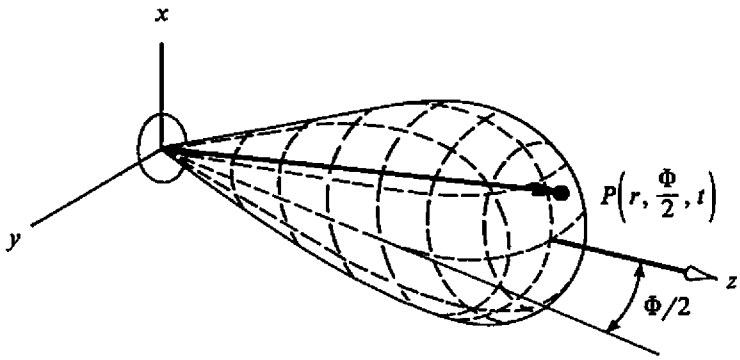

Figure 2-30: Pressure pattern of the major lobe for a piston radiator (Bray et al 1989)

The acoustic-pressure of a probe also depends on the angle from the beam axis. Figure 2-31 shows the far-field angular pressure radiation pattern, consisting of a main lobe centered on the z-axis and several side lobes. The angle at which the main lobe becomes zero = $\sin^{-1}(0.61\lambda/d)$ (Shung 1996). Accordingly, as the ratio of the wavelength

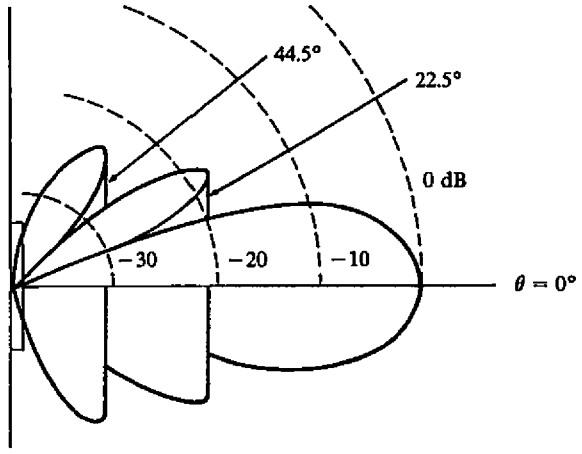

Figure 2-31: Beam pattern for a circular, plane piston (Kinsler et al 2000)

to the transducer aperture increases, this angle decreases and the beam becomes narrower. The minor lobes at larger angles are of little concern in NDE. The decrease of

beam pressure is reported in decibels, maximum at the center = reference (Kinsler et al 2000). The angle of divergence of the beam 'ϕ' can be calculated via diffraction from:

$$\sin\left(\frac{\phi}{2}\right) = 1.2\times10^{-3}\frac{\lambda}{d} \quad (47)$$

In the immersion method, the ultrasonic beam first passes through a liquid, then enters the test object. When the solid test object's surface lies parallel to the transducer face (perpendicular to the beam), a simplified presentation applies. The sound field in the test object appears shortened in the sound direction, irrespective of the location of the interface in the sound field, as per ratio of acoustic velocities. For steel in water, the C_{water}/ C_{steel} ratio is ¼. The sound-field thus is shrunk to ¼ and the angle of divergence of the far field increases 4-fold. In addition, the acoustic pressure values within the test material, for vertical incidence, are reduced by the transmittance factor of the interface (Krautkramer 1983).

Most ultrasonic measurements are conducted in pulsed mode. Thus, it is important to know how the sound pattern (Figure 2-31), changes under transient excitation. Figure 2-32 shows the radiation patterns for transient excitation along the central axis of a circular transducer in the far-field (Wells 1977). The interference patterns determining the shape of the field, may not fully develop under transient excitation, in contrast to the continuous wave condition, thus the field patterns are simpler. Figure 2-33 shows

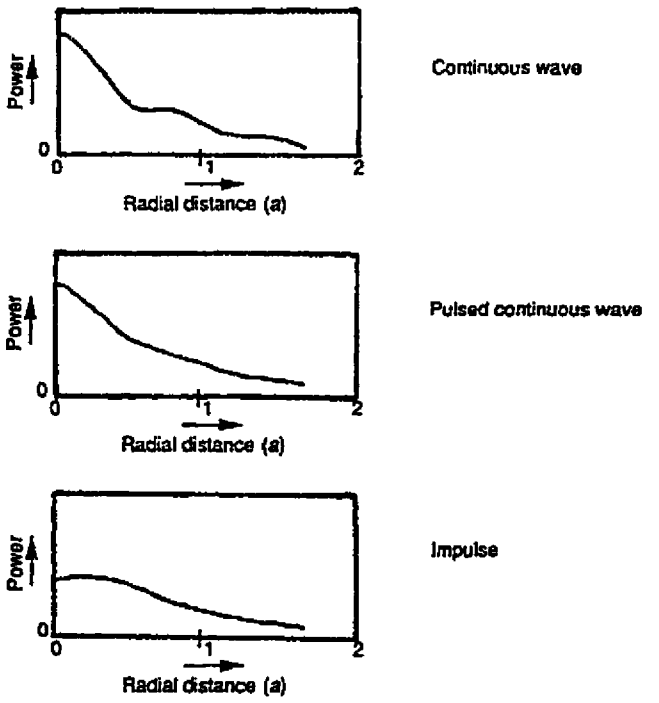

Figure 2-32: Effect of excitation on field pattern across a vibrating piston at normalised axial distance (Wells 1977)

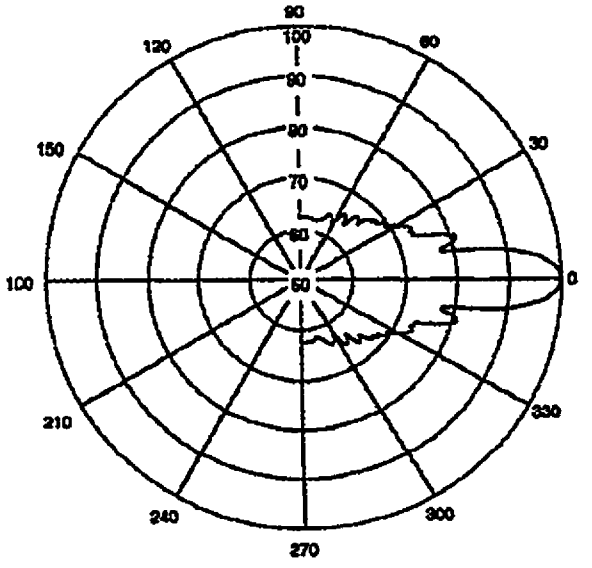

Figure 2-33: Radiation pattern of a single-element disc transducer excited by a pulse (Shung 1996)

the angular-intensity, radiation-pattern in the far-field for a pulsed transducer (Shung 1996). The radiation characteristics are smoother vis a vis a continuous wave transducer.

If the surface from which the ultrasound field is developed is part of a sphere, a focussing effect can be achieved at any position within the near-field of the equivalent flat source and down to the radius of the sphere. This is illustrated in Figure 2-34 (Wells 1977). The focal region in this figure is represented by an ellipse. In practice, a point focus cannot be produced. The width and length of the ellipse, W and L, depend on the radius of curvature and wavelength of the sound field (Wells 1977).

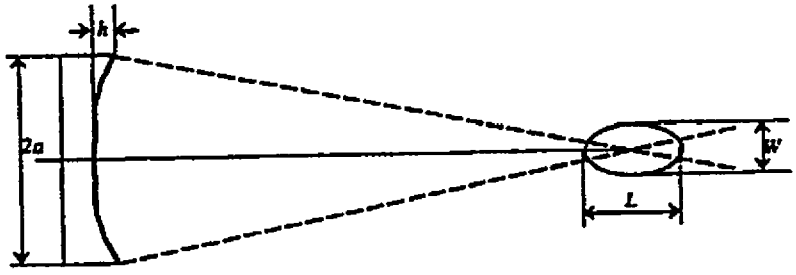

Figure 2-34: The effect of focusing (Wells 1977)

2.8.7 Focused Ultrasonic Transducers

The primary function of acoustic focusing is improved lateral resolution at a certain axial range. Principles are analogous to optics. Focusing can be achieved with a lens or spherical/ cylindrical-shaped transducers (Shung 1996). The latter involve a concave lens cemented to a flat piezoelectric crystal or, a curved, ground piezoelectric material. Curved transducers provide a well-defined acoustic field with limited noise and energy losses. Cylindrical transducers develop a line-focus (Shung 1996).

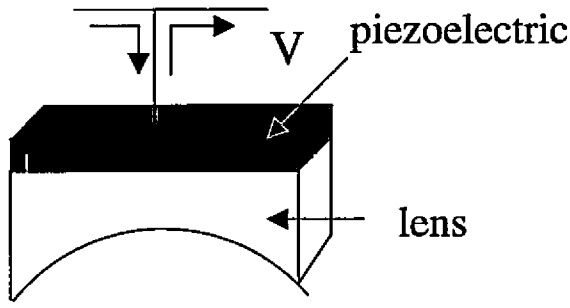

Figure 2-35: Flat piezoelectric element focused by a cylindrical/ spherical lens

A flat piezoelectric element produces a quasi-plane wave pulse, which is focused by a spherical/cylindrical lens (Figure 2-35). Typical lens materials are epoxy, sapphire, silicon, quartz, acrylic, and aluminum; all with low Reflection Coefficients (Shung 1996). The main disadvantages of acoustic lenses are aberrations and energy losses from reflections and attenuation (Gilmore 1999).

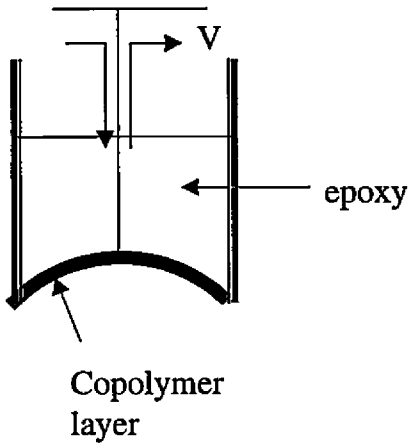

Figure 2-36: Copolymer focused transducer

Figure 2-36 is a schematic of a curved, polymer, piezoelectric, line-focused transducer. To obtain broad-band characteristics, the piezoelectric element is bonded to a matched backing.

The focal distance is the distance between the curved lens/ piezoelectric and the point of convergence of the sound beam. This distance shortens when the ultrasonic beam propagates from a fluid into a solid. The reduction can be determined via geometrical analysis of the position of the front surface of the material along the beam path. Because of the difference of velocities for the sample and water, the sample surface acts as a second lens more powerful than the acoustic lens. Thus the focal spot now occurs very close to the material surface - Figure 2-37 (Bar-Cohen et al 1996).

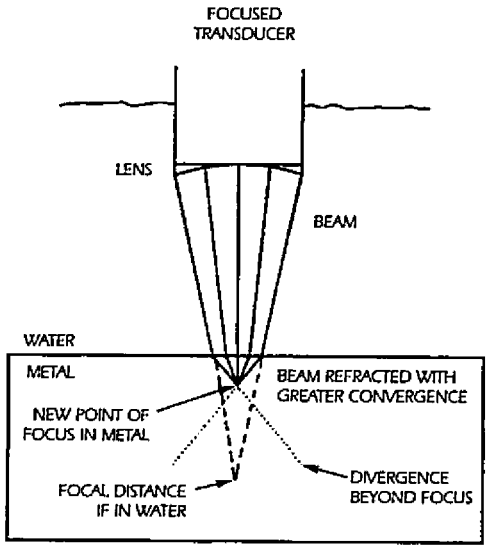

Figure 2-37: Ultrasonic focus effect in metals, demonstrating effect of second lens as result of immersion in water (Bar-Cohen et al 1996)

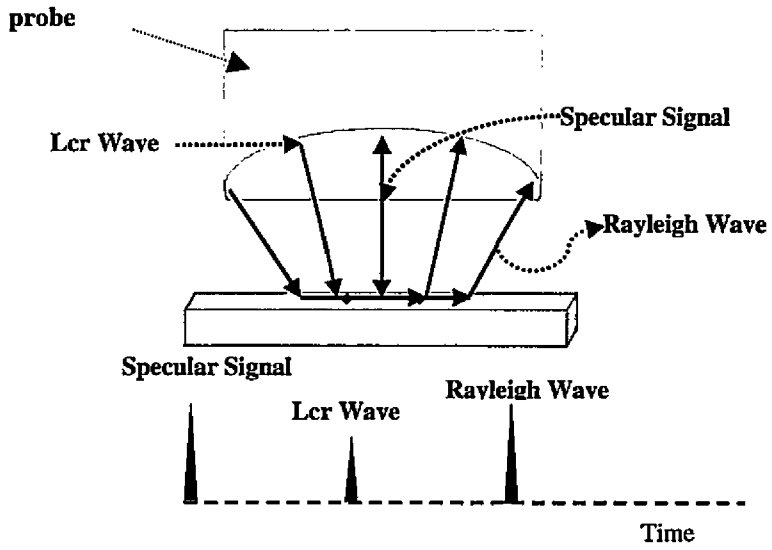

Figure 2-38: Schematic of a focused transducer, indicating the sound propagation paths.

Figure 2-38 shows the output of a defocused transducer in the time domain. The normal (center) component of the incident beam reflected directly back to the lens and is termed the "specular-reflection". Other regions of the transducer excite the R_w and L_{cr} waves (at the appropriate critical angles). These propagate along the surface and re-radiate back into the water to be collected by the lens. The relative arrival times of signals via these paths as a function of the distance between the lens and the solid, give a measure of the surface wave velocities via (Gilmore 1999):

$$V_{SAW} = \frac{V_l}{\sqrt{1-\left(1-\frac{V_l \Delta T}{2z}\right)^2}} \quad (48)$$

where V_{SAW} - velocity of the surface acoustic wave, V_l – the longitudinal wave velocity in water and ΔT – the difference of travel time between the surface and specular waves.

2.8.8 Bulk-Mode Ultrasonic Transducers for Surface Wave Generation

Bulk-mode transducers also generate surface waves. Figure 2-39 shows a schematic thereof. A piezoelectric element is placed on a plexiglas-shoe (wedge) (Bray 2001), the latter cut so the incident wave strikes the sample at the critical angle, producing a surface wave. Thus, depending on the incidence angle, a different mode of surface wave can be created.

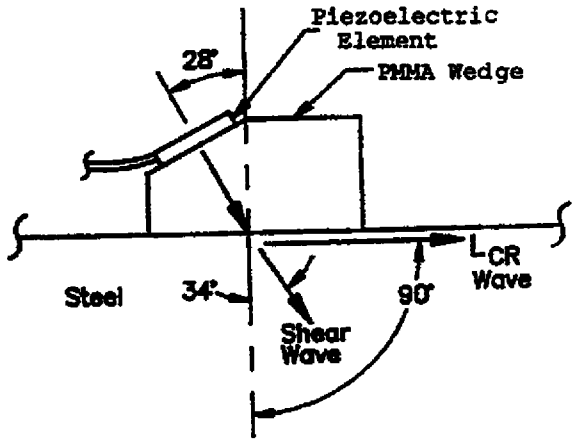

Figure 2-39: PMMA wedge used with a piezoelectric element to create an Lcr wave (Bray 2001)

Part B: Ultrasonic Determination of Residual Stresses in Component Surfaces

2.9 Residual Stresses in Materials

In the absence of external forces or thermal gradients, residual stresses are those locked into a material after manufacture and processing,. They develop during processes involving machining, material deformation, heat treatment, and operations involving chemical reactions, precipitation, diffusion or phase transformation (Chance et al 2001). They challenge the safety of components and structures, i.e., 'silent killers', that lead to failure at external loads far below those predicted.

The magnitude and distribution of residual stress (both critical to component performance), must be considered in design. It is important that stress equilibrium is maintained in a free-standing body (Kandil et al 2001). Surface tensile residual stresses, plus tensile service stresses, can be particularly detrimental, if their combination exceeds the yield of the material. Such stresses are a major cause of premature fatigue failure, stress-corrosion cracking and warping (Bray et al 1996). Surface, compressive residual stresses, that counter applied tensile stresses, can increase the load bearing capacity of a component, its fatigue strength and its resistance to stress-corrosion cracking (Chance et al 2001). Thus residual stresses can be beneficial when they operate in the plane of the applied load and are opposite in sign.

Residual stresses can be divided into macro- and micro-stresses (Kandil et al 2001). Both may be present at one time. Macro-residual stresses (Type 1) vary within the body of the material over a range >> the grain size. Micro-residual stresses (Type 2 or 3)

result from differences within the material microstructure. Type 2 residual stresses operate at the grain size level. Such may be observed in single-phase materials due to anisotropic behavior from grain to grain. They may develop in multi-phase materials as a result of different phases having different properties. Type 3 residual stresses are generated at the atomic level and may result from crystalline defects. Micro-residual stresses can change sign and/or magnitude over distances comparable to the material grain size (Kandil 2001).

A variety of residual-stress-measurement techniques exist, e.g.: hole-drilling, X-ray-diffraction (XRD), neutron-diffraction, layer removal/curvature, ultrasonics and magnetics (Matzkanin et al 2001). Mechanical relaxation methods require material removal, thus are destructive. X-ray and neutron diffraction, the magnetoelastic effect, and ultrasonic techniques are nondestructive. Diffraction methods measure surface stresses by detecting small changes of inter-planar spacing in a crystal. Magnetoelastic and ultrasonic techniques employ 'magnetoelastic' and 'acoustoelastic' effects, respectively, i.e. the effect of internal strain versus the magnetic noise level or the velocity of an acoustic wave (Matzkanin et al 2001). Since the acoustic wave can penetrate deep into a material with limited energy and the acoustoelastic effect mainly depends on the internal strain of the material, this technique is capable of detecting either applied or residual stresses nondestructively. The present work utilizes the ultrasonic method, still in its infancy, that promises to be fast and inexpensive. The results generated are compared with those via XRD.

2.10 The Ultrasonic Method of Detecting Residual Stresses

The acoustoelastic effect is the basis of the ultrasonic stress measurement method. It refers to changes of velocity of elastic wave propagating in a body under static, elastic deformation (stress). The "stress" is determined by transmitting a sound wave of < 1 - several MHz in a specimen and measuring the time-of-flight (or some other velocity-related property). The variation of the velocity of ultrasonic waves in a stressed solid is related to the residual stress state via the third-order elastic constants of the material (Ruud 1982).

2.10.1 Other Material Artifacts that Influence the Velocity of Surface Ultrasonic Waves

A problem with the acoustoelastic technique of stress measurement is that nominally identical materials may exhibit slight differences of wave speed and Acoustoelastic Constant (Thompson et al 1995). The former variations are associated with material texture, grain-scattering and surface roughness (Figure 2-40). These effects must therefore be corrected out, to determine the change of sound-velocity exclusively due to the residual stresses.

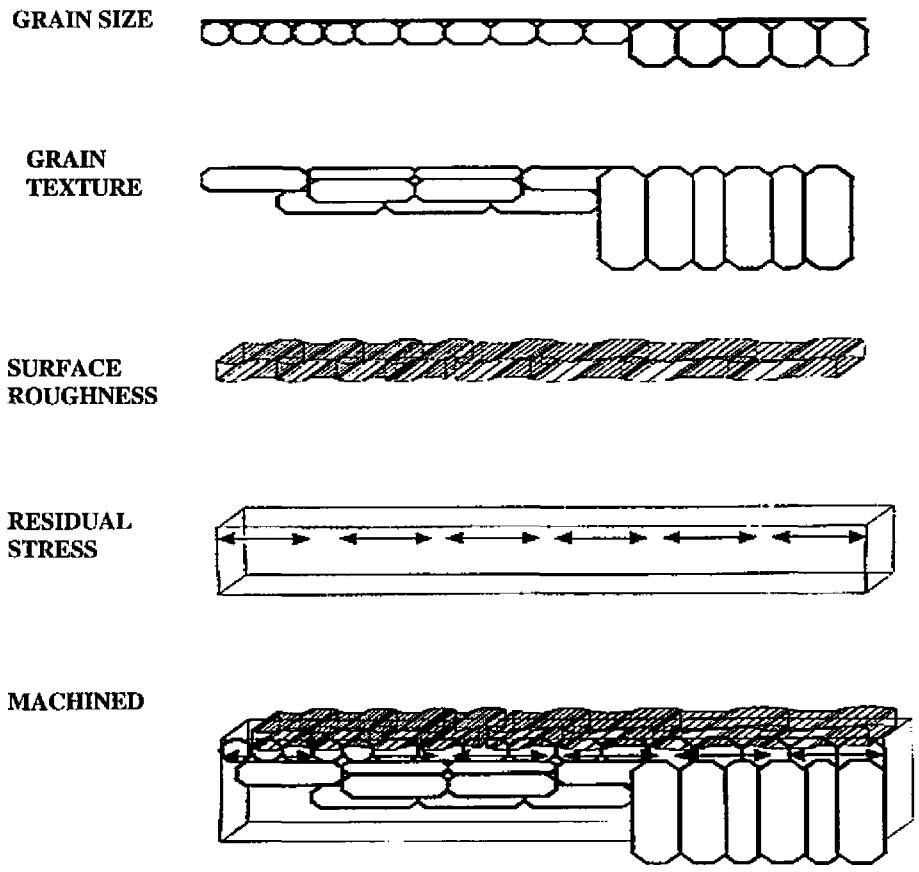

Figure 2-40: Surface artifacts influencing the velocity of the surface waves

Maxfield (2000) developed a model for the interpretation of elastic wave behavior specifically for machined samples. The model assumes the wavelength of a surface wave is larger (at least four times) than the deepest surface anomaly. In this way he removes the surface roughness effect on sound velocity. He also assumes the elastic wave displacement is constant over the effective, wave-penetration depth. He writes the surface wave velocity as the sum of three terms:

$$V_{SW} = (\varepsilon,T) = V_i^m(\varepsilon,T) + \Delta V_g^m(\varepsilon,T) + \Delta V_\sigma^m(\varepsilon,T) \quad (49)$$

where m designates the wave mode being considered (R_w or L_{cr}) and V_i is a reproducible reference state (before machining) that contains some texture and strain contributions to the velocity (obtaining a texture and strain free material is virtually impossible); ΔV_g is the contribution to velocity change of grain scattering and other texture effects; and ΔV_σ is the contribution to the velocity change of residual and applied stresses. Although the two changes in velocity are assumed independent, this is not necessarily true.

Partial differentiation of the Equation 49 with respect to strain (ε) gives:

$$\frac{\partial V_{SW}}{\partial \varepsilon}(\varepsilon,T) = \frac{\partial V_i^m(\varepsilon,T)}{\partial \varepsilon} + \frac{\partial \Delta V_g^m(\varepsilon,T)}{\partial \varepsilon} + \frac{\partial \Delta V_\sigma^m(\varepsilon,T)}{\partial \varepsilon} \quad (50)$$

The left hand side of this Equation is a quantity that can be measured. The $\partial V_i^m(\varepsilon,T)/\partial\varepsilon$ is zero to the first order in the strain, ε. In theory, the remaining two terms can be separated by making measurements at different frequencies because $\partial V_g^m(\varepsilon,T)/\partial\varepsilon$ is the only term with a frequency dependence (due to grain scattering). By plotting $\partial V_{SW}^m(\varepsilon,T)/\partial\varepsilon$ .vs. f^2 at each strain and extrapolating the curves to zero frequency, it should be possible to obtain a reasonable estimate for $\partial V_\sigma^m(\varepsilon,T)/\partial\varepsilon$. Results gathered in the present study are related to this model.

2.10.2 The Physical Principles of Solid Acoustoelasticity

Ultrasonic methods of stress measurement utilize the deviation from linearity of Hookes' Law of Elasticity ($\sigma = M\varepsilon$, where 'σ' - stress, 'ε' - strain and 'M' - elastic modulus). In the presence of residual stress, this deviation is the "anharmonic" property of the solid represented by a power series: $\sigma = M\varepsilon + C\varepsilon^2 + D\varepsilon^3 + ...$, where 'C' – is termed the third-order anharmonic-constant, 'D' – the fourth, etc. (Ruud 1982). Terms past the third-order 'C', are assumed negligible. A simplified form of the anharmonic stress/ strain law is:

$$\sigma = M\varepsilon + C\varepsilon^2 \quad (51)$$

which can be rewritten:

$$\sigma = \varepsilon(M + C\varepsilon) \quad (52)$$

The term in parentheses is approximately related to the velocity of sound, i.e.:

$$\rho V^2 \approx M + C\varepsilon \quad (53)$$

where 'ρ' is the density of the medium and 'V', the velocity of sound therein. If this Equation is rewritten as:

$$V = \sqrt{\frac{M + C\varepsilon}{\rho}} \quad (54)$$

it is clear the ultrasonic velocity depends on the Elastic Modulus and density. If M+Cε = M', then:

$$V = \sqrt{\frac{M'}{\rho}} \quad (55)$$

and by differentiating this Equation and dividing by the initial sound velocity:

$$\frac{\Delta V}{V} = \frac{1}{2}\left(\frac{\Delta M'}{M'} - \frac{\Delta \rho}{\rho}\right) \quad (56)$$

It is readily seen that a fractional change in Elastic Modulus or density influences the velocity. The density of a material changes under stress, hence also does the speed of sound (Ruud 1982).

Equation (53) may be rewritten to give the approximate dependence of velocity on strain (Thompson et al 1995):

$$V = \sqrt{\frac{M}{\rho}}\left(1 + \frac{C}{2M}\varepsilon\right) \quad (57)$$

and, solving for strain:

$$\varepsilon = 2\left(V\sqrt{M\rho} - 2M\right)/C \quad (58)$$

The anharmonic properties of materials result in a number of phenomena used to measure stress. These include the velocity dependence on the Elastic Modulus, the dispersion of frequency-amplitudes of surface-waves and the birefringence of orthogonally-polarized shear-waves (Ruud 1982). The present work focuses on the velocity dependence on the Elastic Modulus for stress measurement in surfaces.

2.10.3 The Acoustoelastic Effect in Solids

The Acoustoelastic Effect can be described by the phenomenological equation:

$$V = V_0 + K\sigma \quad (59)$$

where 'V' is the velocity of a wave in the stressed specimen, 'V_0' the velocity when no stress is applied, 'σ' the stress and 'K' the Acoustoelastic Constant (Thompson et al 1995).

Assuming the material is isotropic and all three principal stresses are present, this Equation becomes:

$$\frac{V_{pp} - V_L^0}{V_L^0} = \hat{K}_1\sigma_p + \hat{K}_2(\sigma_q + \sigma_s) \quad (60)$$

and

$$\frac{V_{pq} - V_T^0}{V_T^0} = \hat{K}_3\sigma_p + \hat{K}_4\sigma_q + \hat{K}_5\sigma_s) \quad (61)$$

where 'V_{pp}' is the velocity of a wave propagating in direction 'p', with particle displacement in direction 'p', 'V_{pq}' the velocity of a wave propagating in direction 'p', with particle displacement in the 'q'-direction, and 'σ_p', 'σ_q', 'σ_s' are the principal stresses in the 'p'-, 'q'-, and 's'-directions, respectively. $K_1, \ldots, K_5$ are the Acoustoelastic Constants, normalized to the stress-free velocity (V_0). The first equation applies to the propagation of longitudinal waves, the second describes the propagation of transverse waves. The 's'-direction is perpendicular to both the 'p' and 'q' directions (Thompson 1995).

The five normalized Acoustoelastic Constants of Equations 60 and 61 have different values, indicating the sensitivity of different measuring configurations will vary. This was illustrated by Egle and Bray (1976) and will now be described.

Figure 2-41 shows a bar under tension wherein a wave propagates in three perpendicular directions. In Figure 2-41 a), the wave propagates parallel to the load with the velocity of particles in the same direction (longitudinal wave), V_{11}, V_{12}, and V_{13} are

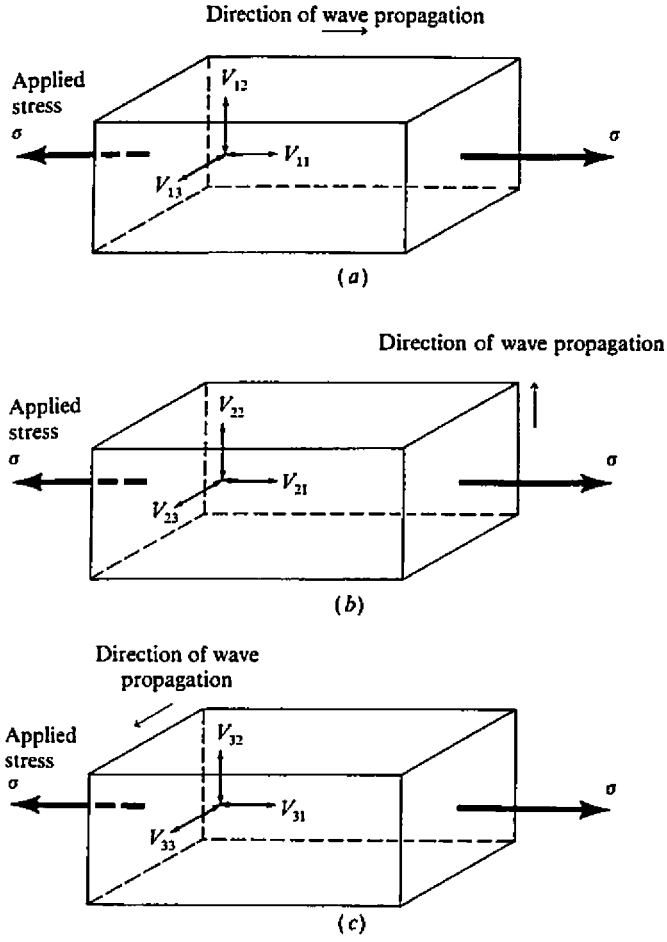

Figure 2-41: Velocity of plane waves and stress field in an orthogonal coordinate system (Bray et al 1989)

the velocities of the perpendicular plane waves (shear-waves). Waves propagating in other directions with other velocities are shown in Figure 2-41 (b) and (c). The velocities are indexed such that the first subscript is the wave propagation direction and the second the direction of polarization (direction of movement of the particles).

Egle and Bray (1976) studied the sensitivity of these waves to strain in rail-steel and their results are shown in Figure 2-42. Most significant variation of travel time with strain is for longitudinal waves, followed by shear waves, when particles vibrate in the direction of the load. Other waves show insignificant sensitivity to the deformation The normalized Acoustoelastic Constants, 'K', are related to the slopes of the plots in Figure 2-42. The

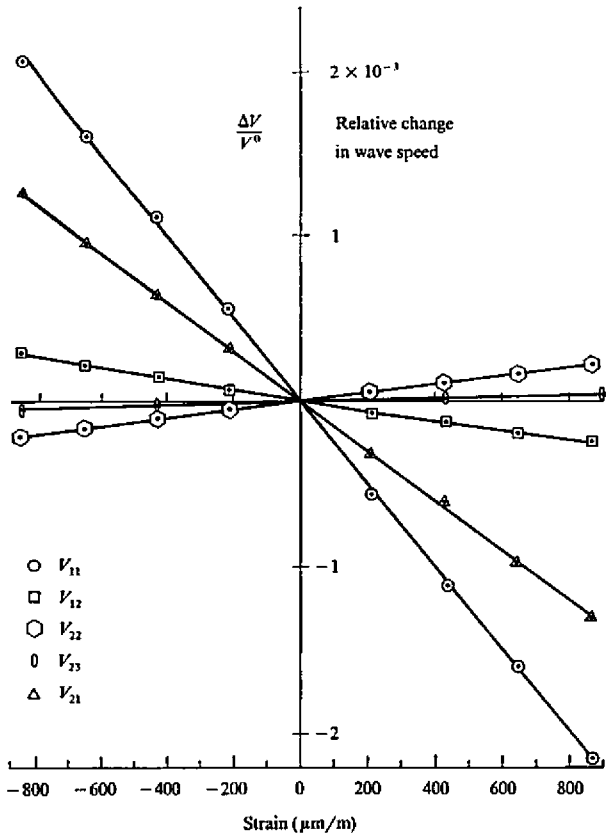

Figure 2-42: Relative changes in wave speed with strain in rail steel (Egle and Bray 1976)

values of the latter can vary from material to material, and/ or with material microstructure. However, the trend illustrated in Figure 2-42 for steel is the same for most other materials (Thompson et al 1995).

Hughes and Kelly (1953) derived expressions for the velocity of elastic waves in a solid under stress. The description here follows a summary prepared by Egle and Bray (1976). The speed of a plane wave traveling parallel to the load is related to the strain (α), via:

$$\rho_0 V_{11}^2 = \lambda + 2\mu + (2l + \lambda)\theta + (4m + 4\lambda + 10\mu)\alpha_1 \quad (62)$$

$$\rho_0 V_{12}^2 = \mu + (m + \lambda)\theta + 4\mu\alpha_1 + 2\mu\alpha_2 - \frac{1}{3}n\alpha_3 \quad (63)$$

$$\rho_0 V_{13}^2 = \mu + (m + \lambda)\theta + 4\mu\alpha_1 + 2\mu\alpha_3 - \frac{1}{3}n\alpha_2 \quad (64)$$

where α_1, α_2, and α_3 are the components of the homogeneous triaxial principal strain, ρ_0 the initial density, λ and μ the second order elastic constants, $\theta = \alpha_1 + \alpha_2 + \alpha_3$, l, m and n the third-order Elastic Constants, V_{11}, V_{12} and V_{13} the velocities of a wave traveling in direction 1 with particle displacement in directions 1, 2, and 3, respectively.

It follows from Equation 62 that, for uniaxial stress ($\alpha_1 = \varepsilon$, $\alpha_2 = \alpha_3 = -\nu\varepsilon$, where ε is strain in direction 1 and ν the Poisson's Ratio), the variation of velocity with the strain follows from:

$$\frac{dV_{11}/V_{11}}{d\varepsilon} = 2 + \frac{(\mu + 2m) + \nu\mu(2 + 2l/\lambda)}{\lambda + 2\mu} = K_{11} \quad (65)$$

where K_{11} is the Acoustoelastic Constant (AC) for the longitudinal-bulk (or L_{cr}) wave. The value of the AC reflects a wave's sensitivity to stress. Values for the other direction Acoustoelastic Constants can be obtained the same way. The variation of velocity V_{11}, controlled by the coefficient K_{11}, is the largest, followed by variations of velocity V_{21} (Figure 2-42). Thus these waves are best employed for stress evaluation.

One-dimensional application of the stress-strain relations for elastic solids ($\sigma = E\varepsilon$), facilitates stress calculation. Combining this relation with Equation 65:

$$\frac{dV_{11}/V_{11}}{d\varepsilon} = \frac{E\left(\frac{dV_{11}}{V_{11}}\right)}{d\sigma} = K_{11} \Leftrightarrow d\sigma = \frac{E\left(\frac{dV_{11}}{V_{11}}\right)}{K_{11}} \quad (66)$$

where '$d\sigma$', is the stress variation (MPa), 'E' the Elasticity Modulus(MPa), 'V_{11}' the velocity with which the wave travels the material (m/s) in the absence of stress.

It has been suggested that this linear relationship persists even beyond the yielding point of the material (Thompson et al 1984). The relative variation of speed can be calculated via the relative variation of the time for the wave to go from the sender to the receiver (dt/dt_0). Equation 66 can be used for the other wave directions, provided values of Acoustoelastic Coefficient K are changed.

Acoustoelastic Coefficient values are obtained by experimental calibration (i.e., tensile-test (Tanala et al 1995) or bend-test of the same material (Tang et al 1996, Lindgren et al 1998)). These Coefficients are determined for a given material and wave mode by measuring the propagation velocity (or propagation-time) versus applied stress on the material.

Duquennoy et al (2002) theoretically determined the Rayleigh wave Acoustoelastic Coefficients for orthotropic Aluminum 2214, via the density and second-, and third-order Elastic Constants. These calculated coefficients were in good agreement with those measured in a tensile test.

Since microstructure and texture determine the elastic behavior of a material, they also influence the Elastic and Acoustoelastic Constants. Heyman et al (1983) studied the

Table 2-3: Acoustoelastic coefficients of various grades of steel; C/A=$1/\hat{K}_1$, C/B=$1/\hat{K}_2$, K/D=$1/\hat{K}_3$, K/H=$1/\hat{K}_4$, K/F=$1/\hat{K}_5$ (Schneider 2001).

Material	C/A	C/B	K/D	K/H	K/F	I/S
Railroad rail,	-66 ± 10%	/	-565	-127 ± 7%	/	-123 ± 5%
Type UIC 60						
different manufacturers,	-67	/	-672	-132	/	-133
straightened						
and not	-67	/	-672	-132	/	-137
straightened	-70	/	-799	-136	/	-141
	-71	/	-830	-137	/	-142
Steel S255N	-150 ± 25%	504	2011	-176	1743	-160
Steel C 105 W1	-190	350	/	-180	787	-147
17CrNiMo 6	-137 ± 20%	485	/	-162	740	-133
20CrNiMo 13	-81 ± 11%	769	-730	-133 ± 6%	/	-118 ± 5%
24CrMo5V	-81	/	-1031	-143	/	-149
24CrMo5V	-80	/	-1554	-148	/	-157
30CrMoNiV 5 11	-91	/	/	-158	/	-163
22NiMoCr 3 7	-133 ± 13%	/	1816	-180 ± 7%	/	-166 ± 6%
22NiMoCr 3 7	-122	1013	/	-173	/	-164
22NiMoCr 3 7	-109	723	/	-162	/	-163
24NiCrMoV 14 5	-204 ± 17%	929	588	-220 ± 8%	/	-227 ± 7%
Ni-Steel	-89 ± 11%	/	/	-152	/	-155
15MnNi 6 3	-91	903	/	-145	/	-136
X6CrNi 1811	-68 ± 11%	/	/	-177 ± 8%	-141	108 ± 11%
X6CrNi 1811	-78	/	734	-189	-149	103
WC-Co Sintered Met.	-312 ± 12%	/	/	-502 ± 8%	/	-484 ± 6%
WC-Co Sintered Met.	-278	/	/	-475	/	-470

sensitivity of Acoustoelastic Constant values to changes of microstructure. They reported the variation of Acoustoelastic Constants and longitudinal-wave velocities, with volume-

fraction of precipitates in carbon steel and heat-treated aluminum alloy. They revealed the Acoustoelastic Constants for 6061 and 2024 alloys decreased as a function of second-phase precipitates. Razvi et al (1987) show the Acoustoelastic Constants do not change significantly with ageing time, although the average size of the precipitate particles changes. Schneider (2001) studied the effect of microstructure and texture on the electromagnetic and acousto-elastic properties of steel samples cut from welded plates. He concluded that texture and microstructural influences were definitely present, but not as significant as expected. Table 2-3 contains the data collected for different grades of steel, Table 2-4 summarizes data from specimens cut from different parts of a welded steel plate, and Table 2-5 from specimens cut parallel and perpendicular to the rolling direction of various steel grades. Tanala (1995), when studying the residual

Table 2-4: The influence of microstructure on the acoustoelastic coefficients in a welded 15MnNi 6 3 steel plate; C/A=$1/\hat{K}_1$, C/B=$1/\hat{K}_2$, K/D=$1/\hat{K}_3$, K/H=$1/\hat{K}_4$, K/F=$1/\hat{K}_5$ (Schneider 2001).

Microstructure	C/A	C/B	K/D	K/H	K/F	1/S
Ferrite-Pearlite Ferrite ☮ 50%	-75	1920	-826	-136		-136
Ferrite 30-40% + Intermediate	-70	1755	-735	-133	1724	-144
Intermediate	-80	1389	-1064	-141		-142
Intermediate + Widmanstätten	-101	1639	/	-165	2273	-178
Intermediate + Retained Austenite	-84	1563	-1449	-146	/	-150
Error	≤⇧ 10%			≤⇧ 10%	/	≤ ⇧ 2%

stresses in welded joints of rolled aluminum 5086 alloy pipe and cold-worked stainless steel pipe, measured the Acoustoelastic Coefficients with Rayleigh and L_{cr} waves in both the rolling and transverse directions. To obtain biaxial stresses, he measured the Acoustoelastic Coefficients parallel and perpendicular to the applied uniaxial load. All stress measurements were performed in the rolling direction.

Table 2.5: The influence of rolling texture on the acoustoelastic coefficients in steel grades used for pipeline tubes; samples cut parallel (R) and perpendicular (W) to the rolling direction; C/A=$1/\hat{K}_1$, C/B=$1/\hat{K}_2$, K/D=$1/\hat{K}_3$, K/H=$1/\hat{K}_4$, K/F=$1/\hat{K}_5$ (Schneider 2001).

Material Elastic Anisotropy %		C/A	C/B	K/D	K/H	K/F	1/S
EStE 690 V A	R	-74	935	-505	-126	741	-107
1,5 ‰	W	-82	765	-704	-135	/	-122
StE 240.7 TM	R	-76	759	-589	-129	/	-117
12 ‰	W	-108	922	-5044	-159	/	-144
StE 240.7 TM	R	-72	561	-433	-120	789	-104
18‰	W	-121	/	4421	-172	1520	-154
StE 385.7 TM	R	-60	475	-296	-107	930	-96
45 ‰	W	-95	793	-2110	-155	/	-167

Of interest is whether the Acoustoelastic Constants are frequency dependent. Tang and Bray (1996) showed the Acoustoelastic Constants for 2.25 and 5.0 MHz frequencies in a uniaxial tensile field in 4140 steel are very close, i.e. –2.2 and –2.365, respectively.

2.11 Bulk Ultrasonic Waves

2.11.1 Residual Stress Measurements via Bulk Ultrasonic Waves

Ultrasonic methods use bulk waves to measure the average stress through a sample section. Waves used are longitudinal, shear, and oblique SH. Each has advantages and disadvantages (Schramm et al 1995).

Much previous work, using the acoustoelastic effect for stress measurement, concentrated on the velocity difference of shear waves, polarized parallel and perpendicular to the uniaxial stress and traveling perpendicular to the stress axis (King et al (1973), Schneider et al (1982), King et al (1983), Thompson et al (1994)). The relationships between stress and ultrasonic wave velocity via acoustic-birefringence was first described by Crecraft (1967). Acoustic birefringence is suitable to determine uniaxial stress in isotropic materials in the absence of applied stress (Hsu 1974). Modifications are required when texture is present. The technique is also limited to materials with highly parallel sides. Stresses measured are average through-the-thickness. Stress gradients cannot be detected (Bray et al 1995).

2.11.2 The Effect of Grain Texture on Bulk Ultrasonic Waves

Metals often exhibit microstructural texture: non-random distribution of crystallite orientations (Barrett et al 1980). Even in the absence of stress, the velocity of sound depends on the orientation of the propagation and polarization directions with respect to the principal texture axes (Sayers 1984). The effect of texture on wave velocity in rolled materials can be predicted. Figure 2-43 shows a plot of velocities as a function of

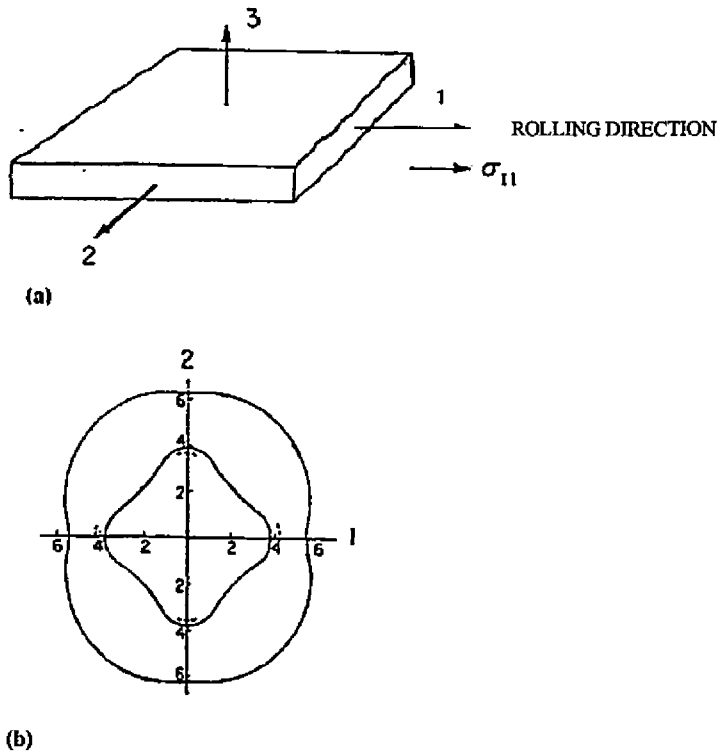

Figure 2-43: (a) Orientation of a rolled sheet of a hypothetical material (b) Angular dependences of the velocities of longitudinal waves (outer curve) and shear waves (inner curves) (Smith et al 1994).

propagation direction in the rolling plane for a unidirectionally-rolled, hypothetical material (Smith et al 1994). The outer ring is the directional variation of the bulk longitudinal wave mode, the inner ring the directional variation of the shear mode polarized in the rolling plane. Bray and Egle (1981) and Bray and Stanley (1997) discuss the effect of texture on wave velocities in rail steels, which are typically hot-rolled, AISI 1080 type with a severely distorted, cold-worked surface. Ultrasonic analysis of waves in several directions in both the cold-worked, and the lower hot rolled, regions showed a (111)[11-2] texture, approximately 30% developed in the cold-worked zone, but no

significant texture in the hot rolled region. Further, the predicted longitudinal wave velocities, within 10° of the rolling direction, showed an insignificant wave velocity change, implying special data collection procedures may be needed to minimize texture effects. Tang and Bray (1996) studied the potential texture effect in a 4140 steel bar and showed that, if spatial position could be well controlled, the texture effect can be as low as 0.02% (a 2ns change in the travel time).

2.11.3 The Effect of Microstructural Grain Scatter on Propagating Bulk Ultrasonic Waves

Grain scattering in polycrystalline materials causes sound attenuation (reorientation and mode conversion, of energy). This attenuation is a function of frequency, grain diameter, grain substructure, grain size distribution and the ratio of the grain diameter (D) to the ultrasonic wavelength (λ); D/λ (Papadakis 1984). In the Rayleigh region (wavelength >> the grain diameter), the frequency (f) dependence of the attenuation is f^4 and due to the grain size, is D^3. When the wavelength is comparable to the grain diameter (Stochastic region), the frequency dependence becomes, f^2, and the grain size dependence, D^1. Between these limits, there is a continuous change (Papadakis 1965). Considerable effort has been expended to characterize grain size via sound attenuation. Conventional ultrasonic attenuation tests measure the Attenuation Coefficient via the change of peak-height for several, backwall-echoes. An increase in grain-size results in increased Attenuation Coefficient (Papadakis 1984, Palanichamy et al 1988, Kumar et al 2002). Moreover, studies have been made of highly-attenuating materials, such as

austenitic stainless steel, where the peak heights beyond the first backwall-echo are often negligible, e.g.; Palanichamy et al (1994) used the peak height of the first backwall-echo exclusively to correlate with the grain size, using a calibration reference of the same thickness. The extent to which the height of the echo dropped was proportional to the increase of grain size.

An inverse relationship has been observed between ultrasonic-velocity and grain-size. The proposed reason is a dispersion effect. Grain scattering increases rapidly with grain diameter 'D' (approximately as D^3 in the Rayleigh region) and concurrently, the dispersion of the ultrasonic pulse becomes more evident, i.e.; higher frequencies are cancelled by scattering along the sound path length and consequently velocities decrease (Saniie et al 1987). Ultrasonic spectroscopy has been used to characterize microstructural features (Fitting et al 1981). It has been reported that, as the grain size increases, the ultrasonic peak frequency and the full-width-at-half-maximum of the autopower spectrum of the first backwall echo, decrease in stainless steel (Kumar et al 1999). Gericke (1971) used ultrasonic spectroscopy for grain-size determination in steel. The frequency characteristic of the transducer showed two, well-defined humps, centered at frequencies $\cong$ 3.5 and 6MHz, respectively. Corresponding frequency responses in steels of varying grain size showed that, as the mean grain size increased, the ratio of the heights of the two frequency humps changed, the higher frequency being preferentially attenuated by the coarser-grained material.

Palanichamy et al (1995) discovered that velocity measurement of grain size is more accurate than attenuation. Master graphs were generated for AISI 316 stainless steel,

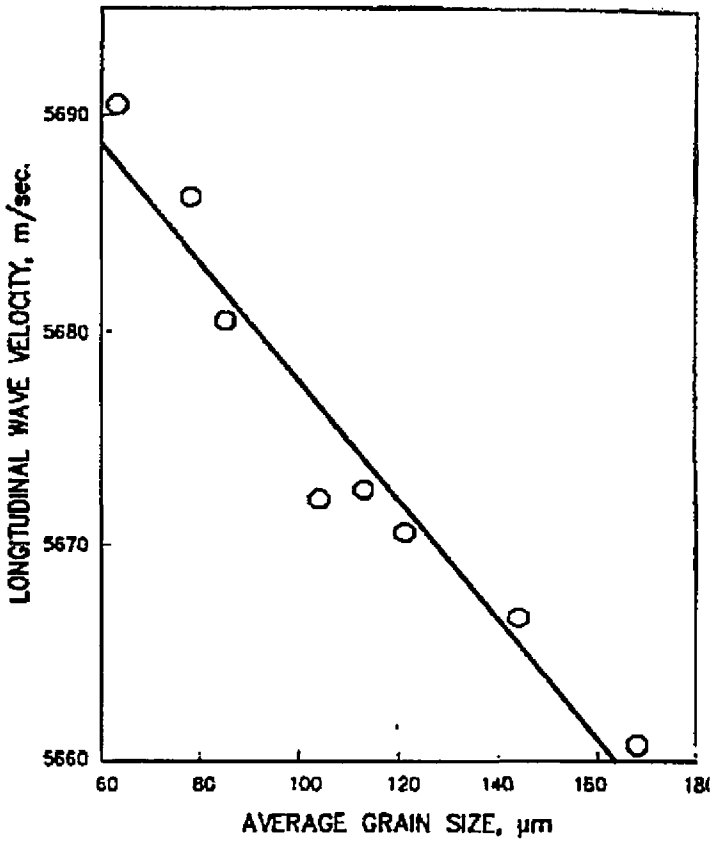

Figure 2-44: Ultrasonic longitudinal wave velocity as function of average grain size in AISI type 316 stainless steel (Palanichamy et al 1995)

relating ultrasonic, longitudinal and shear velocities (2MHz) versus the metallographically-obtained grain-size (Figures 2-44 and 2-45). Shear waves were found more sensitive to change of grain size. Murthy (2000) studied ultrasonic velocity and attenuation in polycrystalline YIG. The results he obtained with 1MHz longitudinal and transverse waves for samples of mean grain size, 3 - 30 μm, are listed in Table 2-6. The density remains ~ constant, so he attributes the continuous decrease of both velocities and the increase of attenuation with sintering-time and temperature, to the variation of

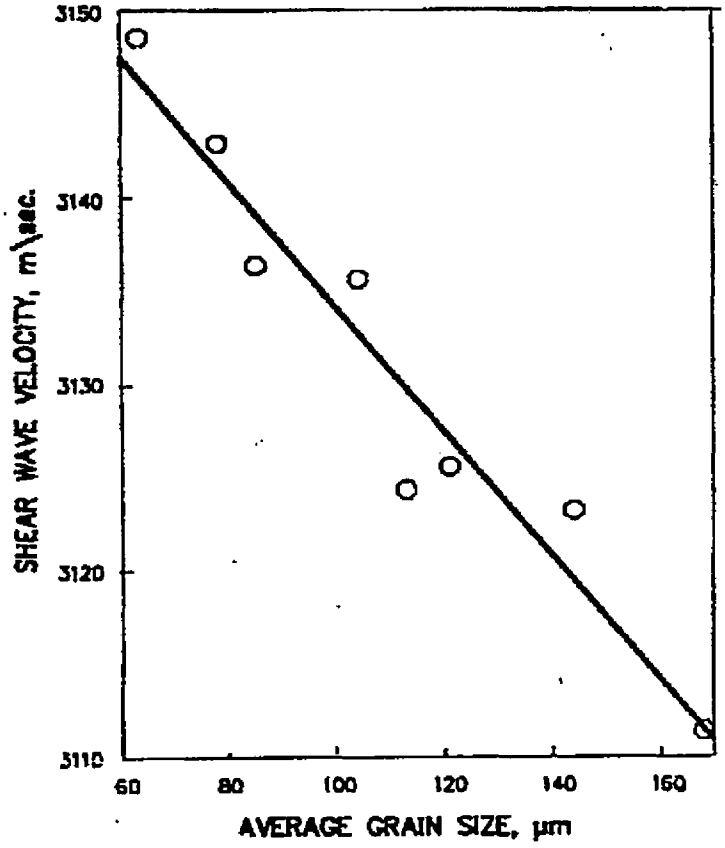

Figure 2-45: Ultrasonic shear wave velocity as function of average grain size in AISI type 316 stainless steel (Palanichamy et al 1995)

Table 2.6: Preparation and ultrasonic properties data for YIG samples (Murthy 2000)

Sample no.	Sintering temp./time (°C/h)	grain size (μm)	Density % theor.	α_1 (dB/cm)	V_1 (m/s)	V_s (m/s)	Y ($\times 10^{10}$ N/m^2)	μ ($\times 10^{10}$ N/m^2)	K ($\times 10^{10}$ N/m^2)	σ
1	1280/48	3.11	98.1	0.55	8618	4698	29.41	11.06	23.54	0.32
2	1300/48	3.62	98.5	0.58	8485	4580	27.54	10.69	22.95	0.31
3	1320/48	4.38	98.8	0.67	8304	4525	26.84	10.59	21.31	0.29
4	1350/100	12.01	99.2	0.72	8018	4488	24.95	9.01	27.72	0.31
5	1370/100	16.03	99.5	0.83	7993	4250	22.98	8.77	20.16	0.31

grain size with sintering temperature. The same inverse relationship between grain size and longitudinal and shear velocities was recently reported by Murthy (2001) for polycrystalline Ni-Zn ferrites, and for steel by Badidi Bouda et al (2003).

Some scientists argue the theoretical basis for the ultrasonic velocity correlation with grain size is non-existent, as velocity depends on the elastic properties of a material, and these have no basic dependence on grain size (Rice (1977), Ambardar et al (1996)). However, the elastic properties and the sonic velocity, in most polycrystalline materials, are influenced by grain boundary impurities and grain orientation. Consequently, there must be instances of correlation between ultrasonic velocity and average grain size in polycrystalline solids (Vary 1980). The same explanation was proposed by Palanichamy et.al (1994), who observed that velocity changes if the total number of grains in the ultrasonic beam path is small and the statistical randomness of all possible grain orientations is not satisfied, i.e., the material is anisotropic. Change of ultrasonic, longitudinal wave velocity vs. grain size was studied in Al-4.5%Cu by Ambardar et al (1996). They discovered that an increase of grain size from 330 μm to 770 μm, at 2MHz frequency, produced a 0.89% decrease of velocity (from 6349.96 to 6293.68m/s.)

2.11.4 The Effect of Surface Roughness on The Propagation of Bulk Ultrasonic Waves

Surface topography results in ultrasonic pulse scattering, which causes changes of shape and time of arrival. The use of sound to assess surface topography (principal application is to macroscopic features in ocean environs), received special attention in the

early 1950's (Tolstoy et al 1987). Scaling down to sub-millimeter wavelength regimes, led to numerous studies of the penetration of ultrasonic bulk waves into a solid, accounting for the surface roughness. The problem has been often tackled by analyzing the relationship between the amplitude 'A' of the wave and 'd_l' the thickness of a contact, liquid layer ($A=f(d_l)$). It has been shown that interference in the liquid layer on a smooth surface leads to a change of beam amplitude and of other parameters of the propagating wave (Mogil'ner (1986), Gmyrin (1992)). Plots of these parameters .vs. the depth of the contact liquid layer ('d_l'), are oscillatory. Introducing surface roughness causes a variation in 'd_l'. Methods to further develop the $A=f(d_l)$ theory have been proposed; e.g. the method of tangential planes (Kirchhoff's method) which considers the fluctuation of the acoustic field scattered by a statistically-rough surface (Gmyrin 1992). It is assumed ultrasound reflects and refracts at each point of the surface roughness as if from an infinite plane, tangential to the given point.

The small-perturbation (Kramarenko et al 1973) method assumes the roughness is small compared with the ultrasonic wavelength and has a sinusoidal profile. A rough layer leads to a reduction of beam amplitude via $A=f(d_l)$. This was confirmed experimentally. As summarized by Gmyrin (1993), the results support that: when $R_z \leq 0.1\lambda_l$ (where R_z is roughness wavelength and λ_l the wavelength of the ultrasonic waves propagating in the layer of contact liquid), the amplitude and spectral composition of the propagating ultrasonic pulse is independent of R_z, but the roughness profile and the direction of propagation of the waves through the layer, play a minor role. For large roughness ($R_z \geq 0.1\lambda_l$,) the situation is different. The amplitude 'A' decreases as R_z

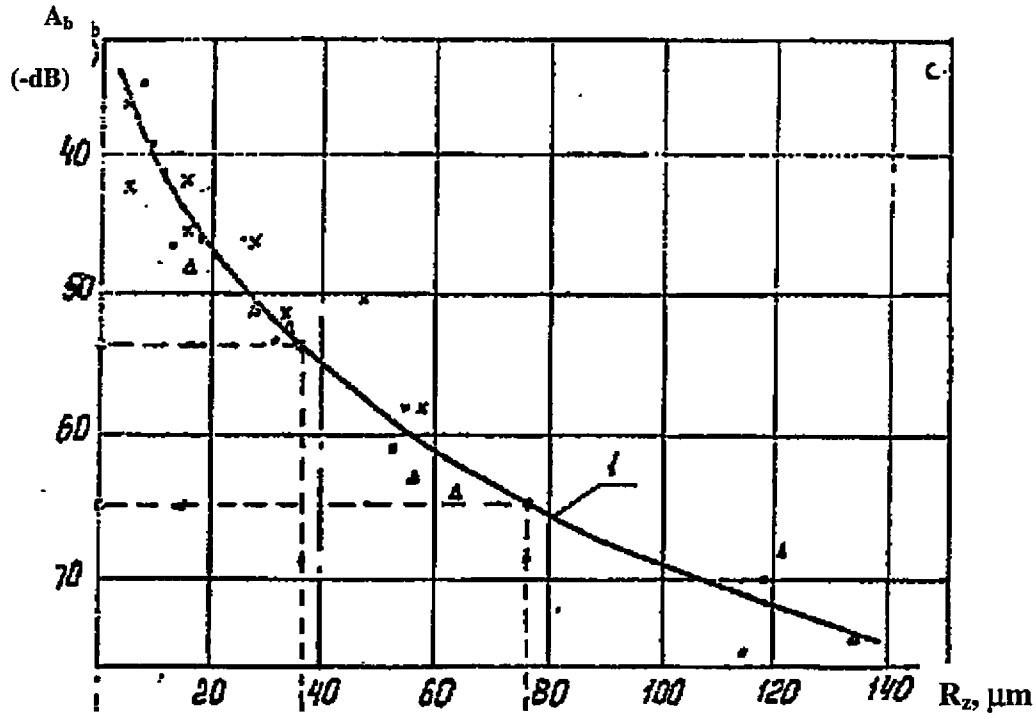

Figure 2-46: The variation of back echo signal amplitude Ab for a 4.3 MHz, 18mm ultrasonic transducer, with Rz (Shcherbinskii 1993)

increases, the spectral- composition changes (increased weight of the low-frequency components) and the pulse length increases. Thus, the roughness profile plays a considerable role, as explained by the variable initial thickness of the contact layer with the liquid (equal to the depth of the roughness layer), (Mogil'ner (1986), Rakhimov (1988)). Attempts have been made to further analyze the processes that occur in the rough surface layer, in the contact liquid layer and how they influence the propagating ultrasonic waves. Studies have focused on the amplitude of the back-echo signal, or the surface reflection amplitude, where the change of transmission or reflection

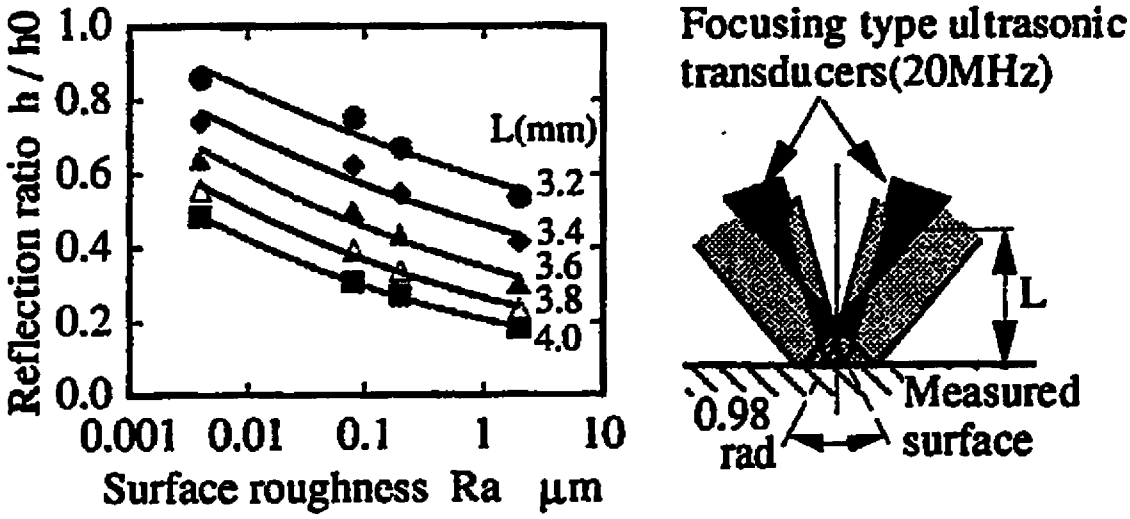

Figure 2-47: Measurement of surface roughness (Nishiwaki et al 1998)

coefficient, respectively, must be considered. Figure 2-46 is a plot by Shcherbinskii (1993) showing the variation of back-echo signal-amplitude, A_b, with R_z for a 4.3 MHz transducer. Figure 2-47 shows the plots of Nishiwaki (1998), i.e. the ratio of amplitude 'h', reflected from the surface at a distance 'L', to a maximum 'h_0' amplitude at the transducer focused distance, L=2.5mm. He observed the reflection ratio varies not only with the distance between the pitch-catch transducers and the measured surface, but also with the surface roughness.

To study stresses induced by machining, ultrasonic energy must be directed along the surface.

2.12 The Rayleigh Ultrasonic Waves

2.12.1 Residual Stress Measurement via Rayleigh Waves

The first theory of surface Rayleigh wave propagation in elastic materials under homogeneous deformation was developed for waves propagating along the principal axes of stress (Hayes et al 1961). This theory has been generalized to cover the case where the propagation direction does not coincide with one of the principal axes of stress (Iwashimizu et al 1978), and the case where the initial stress varies with plate depth (Hirao et al 1981).

Table 2-7: Rayleigh wave velocities for the epoxy and composite samples (Lindgren et al 1998).

Sample	Rayleigh Wave Velocity at 0.5 MHz (m/s)	Rayleigh Wave Velocity at 1.0 MHz (m/s)
Sample 1. Epoxy Only	1319	1385
Sample 2. Unstressed Single Fiber Tape Cured at Room Temperature	1305	1296
Sample 3. Unstressed Single Fiber Tape Cured at 40°C	1370	1314
Sample 4. Single Fiber Tape Stressed to 62 MPa During Cure	1362	1282
Sample 5. Single Fiber Tape Stressed to 103 MPa During Cure	1345	1272
Sample 6. Multi-Layered Composite Sample	1083	1095

Martin (1974) observed the Rayleigh wave velocity to change little with applied stress i.e. a fraction of 1%. A uniaxial tensile stress decreased the sonic velocity and a compressive stress increased it, as per, second order elasticity theory. A number of

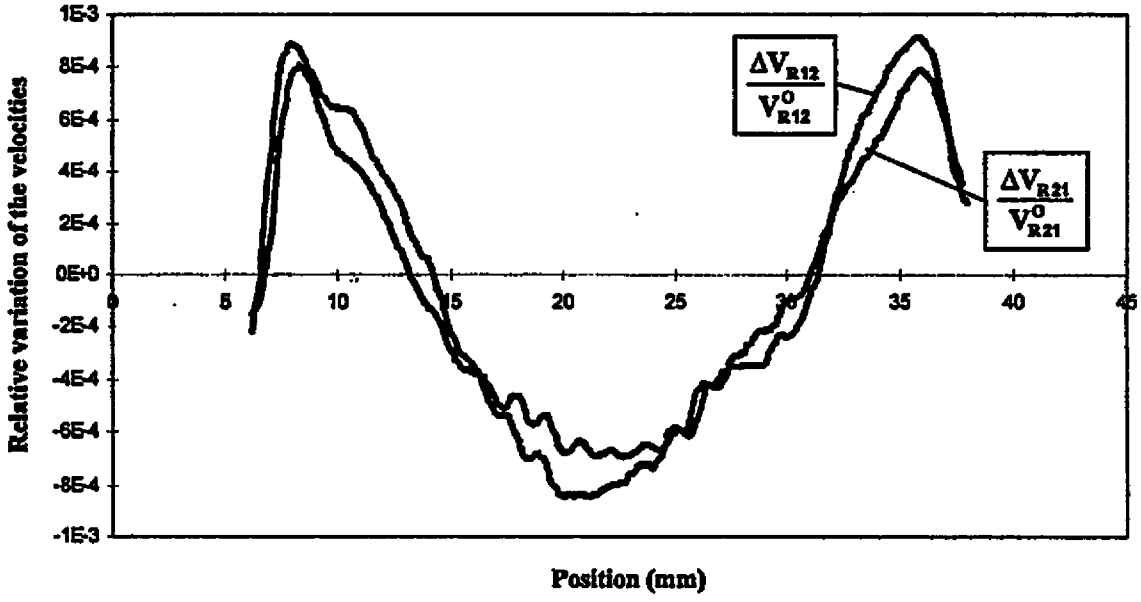

Figure 2-48: Relative variation of the V_{R12} and V_{R21} Rayleigh wave velocities versus the position in the thickness of the sheet (Duquennoy et al 1999).

subsequent studies showed the R_w wave velocity is sensitive to stresses in different materials: iron, aluminum, glass, mild steel (Pao et al (1984), Duquennoy et al (1999), Hirao et al (1981), Adler et al (1977)).

The depth of penetration of R_W into a solid is ≅ one wavelength, so one can measure stress gradients by changing R_w frequency (Hirao et al 1981). Lindgren et al (1998) identified changes of residual stress in graphite-epoxy composites as a function of depth, by controlling the Rayleigh wave frequency (Table 2-7). Compressive residual stresses

were introduced by the cure-process of the epoxy. Duquennoy et al (1999) obtained biaxial residual stress profiles in the thickness of an aluminum alloy 2214 T6 sheet by

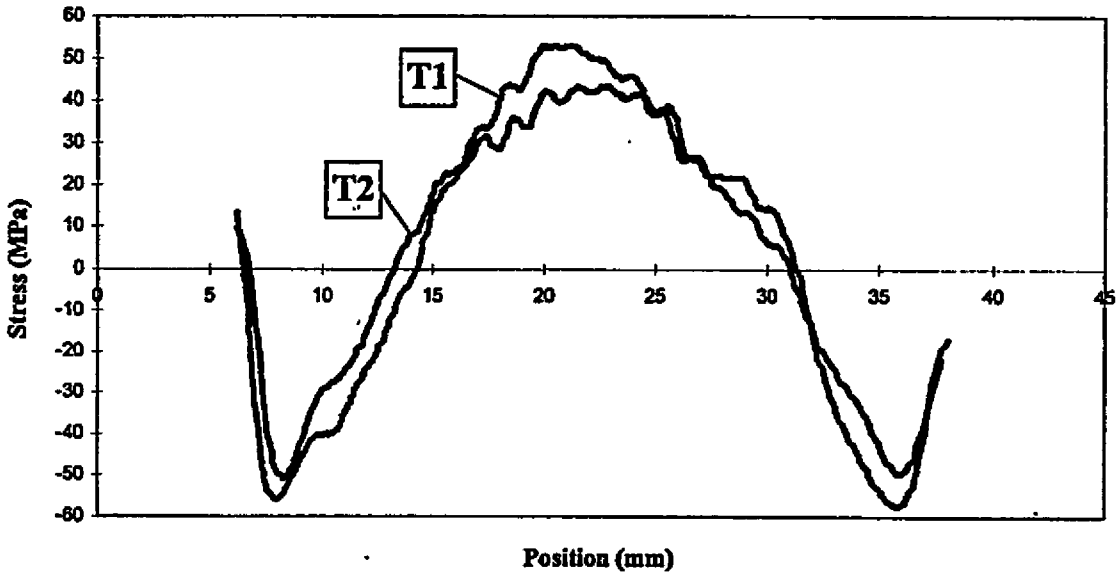

Figure 2-49: Residual stress estimated using Rayleigh waves propagating in the rolling direction (T1) and normal to this one (T2), versus the position in the thickness (Duquennoy et al 1999).

propagating the surface wave from different locations on the quenched sheet. The results for the relative variation of velocity and the corresponding stress in the rolling (T1) and transverse (T2) directions, are shown in Figures 2-48 and 2-49.

R_w has been used to estimate the applied stresses on a material (Jassby et al 1982) and the residual stresses therein (Pao et al 1984). The residual stresses in welds have received much attention. Husson et al (1984) mapped the residual stress fields near a circumferential weld on the inside and outside surfaces of a 304 stainless steel pipe. They measured the axial and hoop stresses in the pipe (Figures 2-50 and 2-51). Lindgren et al (1998) studied the Rayleigh wave velocity change as a function of residual stress in

graphite-epoxy composites. They found velocities depended directly on the magnitude of the residual stress.

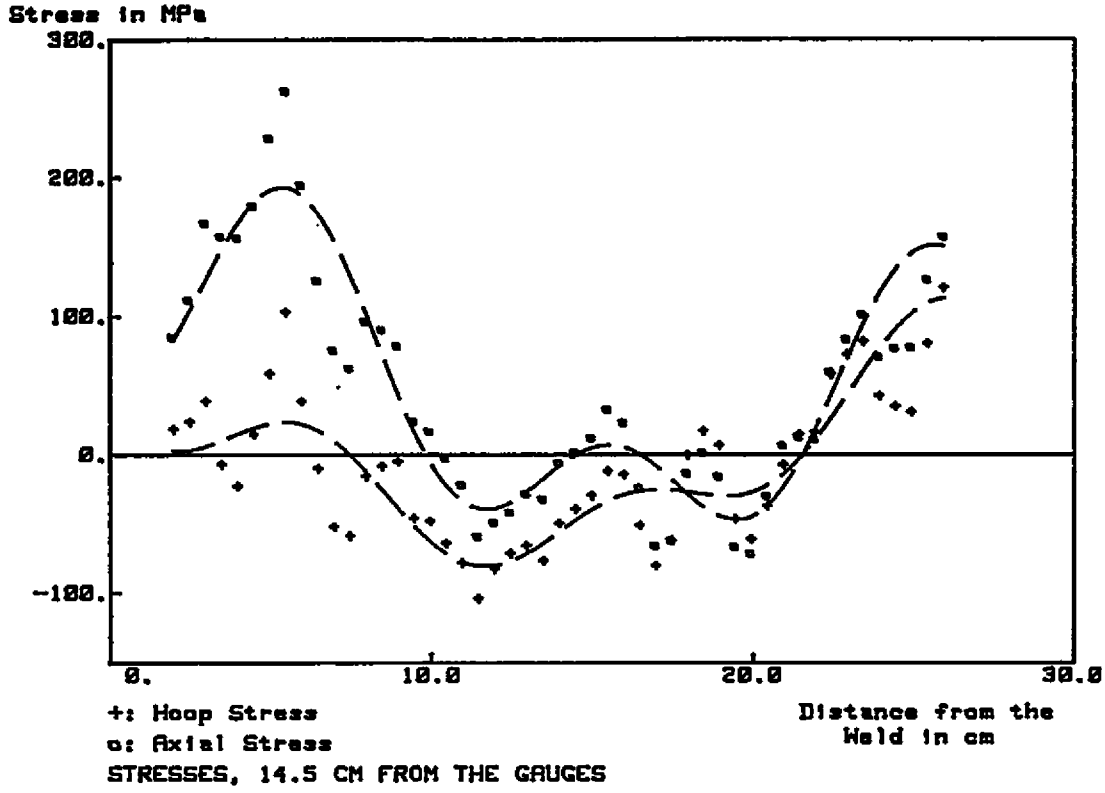

Figure 2-50: Profiles of the axial and hoop stresses on the outside surface of a welded stainless steel pipe (Husson et al 1984)

Acoustic microscopy is used to measure local, near-surface stress (Meek et al 1989). A material acoustic signature, obtained via a line-focus acoustic microscope, has successfully evaluated the residual stress in ceramics, aluminum and polymer materials (Lee et al (1994), Okade et al (1995), Kline et al (1997)).

Laser ultrasonics have been developed recently (Qian et al (2000), Lu et al (1998)). The ultrasonic waves generated by an impact laser are received by a laser interferometer.

Generation and detection are realized without contact with the surface of the material. This protocol results in higher sensitivity to the acousto-elastic effect of R_w. Duquennoy

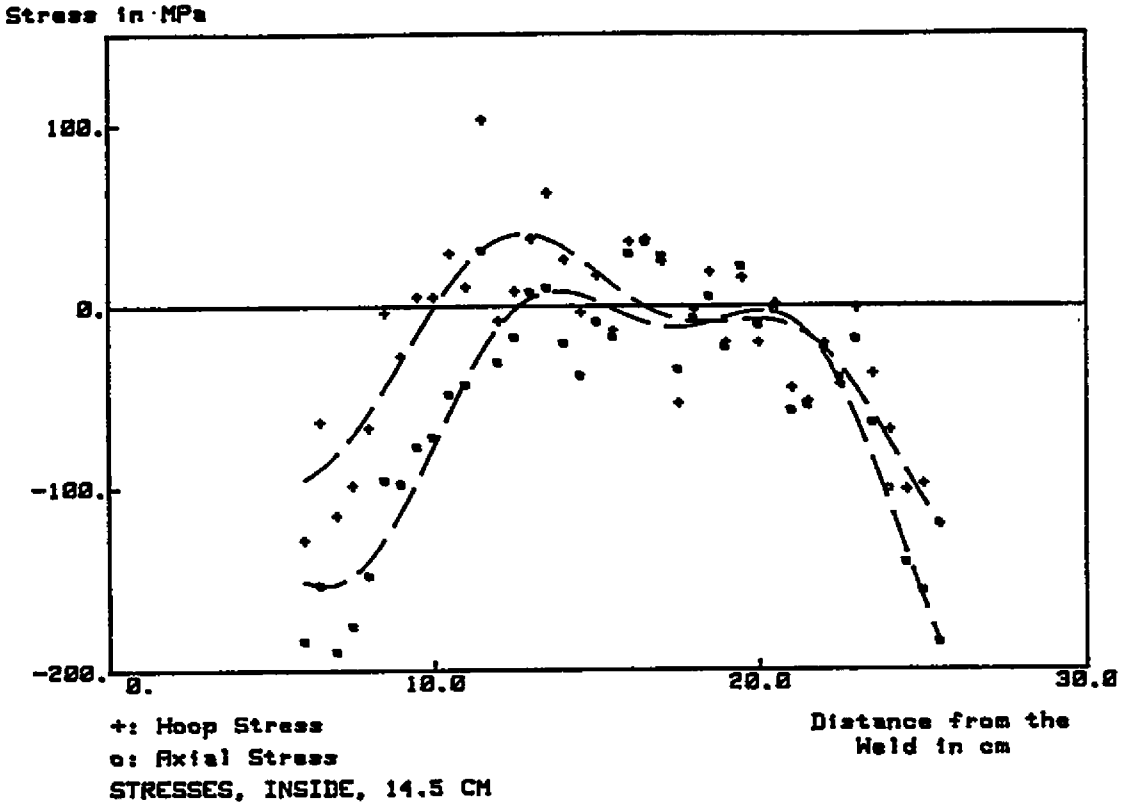

Figure 2-51: Profiles of the axial and hoop stresses on the inside surface of a welded stainless steel pipe (Husson et al 1984)

et al (2001) determined the surface residual stresses in steel rods via a laser line source and showed the results agree well with those of piezoelectric transducers. The measured velocities in rods indicate different stress states according to the heat treatment suffered (Table 2-8).

Table 2-8: The experimental results of V_{RZ} (axial direction velocity) for steel rods A, B, C, where A – machined (compressive residual stresses), B – machined and annealed (stresses relieved), C – machined, annealed and quenched (compressive residual stress) residual stresses (Duquennoy et al 2001)

Rod	Time of flight (μs)	Distance Z (mm)				V_{RZ}^{laser} (m/s)	r	V_{RZ}^{piezo} (m/s)
		20.000	18.000	16.000	14.000			
A	t_{RZ}	6.692	6.032	5.348	4.668	2960.2	0.9999	2966.3
B	t_{RZ}	6.812	6.128	5.448	4.752	2915.4	0.9999	2912.1
C	t_{RZ}	6.772	6.076	5.412	4.723	2936.2	0.9999	2935.6

2.12.2 The Effect of Microstructural Texture on the Propagation of Rayleigh Waves

The combined effects of stress and texture-induced-anisotropy on Rayleigh waves have been much studied. Martin (1974) determined that preferred-grain orientation in aluminum alloys influenced the Rayleigh wave velocity as much as stress did (in the elastic range). Pritchard (1987) studied an aluminum sample and found a change of R_w velocity for a range of frequencies versus the angle of propagation (relative to rolling direction), Figure 2-52. It is evident anisotropy is more important at lower frequencies. These findings imply increased texture with depth, which was verified by neutron diffraction. Sayers (1984) used Roe's formalism to treat the texture of polycrystalline aggregates. He showed that surface-wave-velocity measurements can be combined with the normal shear wave birefringence technique to give a texture-independent determination of the principal stress differences. Tanala et al (1995) used a combination of subsurface longitudinal waves and Rayleigh waves to identify the effect of texture on

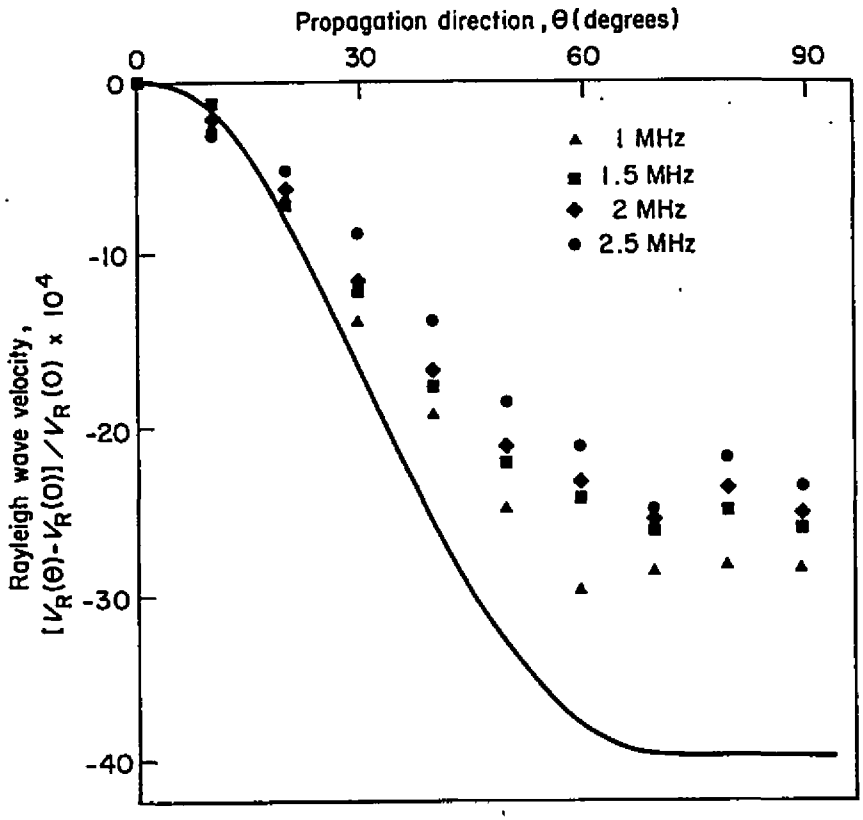

Figure 2-52: Rayleigh wave velocity versus propagation direction relative to the rolling direction in aluminum sample for a range of frequencies (Pritchard 1987)

biaxial residual stress measurements in surfaces near welds in rolled Al alloy and stainless steel.

2.12.3 The Effect of Grain Scattering on the Propagation of Ultrasonic Rayleigh Waves

The velocity of a Rayleigh wave is influenced by grain size. Pecorari et al (2000), noted an increase of phase velocity with annealing temperature for JRQ steel (Figure 2-53). They propose this due to the reduction of average grain size with increasing annealing temperature (62-40 μm) and suggest materials with small grains attenuate (and therefore disperse) the propagating ultrasonic wave to a lesser degree than do larger

grains. This supposition is supported by their results using transducers of two nominal frequencies: 2.5 and 10 MHz. (Figure 2-53). Clearly, 10 MHz produced systematically lower values of phase velocity than 2.25 MHz, indicating that higher attenuation and dispersion are suffered by waves of higher frequency.

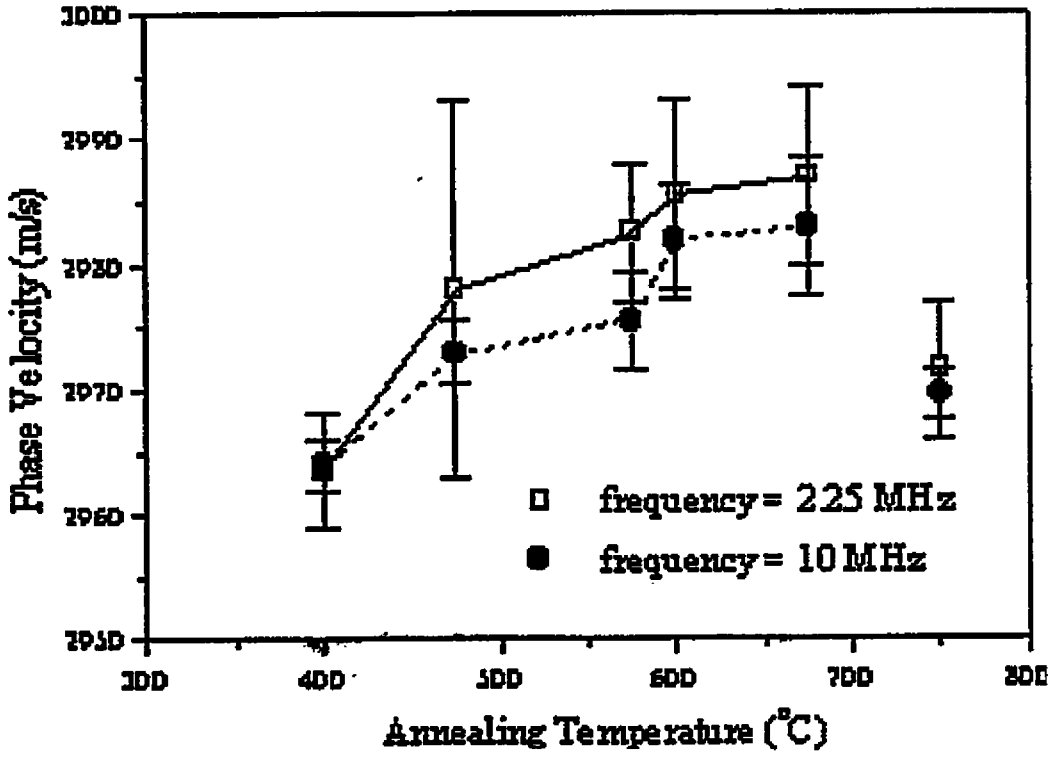

Figure 2-53: Rayleigh phase velocity versus annealing temperature for the JRQ samples (Pecorari et al 2000)

2.12.4 The Influence of Surface Roughness on Rayleigh Waves

The Rayleigh wave penetrates ~ 1 wavelength deep, thus is influenced by surface roughness. Zhang and Achenbach (1990), Warren et al (1996), and Pecorari (2000 and 2001) explored the attenuation and dispersion of Rayleigh waves by surface cracks.

Table 2-9: Machining effect on Rayleigh velocity measurement (Tardy et al 1996)

specimen	velocity VR (m/s)	roughness Ra (•)	damage depth (•)
polished	3132 +/- 4	0.28	4
fine machining	3112+/-12	0.6	12
rough machining	3065 +/- 18	2.03	20

They found the total change of Rayleigh wave velocity is <0.3%. This result emphasises the necessity of measuring the Rayleigh wave velocity with high accuracy. Tardy et al. (1996) compared R_w velocities along ceramic specimens with machined and polished surfaces. They observed the R_w arrival-time increased with surface roughness (Table 2-

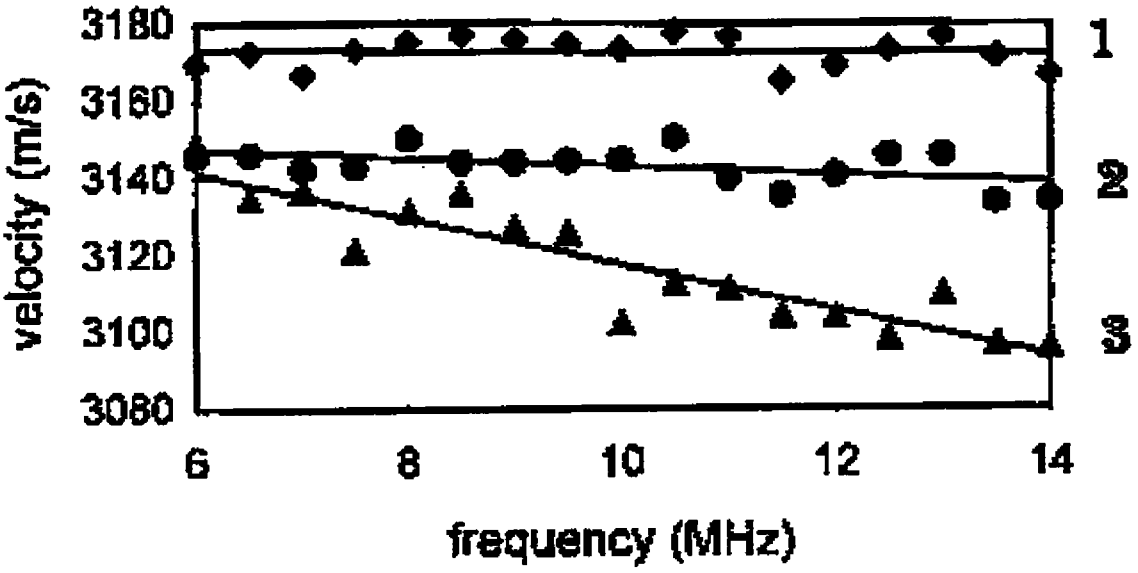

Figure 2-54: Frequency dependent Rw velocity on a ceramic: polished specimen (1), fine machined specimen (2), rough machined specimen (3). The linear regression is indicated by a solid line (Tardy et al 1996)

9). The signal amplitude decreased. They examined the same samples with Rayleigh waves of different frequency (Figure 2-54) and observed the R_w velocity is ≅ constant for the polished specimen but decreased significantly with increasing frequency for roughly machined specimens. Vasil'ev et al (1994), studied the relationship between R_w velocity and surface roughness for Steel 45 and concluded that, as the height of the micro-inhomogeneities increases, the time-of–flight of the ultrasonic wave along the surface increases. Recently, Ruiz et al (2002) recognized a perceivable dispersion of the R_w wave (dependence on frequency) is not only exhibited by 'rough surface' specimens but also occurs in untreated, "smooth," surfaces. This effect ≅ 0.1% i.e. it is comparable to the expected velocity change produced by the near-surface residual stresses in metals

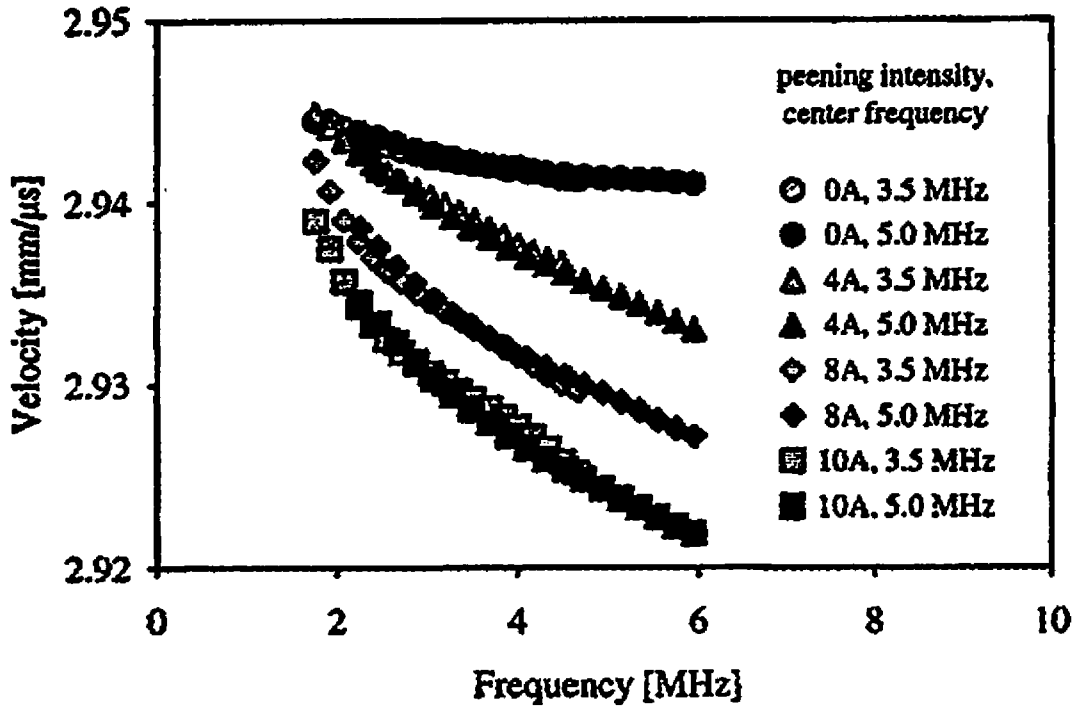

Figure 2-55: Surface wave velocity measurements on four different aluminum specimens using two different transmitters of 3.5- and 5-MHz nominal center frequencies (Ruiz et al 2002)

below their yield point. Figure 2-55 shows their results for four aluminum specimens, shot-peened at different Almen intensities (4A, 8A, 10A), where 0A is the un-peened specimen. R_w dispersion clearly increases with peening intensity. This was attributed to surface-roughness-induced scattering. Peening introduces residual stress, but this was not considered in this work. Although the shot-peened specimens dispersed R_w more strongly, dispersion was still significant for the un-peened smooth surface – 0A. Further studies on polished specimens before and after annealing, (Figure 2-56), showed the apparent dispersion was higher in the heat-treated specimen than the original one, indicating some contribution from the microstructure (grain scattering) is also present in the dispersion.

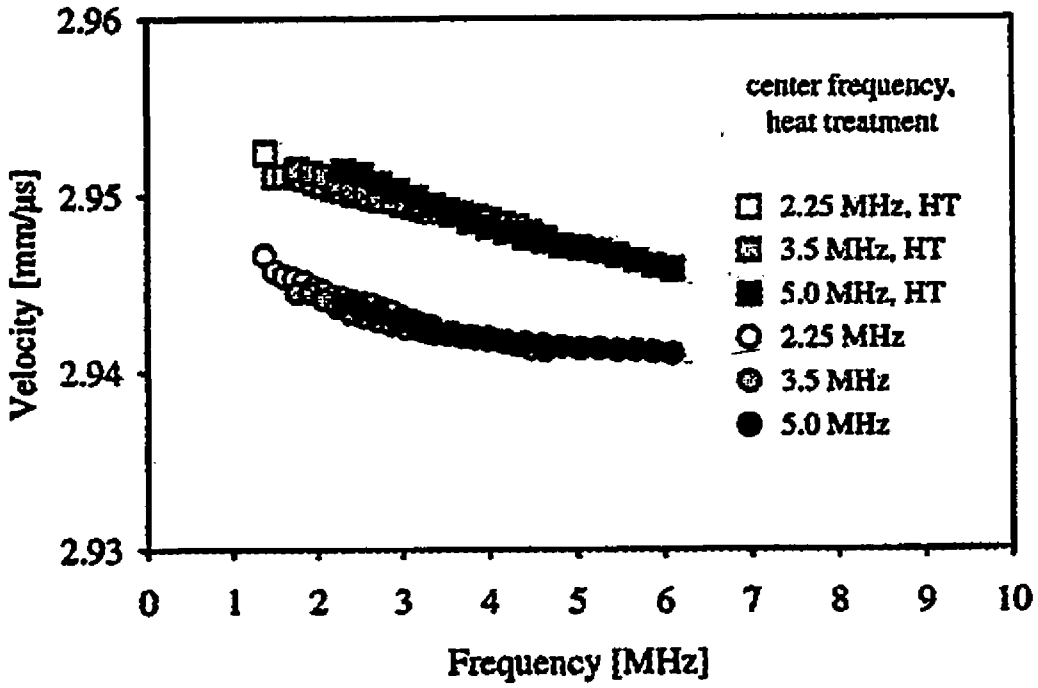

Figure 2-56: Surface wave velocity measurements on unpeened smooth alumnum specimens before an after annealing (HT) using three transmitters of 2.25-, 3.5-, and 5-MHz nominal center frequencies (Ruiz et al 2002).

2.13 Longitudinal Critically-Refracted (L_{cr}) Ultrasonic Waves

2.13.1 Residual Surface Stress Measurements with L_{cr} Waves

L_{cr} waves are directed into the material at the first critical angle and travel as if a bulk wave just beneath the surface. Lower frequencies penetrate deeper. L_{cr} waves can detect in-plane, subsurface stress in a material. The practical use of L_{cr} for stress evaluation has been confirmed. The L_{cr} wave is more sensitive to stress than the shear wave but, as it is non-polarized, it is less sensitive to material texture (Bray et al (1989), Bray et al (1981)).

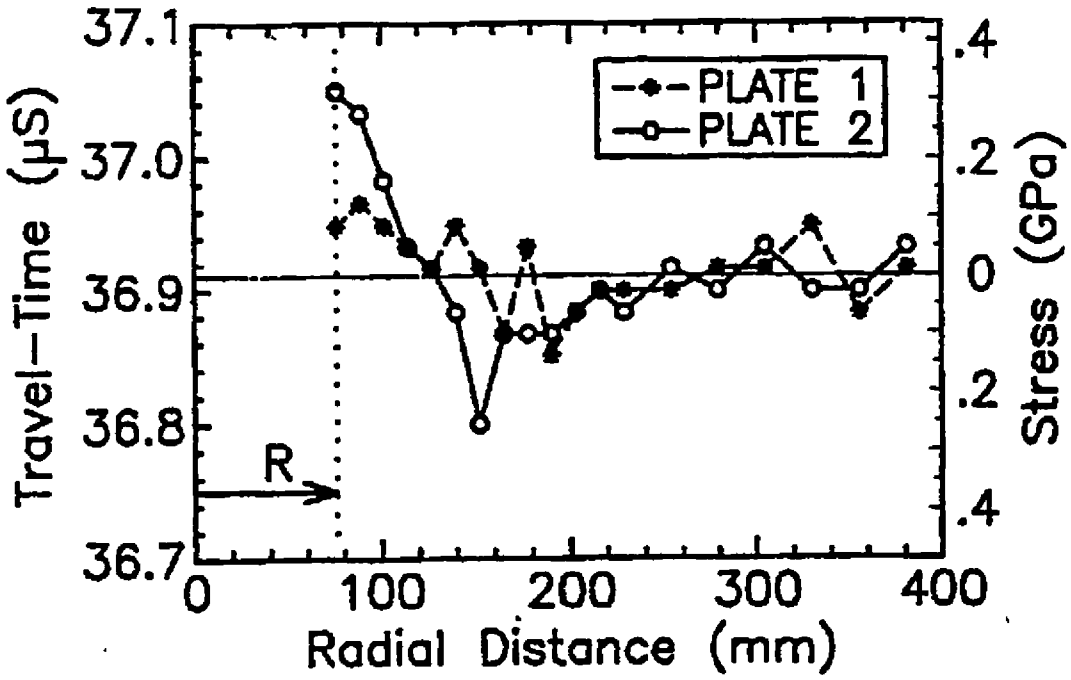

Figure 2-57: Average differential travel times for Lcr waves travelling tangentially to a circular patch weld, R, as a function of the radial distance from the center for a stress relieved plate (No. 1) and non-stress relieved plate (No. 2) (Bray et al 1995)

Much work using L_{cr} waves has focused on determining residual stresses in welds. Leon-Salamanca and Bray (1995) showed the travel time of the L_{cr} wave, near a longitudinal weld in butt-welded steel-plates, corresponds well with the expected distribution from a large longitudinal stress field. This implies, for butt-weld conditions, the assumption of uniaxial stress field is valid. Tanala et al (1995) reported and ultrasonic stress measurement in welded aluminum samples. Bray and Junghans (1995) used L_{cr} waves to obtain the distribution and magnitude of residual stresses in a patch-welded, structural steel plate before and after stress relief. Figure 2-57 is a plot of the average, differential-travel-times as the function of the radial distance from the patch weld, for as-welded and stress-relieved plates (plate 2 and plate 1, respectively. Though the data is scattered for both plates, no distinct minimum or maximum was found for the stress-relieved, plate 1 but a pattern is apparent for plate 2. Data points furthest from the weld are relatively flat but on approaching the weld, a minimum-travel time exists at 152 mm followed by a steep rise to a peak travel time at the weld radius, 76mm. This pattern corresponds well with theoretical predictions for a tangential weld-stress-distribution created by a circular patch-weld on a larger plate, i.e. a region of high tangential, tensile stress at the weld due to circumferential shrinkage of the weld metal, plus a region of lower tangential, compressive stress further from the weld due to radial shrinkage of the patch; plus a stress-free area of unaffected material. Leon-Salamanca and Bray (1995) gathered L_{cr} data for cold-rolled and hot-rolled steel plates with a double-vee, butt weld. Measurements were taken near and away from the weld, before and after stress-relief. The data indicate initial surface compressive stress in the parent metal before stress

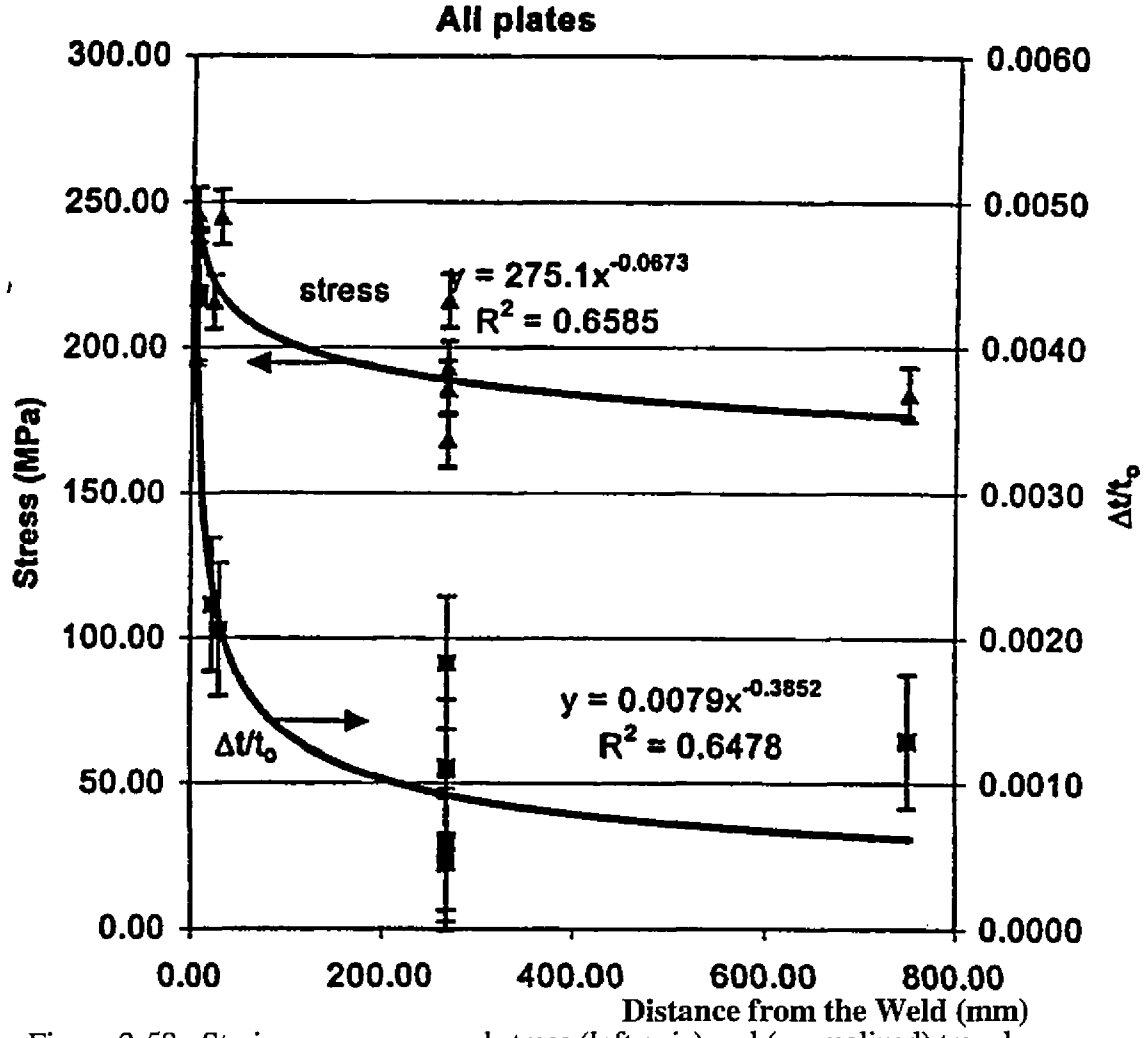

Figure 2-58: Strain gauge measured stress (left axis) and (normalized) travel times (right axis) (Chance et al 2001)

relief, and after: residual internal stress significantly reduced. Belahcene and Lu (2000) applied the L_{cr} method to welded Z8CDWV12 steel plate (duplex ferrite martensite steel). Bray (2001) examined welded pressure vessels. A 12 in-diameter steel vessel was pressurized with water, pressure 0 - 69.9 MPa was measured via L_{cr} wave travel-time change and by strain-gauges. Travel-time plots approaching a weld predicted -190 MPa,

25 mm from the weld .vs. zero stress 142 mm, away. These results are consistent with those obtained using a "blind-hole," drilling method (Bray 2001). Chance et al (2001) employed the L_{cr} wave to investigate transverse stress relaxation in a welded steel plate. They cut T-shaped slots from opposite edges of a specimen and welded them together to provide a uniaxial-tension stress-field in the center. They then cut the welds and studied stress relief via L_{cr} velocity. Figure 2-58 shows a good correlation between L_{cr} and the conventional strain gauges.

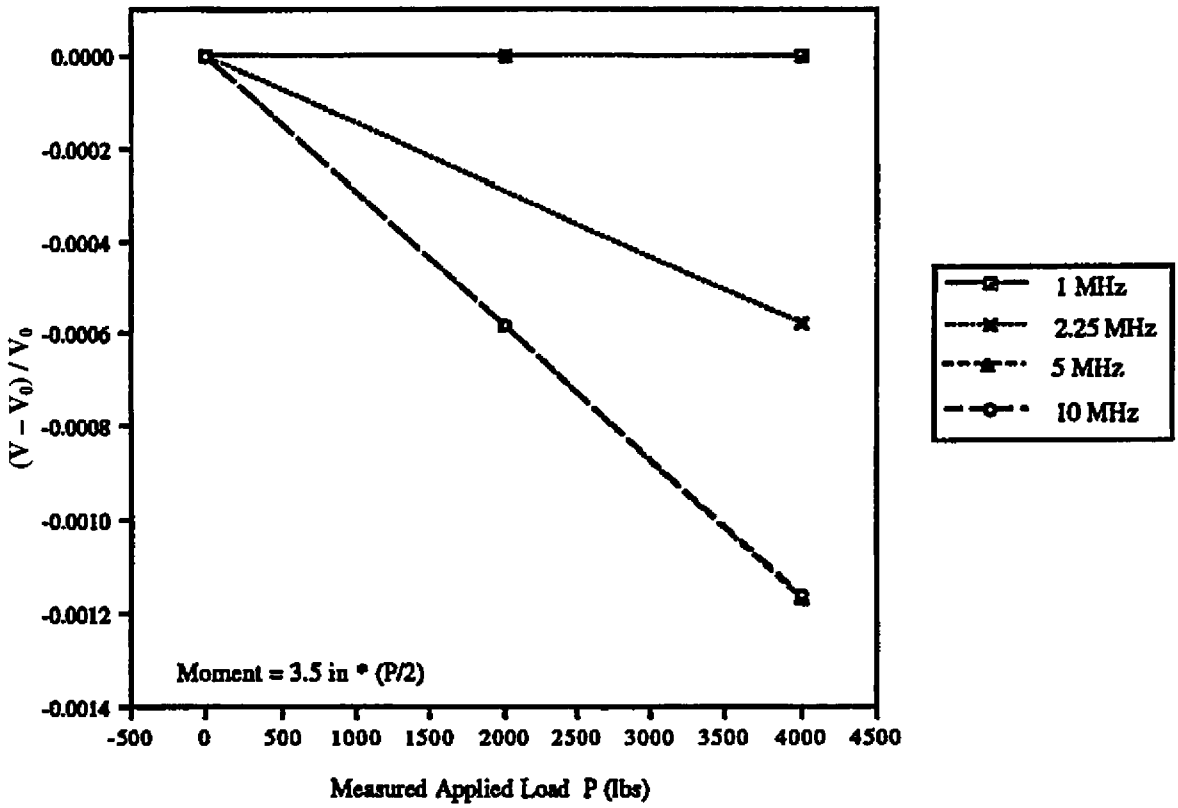

Figure 2-59: Lcr wave velocity changes as a function of applied load obtained in a 4-point bending test of a 4340 steel plate (Leon-Salamanca et al 1994)

Applied stress has been much studied by L_{cr} waves. Leon-Salamanca and Reinhart (1994) explored the bend stresses in plates of 4340 steel, 6061-T6 aluminum, and Ti-6Al-4V titanium using L_{cr} waves. They found a decrease of velocity along surfaces under tension. Several frequencies were employed and, as expected, the high frequency waves suffered a greater decrease of velocity than the low frequency ones (Figure 2-59). Bray and Tang (2001) measured the internal stress in a 3x1in 4140 steel bar under four-point bending. Again, their results were consistent with strain gauge data. In this case, a three-probe transducer arrangement was used i.e. one sender and two receivers in tandem. This configuration eliminates environmental temperature influences on the sound-wave travel-time.

L_{cr} waves have been used to determine stresses in rotating equipment, e.g. a steam turbine disk with uneven stresses on the inlet and outlet sides (Bray et al 1996). The results were confirmed by XRD. Tests on a compressor correctly identified the region causing a bow in the rotor (Bray, Tang and Grewal 1997). The method has also been used to characterize the shot peened titanium turbine blades for aircraft engines (Bray 2000). The "holding," quality of the shrink fit design of the generator retaining rings depends on the residual hoop stress in the ring since the operating, centrifugally-induced stresses tend to release the retention force (Bray 2000). Leon-Salamanca et al (1989) used L_{cr} to determine this stress before and after mounting the ring.

Lcr waves have proved very useful to evaluate the residual stresses in railroads (Bray et al 1989). Szelazek (1998) reported determination of the thermally-induced stress changes in rail.

Table 2-10: Stress calculated using the PC based instrumentation (Santos and Bray 2000)

Stress (Mpa) strain gauges	P2 (μs)	Stress (L=2.38) (MPa) L_{cr}
0	52.2806	0
18.22737	52.2888	20.9
41.57277	52.297	41.9
64.6488	52.3057	64.1
90.59811	52.3136	84.2
99.57711	52.3169	92.7

Table 2.11: Stress calculated using the portable instrument (Santos and Bray 2000)

Stress (Mpa) strain gauges	P2 (μs)	Stress (L=2.38) (MPa) L_{cr}
0	52.513	0
19.1	52.52	17.9
41.6	52.533	51.1
64.6	52.54	68.9
87.1	52.547	86.8
109.6	52.56	120

Low-cost, commercial, ultrasonic flaw-detectors may be used for collecting L_{cr} data for applications where stress variations are high. Santos and Bray (2000) used a load

frame designed to demonstrate application of the Lcr technique for evaluation of a one-dimensional stress field. Data were collected on a strain-gauged steel bar. They employed a PC with a high-speed digitizing-card and an Epoch 3 digital ultrasonic flaw detector was used. Even though the time resolution of the flaw detector was only 7 ns, both systems gave results that agreed with the real stresses. Tables 2-10 and 2-11 summarise the data for stress calculated using the PC-based instrumentation and the portable instrument, respectively. The sensitivity of the latter was judged satisfactory to identify dangerous stresses developing in large parts, in service.

The depth of penetration of the L_{cr} wave is related to its frequency. Lower frequencies penetrate deeper (Egle and Bray 1979). Junghans and Bray (1991) and Tang and Bray (1996) explored wave energy distribution versus depth. Junghans and Bray (1991) suggested the effective penetration layer width and depth is defined as per Figure 2-60. The effective layer width, 'w', is the distance between two, half-power points of the energy distribution curve in the vertical cross section. The effective penetration depth, 'd', is the distance between the outer surface and the peak of the energy distribution curve in the vertical cross section.

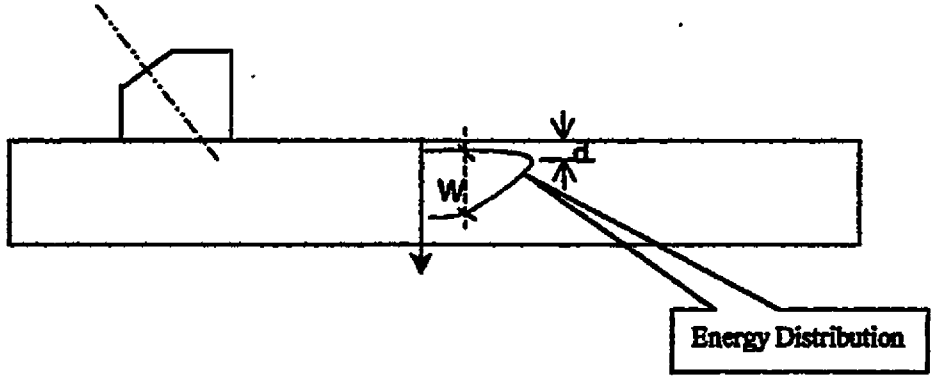

Figure 2-60: Illustration of the penetration energy distribution for L_{cr} wave (Junghans et al 1991)

It must again be emphasized that the penetration depth of the L_{cr} wave is different from the Rayleigh wave. The latter travels on the surface and has a peak energy propagation within one wavelength depth from the surface. The effective inspection layer width for the L_{cr} also depends on the working frequency of the transducer (Tang and Bray 1996). Leon-Salamanca and Bray (1995) used 1.0 MHz and 2.25 MHz transducers to track the internal stresses in a cold-rolled steel plate with a weld. They assumed the 1 MHz wave interrogated a layer ≅ 5.9mm thick as compared with the 2.6 mm layer

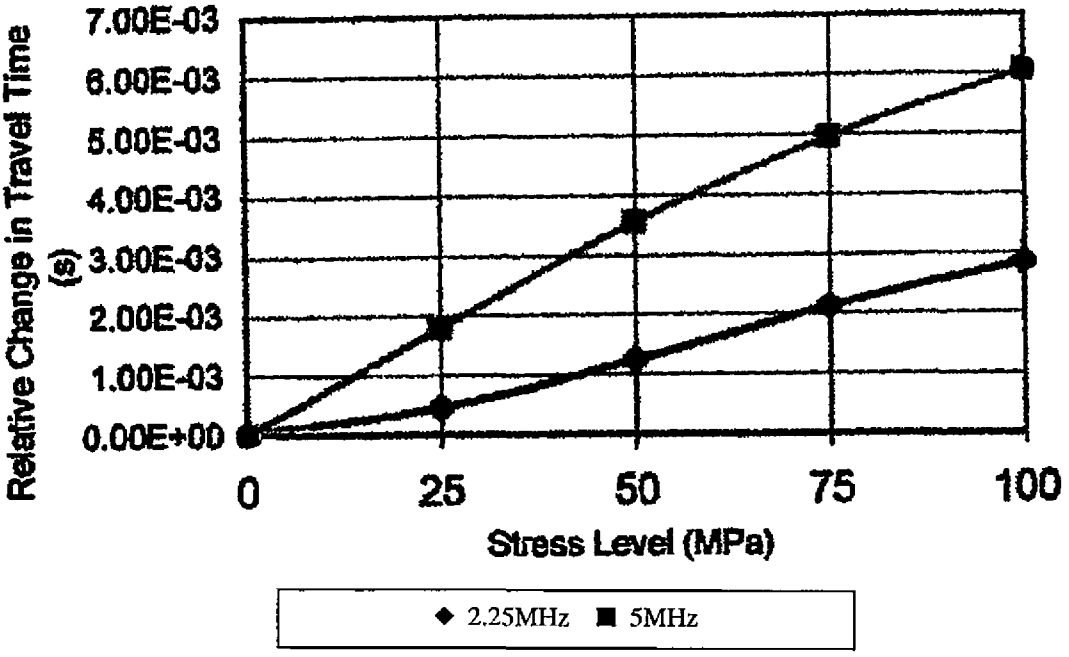

Figure 2-61: Summary of the relative travel time changes (TTR) with load for the two frequencies (Bray and Tang 2001)

Interrogated by the 2.25 MHz wave. The velocity behavior in the parent metal was interpreted as the result of a double stress reversal in the upper half of the plate. This stress field could be described as tensile at the surface, with a thin subsurface compressive layer, then a thicker tensile layer and peak compressive stress at the mid-plane. Near the surface a thin, reversed stress field could influence medium-frequency data more than low frequency, 1.0 MHz, because the stress effect traced by medium and high frequency waves is likely concentrated near the surface. The 1.0 MHz data could be dominated by the thick, tensile region beneath the thin compressive region. The 2.25 MHz data indicated negligible change by stress relief in material away from the weld, indicating an unstressed region near the surface. The 1 MHz ultrasound suffered a significant change of travel time, which matched the phenomena associated with the rolling stress distribution in the plates (slight tension in the surface, significant compression deeper in the material). Bray and Tang (2001) reported that, the 5.0 MHz L_{cr} data was gathered as a steel plate was loaded to various stress levels in four-point bend, with a strain gage on the tensile surface. This Lcr data suffered a greater travel-time change than the 2.25MHz data (Figure 2-61). This is consistent with the calculated four-point bending stress distribution, i.e. high stress near the outer surface wherein the high frequency signal is propagating. Belahcene and Lu (2000) undertook calibration of penetration depth .vs. L_{cr} wave frequency in a gauge block. One side of the gauge block was machined with a series of slits of increasing depth. The ultrasonic beam travel time was measured, observing which slit was the first to affect the wave velocity. (Figure 2-62.) The development of these curves corresponds to the penetration depth of a wave of

given frequency. They concluded the penetration depths for 2.25, 3.2, 5, 6.6 MHz frequencies in Z8CDWV12 steel are 2.5, 2, 1.5, and 1mm respectively. This clearly illustrates the attenuation/frequency relationship.

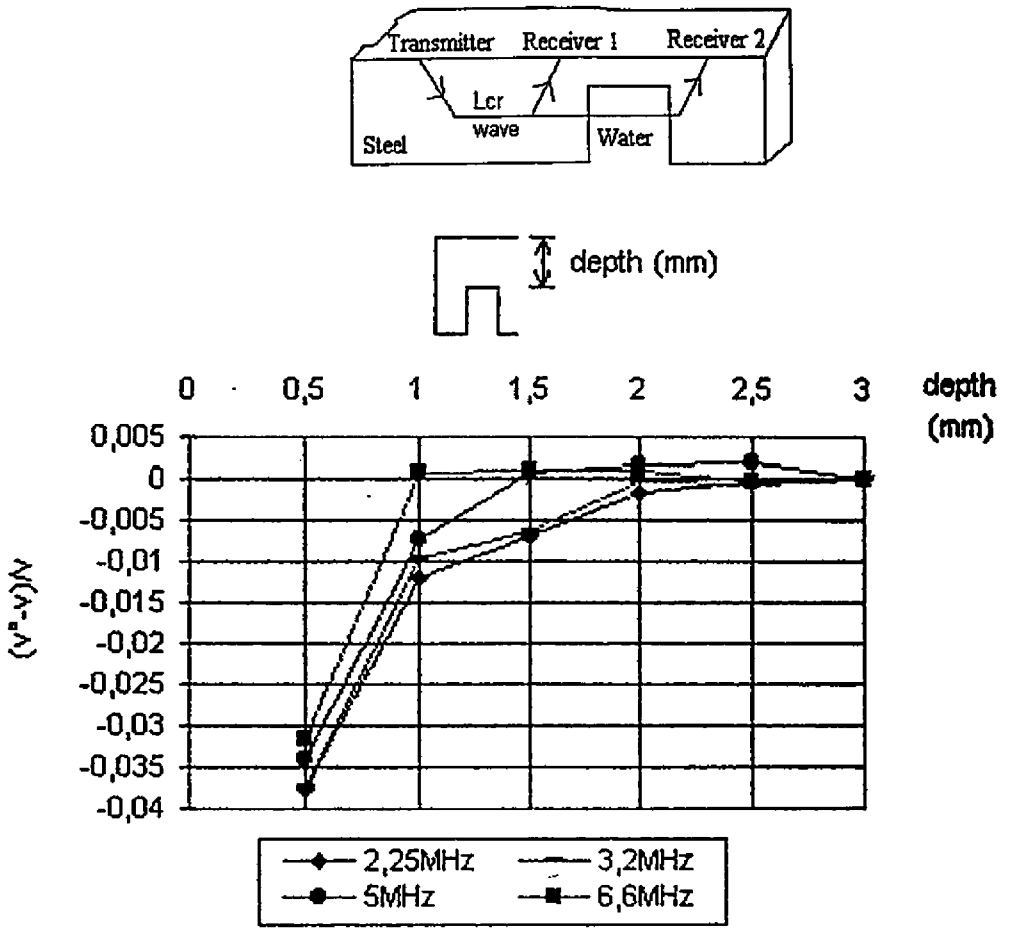

Figure 2-62: Relative change in wave speed as a function to the depth of the slit (Belahcene et al 2000)

2.13.2 The Effect of Texture on the Propagation of L_{cr} Waves

Though the L_{cr} wave is less sensitive to material texture than R_w, texture may still be a significant factor interfering with measuring stresses via L_{cr} (Bray 2000). Wave velocity varies with crystallographic direction, as does the acoustoelastic effect. Methods exist to correct for the texture effect on L_{cr} wave propagation. Assuming texture is uniform throughout, L_{cr} travel times taken with the probe always at the same orientation relative to the geometry of the item may be free of texture influence and the major effect therein is stress (Bray 1998). Bray and Tang (2001) designed test procedures for rolled steel to eliminate potential spatial movement variation during the experiment. The same technique clearly distinguishes between as-rolled and stress-relieved plates of aluminum (Bray et al (1999)). Leon-Salamanca and Bray (1995) used L_{cr} to study residual stresses near a longitudinal, double-vee, groove weld that joined two, structural-steel plates. Data were obtained before, and after, heat-treatment, using L_{cr} and neutron diffraction. The effects of stress-relief were clearly shown by the L_{cr} data but not by the neutron diffraction, implying the heat treatment did not influence texture. Consequently, the travel-time profiles must have been the result of internal stress around the weld and not texture.

Part C

The X-Ray Diffraction Method for Measuring the Residual Stress in a Surface

The importance of XRD method resides in its ability to measure residual and applied stress with high spatial resolution, speed, and accuracy (Pineault et al 2002). The component must be introduced into the XRD unit, thus on-line evaluating is not possible. Residual stress measurement via XRD is limited to polycrystalline materials. The precision and accuracy of results is a function of the instrument, the material condition, the measurement technique used, and data analysis. Data analysis assumes near-random grain orientation is sampled in a homogeneous, isotropic material (Pineault and Brauss 1995).

XRD tracks the distance between material crystallographic planes as a strain gauge, i.e. d-spacing. Thousands of grains are sampled in a typical measurement. Under tension, the d-spacing increases, under compression, it decreases. The new d-spacing is constant from one grain to the next for a particular set of planes. The presence of residual stresses produces a shift of diffraction lines to new 2θ position (Pineault et al 2002) directly measured by a detector. For a known X-ray wavelength, 'λ', 'n' =1, and a diffraction angle, 2θ, measured experimentally, the d-spacing is calculated via Bragg's law:

$$n\lambda = 2d\sin\theta \quad (67)$$

The d-spacing for unstressed (d_0) and stressed (d)material gives the strain via;

$$\varepsilon = (d - d_0)/d_0 \quad (68)$$

Figure 2-63 shows the surface of a stressed body, x and y lying in the plane of the surface (Culllity 1967). Principal stress directions are also indicated. To measure the stress, σ_ϕ, acting in a specified direction OB, (OB makes angle ϕ with the principal direction 1 and an angle β with the x-axis) a number of d-spacings is measured by changing the angle, Ψ (the angle subtended by the bisector of the incident and diffracted

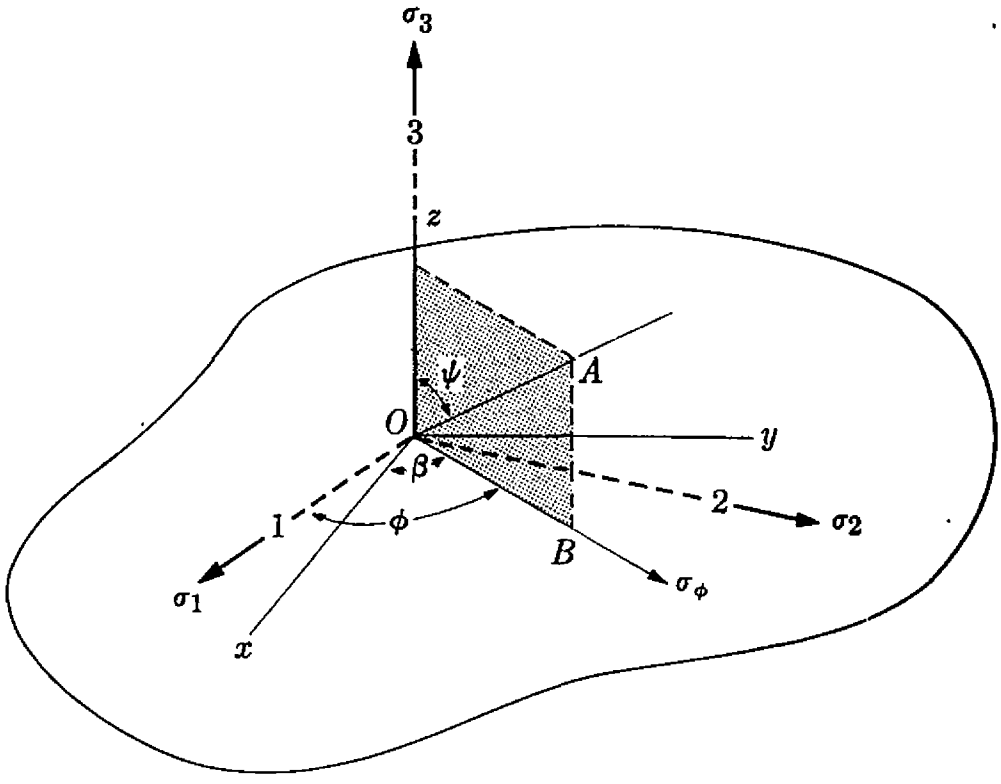

Figure 2-63: Angular relations between stress to be measured (σ_Ψ), principal stresses (σ_1, σ_2, and σ_3), and arbitrary axes (x, y, z) (Cullity 1967).

beam, with the specimen normal). Measurements at $\Psi = 0$, give the strain $\cong$ normal to the surface. When $\Psi > 0$, the strain $\cong$ parallel to OA is measured (OA lies in a vertical plane through the direction OB (in which it is desired to measure the stress)) (Cullity

1967). In applying a plane-stress model, the unstressed lattice spacing, d_0, is substituted for the d-spacing measured at $\Psi = 0$, because the stress at right angles to a free surface is always zero. As a result only the two stress components lying in the plane of the surface exist. Even though the strain normal to the surface is not zero, the unstressed lattice spacing need not be known precisely. (Pineault et al 2002).

Stresses are calculated via the $\sin^2\Psi$ method, using an equation derived from Hooke's law for isotropic, homogeneous, fine-grained materials:

$$\varepsilon_{\phi\psi} = \frac{1}{2}S_2(\sigma_{11}\cos^2\phi + \sigma_{12}\sin 2\phi + \sigma_{22}\sin^2\phi - \sigma_{33})\times$$
$$\sin^2\psi + \frac{1}{2}S_2\sigma_{33} - S_1(\sigma_{11} + \sigma_{22} + \sigma_{33}) + \qquad (69)$$
$$\frac{1}{2}S_2(\sigma_{13}\cos\phi + \sigma_{23}\sin\phi)\sin 2\psi$$

where ½ S_2 and S_1 are the X-ray Elastic Constants for the material, and ½ $S_2 \sim (1+\nu)/E$. Variations of σ_{ij} are the stress-tensor components. Evaluation of the stress-tensor components, σ_{ij}, is straightforward and normally carried out by plotting the measured d-

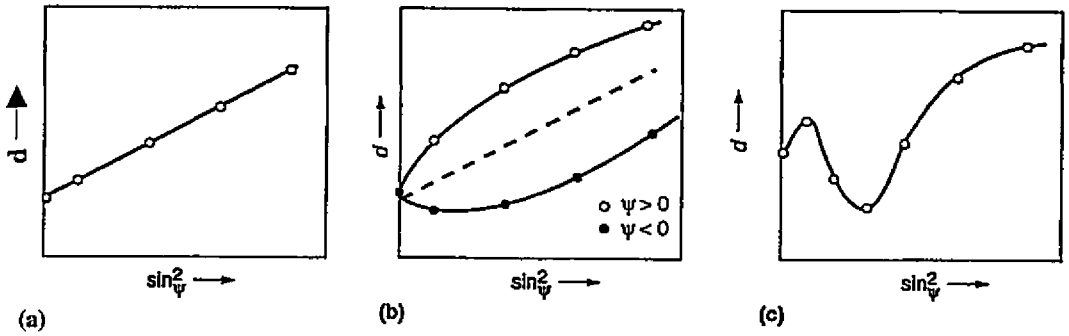

Figure 2-64: Common types of d-spacing versus $\sin^2\psi$ plots. (a) Linear: exhibiting no shear stress. (b) Elliptical: exhibiting ψ-splitting due to shear stress. (c) Nonlinear: oscillatory behavior due to preferred crystallographic orientation (Pineault et al 2002).

spacing versus $\sin^2\Psi$ (Pineault 2002).

d versus $\sin^2\Psi$ data for residual stress measurements can be linear, elliptical with Ψ-splitting, or nonlinear with oscillatory behavior (Figure 2-64). The linear plot is obtained

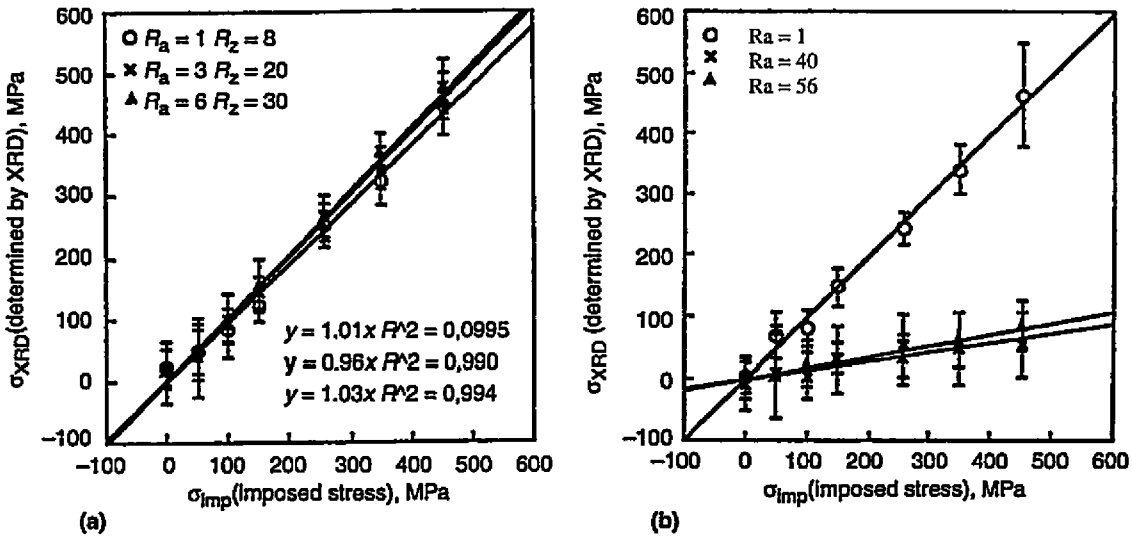

Figure 2-65: X-ray diffraction stress versus applied stress for varying average roughness (R_a). (a) Samples with R_a of 1, 3, and 6 μm. (b) Samples with R_a of 1, 40, and 56 μm (Li et al 1995).

from near-isotropic and homogeneous samples with no shear stress; elliptical data are evidence of shear stresses and/or instrument misalignment; and oscillatory behavior indicates nonrandom crystallographic orientation of coherently-diffracting domains in the volume the incident x-ray beam samples (Pineault et al 2002).

The effect of surface roughness on XRD residual stress measurements is profound. Li et al (1995) measured via XRD, applied tensile stress in a steel specimen machined to produce 3 different roughnesses. They observed the measured stress agreed within

experimental error with the imposed stress (Figure 2-65) when R_a is 1, 3, and 6 μm. Samples studied with regions of different R_a, (≤ 56 μm,) gave different surface stress values than that applied. Figure 2-66 shows sensitivity to the applied load is reduced when R_a >10 μm. It was thus concluded that, when the surface R_a < penetration depth of X-rays, the measured stress results more accurately reflect the applied load. When surface R_a > the penetration depth of the X-rays, the measured stress reflects the applied

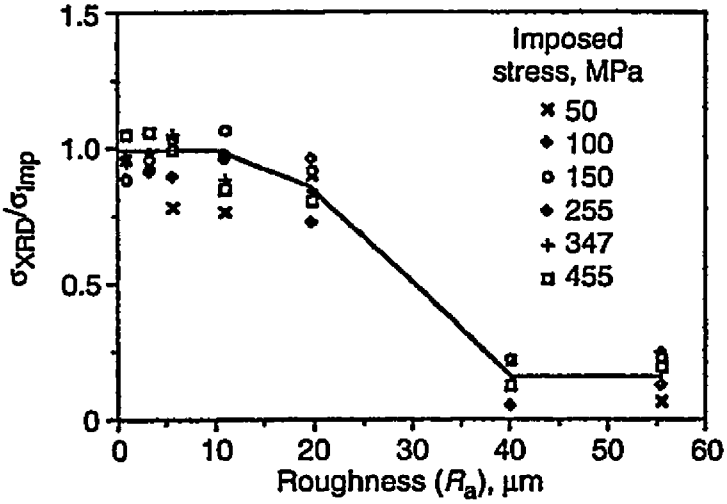

Figure 2-66: Ratio of measured stress and applied stress for varying R_a (Li et al 1995)

load to a lesser degree due to scattering. (Figure 2-67 (a) and (b)).

The information obtained via X-rays only comes from a thin surface layer. In fact, most metallurgical specimens strongly absorb X-rays and the intensity of the incident

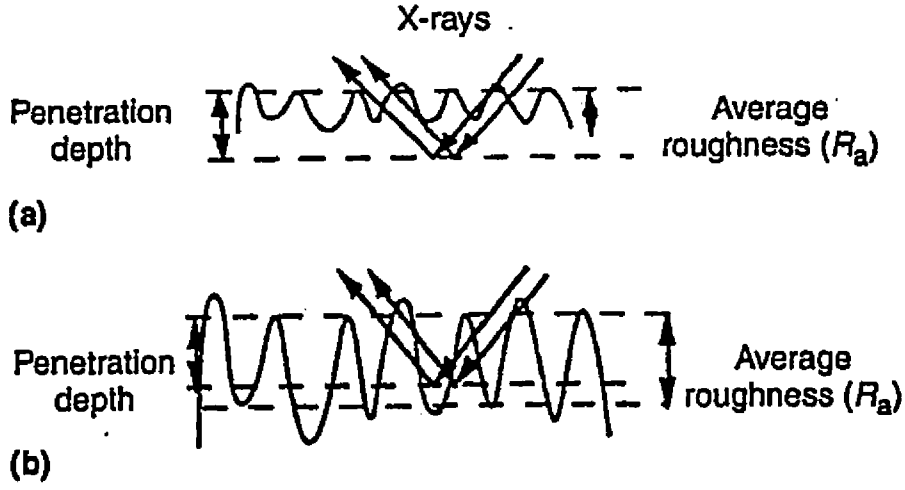

Figure 2-67: Effect of surface R_a on XRD stress measurements. (a) X-ray penetration depth is greater than R_a. (b) X-ray penetration depth is less than R_a (Li et al 1995).

beam is reduced exponentially to almost zero a short distance below the surface. The effective depth of X-ray penetration is estimated by calculating, the fraction G_x of the total diffracted intensity contributed by a surface layer of depth x. For back-reflection cameras, G_x is (Cullity 1967):

$$G_x = \left[1 - e^{-\mu x(1+1/\sin\beta)}\right] \quad (70)$$

where $\beta = 2\theta - 90°$, and μ = mass absorption coefficient x material density.

The mass absorption coefficient must be known to use the above formula. When the value is unknown, it can be simply calculated as a weighted average of the mass absorption coefficients of constituent elements for a substance containing more than one

element. For example, if w_1, w_2, etc. are the weight-fractions for elements 1, 2, etc., in the substance and $(\mu/\rho)_1$, $(\mu / \rho)_2$, etc., their mass absorption coefficients, the Mass Absorption Coefficient (Cullity 1967):

$$\frac{\mu}{\rho} = w_1\left(\frac{\mu}{\rho}\right)_1 + w_2\left(\frac{\mu}{\rho}\right)_2 + \ldots \quad (71)$$

Chapter 3

EQUIPMENT

Fallon Ultrasonics have developed equipment capable of exciting stable, L_{cr} and R_w waves, and measuring picosecond changes of ultrasonic travel-time (ps). The rig consists of the following components:

1) focused, copolymer, L_{cr} and R_w transducers
2) a test tank with water couplant
3) an ultra- high-sensitivity pulser / receiver
4) a Tektronix Model TDS 210 oscilloscope
5) a PC with high-speed digitizer board and Mark IV Dimension Monitoring software.

The uniqueness of the equipment utilized is the 50 ps resolution of the measurements. The latter allows use of high-frequency, focused transducers. High frequency (required to study surface residual stress) dictates a focused transducer configuration with short surface-wave-travel paths (up to 1.2 mm). The latter results in short wave-travel-time and, as the changes of travel time due to residual stress are small (0.1 – 7ns), high accuracy tracking equipment is necessary.

A block diagram of the components of the ultrasonic system is shown in Figure 3-1. A specially-designed, cylindrical-transducer for the Rayleigh (or L_{cr}) wave is excited by a pulser-receiver system that generates waves, as shown in Figure 3-2. The first strong

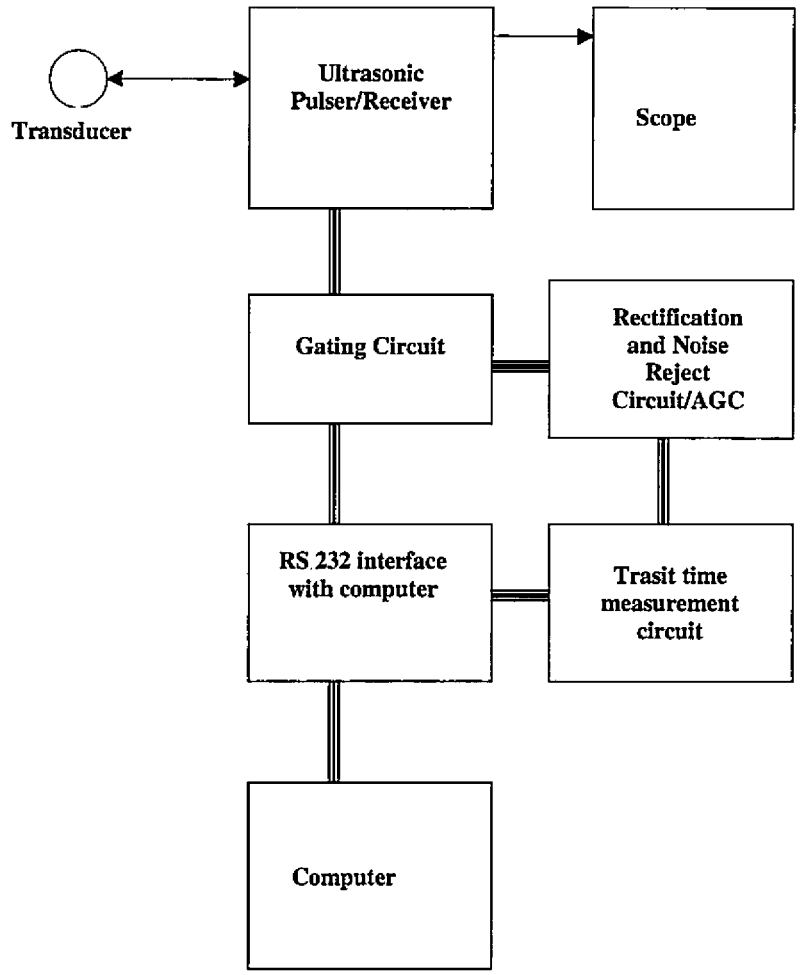

Figure 3-1: Ultrasonic system components diagram

signal, (the "main-bang.") and the satellite (= specular) signal (normal-incidence reflection from the surface) are followed by the surface-wave signal. Surface wave velocity changes are detected by changes of arrival times. The shear wave R_w, moves at $\cong 0.5$ the velocity of the L_{cr} wave. Thus it appears later than the L_{cr} signal.

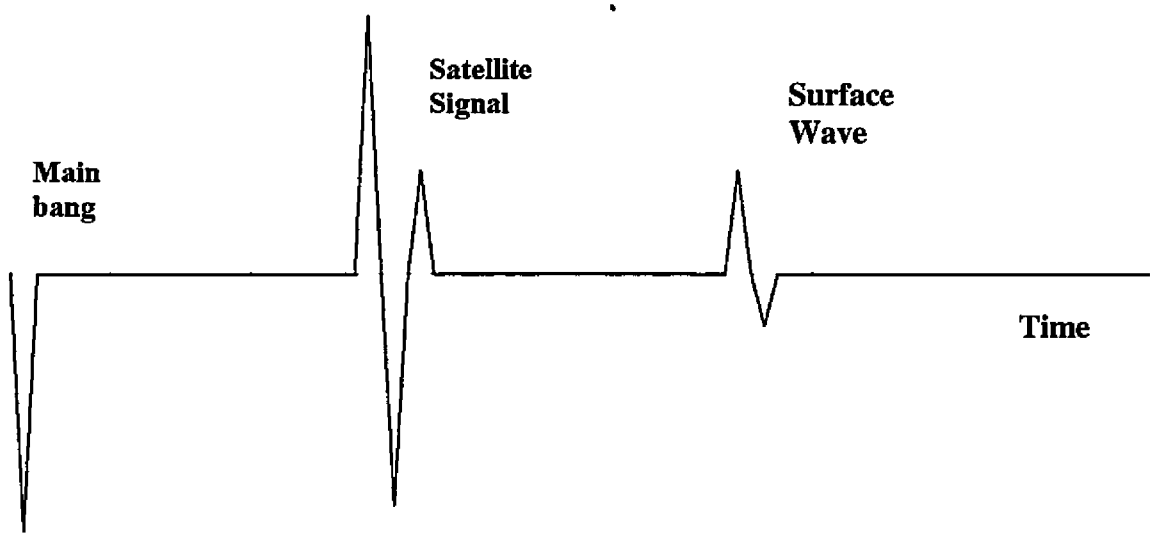

Figure 3-2: Typical signals observed from a focused ultrasonic probe that generates surface waves.

Stress-induced, propagation-velocity-changes are small ($\cong 0.1\%$). Thus, variations due to testing procedure must be minimum (at least one tenth the level for the desired stress resolution). Procedure variations are associated with the instrumentation and the reproducibility of the probe system.

The instrumentation is capable of 50 ps resolution. This is the fastest equipment available. Fallon Ultrasonics Inc. developed this system to accurately measure the time between two arrival signals from a target. The "specular,"/ "satellite," signal (directly from the sample surface) is normally strong, but R_w and L_{cr} signals are weak. Further, the strength of the latter decreases with distance from the specular reflection, thus electronics have been developed that have independent gain-control for each gate, i.e., each is adjustable manually or automatically (AGC), allowing increase of height of R_w or

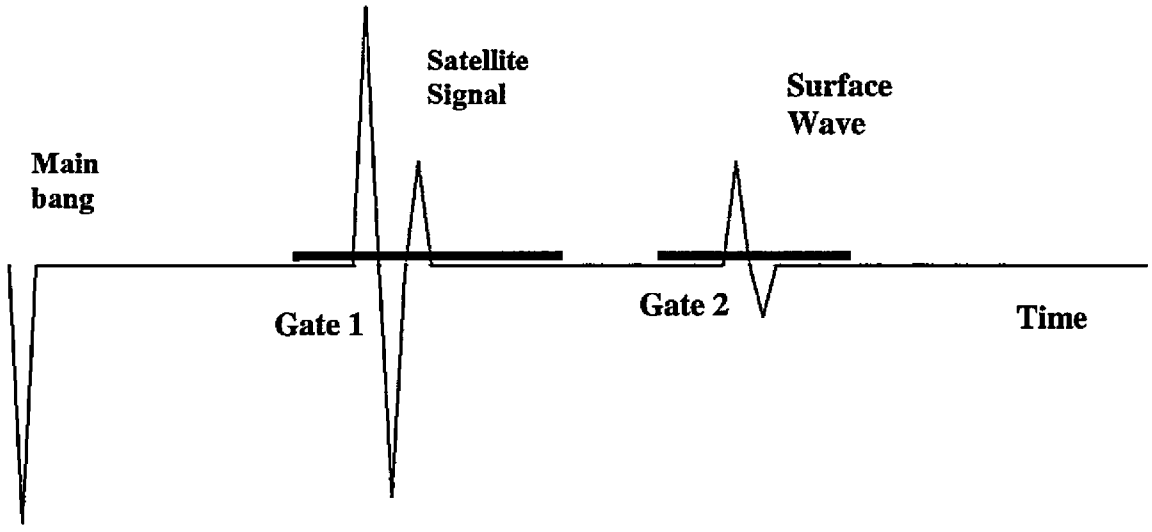

Figure 3-3: Separate gates on the satellite and the surface wave signals

L_{cr} signals without saturating the already-strong, surface reflection. Further, a noise-reject circuit has been introduced to remove acoustic and electrical noise that hinders measurements. The energy delivered to the transducer has been maximized to enhance the signal strength and arrival time is measured with a 1 GHz timing clock (1 ns resolution in a single shot). The computer averages the data collected at 20 KHz a hundred times to produce measurements with 50 ps accuracy.

The gate-delay (start-point for the signal) and width are adjusted (in 10 ns steps), such that the specular signal falls within Gate 1 and the Surface Wave in Gate 2 (Figure 3-3).

The half-wave-rectification mode removes negative portions of the signal (Figure 3-4). Then the signal undergoes gain adjustment (to obtain same-height signals) and noise rejection. This facilitates accurate, transit-time measurement. The system also has a built-in, phase-reversal circuit which allows the signal in Gate 2 to be phase-reversed, facilitating absolute transit-time measurement.

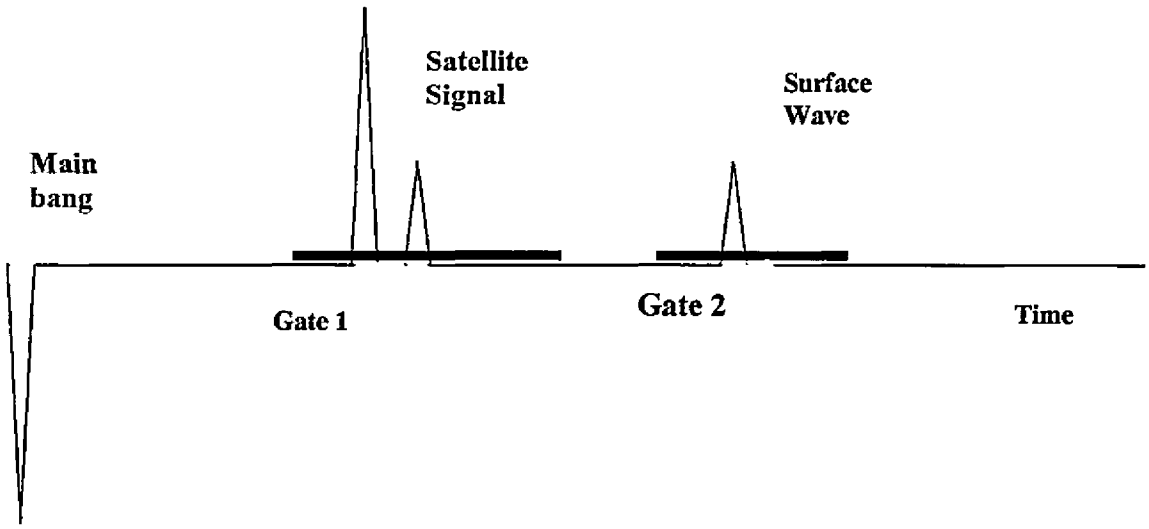

Figure 3-4: Half-rectified signals used for time measurements

Figure 3-5 (a) is a typical RF waveform for the specular and Rayleigh waves for a sample with normal gains. The equipment was adjusted via 'manual mode'. Figure 3-5 (b) shows these signals in half rectified form in manual mode, with the noise-reject function active. Figure 3-5 (c) shows the form of the signal used. The auto-mode therein is activated i.e. the peak heights are adjusted to be equal and subsequent changes of signal height due to surface condition are automatically compensated for, by the AGC (Automatic Gain Control, to 40 dB gain adjustment).

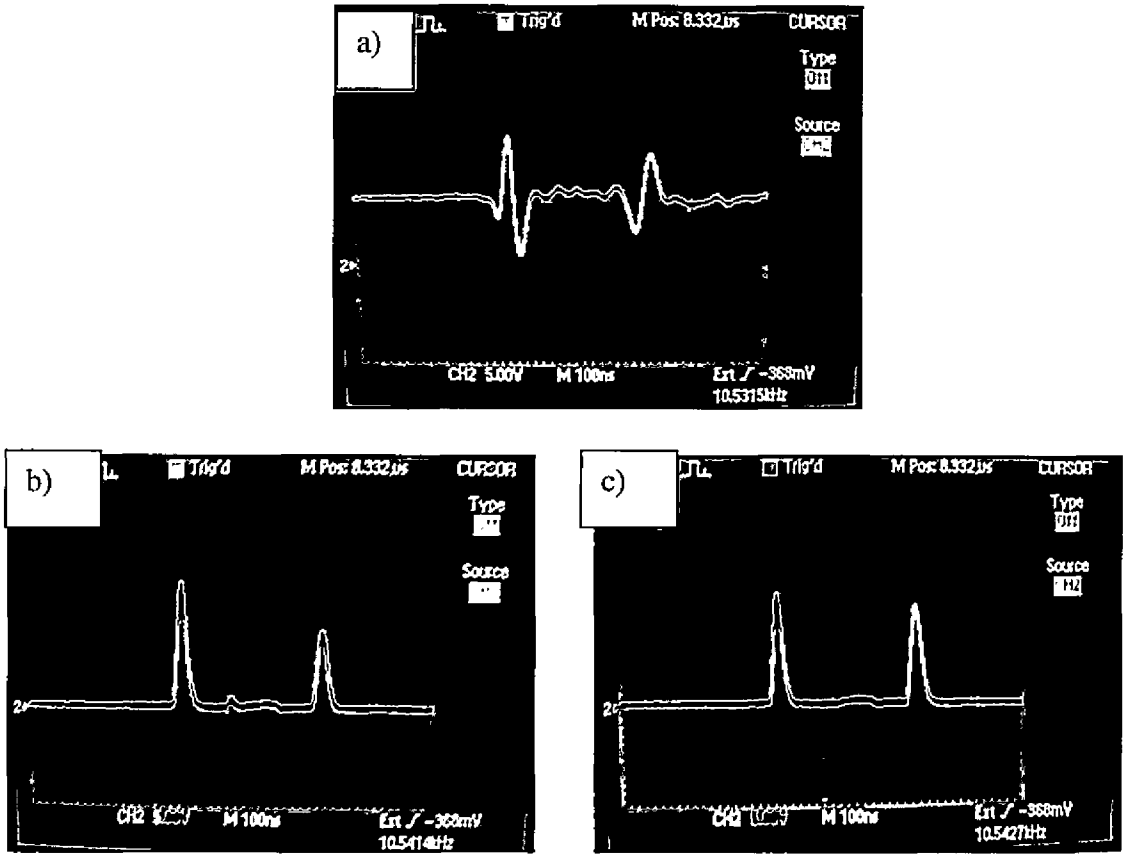

Figure 3-5: Signal processing before time measurement: (a) RF signals for the specular and Rayleigh waves, for normal gains in 'manual mode'; (b) the signals in half rectified form manual mode, noise-reject active; (c) auto-mode activated (i.e.peak heights equal)

The transducers were 'tuned' to obtain frequencies within their bandwidths by electrical impedance matching. A Fallon Ultrasonics pre-amp unit was used which proved useful as it allows a number of frequencies to be generated by a single transducer.

The accuracy of the system is demonstrated by the plot for loading a titanium sample in four-point bending (Figure 3-6). As the load increases, the plate deflects and

the arrival time of the specular, signal increases. Strain gauge readings are included at

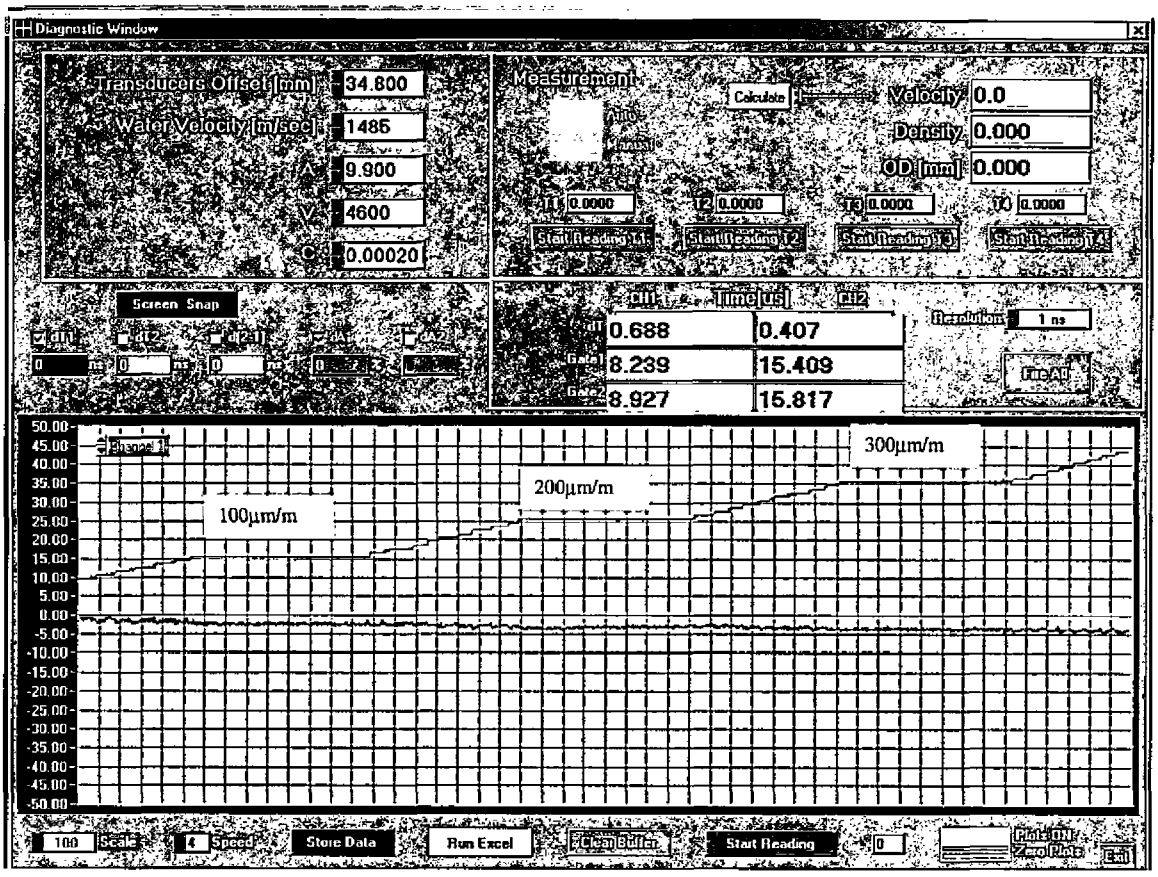

Figure 3-6: Ultrasonic output during the bend test loading of a Ti sample (1 ns = 100 on the scale).

each 'stop' (the sample held for 2 minutes at each load value and a microstrain reading taken). The change of time due to specimen deflection (0 to 300 μm/m strains) was less than 1 ns between loads yet the plot is continuous and the loading steps are clearly distinguished. Thus the system is capable of measuring times < 1 ns.

Chapter 4

EXPERIMENTAL PROCEDURE

4.1 Sample Preparation and Characterization

4.1.1 Corning 9604 glass and Corning 9606 glass-ceramic

As glass has no grains, it was decided to explore a crystallisable glass as a model material. It was impossible to obtain sufficiently big samples of precursor glass that could be subsequently crystallized. Finally, Corning kindly provided two 90 mm x 26 mm x 6 mm plates of glass, Code 9604, the precursor material for their cordierite glass-ceramic, Code 9606. They also provided three crystallized specimens of the same material. Each had suffered a different heating cycle to produce different grain sizes but, TEM examination showed that all heats had resulted in similar grain size. Corning did not reveal the heat treatments. XRD spectra of the parent glass and daughter glass-ceramic confirmed the amorphous of the former and the single phase of the latter. Densities were measured by the Archemedes Method.

A number of small samples (10 mm/ 10 mm/ 6 mm) were provided by Corning. Two glass and two ceramic samples were laser-etched to provide two fine surface roughnesses. Samples were polished before etching. The steps involved are listed in Table 4-1.

Table 4-1: The Grinding and Polishing procedures for Corning 9606 and 9604.

Grinding/ Polishing Medium	Lubricant	Wheel Speed, RPM	Pressure, N	Time
Resin with 1200 grit diamond	Water	300	120	7 min
9-μm-particle diamond spray on the composite 'allegro' cloth	80% ethanol, 20% ethylene glycol, 1 drop/ minute	300	60	5 – 6 min
3-μm-particle diamond paste on the polishing cloth	80% ethanol, 20% ethylene glycol, 1 drop/ minute	300	60	5 – 6 min
0.05-μm-particle suspension of colloidal silica	low-pressure water stream	300	30	6 min

A glass and a cerammed plate were sent to Gennum Corp., Burlington, ON for machining. A dicing saw machined a series of parallel grooves in three positions in other samples, each with different groove spacing and depth.

Alpha-Step was used to determine the surface profiles. The corresponding surface roughness (Ra) values were measured.

Residual stresses in the dice-saw-machined and laser-etched 9606 samples were measured at Proto Inc., Windsor ON by XRD. A chromium cathode was used for the X-ray source.

After ultrasonic examination, samples were annealed to remove residual stress. The schedule was developed based on the 'Corning method' (Doyle 1979) and details are listed in Table 4-2.

Table 4-2: The stress-anneal schedule derived for Corning 9604 and Corning 9606.

RAMP	RATE, ° / hour	TIME, min
23C° - 705C°	820	50
705°C	hold	30
705°C - 638°C	84	48
638C°-588C°	168	18
588C° – 23C°	847	40

4.1.2 Single Crystal Magnesium

Magnesium was obtained as a phase-stable model for Titanium. Magnesium single crystal, 99.99% pure was purchased from Accumet Materials Co., NY, USA (25 mm diameter, 65 mm long cylinder). The orientation of the as-received crystal was random, thus back-reflection Laue patterns were used to identify the planes of interest via copper radiation. The diffraction spots were indexed and corresponding stereographic projection drawn using Orient Express 3.3 software. Once the basal (001) plane was determined, two parallel cuts were made by Electric Discharge Machining (EDM). The sample was cut sitting on the goniometer to preserve the X-ray machine orientation. A special bracket was machined to attach the goniometer inside the EDM tank (one side was precisely parallel to the EDM wire). A parallel-sided sample with basal plane surfaces

was thus produced. Laue inspection confirmed the cuts were accurate. A new stereographic projection identified the (010) planes so two more cuts were made. The last Laue indicated the (001) cut was ~2° off, so a special 2° wedge was used to position the sample correctly when making the (001) cuts. The resulting sample was orthorhombic. Surfaces resulting from EDM cutting were rough, thus they were ground on 4000 grit SiC paper, and polished with 3μm and 1μm diamond paste. A special TEM sample preparation holder was used to assure material was removed uniformly and parallel to the cuts. X-ray diffraction spectra and rocking curves were obtained on the exposed surfaces to determine cut accuracy.

4.1.3 Titanium

Titanium was obtained in two forms: hot pressed (minimum texture) and cold-rolled. Sheets of cold-rolled, commercially pure (CP), Grade 4, titanium (6mm thick) were purchased from RJ Enterprise LLC, Connecticut, USA. The chemical composition and mechanical properties, as provided by the manufacturer, are listed in Tables 4-3 and 4-4, respectively. The hot-pressed, CP, CHIP process, titanium plates were purchased from Dynamet Technology, Inc., MA, USA. The CHIP process involves cold isostatic pressing and vacuum sintering, followed by hot isostatic pressing. The powder used was ~325 mesh (45 μm). Such material preparation provided minimum texture samples.

Four plates, 90 x 25 x 6 mm^3, were cut from the rolled sheets: two with the long dimension parallel to the rolling direction and two parallel to the transverse direction.

Table 4-3: Chemical composition of the CP, grade 4 titanium

CHEMICAL ANALYSIS					
Fe	O	H	C	N	Ti
0.14	0.33	0.0023	0.03	0.027	99.4707

Table 4-4: Mechanical properties of the CP, grade 4 titanium.

MECHANICAL PROPERTIES		
Yield Point, MPa	Tensile Strength, MPa	%Elongation
570	650	26.0

The rolled and hot-pressed plates were lapped on Logitech Precision Lapping and Polishing Machine, with 1200 grit SiC using ethylene glycol as lubricant.

The rolled plates were heat-treated in an argon atmosphere to promote grain growth. The furnace profile used was 4 hours to 850°C, holding time 't', then furnace cooling. Details are listed in Table 4-5. A thin oxide layer developed on the specimen surfaces so they were lapped (1200 grit SiC), ground on 4000 grit SiC, then polished. The polishing process is summarised in Table 4-6. X-ray diffraction confirmed that after the heat treatment, the resulting microstructure consisted of single, α-phase.

A 10 mm x 25 mm x 6 mm sample was cut, from each specimen's end, with the 25 mm x 6 mm side being the cross-section (CS) of the heated plate. These samples were mounted in Lucite (CS side exposed), ground and polished on the automatic polisher

Table 4-5: Titanium heat treatments (A is the untreated specimen)

Specimen	Hold Time 't' at 850°, h
B	5
C	20
D	50

Table 4-6: Steps for polishing of Ti plates.

Polishing Medium	Lubricant	Wheel Speed, RPM	Time
6-μm-particle diamond paste on the nylon cloth	Si-based lubricant	300	2 h
3-μm-particle diamond paste on the cotton cloth	Si-based lubricant	300	2 h
1-μm-particle diamond paste on the cotton cloth	Si-based lubricant	300	½ h
0.05-μm-particle suspension of 85% colloidal silica and 15% hydrogen peroxide	low-pressure water stream	300	5 min

(steps described in Table 4-7). The samples were then etched with Kroll's etchant (3% HF, 6% HNO_3 and de-ionised water) for 6-10 seconds. Microstructures were observed with an optical microscope.

Pole figures (Brockhouse Institute, McMaster University) identified texture in the hot-pressed and as-received rolled specimens, and its development upon heating specimens B, C, and D.

To introduce surface residual stresses, titanium plates were machined by face-milling. The same cutter used a constant 400 RPM velocity, but the feed rate varied: 0.001, 0.0025, and 0.004 "/min for the rolled plates and 0.0025, 0.004, and 0.006 "/min for the hot-pressed plates. This introduced different magnitudes of stress and different surface-topographies.

Table 4-7: Steps for polishing lucite-mounted Ti-samples.

Grinding/ Polishing Medium	**Lubricant**	**Wheel Speed, RPM**	**Pressure, N**	**Time**
800 mesh SiC paper	water	300	60	3 min
9-μm-particle diamond spray on the nylon cloth	80% ethanol, 20% ethylene glycol	300	60	5 – 6 min
3-μm-particle diamond paste on the cotton cloth	80% ethanol, 20% ethylene glycol	300	60	5 – 6 min
0.05-μm-particle suspension of 85% colloidal silica and 15% hydrogen peroxide	low-pressure water stream	300	30	5 min

Optical pictures were obtained of each surface. Alpha Step apparatus was used to plot the surface topography. The stresses in the surfaces were measured by X-ray at Proto Manufacturing, Ltd, Windsor, Ontario.

Samples, after ultrasonic examination, were annealed at 560° C for 45 minutes then furnace cooled to remove residual stresses.

4.2 Acoustoelastic Constant Determination

A special jig was designed (Figure 4-1), which allowed attachment of the transducer over the specimen's top surface. This was to monitor the velocity changes on compressive loading. Strain gauges (350Ω) were mounted on the bottom surfaces and the corresponding tensile strain measured. The load was applied with an Instron 810 MTS machine, (McMaster, Automotive Center). Ultrasonic readings (specular signal and surface wave arrival times) were recorded at each step, along with the corresponding strain on the strain-gauge meter. The resulting stress was calculated via the Dynamic Elastic Modulus (E x ε). The Acoustoelastic Constants were measured with a 15 MHz R_w cylindrical transducer and a 12 MHz, L_{cr}, spherical transducer. The loading force was applied to the Corning plates in 200 N steps, up to 1200 N (glass) and 2400 N (glass-ceramic). Titanium, was loaded in 500 N steps, up to 7000 N. The Acoustoelastic Constants for rolled titanium were measured in the rolling and transverse directions.

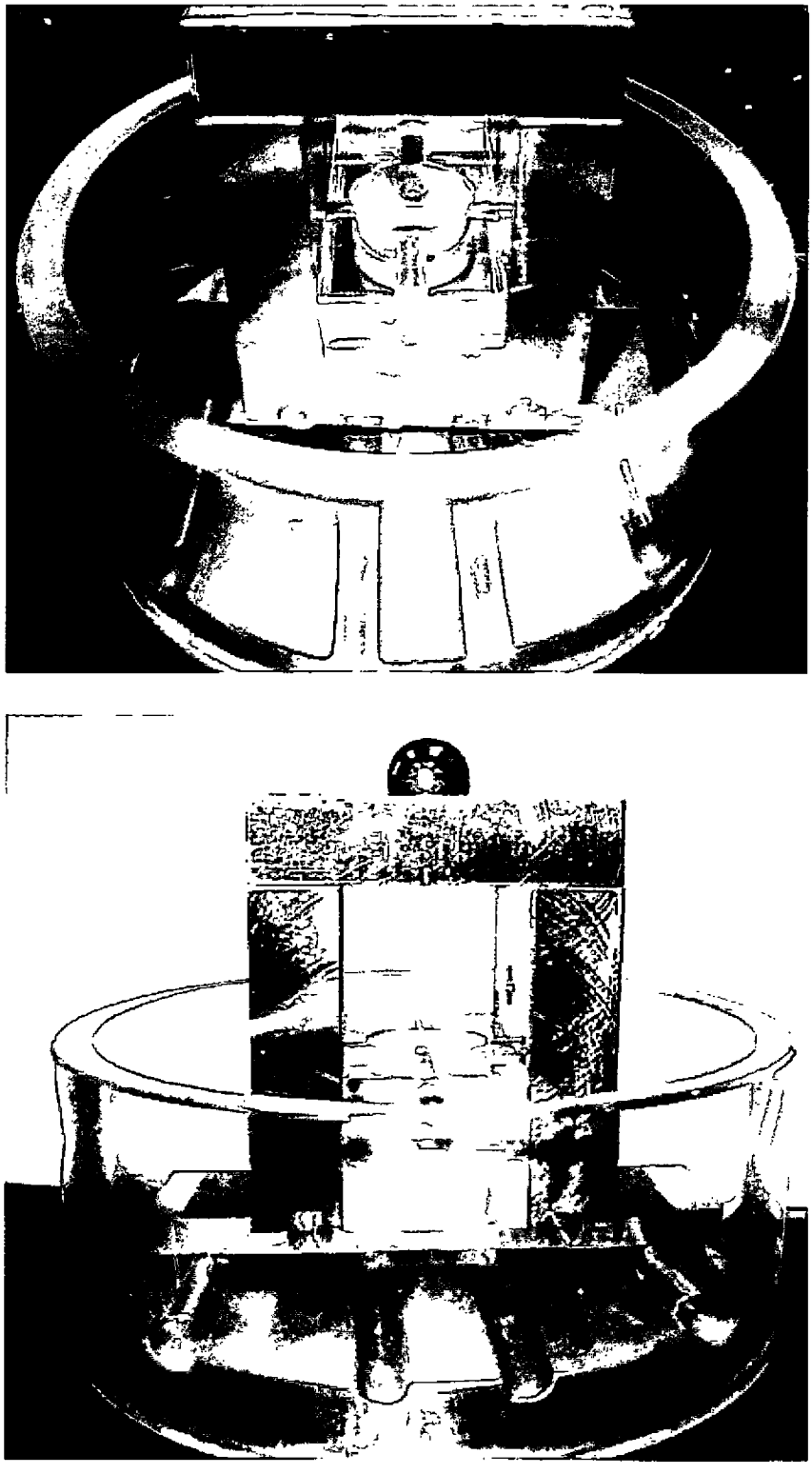

Figure 4-1: UT test jig for measuring Acoustoelastic Constant via 4-point bending.

4.3 Ultrasonic Examination

4.3.1 Corning 9604 and Corning 9606

Longitudinal and shear (bulk) ultrasonic velocities were measured to study the difference between amorphous and crystalline materials of the same chemical composition. The shear transducer was rotated 360° and the maximum and minimum velocities (if such existed) were recorded. The latter describe the anisotropy in the as-received samples. Bulk velocities were used to calculate the Young's and Bulk Modulii of the samples (Equations 34-36). The Rayleigh wave velocity was measured at different frequencies on the flat surface of the crystalline sample to track the effect of grain scatter.

The Rayleigh wave (10, 12, 16, 20MHz) and Lcr (12MHz) velocities were measured in each machined location, as well as for the smooth (reference) surface. The Rayleigh transducer was cylindrical (had a line-focus), and the waves propagated across the grooves on the samples. The Lcr transducer had spherical-focus ("point"-focus).
The measurements were repeated after the plates were stress-relieved. The changes of ultrasonic velocity were related to relieved residual stresses using the predetermined Acoustoelastic Constants.

4.3.2 Single Crystal Magnesium

The <001>, <110> and <010> directions were drawn on the oriented crystal and the longitudinal ultrasonic velocities therein measured using a 5 MHz transducer in the <001> and <010> directions (a surface parallel to (110) plane was unavailable). The shear ultrasonic velocities were measured with a 5 MHz transducer in the <0001>

direction (particles polarized along the <110> and <010>) and the <010> direction (particle displacement along the <001>). These velocities were compared with those for polycrystalline magnesium.

4.3.3 Titanium

Ultrasonic longitudinal, shear, Rw and Lcr velocities were measured for Ti plates. Microstructure effects were observed. Bulk velocities were used to determine the elastic properties. Since the Rayleigh transducer has a line-focus, and since the shear waves are polarized, taking readings in rolling and transverse directions, allowed texture effects to be examined.

The R_w (frequencies 15, 16, 17, and 20 MHz) and L_{cr} (10 MHz) velocities were measured at each machined location, before and after stress-relief. Ten readings were taken at each point of interest, and the values averaged. The transducer, after adjusting its position to produce the strongest signal, was fixed permanently. Care was taken to position the transducer over the same location on the sample each time. The measurements were repeated after stress-relief and the percent change of velocity converted to 'relieved stress' via the Acoustoelastic Constants.

Chapter 5

Results and Discussion

5.1.1 Corning 9604 Glass and 9606 Glass-Ceramic

Transformation from non-crystalline glass to crystalline solid is called devitrification and the product is called a glass-ceramic. Corning Code 9604 is a precursor glass, which

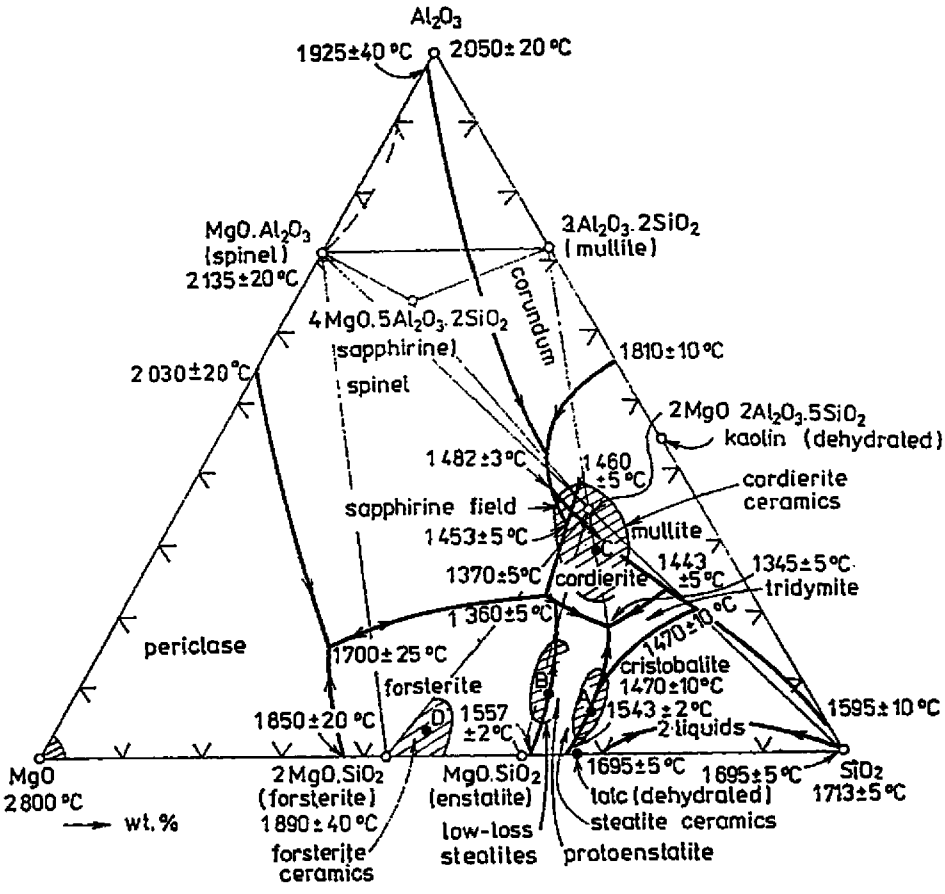

Figure 5-1: Phase diagram of the system MgO- Al_2O_3 – SiO_2 with plotted regions showing the composition of ceramic materials (Hlavac, 1983)

upon heating, crystallizes to orthorhombic cordierite: $2MgO \cdot 2Al_2O_3 \cdot 5SiO_2$. The desired microstructure is ~ 98 vol.% crystalline phase within 2% original glass. The ternary phase diagram of $MgO\text{-}Al_2O_3\text{-}SiO_2$ is shown in Figure 5-1. The cordierite phase field is cross-hatched.

Bulk crystallization of 9604 is catalised by TiO_2 as nucleating agent. The particular heat cycle is proprietary. The glass is heated rapidly to $\cong$ 50-100^{0}C above the annealing point and held there for a time to ensure nuclei growth. Temperature is then raised slowly to the top temperature where crystals grow on the nuclei. Strnad (1986) reported material of similar composition must be heated for 16 hours at 1300°C. Rabinovich (1982) observed glasses containing TiO_2 began to nucleate $\cong$ 750° C.

The chemical composition and relevant properties of Corning 9604 and 9606 are listed in Tables 5-1and 5-2.

Table 5-1: Chemical composition of Corning Code 9604 and 9606.

	Composition (wt%)
SiO_2	56
Al_2O_3	20
MgO	15
TiO_2	9
Crystalline Phase	Cordierite Rutile

Table 5-2: Properties of Code 9606 glass-ceramic (Strnad, 1986)

Property	**CorningCode 9606**
Colour	White
Density, g/cm^3	2.61
Softening point, °C	1350
Porosity	0.00
Bending strength, MPa	241
Young's modulus, GPa	120
Shear modulus, GPa	47
Bulk modulus, GPa	79
Poisson's ratio	0.245
Coefficient of thermal expansion, K^{-1}, 20 – 320°C	57×10^{-7}

Figures 5-2 and 5-3 are TEM micrographs of amorphous (9604) and crystalline 9606, respectively. Specimens were very beam-sensitive so it was difficult to obtain satisfactory pictures. The unusual strength and toughness of glass-ceramics is attributed to the long, acicular blade-shaped particles, clearly seen in Figure 5-3. It was difficult to distinguish the rutile particles, which suggests there are very few. The average grain size was estimated to 0.6 +/- 0.2 μm.

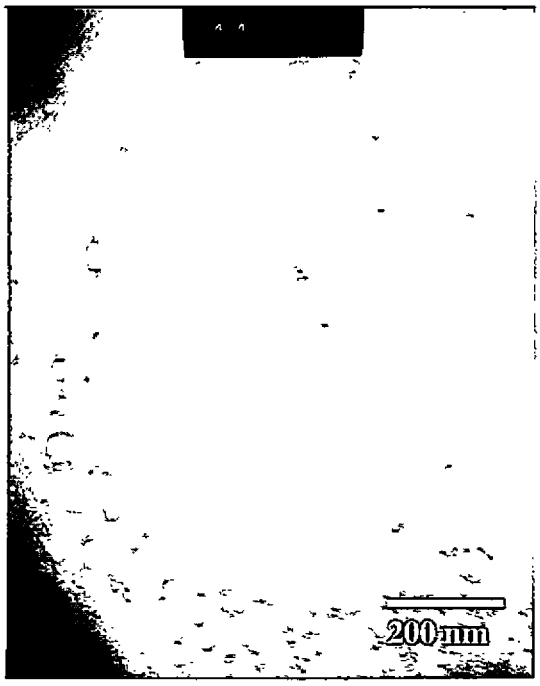

Figure 5-2: TEM micrograph of amorphous 9604, 100 K X.

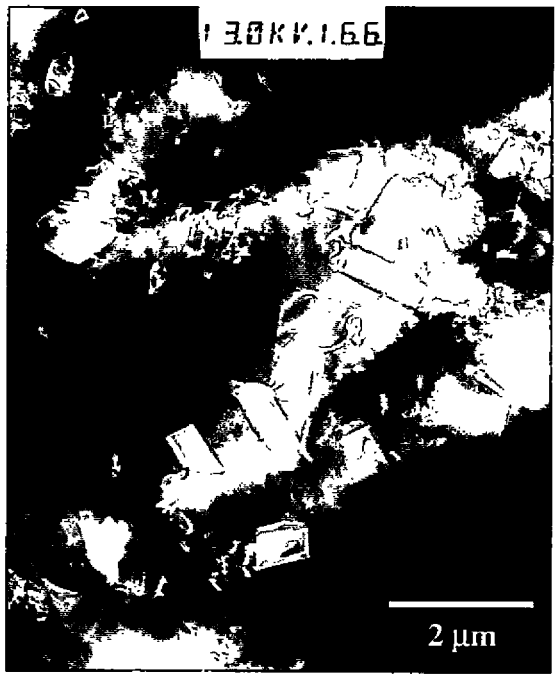

Figure 5-3 : TEM micrograph of glass-ceramic 9606, 13 K X.

X-ray diffraction spectra are presented in Figures 5-4 and 5-5. The amorphous sample has no reflections. 9606 was mostly cordierite, with two minor rutile peaks. The rutile was presumed negligible and single phase assumed.

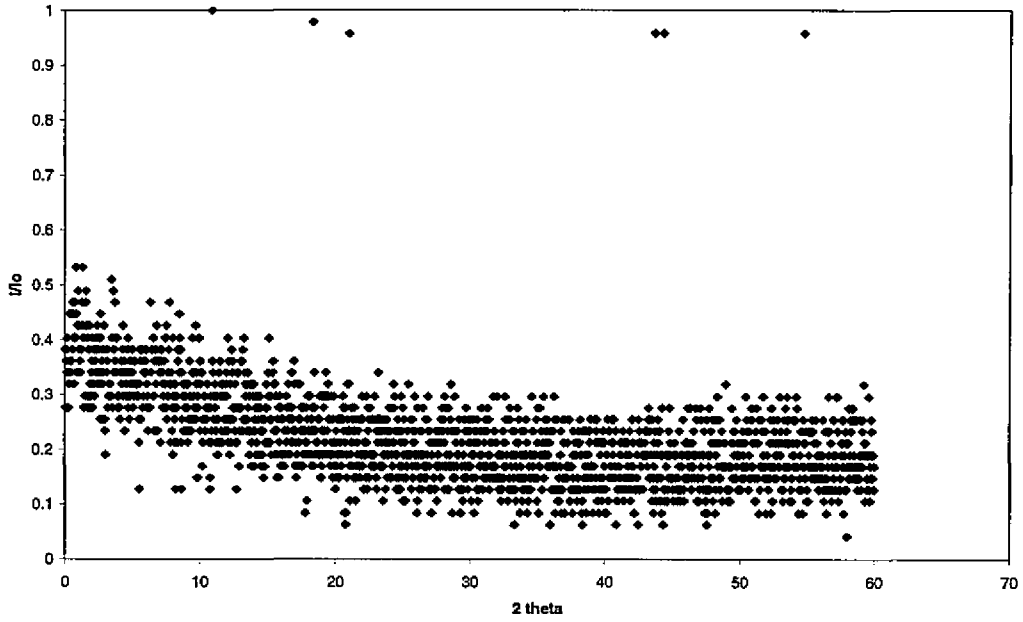

Figure 5-4: XRD on amorphous Corning 9604.

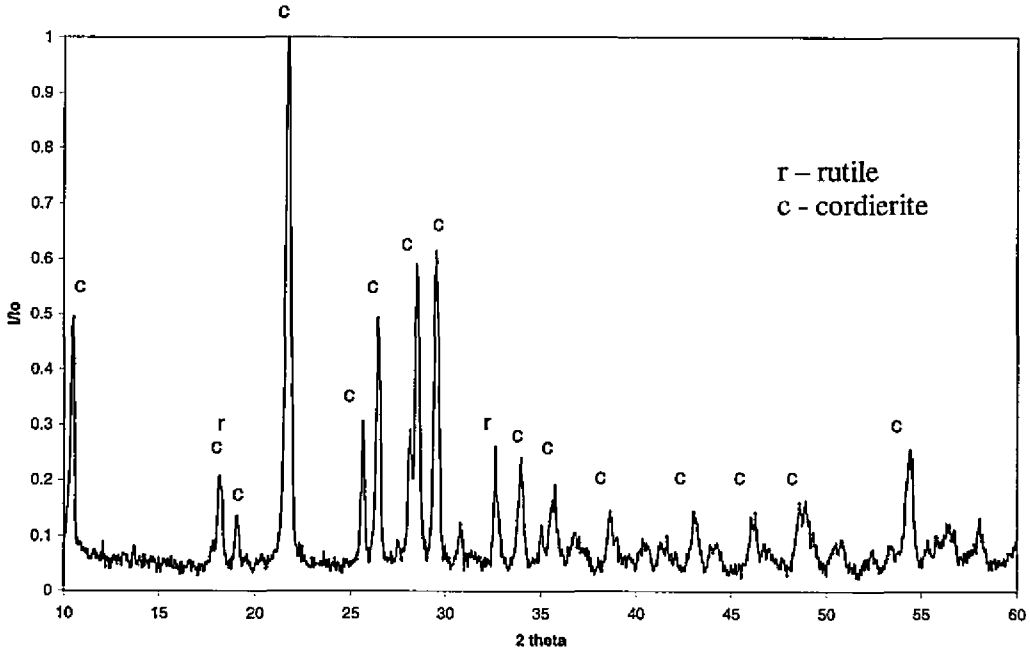

Figure 5-5: XRD on glass-ceramic Corning 9606.

Glass and glass-ceramic densities were measured by Archemedes method. Values are listed in Table 5-3. The density of the parent glass is higher than crystallized 9606. This is because 9606 contains a small percentage of amorphous phase (Strnad, 1986). The measured density of 9606 is 0.6% higher than reported in the literature. This may be experimental error or, since the density of glass-ceramics is additive, the content of parent glass may be different than material in the literature.

Table 5-3: Measured Properties of Corning 9604 glass and Corning 9606 glass-ceramic

	Density g/cm^3	**Longitudinal Wave Velocity, m/s**	**Shear Wave Velocity, m/s**
Corning 9604 glass	2.67 +/- 0.01	6758 +/- 5	3876 +/- 3
Corning 9606 glass-ceramic	2.63 +/- 0.01	7419 +/- 5	minimum = 4293 +/- 3 maximum = 4304 +/- 3

Ultrasonic longitudinal and shear wave velocities were measured in the glass and glass-ceramic (Table 5-3). The longitudinal velocity increased by ~9.8% on crystallization. The shear velocity increased ~10.9%. Such behavior was explained by Patel (1982). On crystallization, the density of cross-linking between neighboring ions increases, resulting in an increased overall bond strength (higher inter-atomic forces). Consequently the-speed-of-sound increases.

Table 5-4: Ultrasonically determined elastic properties of Corning 9604 and Corning 9606

Sample	Shear Transducer Orientation	Bulk Modulus K (GPa) +/- 0.1	Young's Modulus E (GPa) +/- 0.3	Poisson's Ratio υ +/– 0.005
Corning 9604 (glass)	0 degrees	68.5	100.7	0.255
	90 degrees	68.5	100.7	0.255
Corning 9606 (glass-ceramic)	0 degrees	79.7	121.2	0.246
	90 degrees	80.0	120.8	0.248

The measured bulk velocities were used to calculate the Poisson's Ratios and the dynamic Young and Bulk Moduli of the specimens (Table 5-4) (Equations 34 through 36). The Poisson's Ratio of the glass-ceramic is lower, but the moduli higher. Static Elastic Moduli values for the precursor glass are not available in the literature, however those published for Corning 9606 (E = 120GPa, and K = 79 GPa, ν = 0.245) agree well with those measured in this study (Strnad 1986). Further experiments revealed these values are influenced by residual stress in the as-received samples (see later). The ultrasonic shear wave transducer is polarized so was rotated to identify anisotropy via the minimum and maximum velocity values. The velocity difference for glass was ~0, for glass-ceramic 0.26%. Glass-ceramic material was chosen for its isotropic properties and these results verify the choice. Such a small change of shear velocity does not influence the Elastic Moduli values.

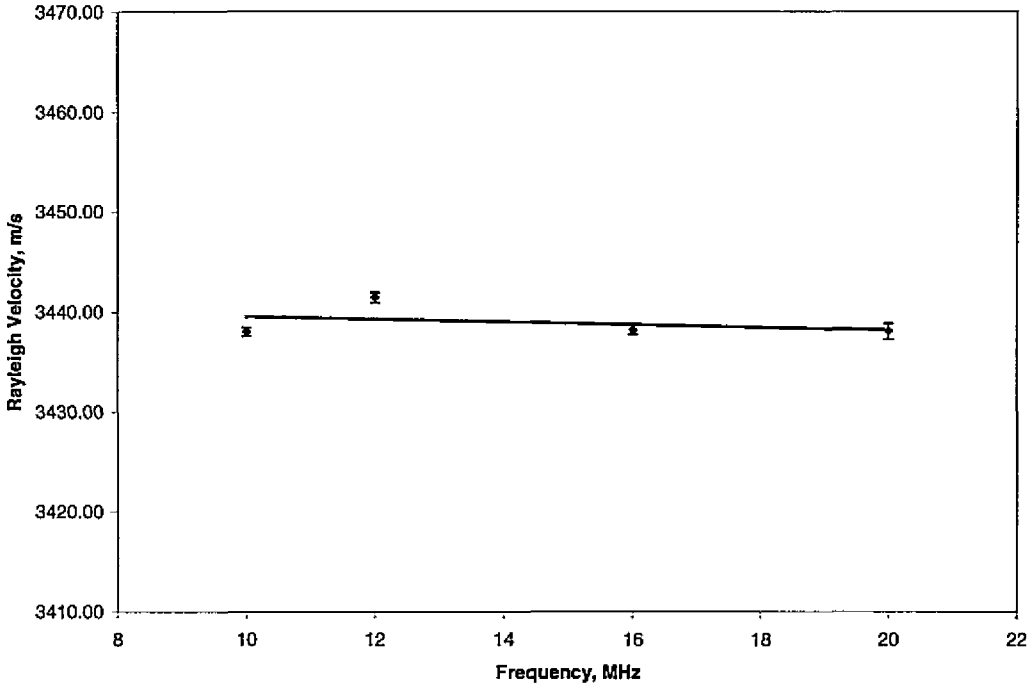

Figure 5-6: Rayleigh wave velocities along amorphous 9604 surface .vs. frequency.

Rayleigh (R_w) velocities were measured in 9604 and crystalline 9606 sample surfaces. Since the Rayleigh wave is nondispersive, its velocity does not depend on frequency. The latter is true unless material conditions such as grains cause sonic dispersion. Thus velocity should be constant with frequency in the amorphous material and it is (Figure 5-6). When grains are present, dispersion broadens the pulse as the high-frequency components of the frequency spectrum attenuate and the remaining partial waves travel at a different velocity. Velocities are influenced as the center frequency of the pulse changes. Figure 5-7 shows this effect for the Corning 9606, i.e. velocity decreases with frequency. A 10 MHz increase of frequency causes a velocity drop of 33.0 +/- 1.2 m/s. This agrees with previously published work, i.e. Pecorari et al (2000)

observed a significant decrease of Rayleigh wave velocity (R_w) in JRQ steel, as frequency increased from 2.5 MHz to 10 MHz. Ruiz et al (2002) also observed increased frequency caused a reduction of R_w velocity along an aluminum specimen (Chapter 2).

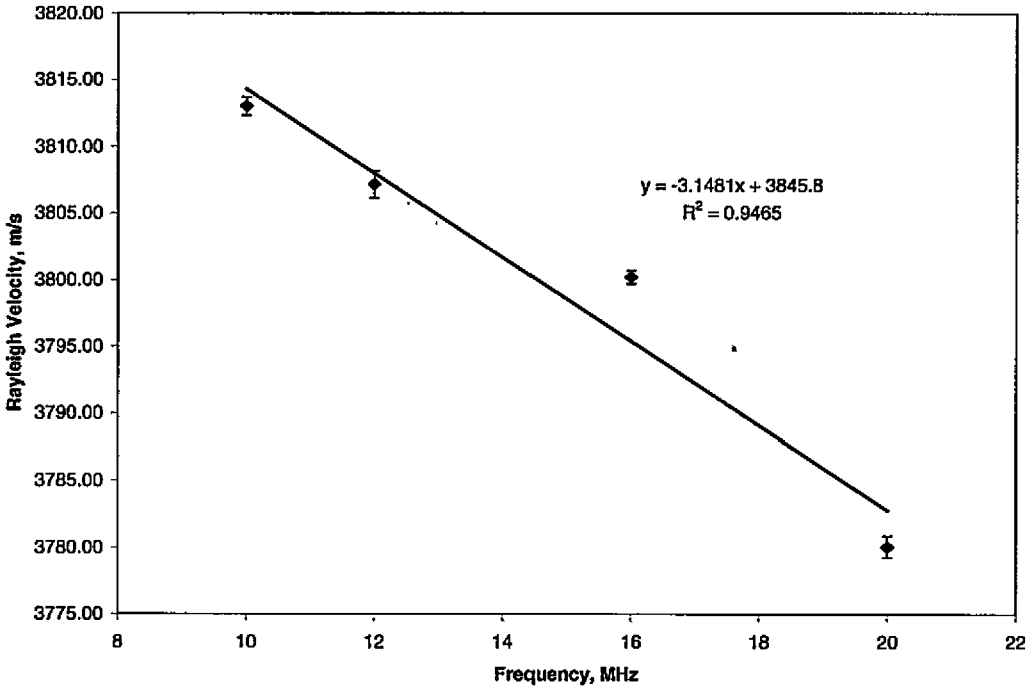

Figure 5-7: Rayleigh Wave Velocities in glass-ceramic at different frequencies in glass-ceramic Corning 9606

The specular-signal arrival time was corrected for, as frequency increase sharpened the incident signal (see Figure 5-8). The time position of the signal did not change but the rise-time decreased, as expected. Because the system measures the arrival time at some fixed threshold height, sharpening the peak results in a shorter central, specular-wave time-of-travel. This is incorrect as, no matter what the frequency, the distance between the sample and transducer remains constant, so, as the velocity-of-sound in the water couplant is constant, the arrival-time should have a fixed value. To deal with this

anomaly, a Ziadore glass sample was used for calibration and to facilitate the correction of subsequent measurements.

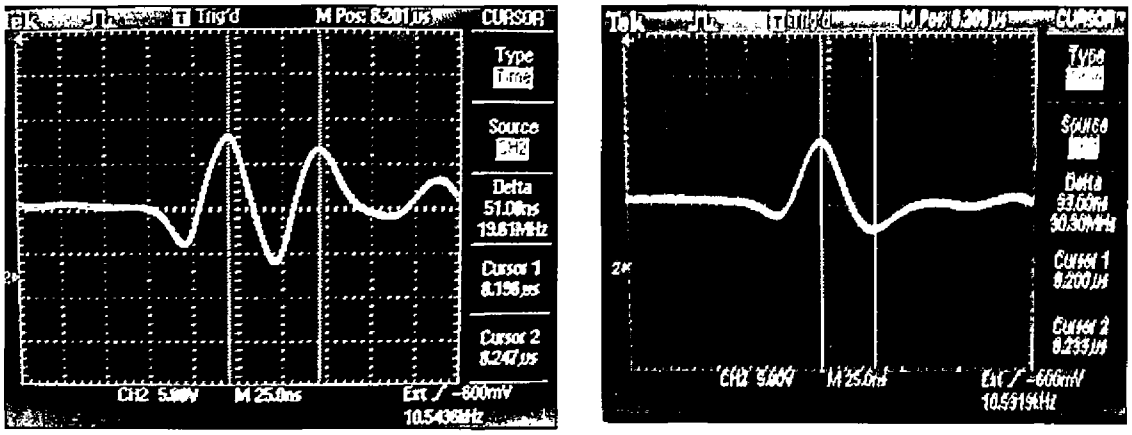

Figure 5-8: 20 MHz and 15 MHz waveforms of a specular reflection obtained with pre-amp tuning.

5.1.2 The Acoustoelastic Constants for Glass 9604 and Glass-Ceramic 9606

The Acoustoelastic Constants for glass 9604 and glass-ceramic 9606 were determined via the 4-point bend test. A 15 MHz, cylindrical transducer was used to generate R_w and a 15 MHz spherical transducer, L_{cr}. The Rayleigh waves propagated the sample surface in the longitudinal direction and ultrasonic velocity vs. applied microstrain, is plotted in Figures 5-9, 5-10 and 5-11. The compressive stress in the top surface of the bend specimen causes the ultrasonic velocity to increase.

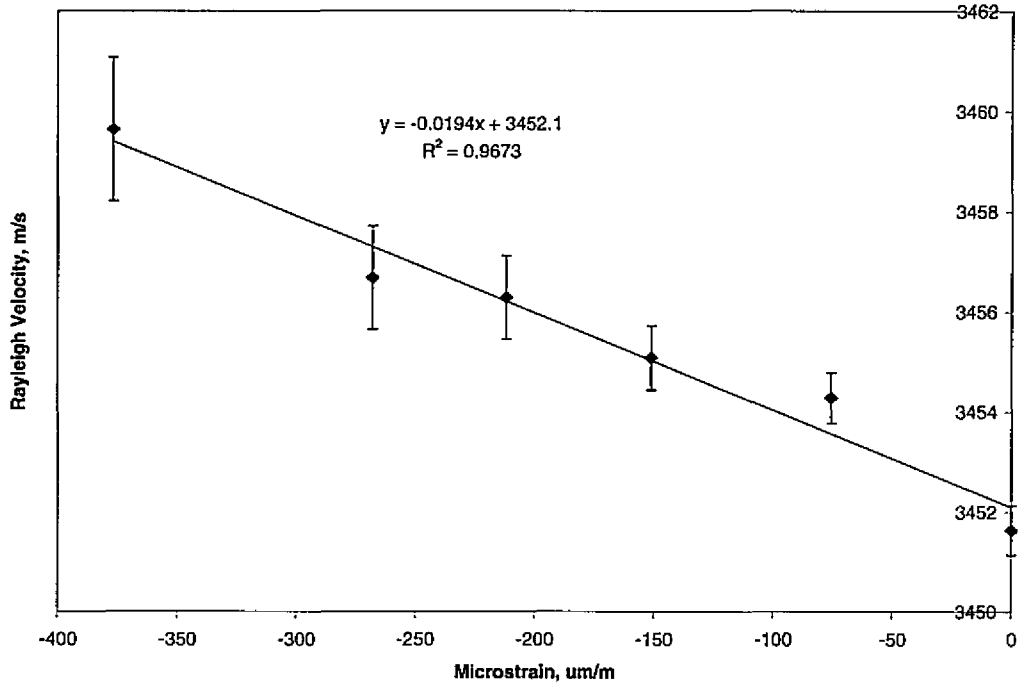

Figure 5-9: Rayleigh Velocity vs. microstrain for Corning 9604 glass.

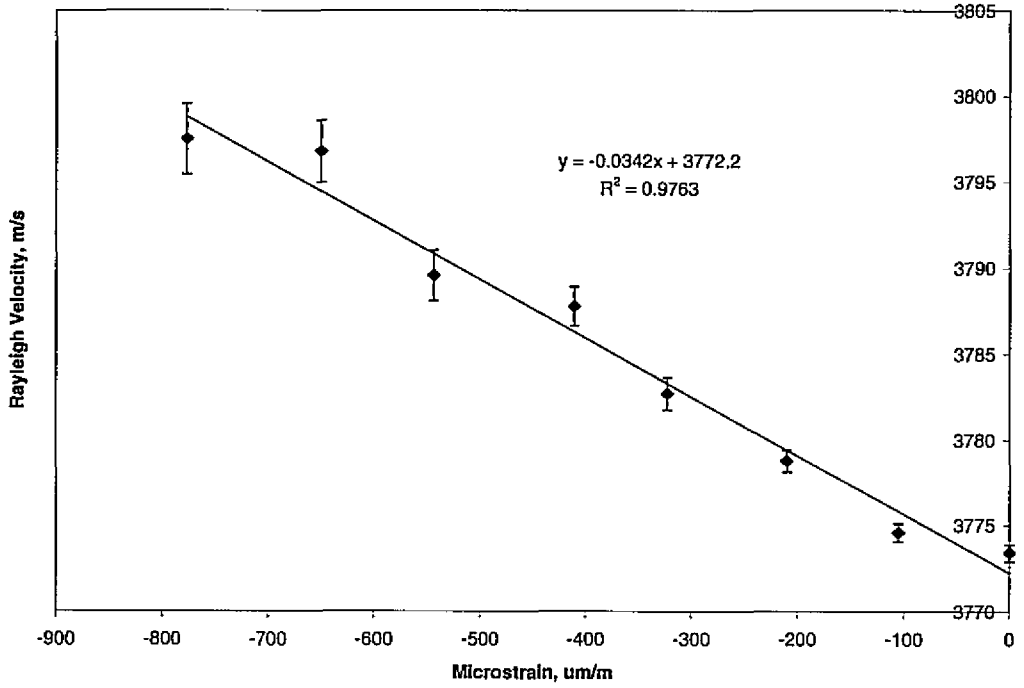

Figure 5-10: Rayleigh Velocity vs. microstrain for Corning 9606 glass-ceramic.

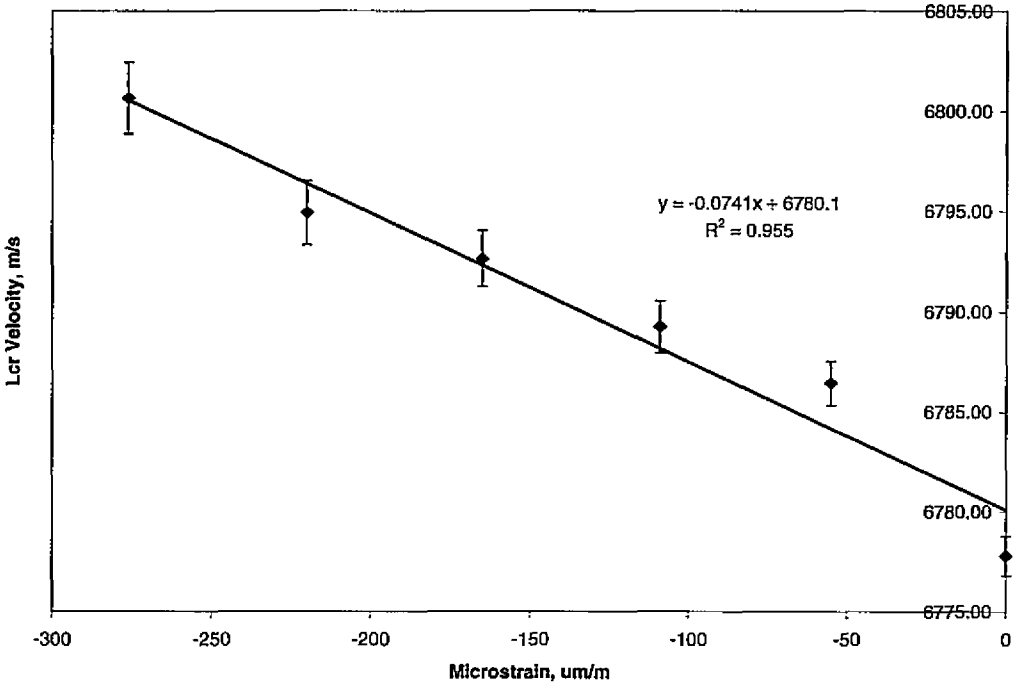

Figure 5-11: L_{cr} velocity dependence on compressive strain in the Corning 9606 glass-ceramic (L_{cr} wave generated with a spherical transducer)

The arrival time of the specular signal increased as the samples were loaded. This implies samples were elastically deflecting. Since the transducers are not perfectly spherical/ cylindrical and sound is thus not generated by a single source, rather by the whole area of the transducer, the influence of the distance between sample and source was examined with the R_w transducer. As this distance increased, the velocity decreased such that $(\Delta V/\Delta T_1) = -35.9$m/s / μs for glass and $\Delta V/\Delta T_1 = -30.5$m/s / μs for the glass-ceramic (T_1 is the arrival time of the specular signal). Thus, the arrival-time-change of the specular signal, on conversion to the corresponding change in velocity, is included in the error value.

The resolution accuracy of the ultrasonic system was 50 ps. This is considered in estimating the error bars. When measurement of one, or both, arrival times is 50 ps in error, the maximum error in the Rayleigh wave velocity is (+/-0.5 m/s) and (+/-1 m/s) for the L_{cr}.

Since the transducer was placed over the top of the sample and the strain-gauge on its bottom, (directly opposite the transducer), an experiment was conducted to confirm that the strain measured is the same. A titanium plate was bent with two strain gauges, one on top, one on the bottom. The measured strain was identical (see Figure 5-12).

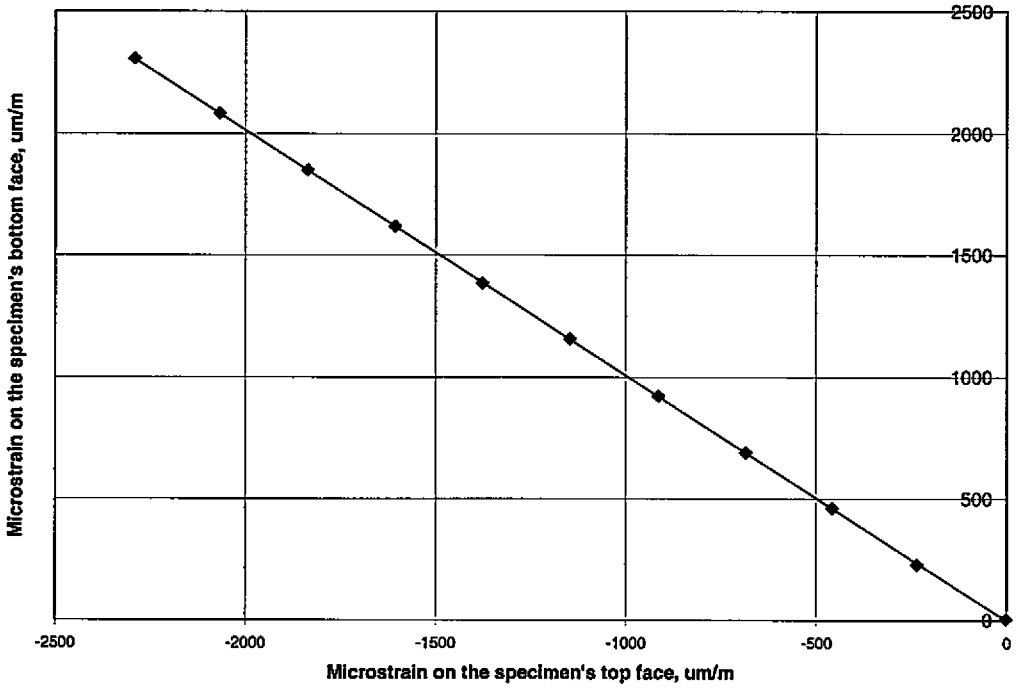

Figure 5-12: Strain Measured on a sample bent in 4-point bend test, measured at two points exactly opposite, one in compression and one in tension.

The percentage change in velocity ($\Delta V/V_{initial}$ x 100%) was calculated from the data and plotted versus stress via ($\sigma = E \varepsilon$). The best-fit line was drawn through the origin and points (Figures 5-13, 5-14 and 5-15). Slopes give the Acoustoelastic Constants and these are summarized in Table 5-5.

Table 5-5: Acoustoelastic Constants for the Rayleigh Wave propagating in the longitudinal direction and for the Lcr Wave generated by a spherical transducer.

	Rayleigh Wave Acoustoelastic Constant, %/GPa	**Lcr Wave Acoustoelastic Constant, %/Gpa**
Corning 9604	**- 6.00 +/- 0.52**	
Corning 9606	**- 6.85 +/- 0.48**	**-10.42 +/- 0.61**

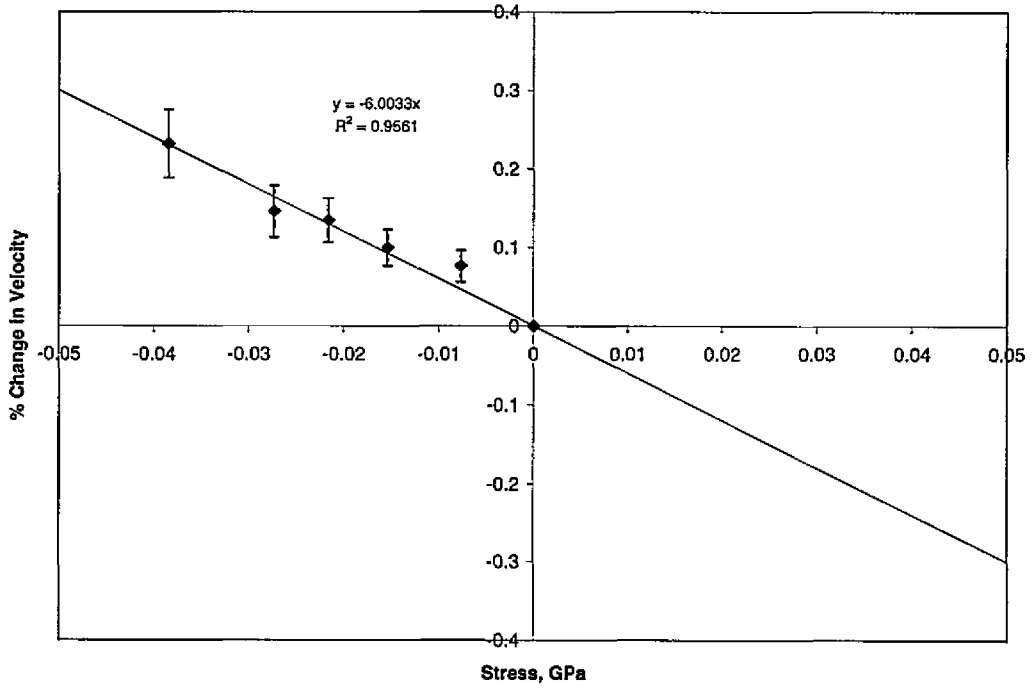

Figure 5-13: The shift of Rayleigh wave velocity and strain-in-four-point-bend, for Corning 9604 glass (sound propagation along the sample).

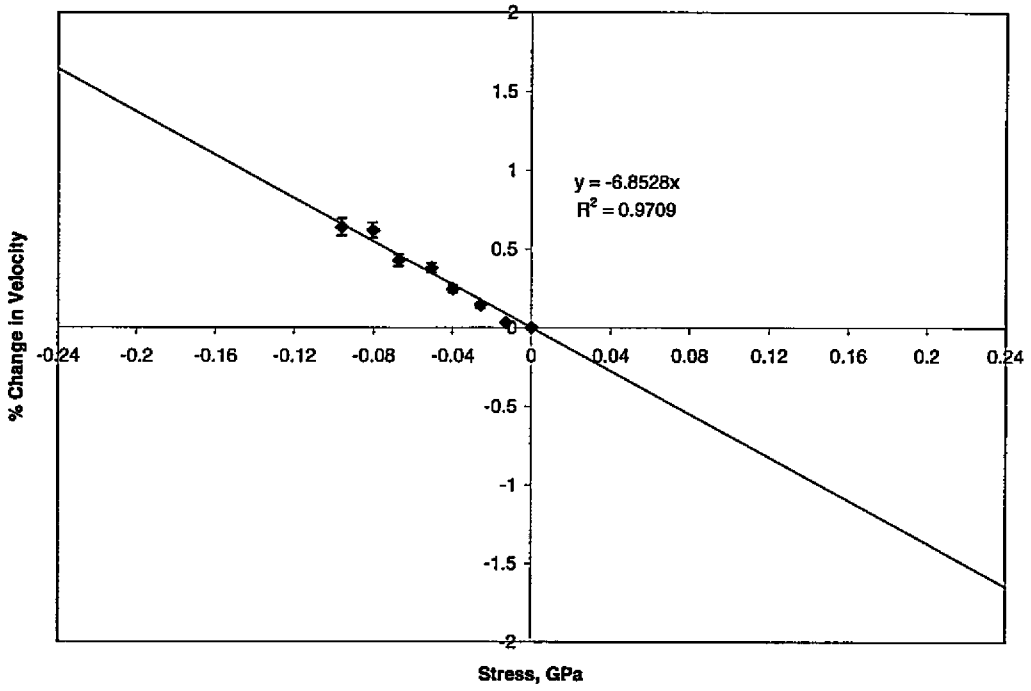

Figure 5-14: Shift of Rayleigh wave velocity and strain, in four-point bend, for Corning 9606 glass-ceramic (sound propagation along the sample).

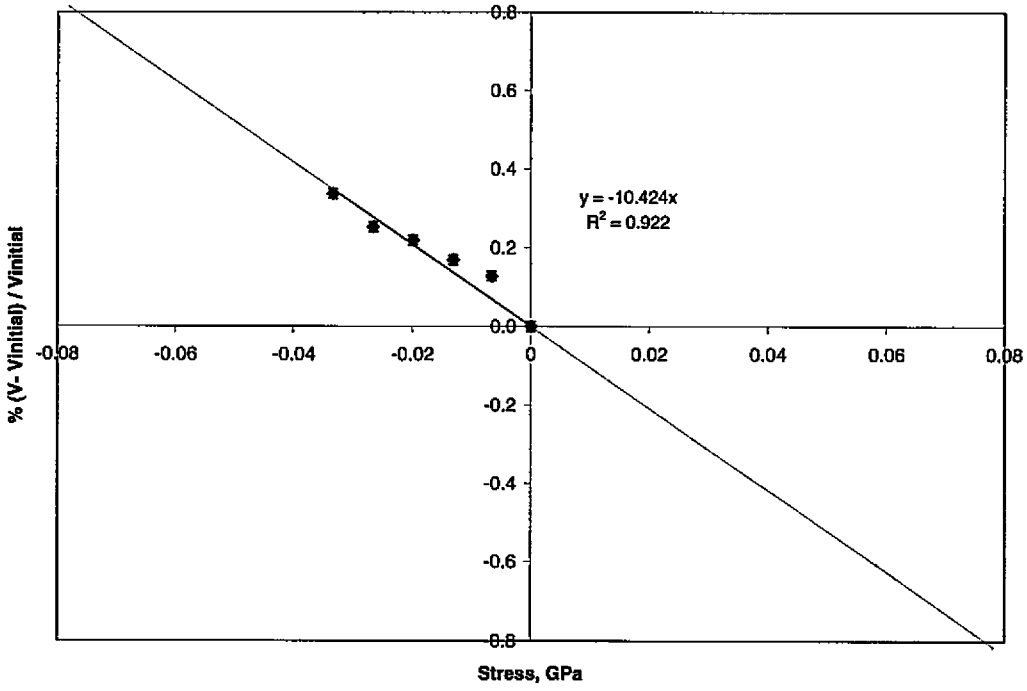

Figure 5-15: Shift of L_{cr} wave velocity and strain, in four-point bend, for Corning 9606 glass-ceramic (L_{cr} wave generated by a spherical transducer).

5.1.3 Machined Surfaces of Corning 9604 Glass and 9606 Glass-Ceramic

Conventional machining could not be used to introduce surface roughness and residual stresses into the glass and glass-ceramic. Samples were thus laser-etched to produce a low-stress/ fine-finish. A series of grooves were also introduced with a dicing saw to produce rough surfaces. Local heating and quenching during both methods of cutting introduces stress. A summary of groove spacing/ depth and corresponding R_a values, is included in Table 5-6. Optical micrographs of the surfaces and their profiles via Alpha Step are shown in Figures 5-16 and 5-17.

Table 5-6 : Machined Surfaces on Corning 9604 glass and Corning 9606 glass-ceramic.

	Ra, μm	Groove Spacing, μm	Groove Depth, μm
Corning 9604 Glass	0.07 +/- 0.02		
	0.51 +/- 0.05	20 +/- 2	1.6 +/- 0.1
	2.3 +/- 0.1	51 +/- 2	6.0 +/- 0.1
	6.6 +/- 0.06	150 +/- 2	25.5 +/- 2
	8.9 +/- 0.22	310 +/- 2	23 +/- 2
	12.9 +/- 0.7	500 +/- 2	45 +/- 2
Corning 9606 Glass-Ceramic	0.06 +/- 0.02		
	0.14 +/- 0.02	20 +/- 2	0.15 +/- 0.05
	0.98 +/- .015	50+/- 2	2.4 +/- 0.5
	6.8 +/- 0.4	150+/- 2	24 +/- 8
	9.3 +/- 0.1	300 +/- 2	27 +/- 4
	16.1 +/- 0.8	500+/- 2	63 +/- 8

(a)

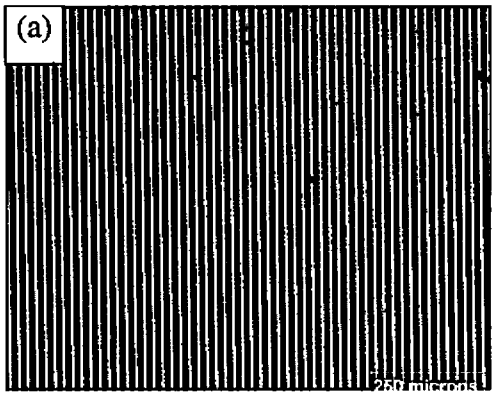
250 microns

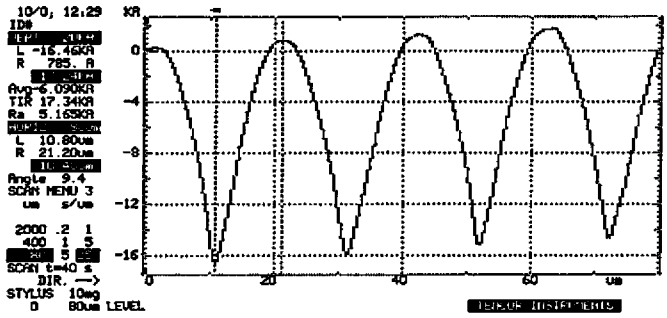
10/0, 12:29
ID#
L -16.46KA
R 785. A
Avg-6.090KA
TIR 17.34KA
Ra 5.165KA
L 10.80um
R 21.20um
Angle 9.4
SCAN MENU 3
um s/um
2000 .2 1
400 1 5
80 5 25
SCAN t=40 s
DIR. —>
STYLUS 10deg
0 80um LEVEL
KA
0
-4
-8
-12
-16
0
20
40
60
um

(b)

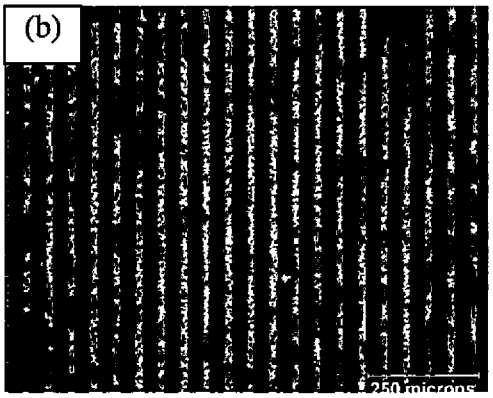
250 microns

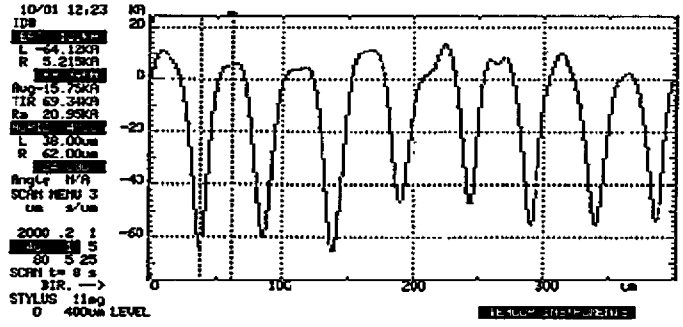
10/01 12:23
ID#
L -54.12KA
R 5.215KA
Avg-15.76KA
TIR 69.34KA
Ra 20.95KA
L 38.00um
R 62.00um
Angle N/A
SCAN MENU 3
um s/um
2000 .2 1
80 5 25
SCAN t= 8 s
DIR. —>
STYLUS 11deg
0 400um LEVEL
KA
20
0
-20
-40
-60
0
100
200
300
um

(c)

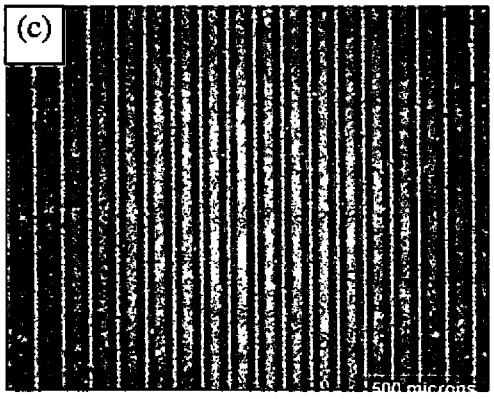
500 microns

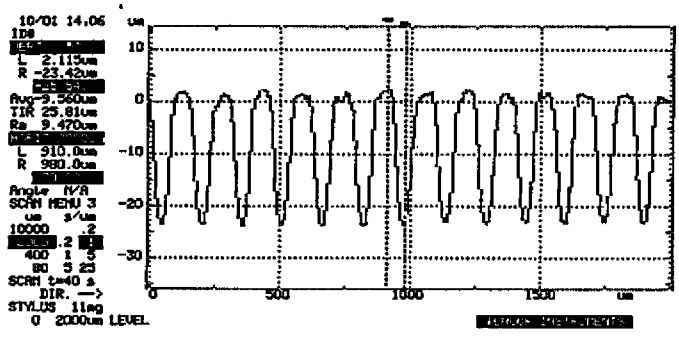
10/01 14:06
ID#
L 2.115um
R -23.42um
Avg-9.560um
TIR 25.81um
Ra 9.470um
L 910.0um
R 980.0um
Angle N/A
SCAN MENU 3
um s/um
10000 .2
400 1 5
80 5 25
SCAN t=40 s
DIR. —>
STYLUS 11deg
0 2000um LEVEL
um
10
0
-10
-20
-30
0
500
1000
1500
um

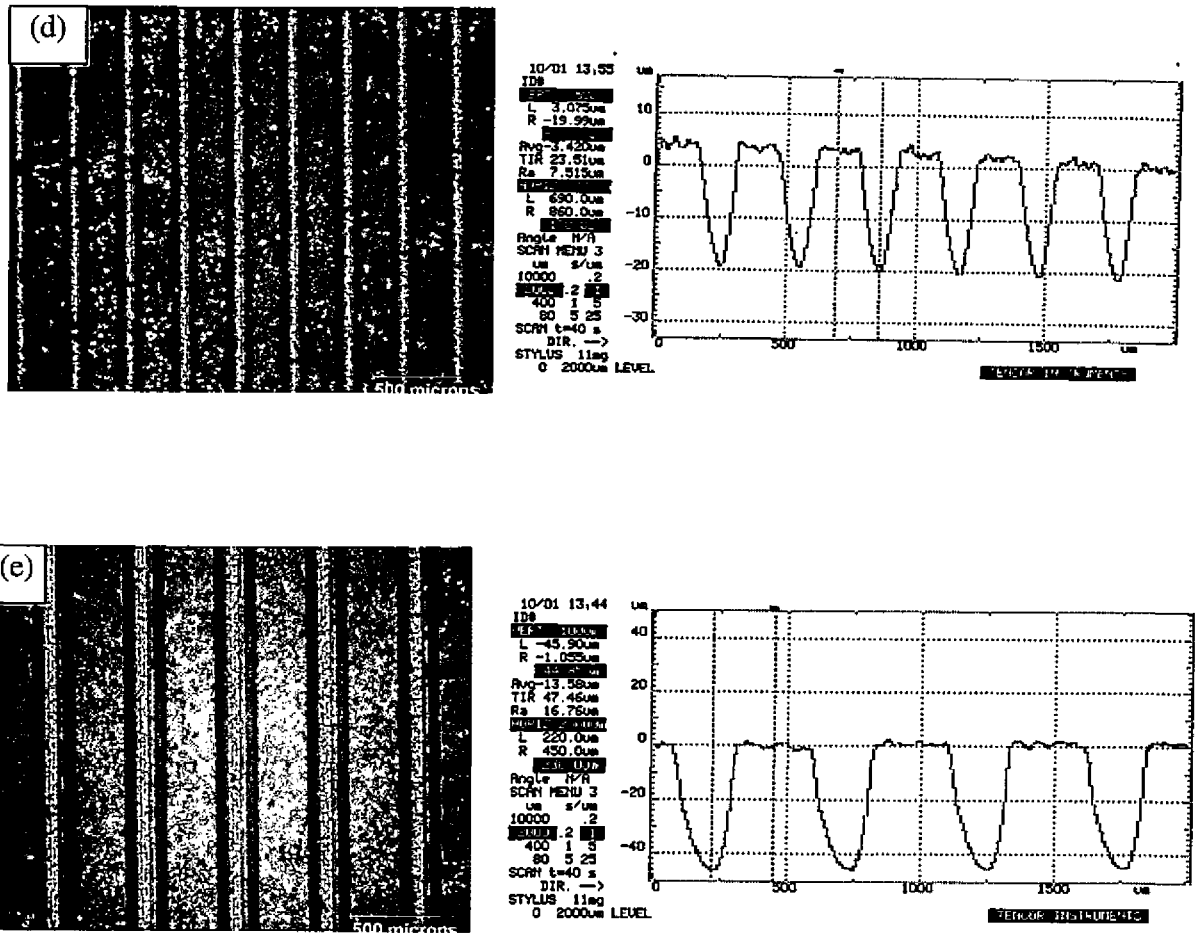

Figure 5-16: Optical photographs of the machined glass surfaces with the corresponding surface profiles obtained via Alpha Step; (a) Ra = 0.51μm, (b) Ra = 2.3μm, (c) Ra = 6.6μm, (d) Ra = 8.9μm, (e) Ra = 12.9μm.

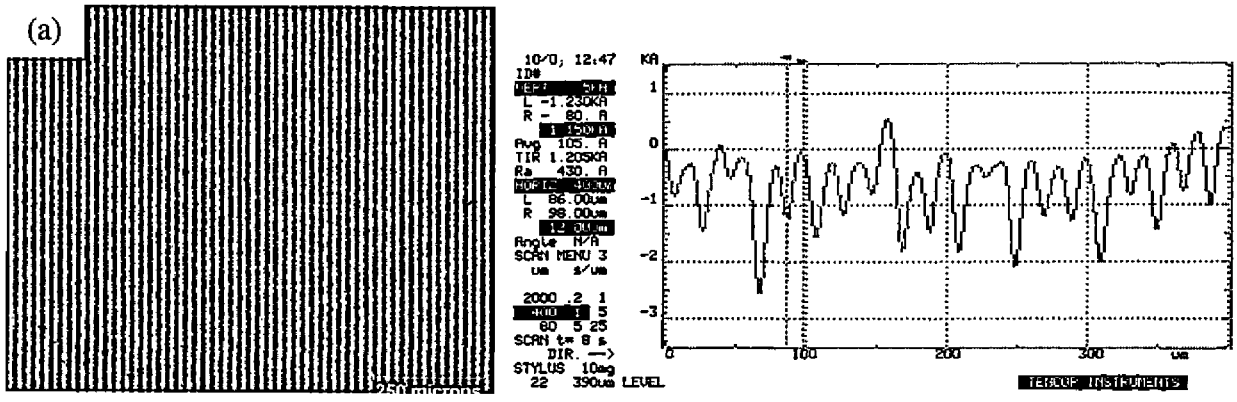

(b)

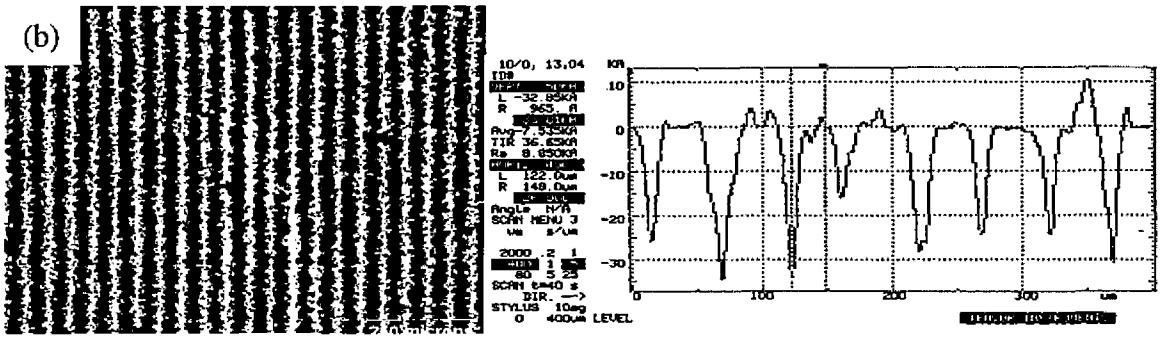
10/0, 13:04
ID#
L -32.85KA
R 965 A
Avg-7.535KA
TIR 36.85KA
Ra 8.850KA
L 122.0um
R 148.0um
Angle N/A
SCAN MENU 3
um s/um
2000 .2 1
400 1 5
80 5 25
SCAN t=40 s
DIR. —>
STYLUS 10mg
0 400um LEVEL
KA
10
0
-10
-20
-30
0
100
200
300
um

(c)

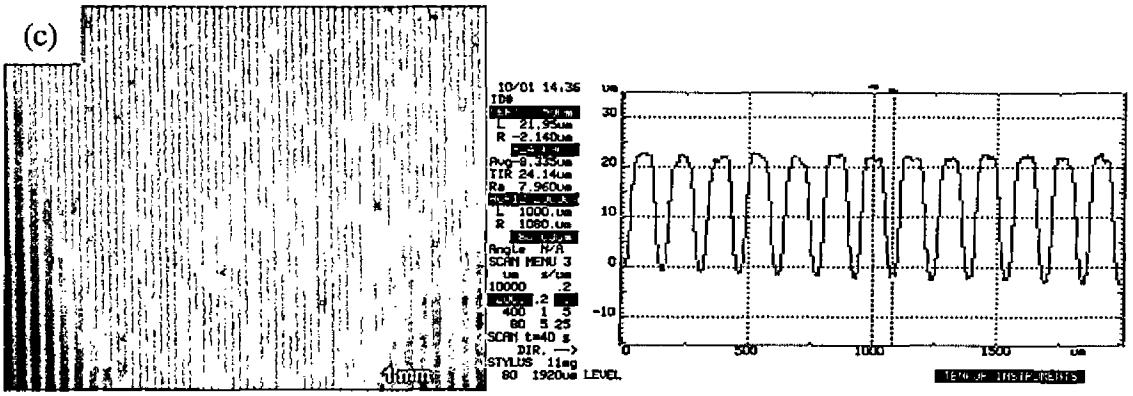
10/01 14:36
ID#
L 21.95um
R -2.140um
Avg-8.335um
TIR 24.14um
Ra 7.960um
L 1000.um
R 1060.um
Angle N/A
SCAN MENU 3
um s/um
10000 .2
400 1 5
80 5 25
SCAN t=40 s
DIR. —>
STYLUS 11mg
80 1920um LEVEL
um
30
20
10
0
-10
0
500
1000
1500
um

(d)

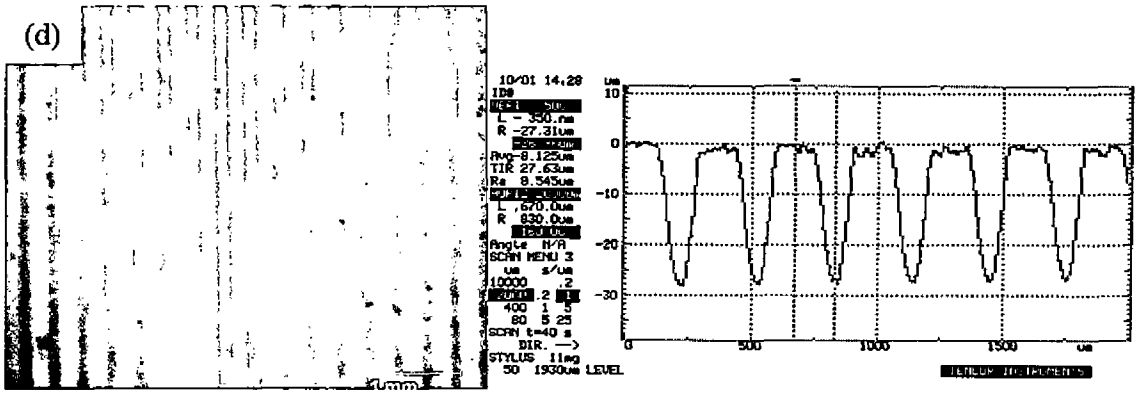
10/01 14:28
ID#
L -350.nm
R -27.31um
Avg-8.125um
TIR 27.63um
Ra 8.545um
L 670.0um
R 830.0um
Angle N/A
SCAN MENU 3
um s/um
10000 .2
2000 .2 1
400 1 5
80 5 25
SCAN t=40 s
DIR. —>
STYLUS 11mg
50 1930um LEVEL
um
10
0
-10
-20
-30
0
500
1000
1500
um

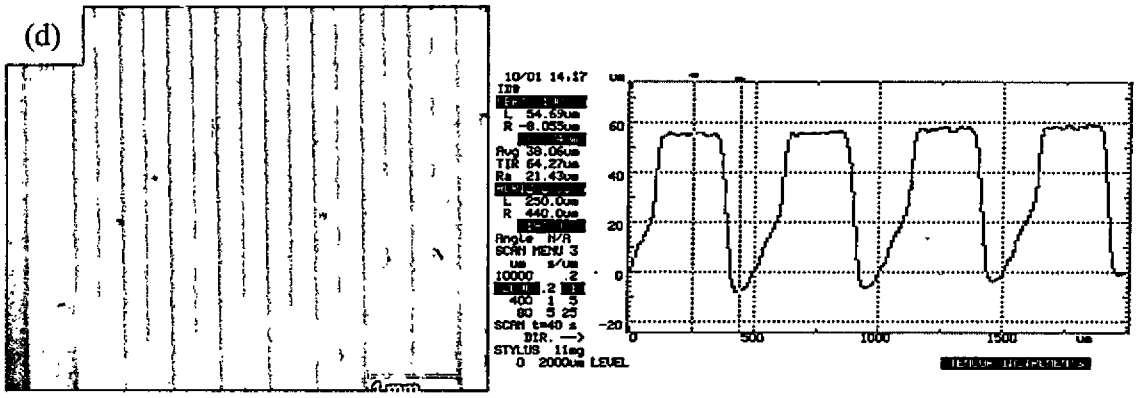

Figure 5-17: Optical photographs of machined Corning 9606 glass-ceramic surfaces with corresponding surface profiles obtained via the Alpha Step; (a) Ra = 0.14 μm, (b) Ra = 0.98 μm, (c) Ra = 6.8 μm, (d) Ra = 9.3 μm, (e) Ra = 16.1 μm

5.1.4 XRD-Determined Residual Surface Stresses in 9604 Glass and 9606 Crystallised Glass.

Chromium radiation was used (K_α λ = 2.291Å) to measure the residual surface stresses in Corning 9606 glass-ceramic. Figure 5-18 shows the effective

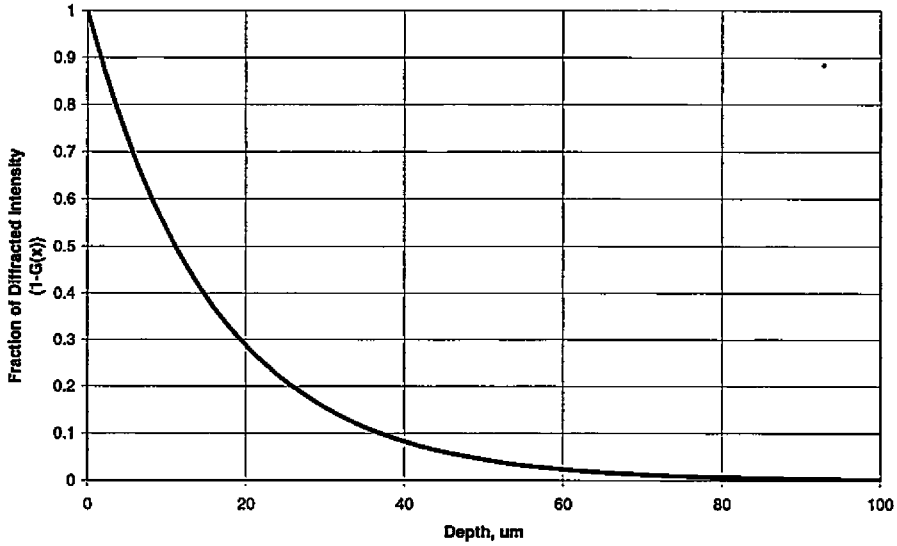

Figure 5-18: Effective depth of penetration of X-ray Cr radiation into Cordierite.

X-ray penetration depth into cordierite as calculated via Equations 70 and 71 (Chapter 2). 80% of radiation is diffracted by a 25 μm layer and no radiation penetrates beyond 75μm. So information from XRD gives an average stress value over a 25 μm surface layer. Stress was measured transverse to the machined grooves with an aperture size of 1.5 mm x 5 mm. The measurements were made on a high-angle plane with d-spacing ~1.219 Å at $2\theta = 140°$. Figure 5-19 shows the, d vs. $\sin^2\Psi$ plot for a polished surface of glass-ceramic 9606.

Multiple Exposure Stress Report: EM Method (File:03MAR03_0019.mt)
Method for Phi=0.00
Stress = -85.353 +/- 13.45[MPa]
ShearStress = -7.778 +/- 5.81[MPa]

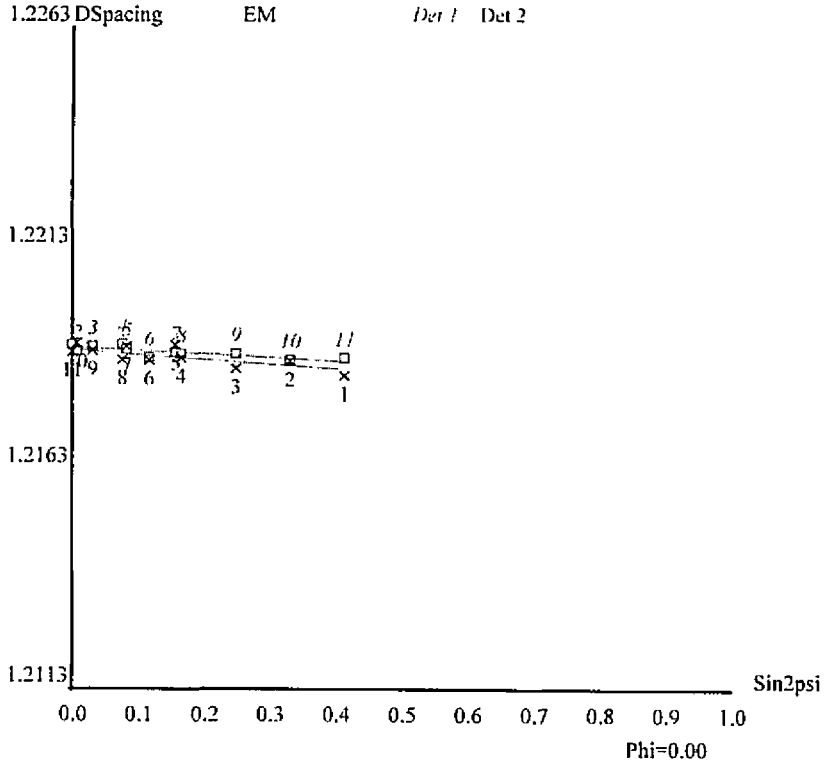

Figure 5-19: d-spacing versus sin2Ψ plot for polished, Corning 9606 glass-ceramic.

The plot is slightly elliptical and exhibits Ψ splitting, suggesting presence of shear stress (Pineault et al 2001).

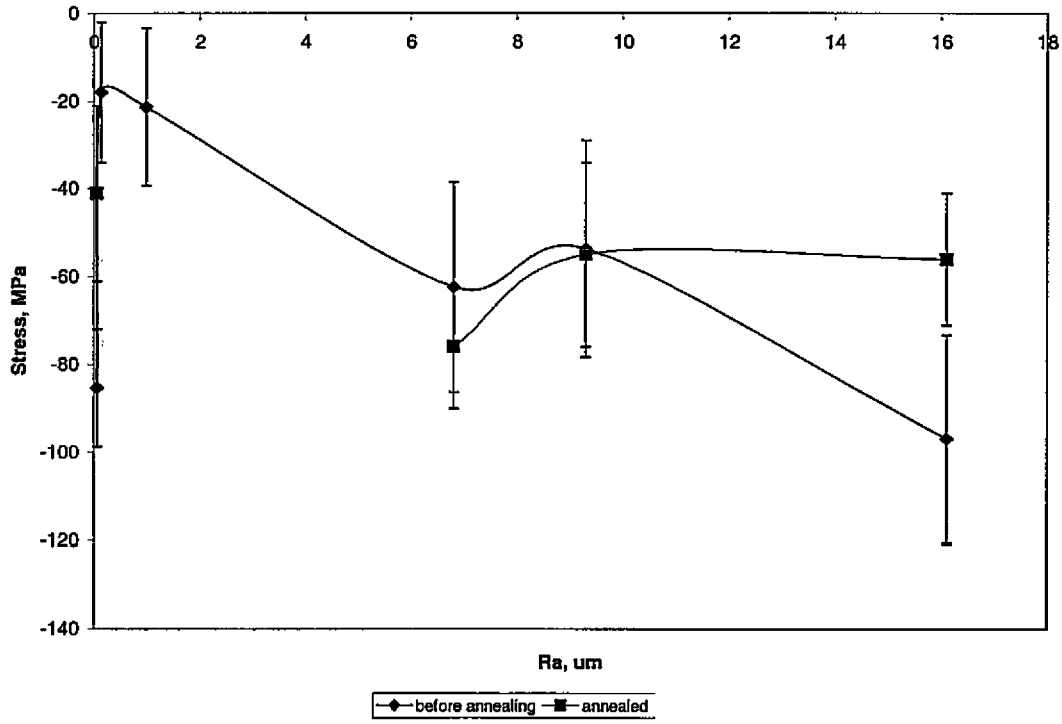

Figure 5-20: X-ray determination of residual stress in the surfaces of 9606 glass-ceramic.

Similar plots were obtained at each location on the surface of polished glass-ceramic.

Stresses were measured on the surface of ceramic specimens before and after annealing and the results versus R_a for the locations considered are plotted in Figure 5-20. The compressive stresses measured were small with relatively large error bars. The stress along the smooth (unmachined) surface was higher than machined, i.e., the as-received material was apparently 'strained'. This strain could be due to cooling. Consequently machining introduced tensile stresses which, in turn, released the already-present,

compressive-stress. Laser-etching, with its melting, would introduce a maximum tensile change of stress, i.e. result in a low value of compressive stress. Two dice-sawed-groove-locations with lower-R_a, showed a compressive stress ~ 20 MPa lower than present before machining. The stress for the 16.1 μm R_a location remained the same as the smooth surface (within the error). The error could be larger than indicated by the XRD average reading as Ra = 16.1μm is relatively close to the penetration depth for X-ray chromium radiation. In fact ~65% of the X-ray intensity is diffracted within 16 μm of the surface (Figure 5-18). Li et al (1995) showed that X-ray stress measurement is less reliable due to scattering when the surface R_a approaches the X-ray penetration depth.

Stress in the smooth surface was reduced (–85 MPa to –41 MPa) upon annealing. At the 16.1μm R_a location the stress was also reduced (-97 MPa to –56 MPa). Both reductions remain valid when errors are considered. Surprisingly, the change of stress at the 6.8 μm- and 9.3μm-R_a locations is much lower and of opposite sign (higher compressive stress). This change is considered insignificant vis á vis the large error bars for the measurements.

Dice-sawn locations on the same 9606 plate, (3.75″ x 1/4″ x 1″) were annealed in a tube furnace (temperature variation < 5°C). Similar results were expected from all locations but this was not observed. It was thus concluded, the stresses present are too small as compared with the uncertainty of the X-ray readings. Also, the amorphous phase in the glass-ceramic possibly influences the measurements. Moreover, in the grooved location with highest R_a (16.1μm), there is ~ 250 μm between the grooves. This possibly renders the sample smooth to the X-ray beam. The next lower R_a (9.3 μm) with spacing

300 μm, has flat areas between the grooves ~150 μm wide. Thus sharply grooved (lower R_a) areas produce less-true X-ray readings. Another possible explanation is that the lower the Ra in the grooved locations, the sharper the groove peaks. As the groove spacing changes from 500 μm to 150 μm, the depth decreases from ~60 μm to ~25 μm so though much finer they are still relatively deep and sharp. Sharp points are normal locations of high stress which are possibly more difficult to relieve during annealing. Thus the stress change on annealing a sharp-grooved location may be less than elsewhere. Stress measurements were not repeated on the laser-etched (low R_a) annealed specimens.

5.1.5 Rayleigh Wave (Rw) and Lcr Wave Measurements

R_w and L_{cr} surface waves were used to define the influence on sound velocity of surface residual stress, surface roughness and grain presence. The R_w frequencies were 10, 12, 16, and 20 MHz. L_{cr} was 12 MHz.

The measurement point was marked on the samples and special transducer holders were designed and attached to the sample stage. They allowed sample replacement in the same position. Values reported are the average of 10 readings at the same location. The sample-transducer distance in the water was maintained constant (as the focused-transducer geometry must be corrected, discussed earlier). The errors reported account for the average and the slightly-changed distance from the sample.

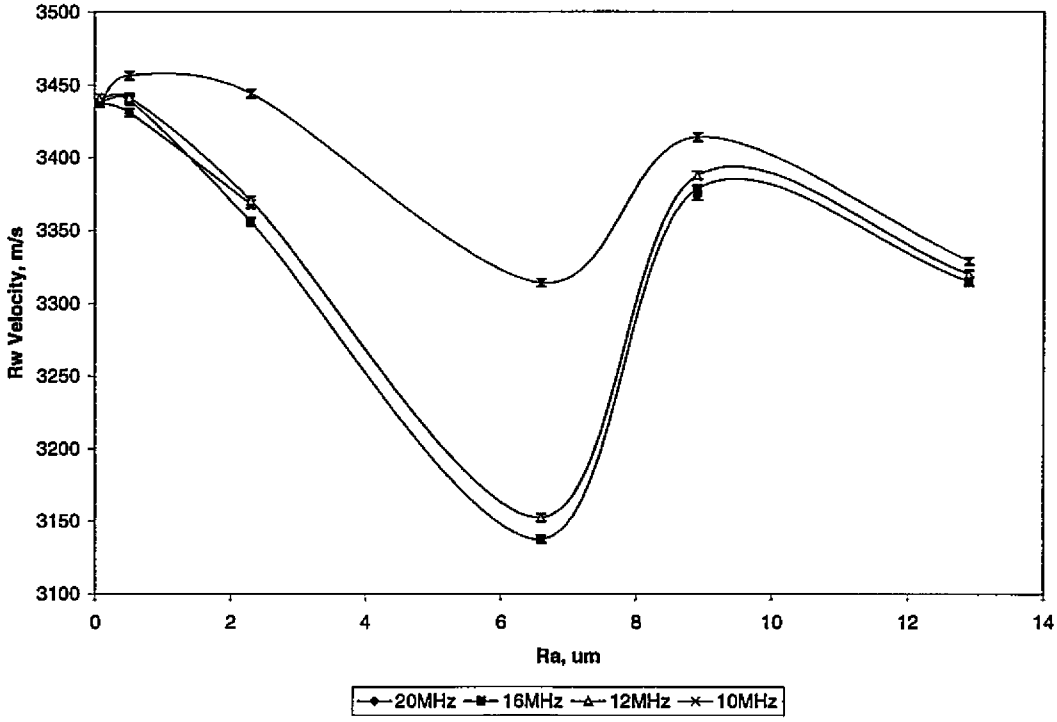

Figure 5-21: Rayleigh wave velocities in Corning 9604 glass (average error of velocity = 0.7m/s).

Figure 5-21 shows the results for Corning 9604 glass. The average error is 0.7 m/s though the error bars are not visible due to the large scale of the velocity axis. Every frequency plot betrays the same trend i.e., velocity decreases with increased surface roughness, up to R_a = 6.6 μm. It should be noted that sound is influenced by the surface condition as well as the machining residual stress. The magnitude of the contributions of each is presented later. The smallest velocity change was for 10 MHz, i.e. ~124 m/s (3.6%). The velocity suffered a maximum influence at 16 MHz, i.e., it decreased 300 m/s (8.7%). The velocity at 20 MHz could not be measured for $R_a > 2.3\mu m$. The decrease of R_w velocity with increasing surface roughness agrees with previous work (i.e. Tardy et al, 1996, Ruiz et al 2002). The latter authors suggest this behavior is due to surface-

roughness-induced energy scattering. Attenuation causes dispersion as described earlier for grain boundary scattering. This dispersion of sonic energy broadens the ultrasonic pulse as the high-frequency components are attenuated and partial waves travel at different velocities. Thus the measured-pulse group-velocity is affected.

As the size of the surface inhomogeneities approaches the Rayleigh wave wavelength (at some ratio to be determined), it can be argued that the surface-wave no longer propagates across the inhomogeneities but follows their surface topography. The latter distance traveled is further so the time-of-propagation increases. The surface wave velocity formula does not take this increase of travel distance into account, only the different travel time. Consequently, the measured velocity is apparently lower (Patel, 2003).

Table 5-7: Rw frequencies and corresponding wavelengths (μm) in Corning 9604 precursor glass.

Frequency MHz	**Wavelength in Corning 9604 μm**
20	172
16	215
12	287
10	344

Once the surface roughness, R_a > 6.3 μm, the sound velocity increases. It is important at this point to note, the repeatability of the measurements is good and the error

bars are small. Table 5-7 lists the wavelengths for each frequency. According to Hirao et al (1981), the depth of penetration of a Rayleigh wave is approximately one wavelength. As summarized in Table 5-6, the depth of the groove (R_a ~ 6.6 μm) is ~25.5 μm whereas the inhomogeneity spacing is 150 μm. Now, 6.6 μm is ~14% of the 20 MHz wavelength and ~7% of the 10 MHz wavelength. Thus, as the depth of damage in the surface exceeds a certain percentage of the Rayleigh wavelength (depending on the frequency) for an average spacing >150 μm, the results no longer follow the pattern observed with lower (more polished) roughness. Possible reasons for this will be presented later, when the results for annealed glass, glass-ceramic and titanium, are compared.

The Rayleigh wave velocity vs. surface roughness for Corning 9606 glass-ceramic is plotted in Figure 5-22. The behavior is similar to that of Corning 9604 glass, i.e., the R_w velocity decreases with surface roughness for $R_a \leq 6.8$ μm. The 20 MHz Rw wave is again influenced most, velocity being decreased by ~ 6.3%. The velocity of the 10 MHz R_w wave decreases less, ~5%. The 20 MHz velocity drop, however is less vis á vis the velocity drop for amorphous Corning 9604, whereas the drop suffered by 10 MHz is higher. This difference must be due to the grains present in the glass-ceramic.

As surface roughness Ra > 6.8 μm, the results depart from this trend. Wavelengths for each frequency in the glass-ceramic are listed in Table 5-8. The depth of damage at R_a = 6.8 μm is ~ 12.7% for 20 MHz and ~ 6.3% for 10 MHz.

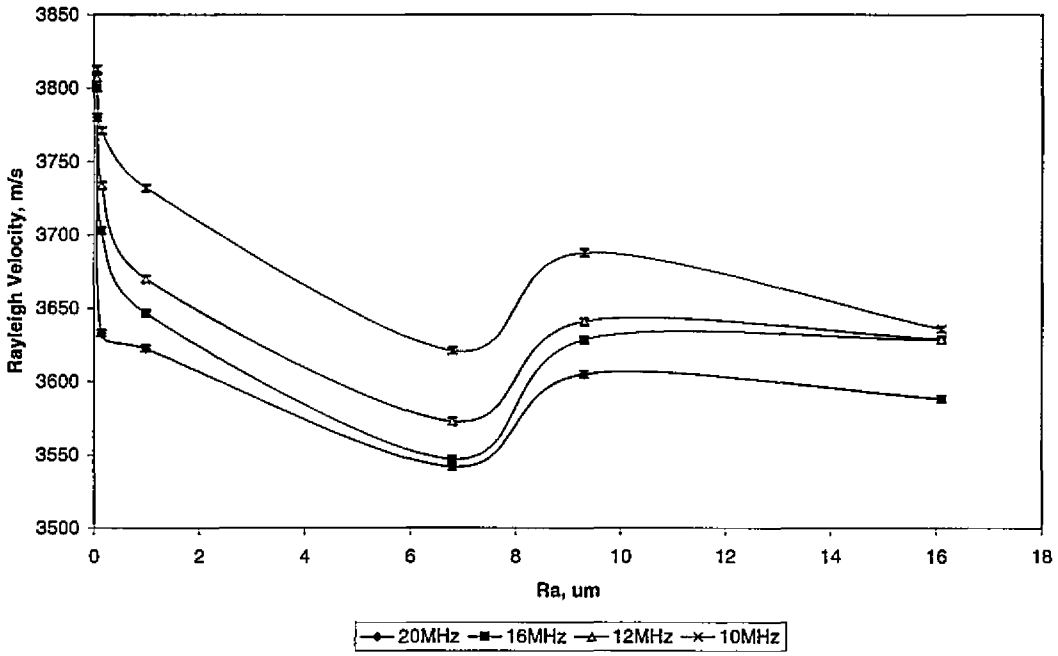

Figure 5-22: Rayleigh velocities measured in Corning 9606 glass-ceramic (average error of velocity = 0.8 m/s).

Table 5-8: Rayleigh wave frequencies and corresponding wavelengths (μm) for Corning 9606 glass-ceramic.

Frequency MHz	**Wavelength in Corning 9606 μm**
20	189
16	237
12	317
10	381

Velocity changes for L_{cr} (12 MHz) in Corning 9606 specimens vs. surface roughness are plotted in Figure 5-23. The Lcr transducer has a spherical focus as opposed to the cylindrical one for R_w, i.e., whereas R_w measurements are directional across the grooves, L_{cr} measures the average surface properties over a 360° rotation. This difference is schematically shown in Figure 5-24. Lcr velocities are less sensitive to surface roughness. However, if the residual stress in a direction parallel to the grooves is different than across the grooves, it should be detected by the L_{cr} wave. The latter has a higher Acoustoelastic Constant so is more sensitive to residual stresses than the line-focused R_w velocity.

The L_{cr} velocities in ceramed Corning 9606 drops rapidly as R_a increases to 0.98 μm and then levels. The velocity reduction observed is 49 m/s (~0.7%). This value is significantly less than the 3.6% drop measured for the Rw, though L_{cr} is more sensitive to residual stress. This may be because L_{cr} is less sensitive to surface roughness whereas surface roughness is probably the major contributor to drop of the surface velocity in machined locations.

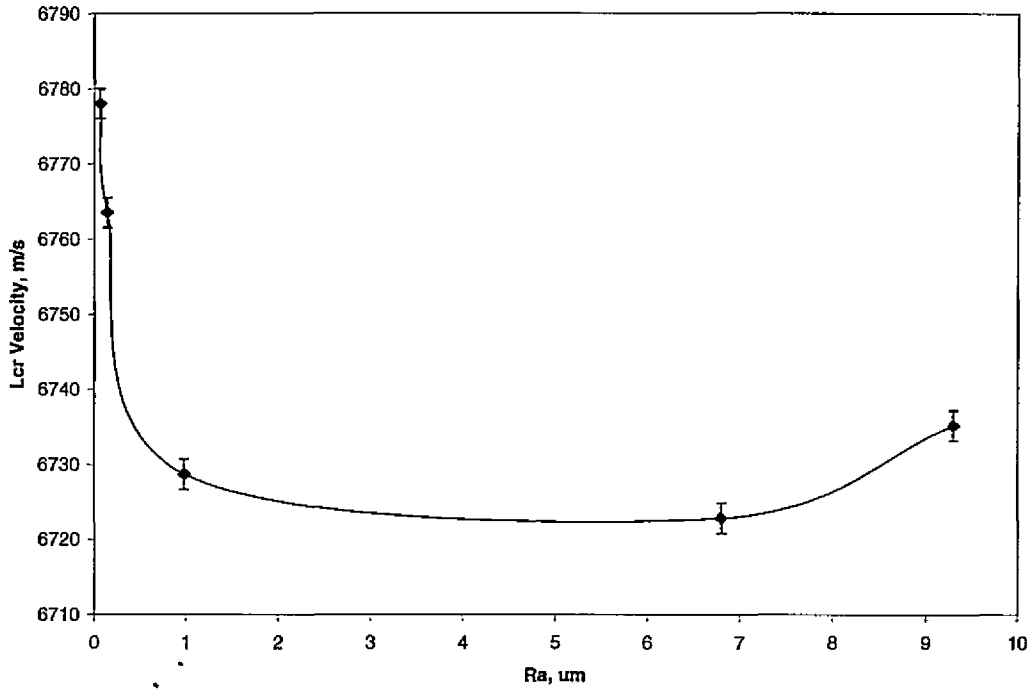

Figure 5-23: L_{cr} velocity dependence on the surface roughness, Ra, on Corning 9606 glass-ceramic (12 MHz).

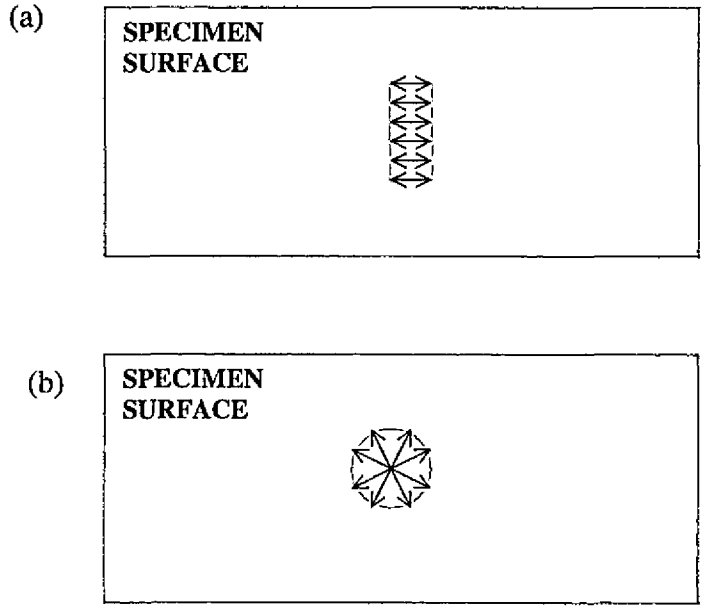

Figure 5-24: Specimen surface with an outline of the ultrasonic beam and sound direction: a) sound generated by focused cylindrical transducer, b) sound generated by spherical transducer.

5.1.6 Ultrasonic Exploration of Annealed Specimens of Corning 9604 and 9606.

The Corning 9604 and Corning 9606 specimens were annealed and the ultrasonic measurements repeated. Tables 5-9 and 5-10 summarise the results for bulk-compressional-, and shear-, ultrasonic waves. Both velocities decreased. This decrease was insignificant on accounting for the error. However, the fact that the same trend was observed in both samples, leads to the conclusion that some compressive bulk stress is relieved. Longitudinal wave velocities are more influenced by heat treatment than shear waves. The percent change of longitudinal wave velocity for amorphous 9604 is tenfold that in shear, as per the famous Egle and Bray (1976) results, i.e. longitudinal waves are most sensitive to stress in a material.

Table 5-9: The Measured Properties for Corning 9604 and Corning 9606 after stress-relief.

	Density g/cm^3	Longitudinal Velocity,	% Change Due to Stress Relief	Shear Velocity, m/s	% Change Due to Stress Relief
Corning 9604 (glass)	2.67+/- 0.01	6744 +/- 5	0.208 +/- 0.1	3875 +/- 3	0.026 +/- 0.1
Corning 9606 (glass-ceramic)	2.63+/- 0.01	7414 +/- 5	0.067+/- 0.1	minimum=4292+/-3 maximum=4302+/-3	0.023 +/- 0.09 0.046 +/- 0.09

Table 5-10: Ultrasonically determined Elastic Properties of Corning 9604 and Corning 9606 after stress relief.

Sample	Shear Transducer Orientation	Bulk Modulus K (G Pa)	% Change Due to Stress Relief	Young's Modulus E (G Pa)	% Change Due to Stress Relief	Poisson's Ratio υ,+/–0.005	% Change Due to Stress Relief
Corning 9604 (glass)	0 degrees	68.1 +/- 0.1	0.6 +/- 0.2	100.7 +/- 0.3	0.1 +/- 0.1	0.253	0.8 +/- 2
	90 degrees	68.1 +/- 0.1	0.6 +/- 0.2	100.7 +/- 0.3	0.1 +/- 0.1	0.253	0.8 +/- 2
Corning 9606 (glass-ceramic)	0 degrees	79.6 +/- 0.1	0.1 +/- 0.2	121.2 +/- 0.3	0.1 +/- 0.1	0.246	0
	90 degrees	79.9 +/- 0.1	0.1 +/- 0.2	120.8 +/- 0.3	0.1 +/- 0.1	0.248	0

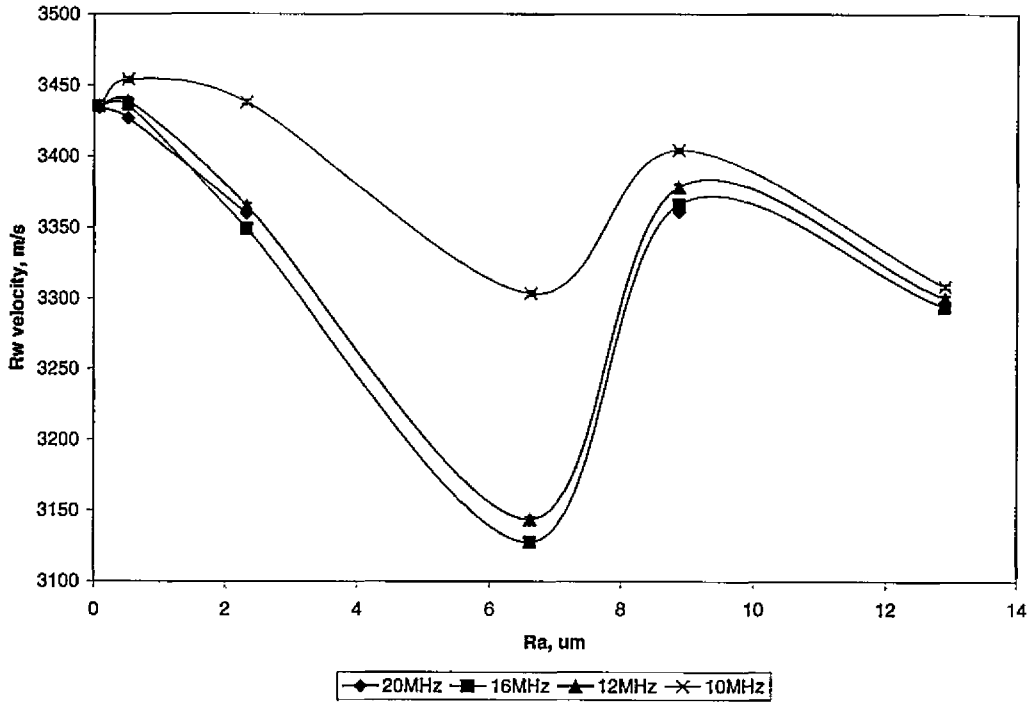

Figure 5-25: Rayleigh velocities in Corning 9604 glass, after annealing.

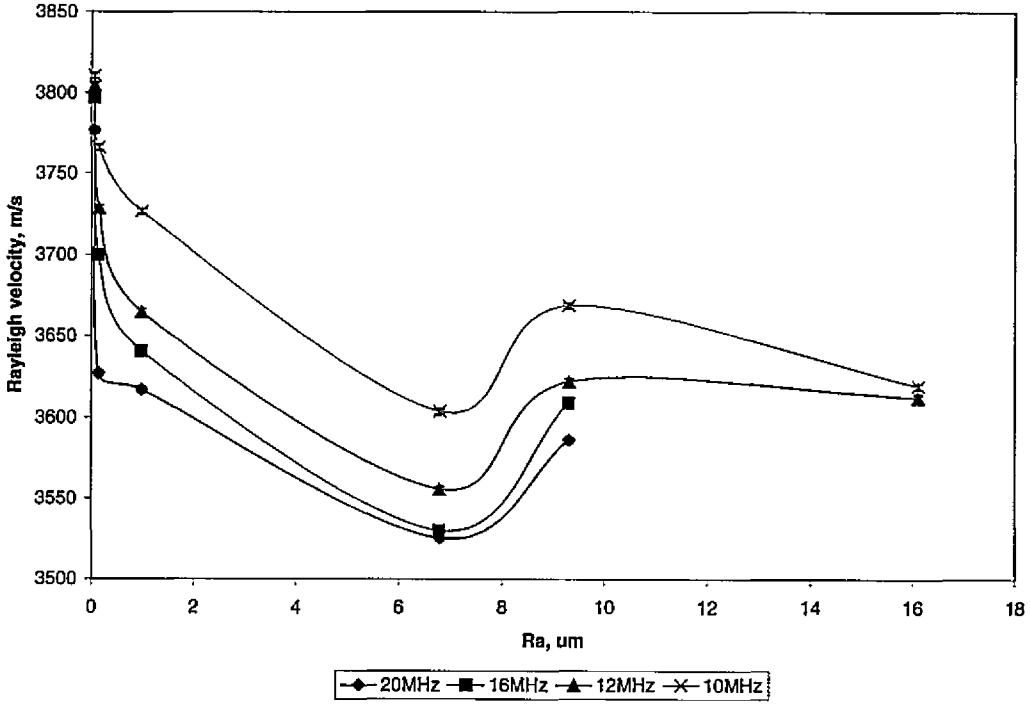

Figure 5-26: Rayleigh velocities in Corning 9606 glass-ceramic, after annealing.

5.1.7 Rayleigh and Lcr Waves Measurement following Annealing of Corning 9604 and Corning 9606

The Rayleigh wave velocity measurements were repeated on annealed specimens. Figures 5-25 and 5-26 show the plots for glass and ceramed samples. The small errors (0.8 m/s average) cannot be distinguished on the plots. Graphs have the same shape but shift to lower velocities. Comparison of velocities before and after annealing are shown in Figures 5-27 and 5-28. The magnitude of the velocity difference before and after heat-treatment, is different suggesting different levels of stress must have been originally present.

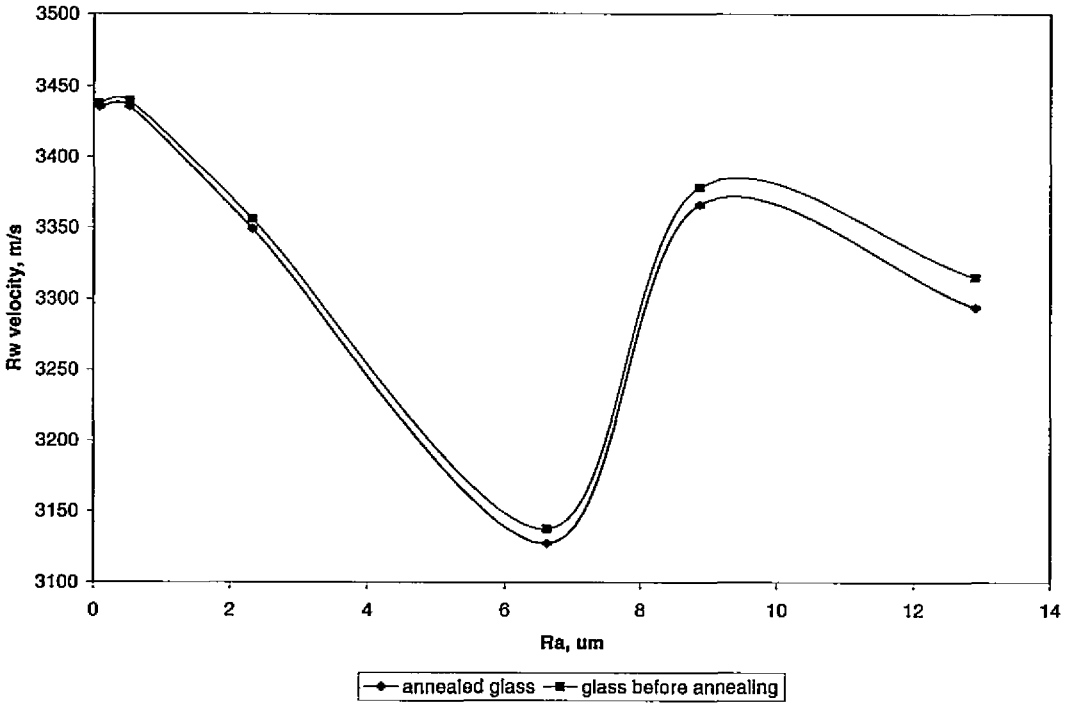

Figure 5-27: Comparison of the 16 MHz Rayleigh wave velocity before and after annealing for Corning 9604 glass (Average Error = 0.7 m/s)

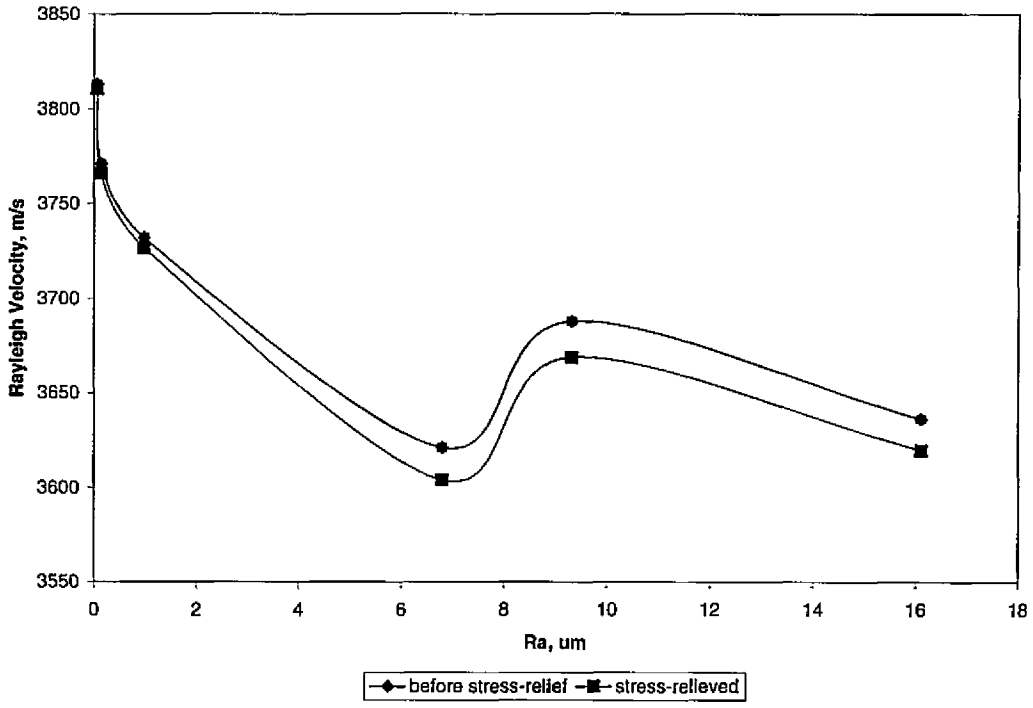

Figure 5-28: Comparison of 10 MHz Rayleigh-wave velocity in Corning 9606 glass-ceramic, before and after annealing (Average Error of velocity = 0.8m/s)

Acoustoelastic Constants (measured earlier) were employed to convert the percentage change-of-velocity, to stress. Ultrasound measures the change of stress, not its absolute value. The stress results values plotted in Figures 5-29 and 5-30 show stress removed from 9604 on annealing, increased from a minimum value for the polished surface, to a maximum value at highest R_a. This observation holds even when errors are considered. The 9606 glass-ceramic exhibits a similar trend to $Ra \leq 9.3\mu m$.

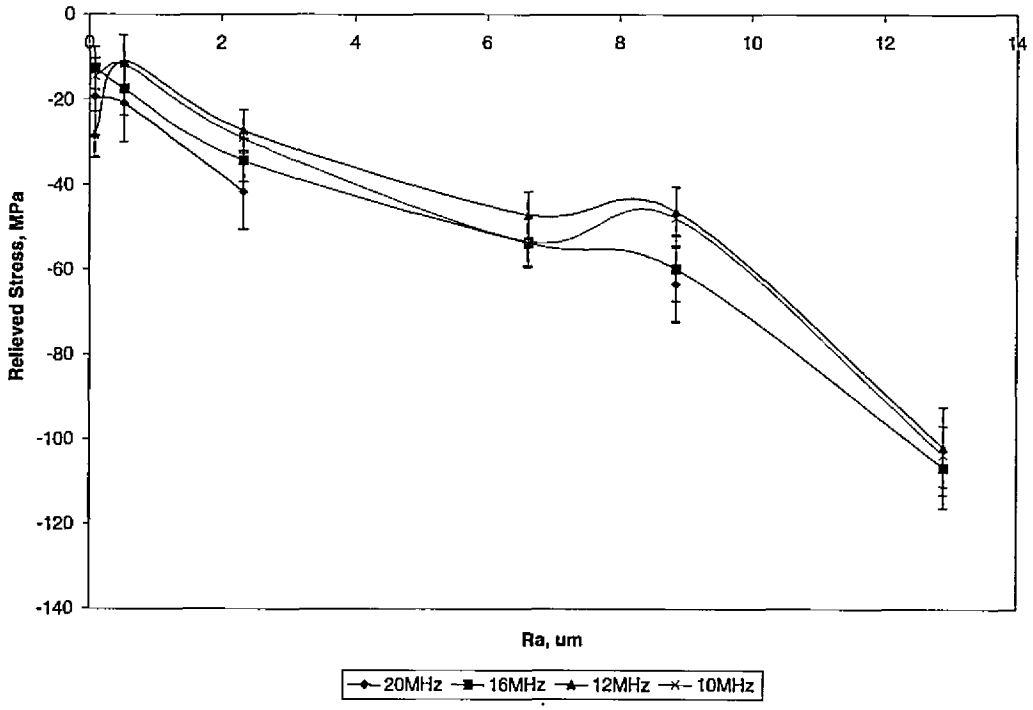

Figure 5-29: Stress relief tracked by frequency on annealing Corning 9604, via Rayleigh wave velocities at different frequencies

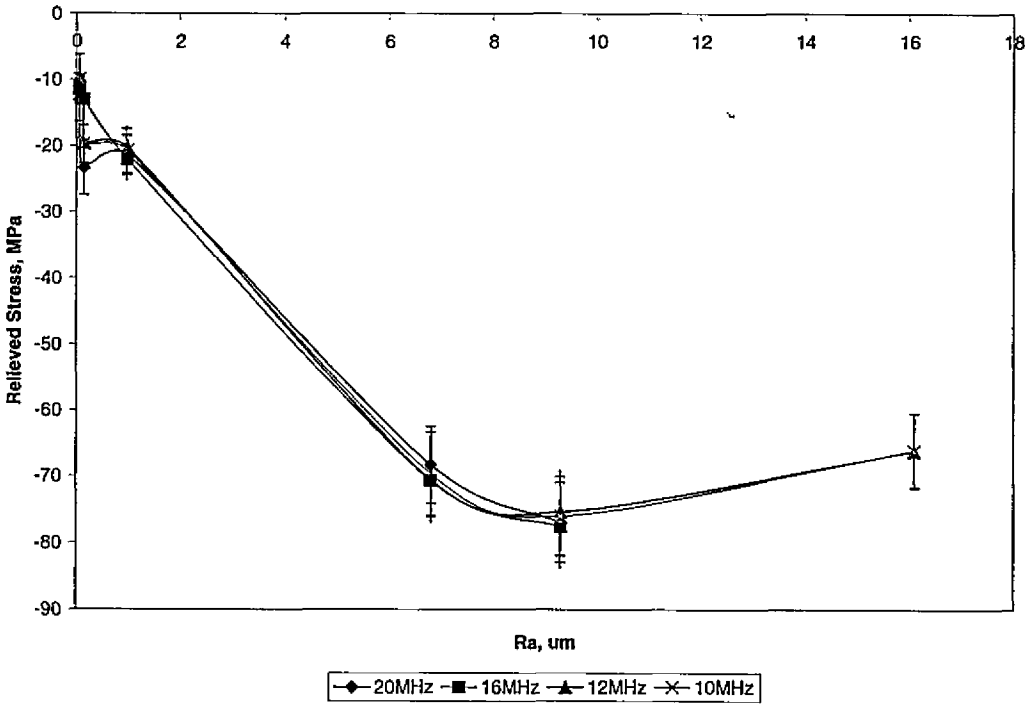

Figure 5-30: Stress relief on annealing, 9606, as determined via Rayleigh wave velocity at different frequencies

In the Introduction it was suggested that, by varying the ultrasonic frequency, the stress can be determined at different depths beneath the surface. Figures 5-31 through 5-34 show the stress variation with frequency. A real difference exists, though the error bars are large. Unfortunately, X-ray data of stress variation with depth was not available. X-ray data for machined surfaces (milled, shot-peened) in the literature (Pineault et al (2001)) shows stress is high close to the surface and varies between compressive and tensile over depth but then levels out. No information is in the literature for the sawn-groove surfaces introduced into specimens in the present work.

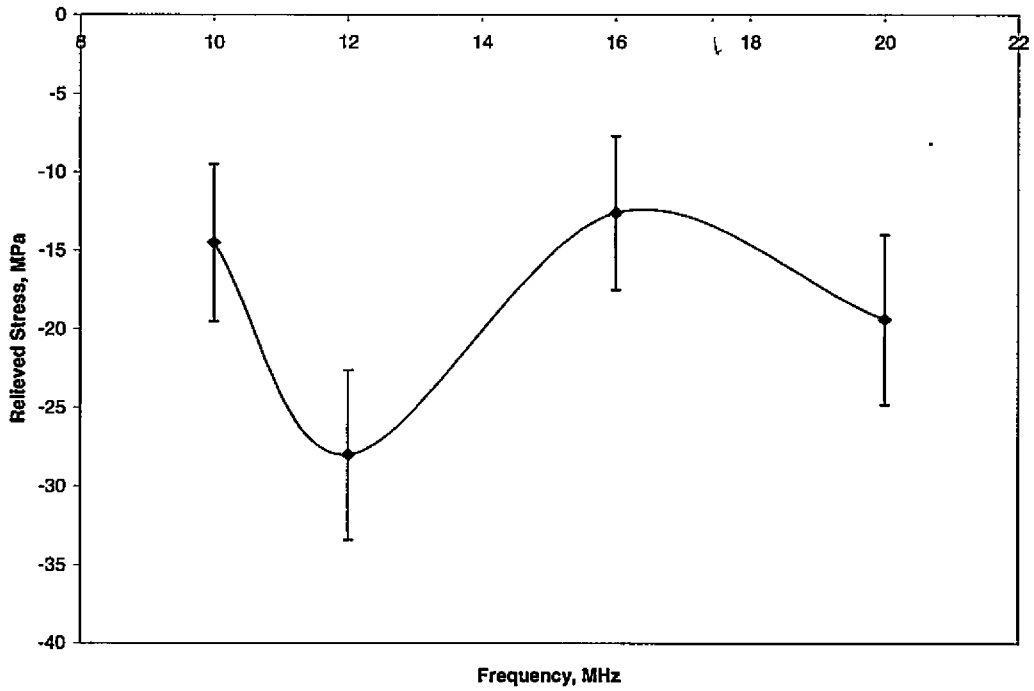

Figure 5-31: Stress relieved in the Corning 9604 glass polished surface versus R_w wave ultrasonic frequency

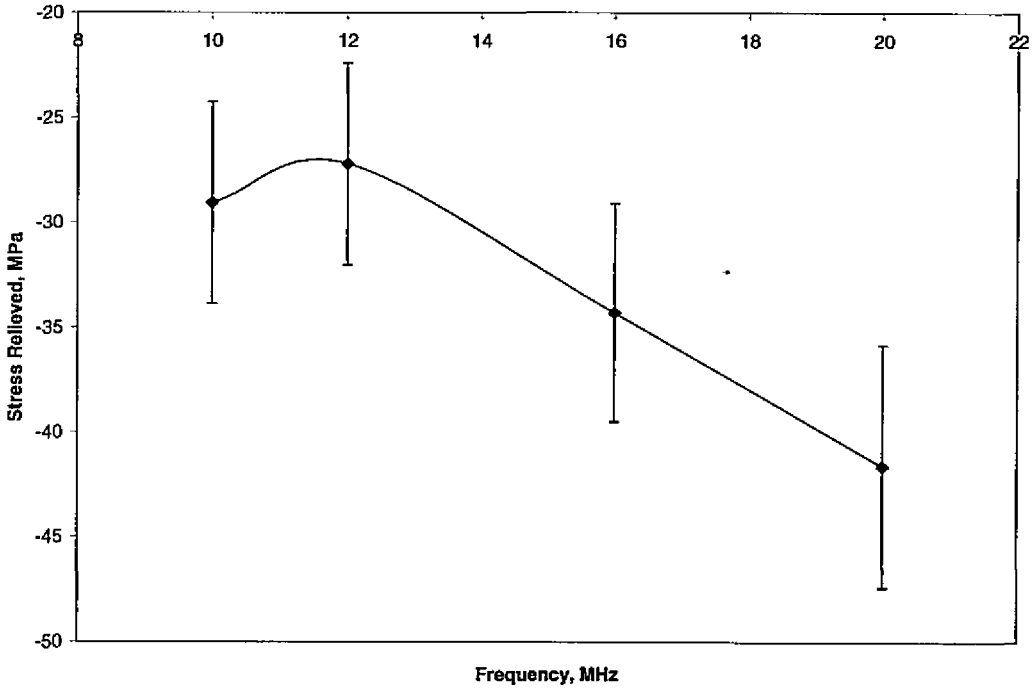

Figure 5-32: Relieved Stress versus ultrasonic frequency for Corning 9604 (Ra = 2.3 μm).

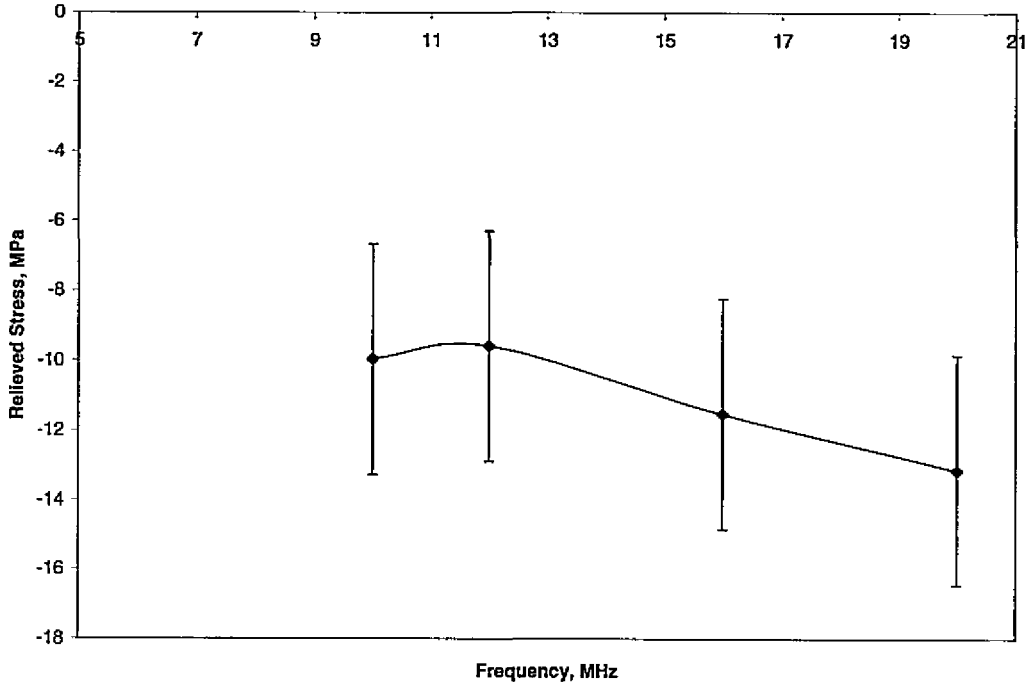

Figure 5-33: Relieved Stress versus ultrasonic frequency for Corning 9606 glass-ceramic polished surface.

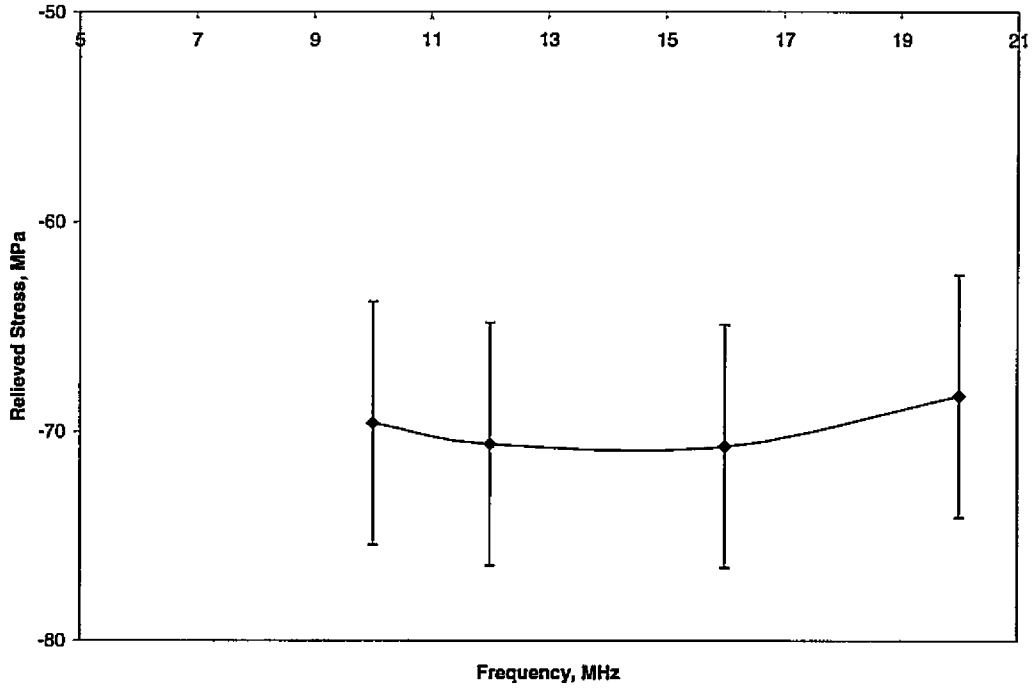

Figure 5-34: Relieved stress versus ultrasonic frequency for Corning 9606 (surface Ra = 6.8μm)

The stress relief in Corning 9606 via ultrasonic measurement and values obtained by XRD are compared in Figure 5-35. There seems little correlation but X-rays detect stress to ~25μm depth, whereas the ultrasonic penetration is 189μm (20MHz) and 381μm (10MHz). Thus the stress detected thereby is an average value over this depth.

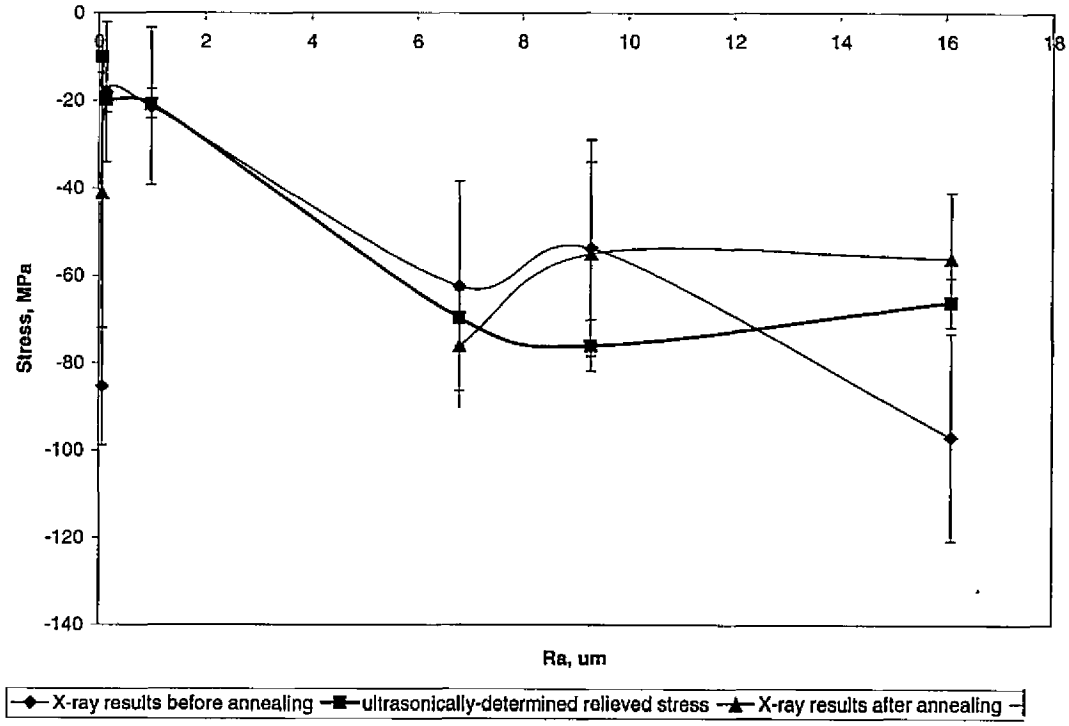

Figure 5-35: Comparison of X-ray and ultrasonic residual stress data.

Plots of R_w velocity vs. frequency for glass-ceramic are shown in Figures 5-36 and 5-37. These plots show how frequency is influenced by surface roughness (Corning 9604) and both surface roughness and grain scattering (Corning 9606), after some stress is relieved. Annealing seeks to remove all stress and thus identify the influence of surface roughness exclusively for Corning 9604 and of both surface roughness and grain scattering for 9606. X-ray indicated stress was still present after annealing but some conclusions can be reached.

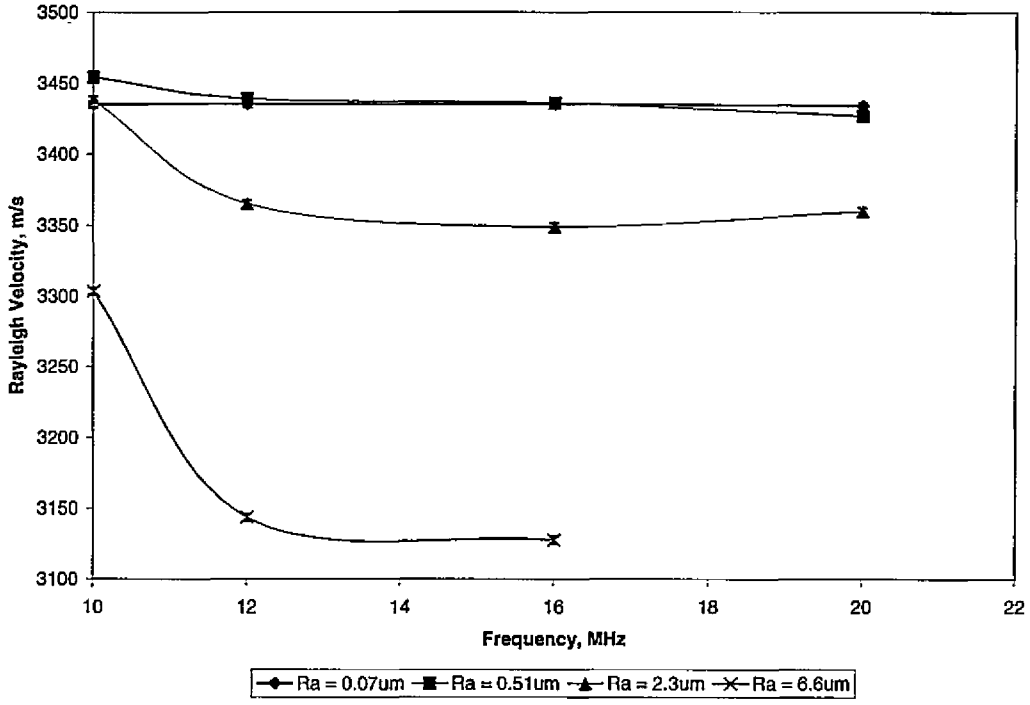

Figure 5-36: Frequency dependence of the Rayleigh wave velocity for stress-relieved Corning 9604 glass (Avg. Error in velocity = 0.7 m/s).

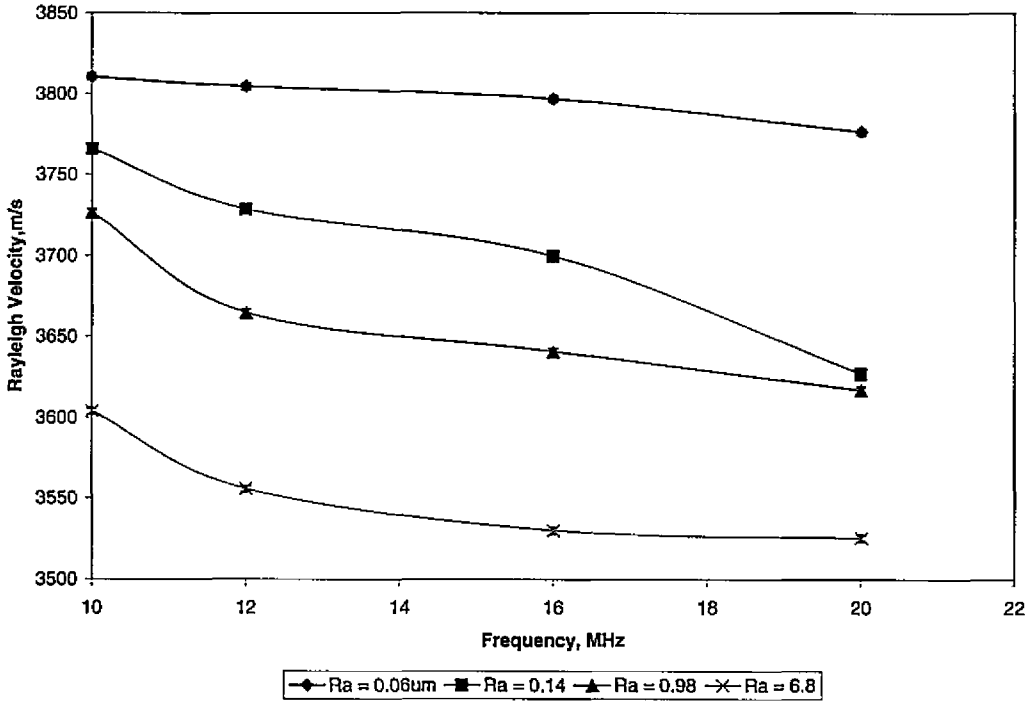

Figure 5-37: Frequency dependence of Rayleigh wave velocity for stress relieved Corning 9606 glass-ceramic (Avg. Error in velocity = 0.8 m/s).

It is clear in Figure 5-36 (Corning 9604 glass), the readings for low-roughness surfaces are not influenced by frequency change. However, the velocity across the 6.6μm R_a surface drops by 176 +/- 1.5 m/s (5.3%) as the frequency increases from 10 to 16 MHz. In fact, the signal from this surface for a 20MHz wave is too dispersed to measure. The reduction of velocity was 76 m/s (2.2%) along the 2.3μm R_a surface.

The R_w velocity vs. frequency for Corning 9606 is plotted in Figure 5-37. Velocity decreases with frequency as per Corning 9604. However, in this case even low R_a surfaces produce decreasing R_w velocities, as frequency increases. This can be attributed to the grain boundaries not present in 9604. The R_w velocity measured along the polished surface at 9606 drops by 33m/s (0.86%) as the frequency increases from 10 to 16 MHz. The velocity decrease for 6.8μm-R_a surface is 79 m/s (2.2%). It can be argued that 0.86% of this 2.2% is due to grain presence and the remaining 1.34% due to the surface-roughness-scatter and residual stress. Similar behavior was reported by Tardy et al (1996) and Ruiz et al (2002). The former measured Rayleigh wave velocities along polished, fine and roughly machined, polycrystalline ceramics. Their plots were approximately linear. This is not so in the present case. Their highest frequency was 14MHz and this may be the reason. The ratio of ultrasonic-wavelength to surface-damage-depth clearly influences velocity. High-frequency signals are more attenuated and, from the above results, suffer more from surface-roughness scatter. Surprisingly, Tardy et al observed no grain-scattering dispersion in their polished specimens.

The L_{cr} wave velocity for stress-relieved Corning 9606 is compared to the unrelieved material in Figure 5-38. The velocity decrease suggests compressive stress is present

before heat-treatment, as per results for R_w. The magnitude of the veloity change for the L_{cr} wave is significantly higher than for the R_w, i.e. 4.3 m/s for R_w vs. 10.2 m/s for the L_{cr}. This result follows from the higher Acoustoelastic Constant values for L_{cr} versus that for R_w.

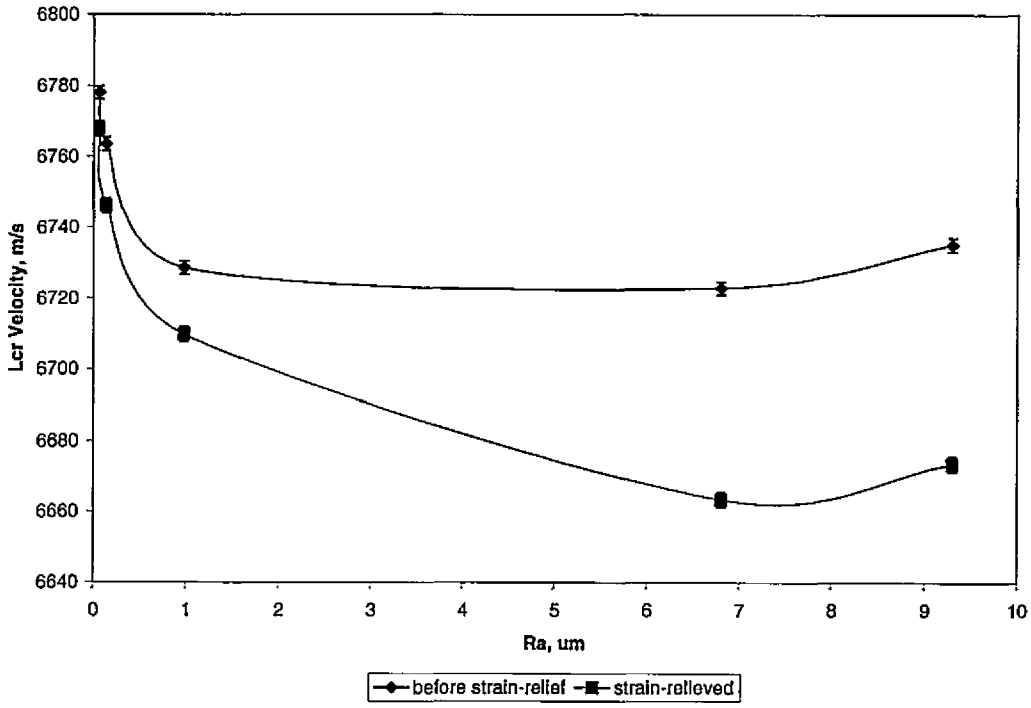

Figure 5-38: Lcr wave velocities before and after stress relief for Corning 9606 (Avg. Error in velocity = 1.5 m/s).

The changes of Lcr velocity were converted to stress and the results plotted in Figure 5-39. The stress measured via R_w is included for comparison. The results are similar, though L_{cr} and R_w are different waves, i.e., L_{cr} is purely compressional, and R_w has a shear component; L_{cr} is spherically-focused and R_w is line-focused in this work. The Lcr wave penetrates deeper than one wavelength (Tang and Bray, 1996) so,

considering the Lcr wavelength at 12MHz in 9606 is 565μm and the Rw wavelength is 317μm, the former tracks an average value of a significantly deeper region. The higher stress indicated by Lcr suggests that stresses extend deeper into the solid than one Rayleigh wavelength.

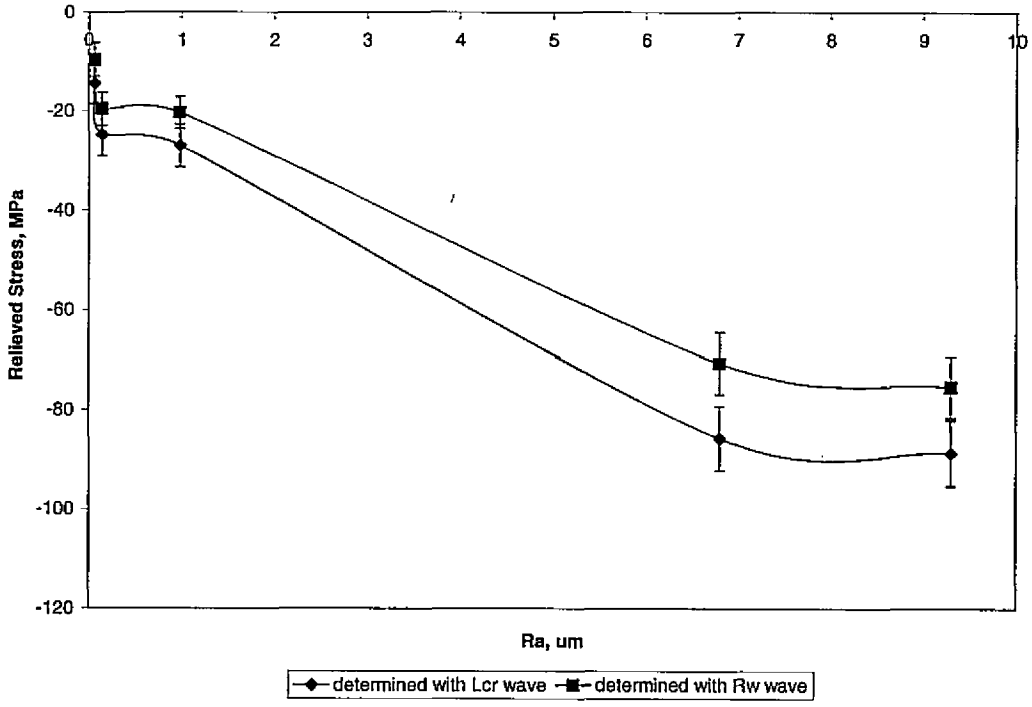

Figure 5-39: Comparison of the stress .vs. Ra measured by the 12 MHz R_w (line-focus) and 12 MHz Lcr wave (spherical focus).

Also, as the Lcr transducer has a spherical focus, the measured stress is an average over 360°, whereas the Rw transducer, with cylindrical focus, measures stress in one direction (across the grooves), unless rotated thereabout. Higher stress in a direction other than across the grooves also results in the Lcr measured stress being higher. A better

understanding of the results would be possible if the stress gradient before annealing and that along the grooves were known.

5.2 Ultrasonic Exploration of Magnesium Single Crystal

As pointed out earlier, magnesium is considered a valid model for titanium that does not suffer phase-transformation. Bulk sonic velocities were measured in single-crystal magnesium and compared with a polycrystalline sheet, to identify the influence of grains and texture on the ultrasonic velocities. The crystal was a randomly oriented cylinder. A 2.2 cm x 1cm x 0.6 cm sample was cut from the cylinder in such a way to expose the (001) and (010) planes.

To orient the Mg single crystal, back-scattering Laue patterns and stereographic projections were constructed. Figure 5-40 is a Laue pattern after a cut along the (001) plane. The center is 2.5° vertically and 0.5° horizontally off the film center. This suggests a slight misalignment of the crystal.

Orient Express software was used to index the pattern and produce the corresponding stereographic projection (Figure 5-40 and 5-41). The (010) plane position was related to the specimen geometry and a cut was made to expose the (010) plane.

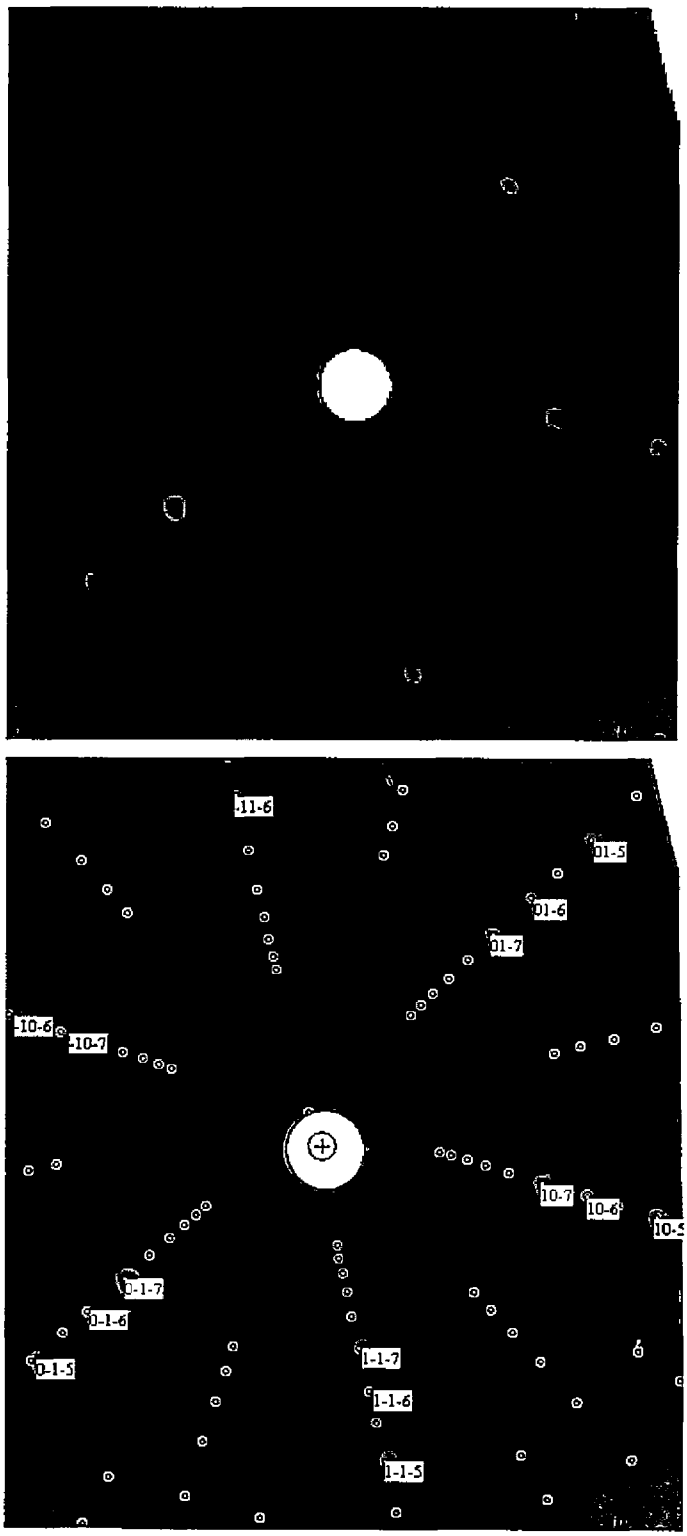

Figure 5-40: (a) Laue Pattern from the (001) plane, (b) pattern indexed

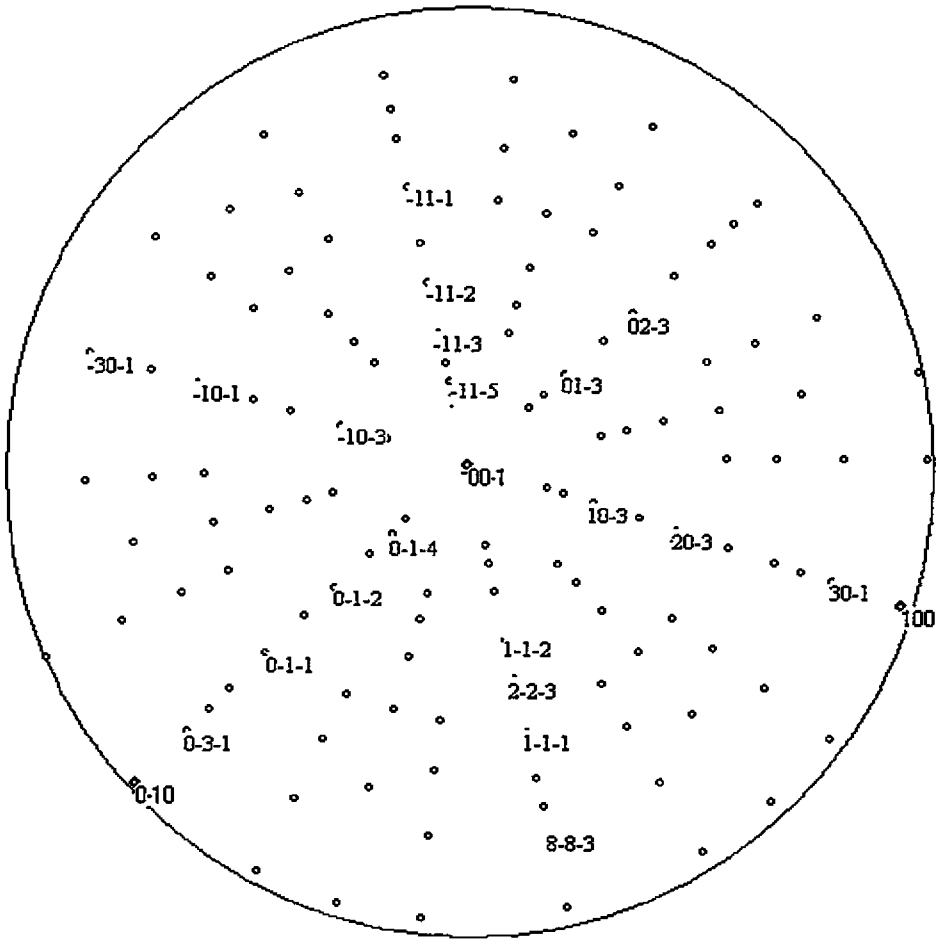

Figure 5-41: Stereographic projection from the (001) plane.

Rocking curves were measured for both cut sides after the sample was ground and polished. This confirmed the position of the (001) and (010) planes (Figures 5-42 and 5-44). The (001) side plot showed a peak at $\omega = 16.4°$, whereas the (001) Bragg angle is 17.2°. This suggests a ~0.8° misallignment (only one 'rocking direction' considered). The sample was then repositioned to correct this and XRD produced a single reflection (001) spectrum (Figure 5-42). Similarly, the (010) side plot suggested a ~0.5° misalignment with the peak maximum at $\omega = 16.58°$ versus the Bragg angle of 16.1°. The XRD spectrum was measured after correction for this misalignment, and a strong reflection obtained from the (010) plane (Figure 5-43). Two very low intensity reflections were noted at $2\theta = 34.5°$ and 36.8°. These suggest the rocking curves should be measured in other directions to completely identify the crystal misalignment. Due to the relatively low magnitude of misalignment, it was decided the results obtained were enough, i.e., the cuts were concluded to be satisfactory.

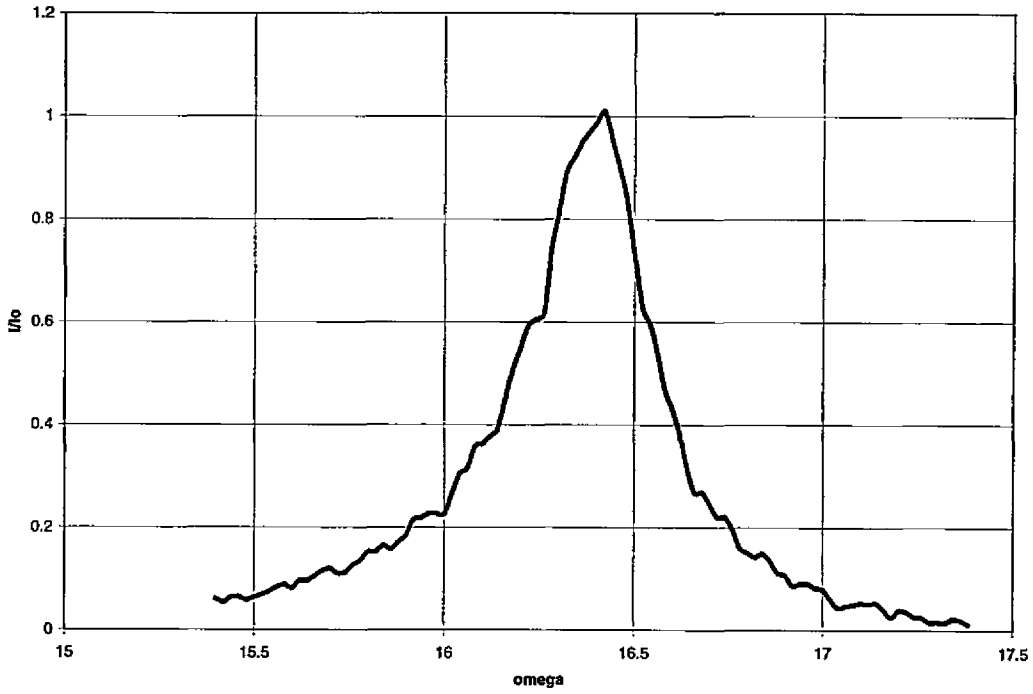

Figure 5-42: Rocking Curve on the (001) face.

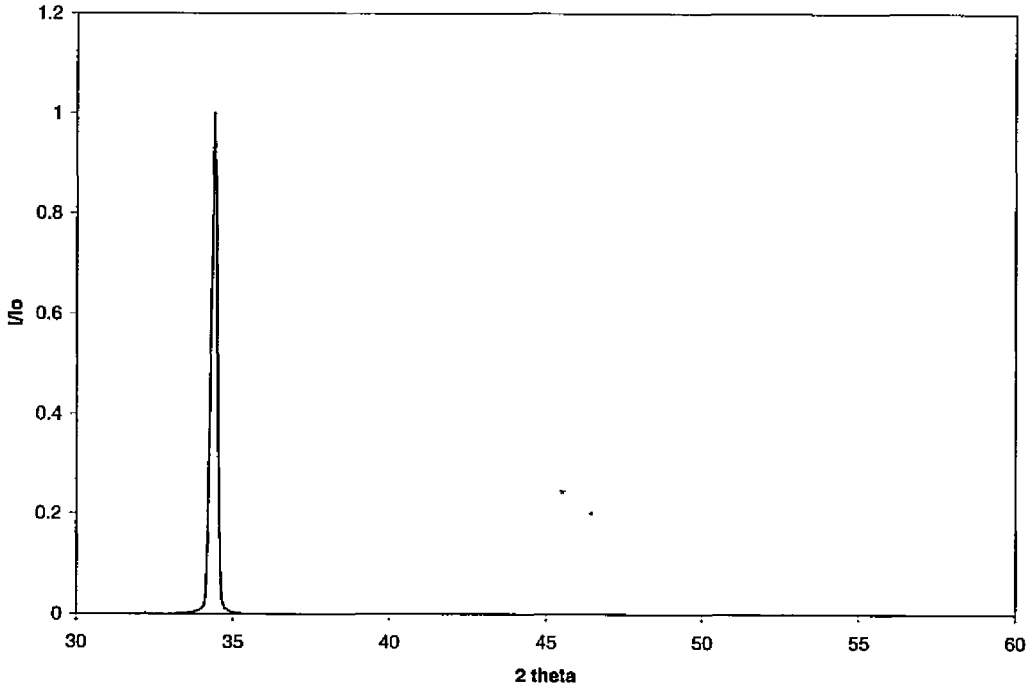

Figure 5-43: XRD spectrum obtained on the 001 plane face, 0.8° correction

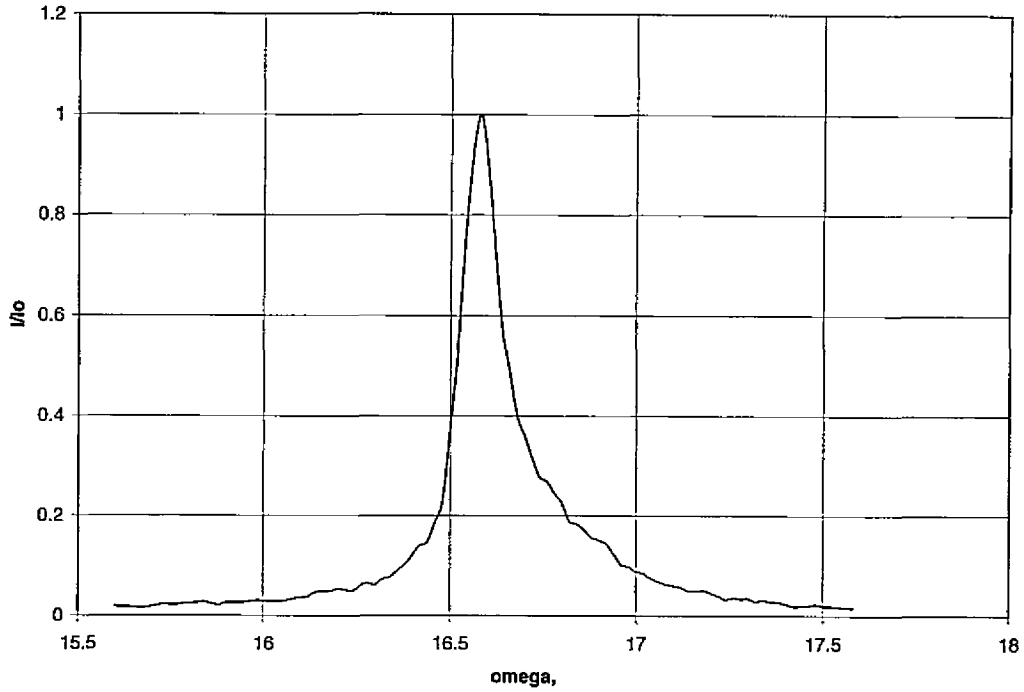

Figure 5-44: Rocking Curve on the (100) face.

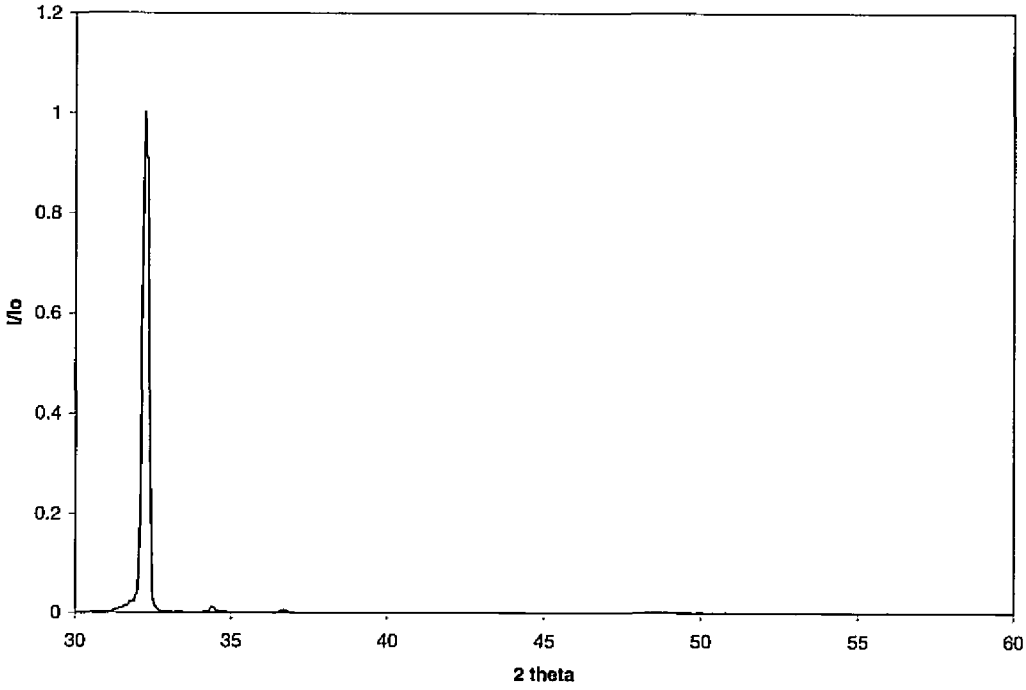

Figure 5-45: XRD spectrum obtained on the 100 plane face, 0.5 degree correction

Bulk sonic velocities were measured in the identified directions and the results are tabulated in Table 5-11. Values agree well with those published by Truell et al (1969). The slight differences observed are attributed to cutting and polishing. It was found the crystallographic direction had little effect on longitudinal velocities in the [010] and [001]. Truell et al (1969) showed that the longitudinal velocity in the [011] direction is 5940m/s, i.e., ~85m/s (1.5%) higher than the velocities in the [010] and [001]. Shear wave velocities clearly differ with wave propagation and polarization directions.

The bulk velocities measured were used to determine the elastic properties and illustrate the effect of crystallographic texture. The changes of Bulk-Modulus and Young's Modulus for the directions available in this work are as large as 2.1 and 2.6%, respectively.

Table 5-12 lists the results for polycrystalline-Mg, rolled sheet. The elastic properties are close to those of the [010] of the single crystal. As few Mg directions and velocities are known, it is difficult to draw specific conclusions. Clearly preferrential orientation in the polycrystalline material plays a major role in determining the ultrasonic velocities and the elastic properties thereof. The presence of grains caused an increase in bulk velocities, as compared to the single crystal. Such conclusion can be drawn only under the assumption that the other crystallographic direction velocities fall in-between or below the values measured for the [010] and [001]. However, the polycrystalline material velocity would be expected to be lower than the average of the single crystal velocities due to grain scatter.

The single-crystal-Mg was too small to determine the Acoustoelastic Constants and accurately measure surface waves velocities. The limited results presented above were not sufficient to deduce the texture and grain effect on the stress measurements with Rayleigh waves.

Table 5-11: Ultrasonic measurements on Magnesium single crystal (literature values - Truell et al, 1969).

Density, +/- 0.01 g/cc	Propagation Direction	Longitudinal Velocity, +/- 3 m/s	Literature Value	Polarization Direction	Shear Velocity, +/- 2 m/s	Literature Value	Bulk Modulus +/- 0.1 GPa	Young's Modulus +/- 0.2 GPa	Poisson's Ratio, v +/- 0.004
1.76	[010]	5855	5840	[001]	3092		37.8	43.9	0.307
				[110]	3107		37.6	44.2	0.304
	[001]	5860		[010]	3060	3060	38.4	43.1	0.313
				[110]	3063	3060	38.3	43.2	0.312

Table 5-12: Ultrasonic measurements for polycrystalline magnesium (RD = rolling direction).

Density, +/- 0.01 g/cc	Longitudinal Velocity, +/-5 m/s	Polarization Direction	Shear Velocity, +/- 3 m/s	Bulk Modulus +/- 0.2 GPa	Young's Modulus +/- 0.3 GPa	Poisson's Ratio, v +/- 0.007
1.74	5899	0 degrees to RD	3139	37.9	44.3	0.305
		90 degrees to RD	3122	37.7	44.7	0.303

5.3 An Ultrasonic Study of Titanium

5.3.1 Textured and Hot-Pressed Titanium

The study of residual stresses in Corning glass and glass-ceramic demonstrated that the surface roughness affects the velocity of the R_w and L_{cr} surface waves. Now, an attempt is made to detect residual stresses in a single-phase metal, wherein the texture and grain-size must be considered. The metal is commercially-pure titanium.

Two forms of Ti were investigated i.e. rolled sheet (heavily textured) and hot pressed (minimum texture). Plates cut from the rolled sheet were heat-treated to produce different grain sizes.

Unalloyed titanium has a close-packed hexagonal structure (α-phase), which changes to body-centered cubic (β-phase) at 885^0C. The latter structure persists to the melting point. Oxygen is added to commercially pure grades to raise the α to β transformation temperature (Lampman, 1990). For the CP Grade 4 titanium studied in this work, this temperature is 945 ± 15 °C , so heating at 850°C for 5, 20 and 50 hours, resulted in grain growth from 15 μm up to 45μm. Metallographic inspection was carried out on the cross-sections (Figure 5-46). The equiaxed grain structures are apparent. Figure 5-47 is a micrograph of the surface of the hot-pressed sample. The cross-section of the plates appear identical. Grains are plate-shaped, suggesting preferred orientation.

X-ray pole intensity plots of the (002), (012) and the (011) planes were generated from the Ti plates surfaces. The results are presented in Figures 5-48 to 5-52, where a) is the measured ring pattern, b) the (002) pole figure, c) the (012) pole figure and d) the (011) pole figure. The 15 μm specimen ring pattern produced smooth lines. These

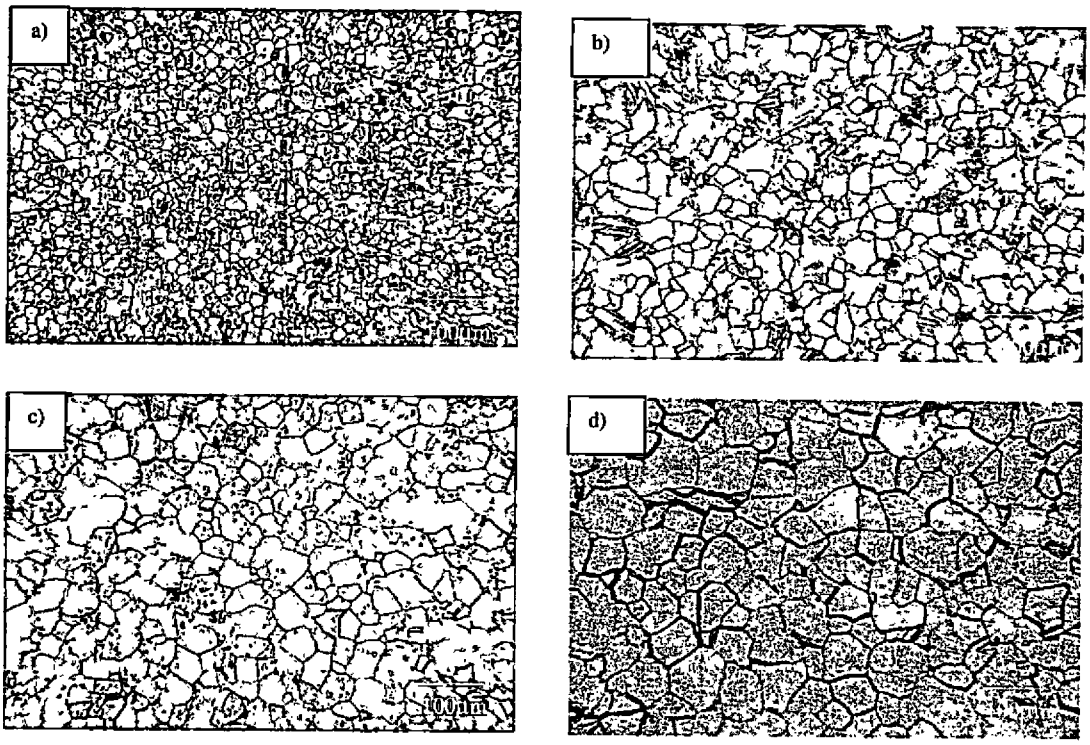

Figure 5-46: Optical micrographs of cross-sections of the CP4 rolled Titanium; grain size: a) as-received, 15μm, b) 27μm, c) 35μm, d) 45μm.

Figure 5-47: Optical micrograph of the hot-pressed Titanium, 75μm grain size.

became more 'spotty' in the heat-treated samples, confirming an increase in grain size. The as-received (no anneal) specimen (Figure 5-48) showed the basal planes mainly in the rolling plane and some distributed broadly to the transverse direction, that is tilted between 0 and approximately +/- 40° from the rolling plane about the rolling direction. The (012) and (011) plane poles are concentrated at positions approximately +/- 50 and +/- 65°, respectively, tilted from the normal to the rolling plane toward the rolling direction and slightly rotated about the <001> axis. This implies the [100] directions are mainly parallel to the rolling direction. Such texture is similar to (001) [100], $\gamma = 40°$ texture reported by Yoshimi et al (1991) in cold-rolled sheets of CP Titanium.

The annealed specimens' textures were slightly different from the original deformation texture. The pole figures for specimens annealed for 5, 20 and 50 hours are shown in Figures 5-49 to 5-51. The basal planes remained in the rolling plane, with some tilted towards the transverse direction. However, the heat treatment randomized the <012> and <011> directions around the symmetry <001> axis.

Literature states that at temperatures above 700°C (as in this work), at which appreciable grain growth takes place, the (001)[110] γ = +/- 30° towards TD (transverse direction) orientation develops (Inagaki, 1992). Unfortunately, using the Mo X-ray source did not allow the investigation of the (110) diffraction. For future work, Cu-radiation is recommended.

The ring patterns measured from the hot-pressed specimen were clearly composed of the single-crystal diffraction spots. This was due to the grains being relatively large (75 μm). The (012) pole intensity map showed high intensity areas distributed randomly.

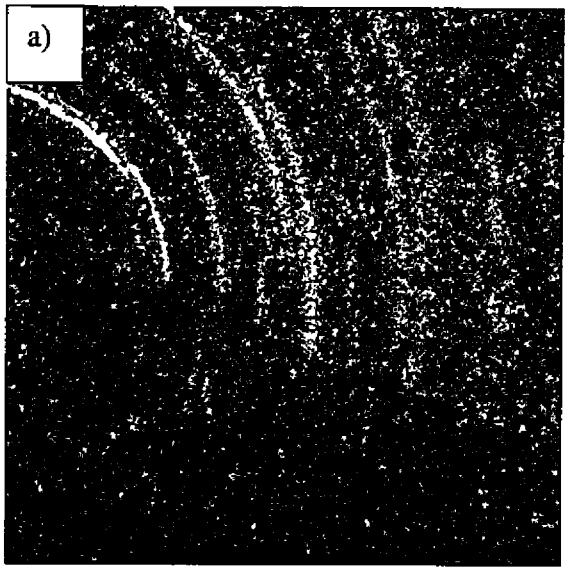
a)

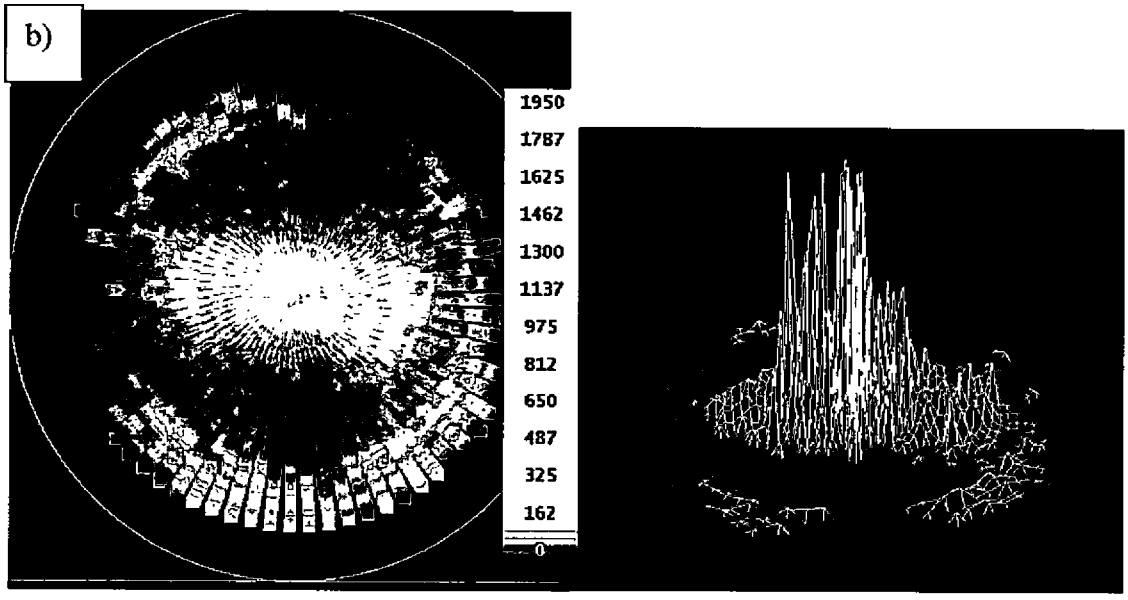
b)
1950
1787
1625
1462
1300
1137
975
812
650
487
325
162
0

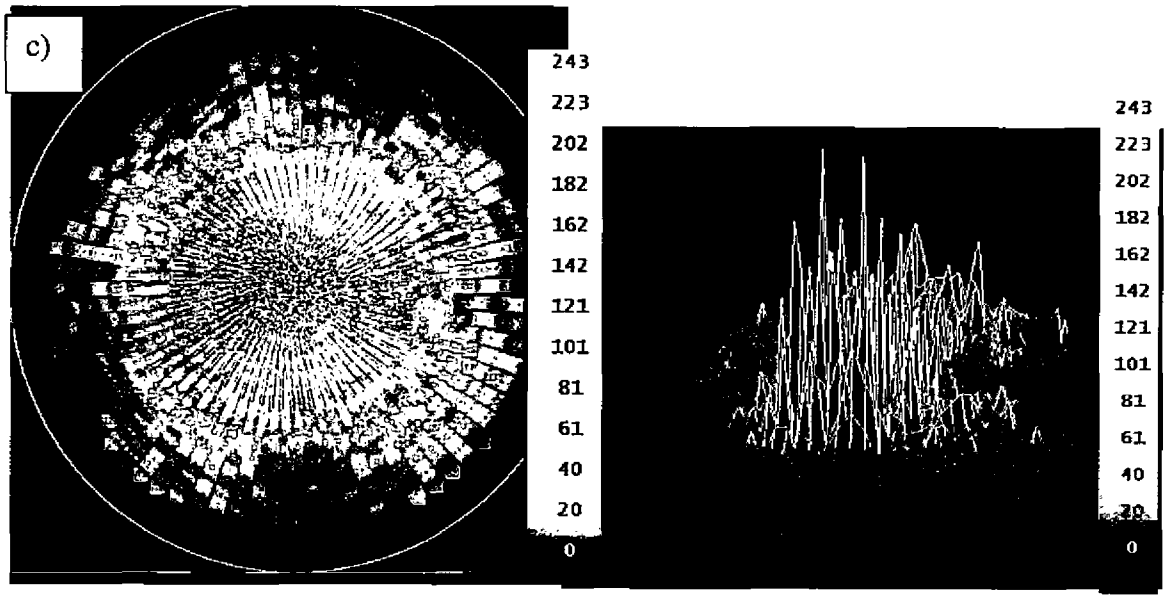

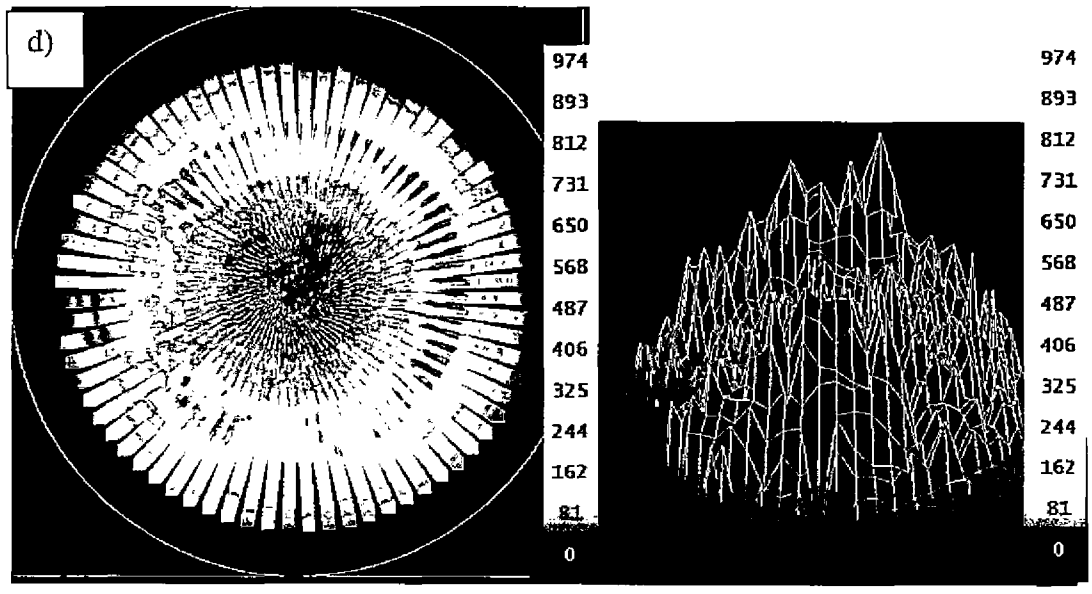

Figure 5-48: Pole figures of as-cold-rolled titanium sheet measured by X-ray diffraction, a) {002} pole figure, b) {012} pole figure, c) {011} pole figure.

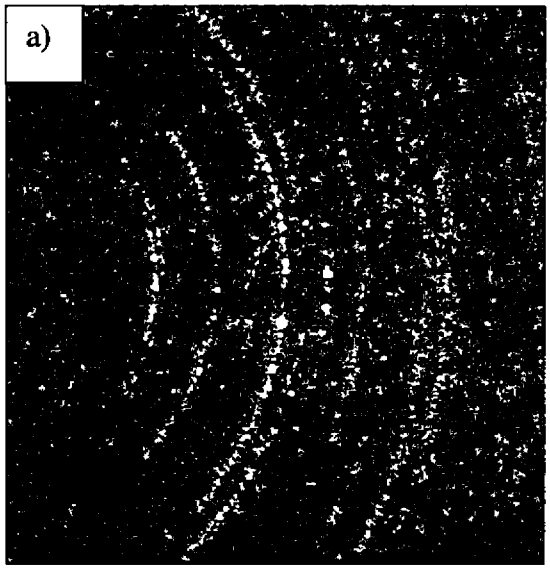
a)

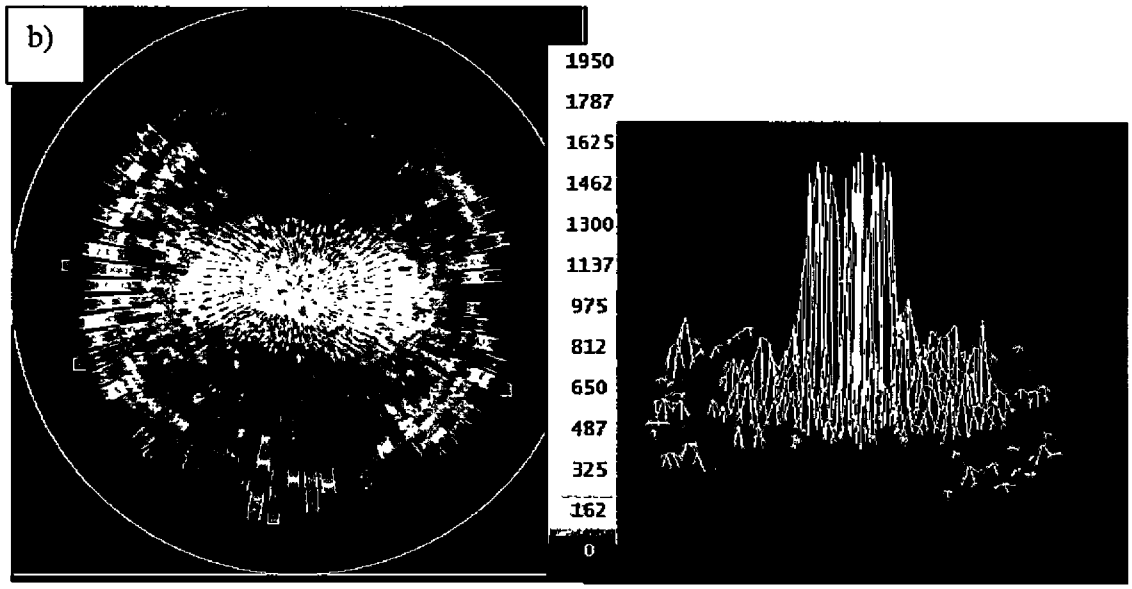
b)
1950
1787
1625
1462
1300
1137
975
812
650
487
325
162
0

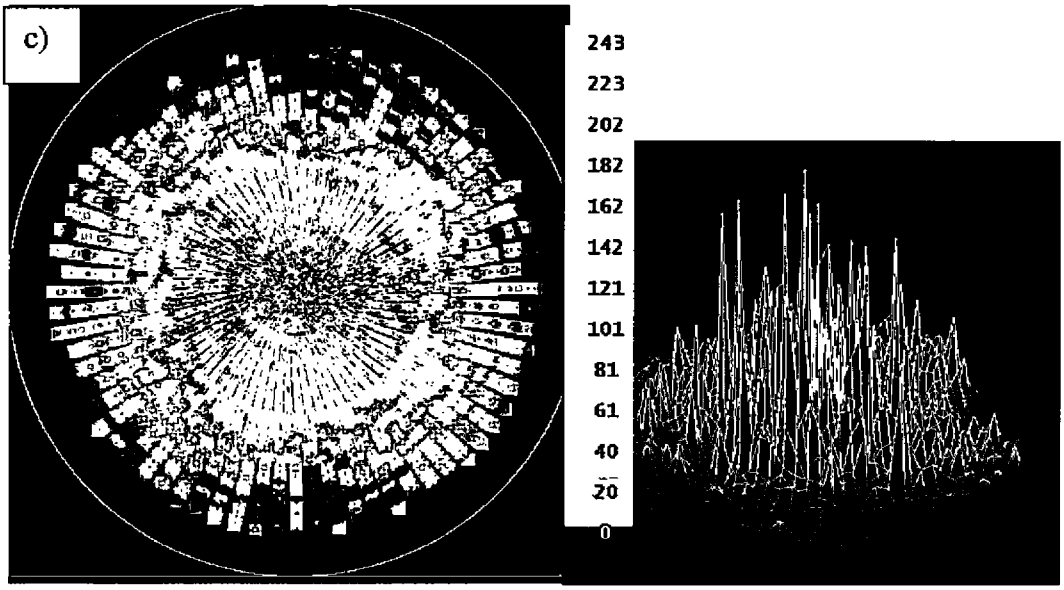

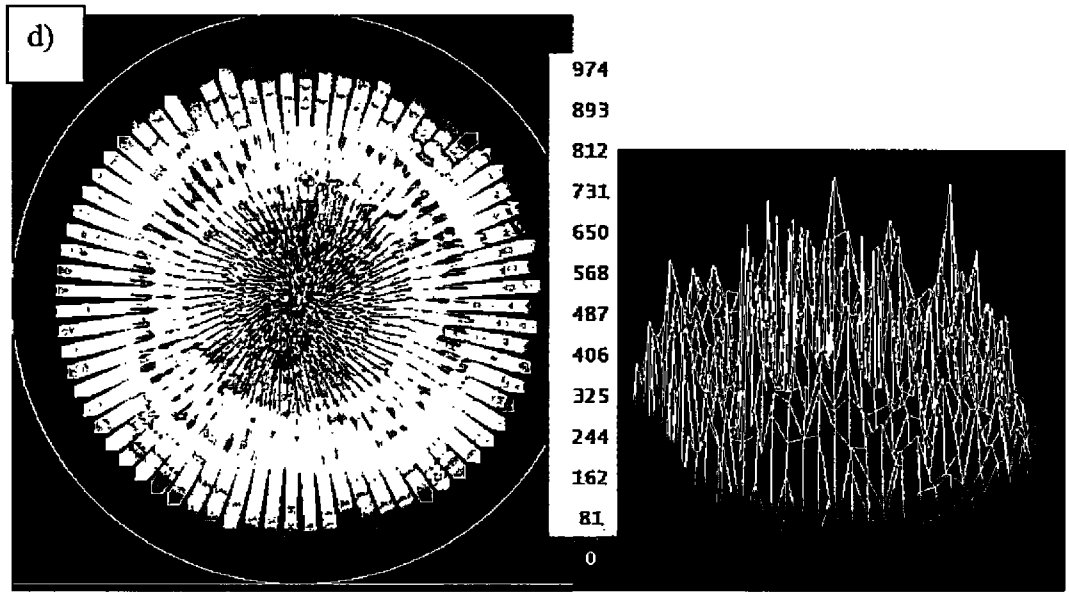

Figure 5-49: Pole figures of cold-rolled Ti sheet, annealed for 5h, measured by X-ray diffraction, a) {002} pole figure, b) {012} pole figure, c) {011} pole figure.

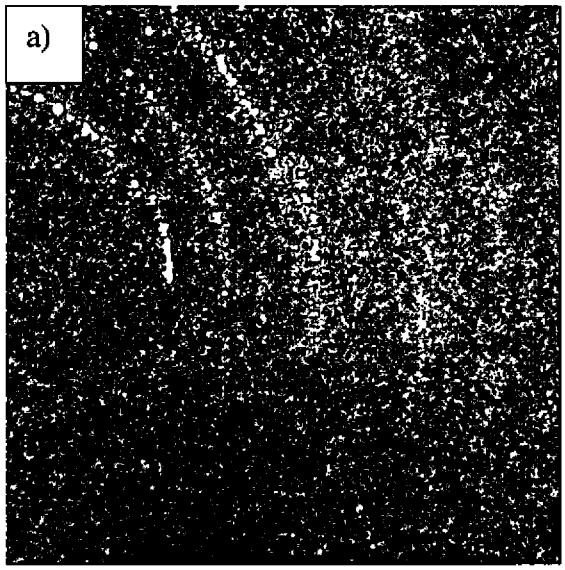
a)

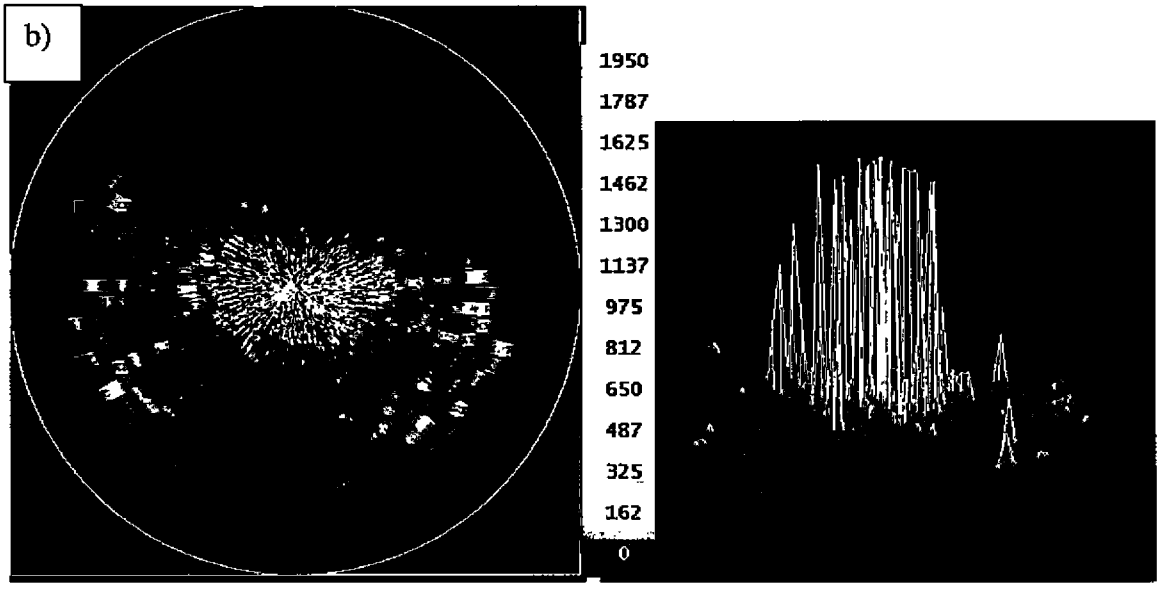
b)
1950
1787
1625
1462
1300
1137
975
812
650
487
325
162
0

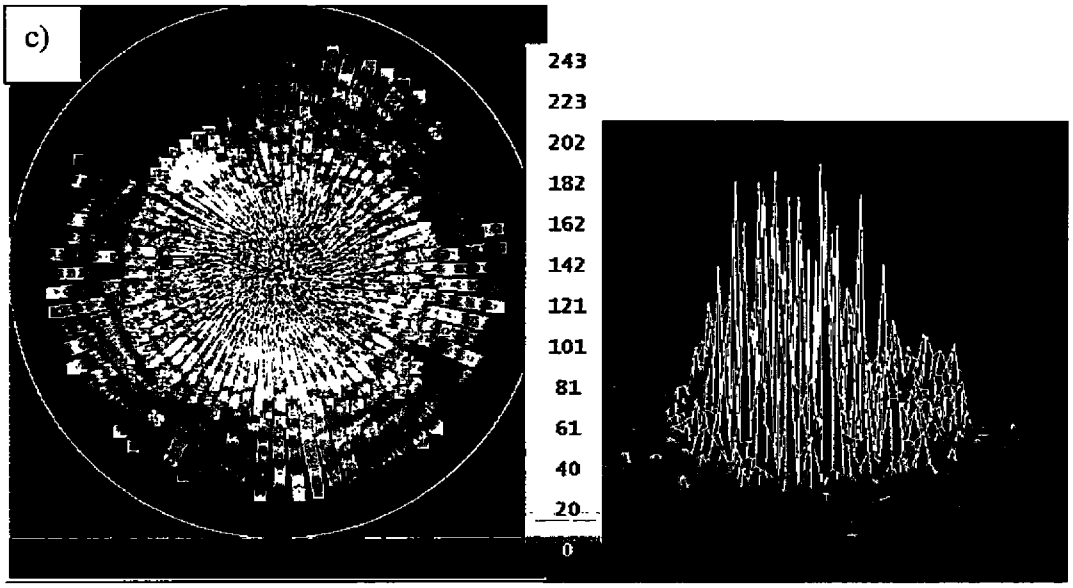

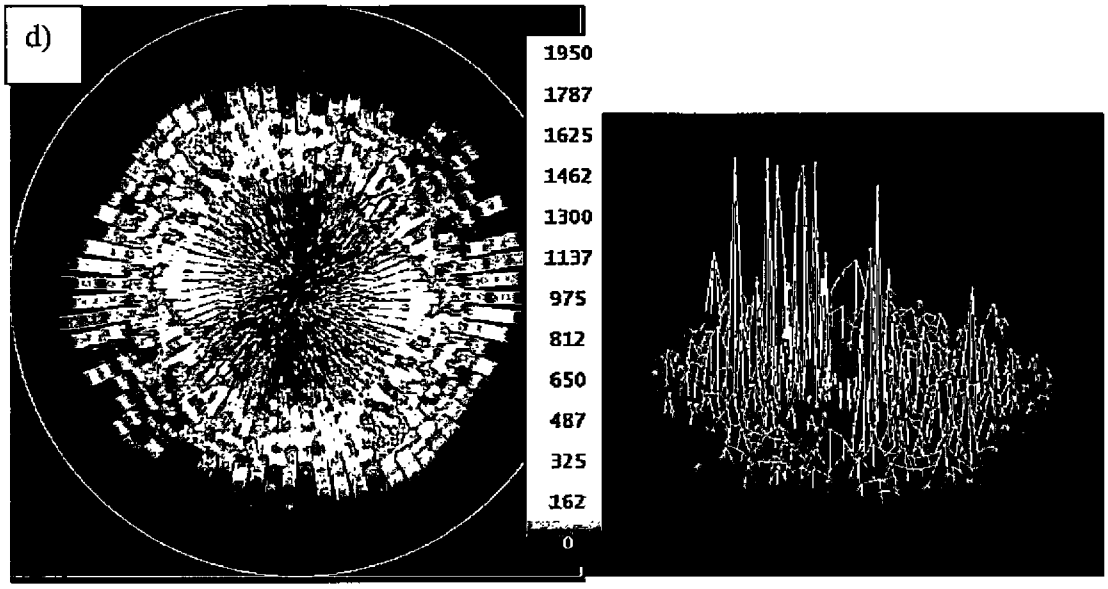

Figure 5-50: Pole figures of cold-rolled Ti sheet, annealed for 20h, measured by X-ray diffraction, a) {002} pole figure, b) {012} pole figure, c) {011} pole figure.

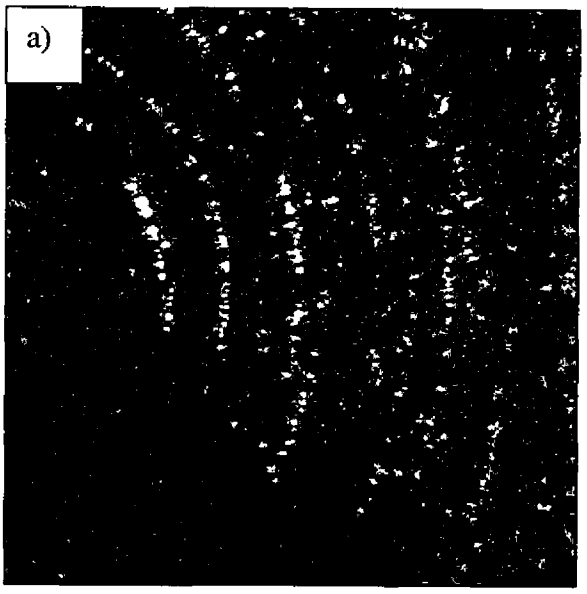
a)

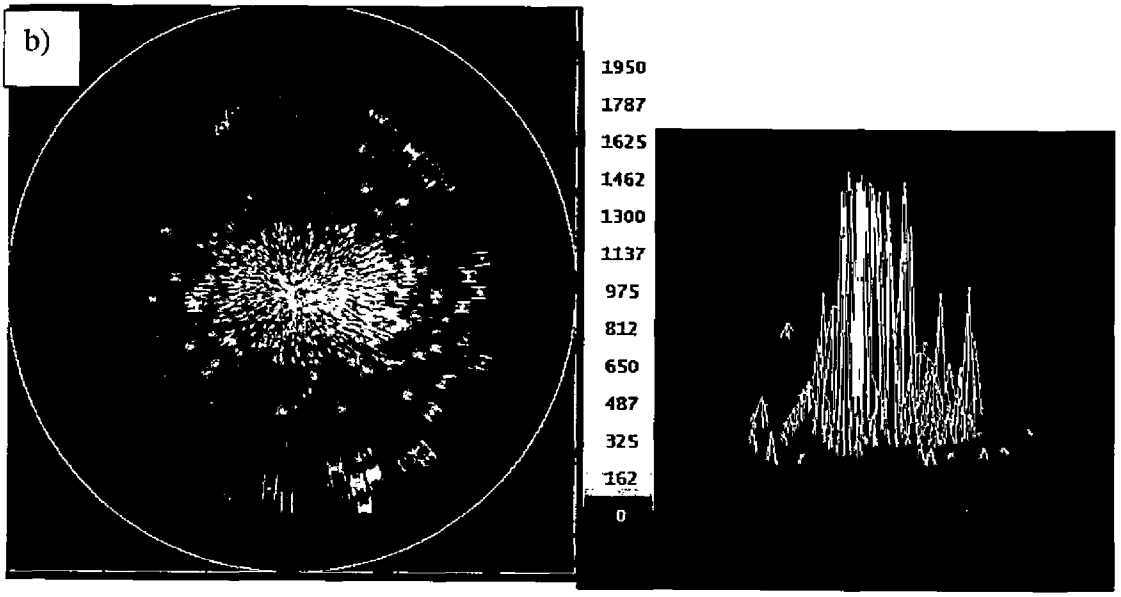
b)
1950
1787
1625
1462
1300
1137
975
812
650
487
325
162
0

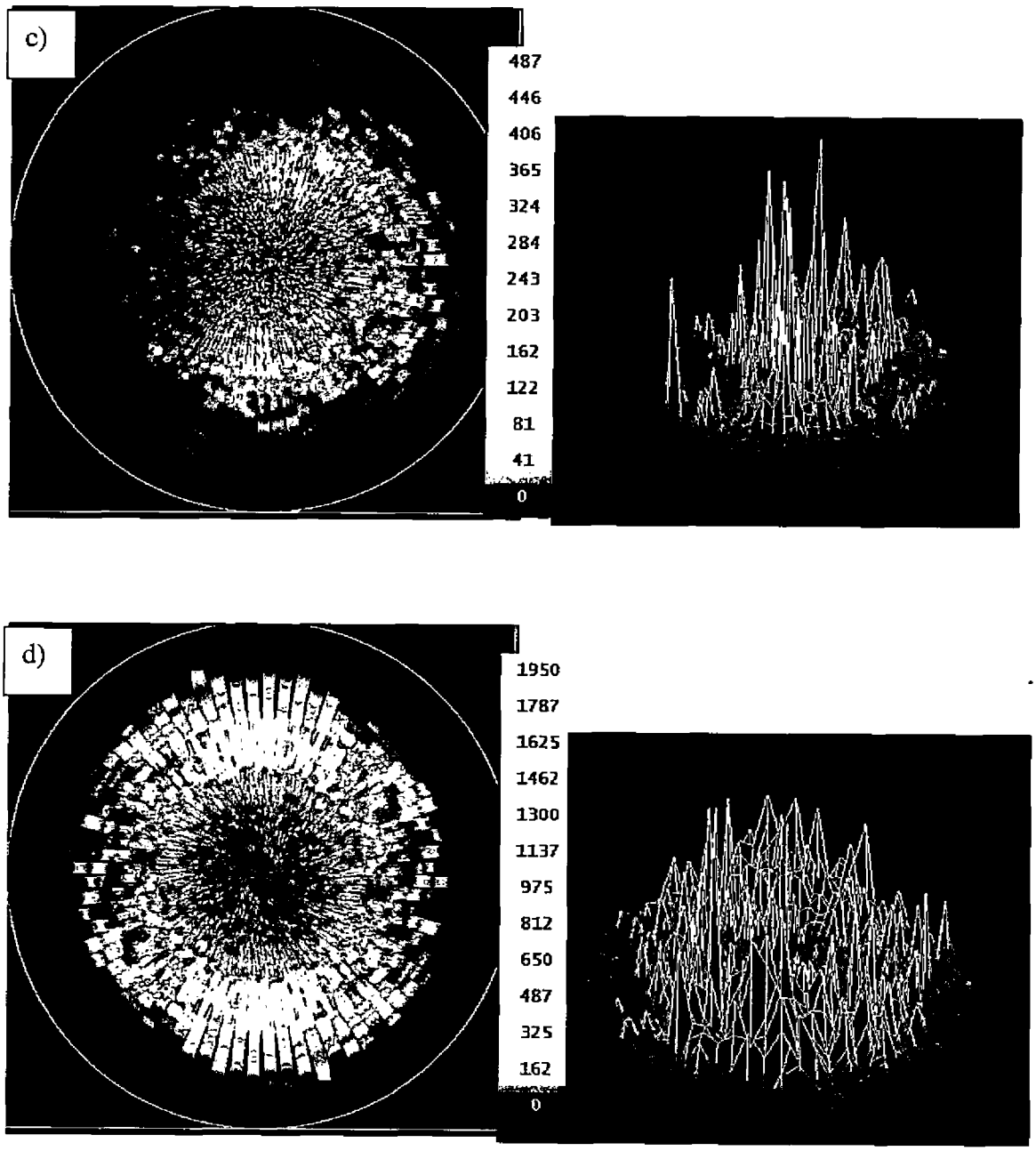

Figure 5-51: Pole figures of cold-rolled Ti sheet, annealed for 50h, measured by X-ray diffraction, a) {002} pole figure, b) {012} pole figure, c) {011} pole figure.

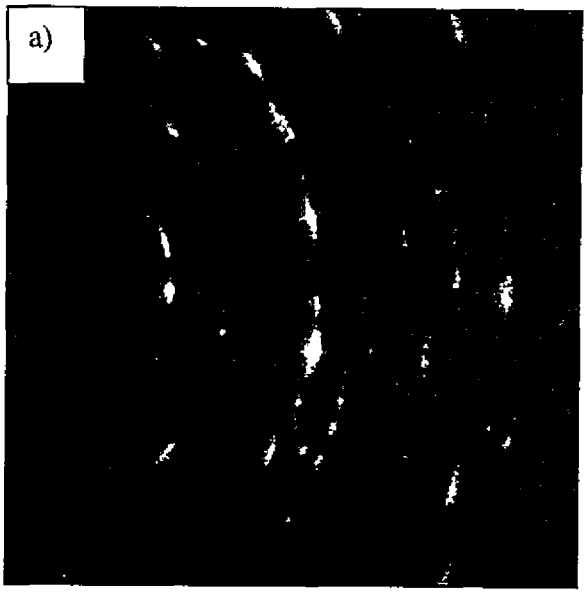
a)

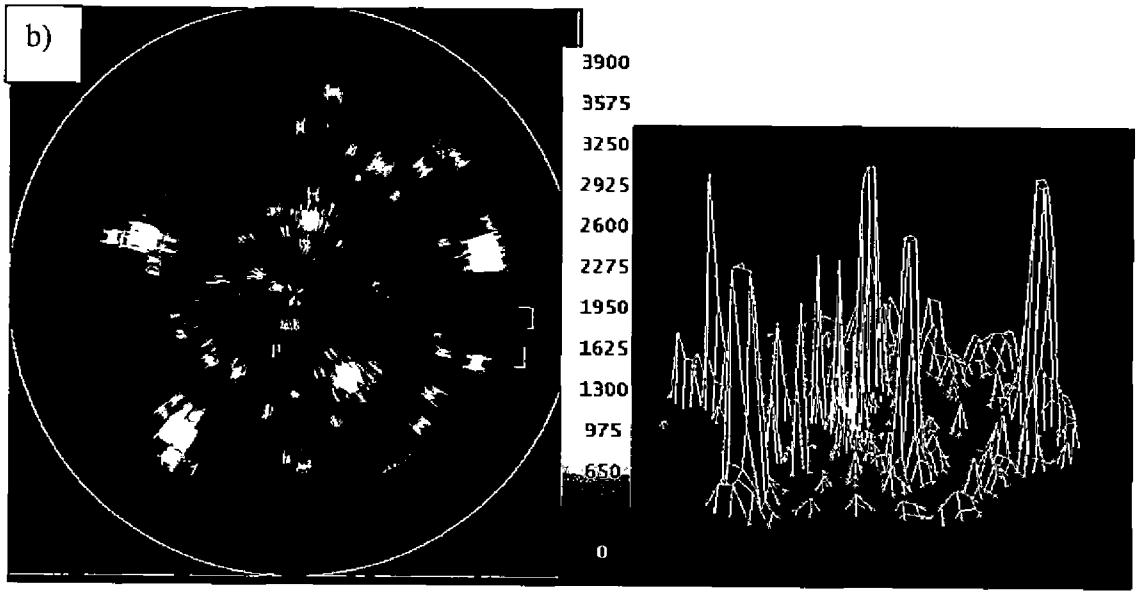
b)
3900
3575
3250
2925
2600
2275
1950
1625
1300
975
650
0

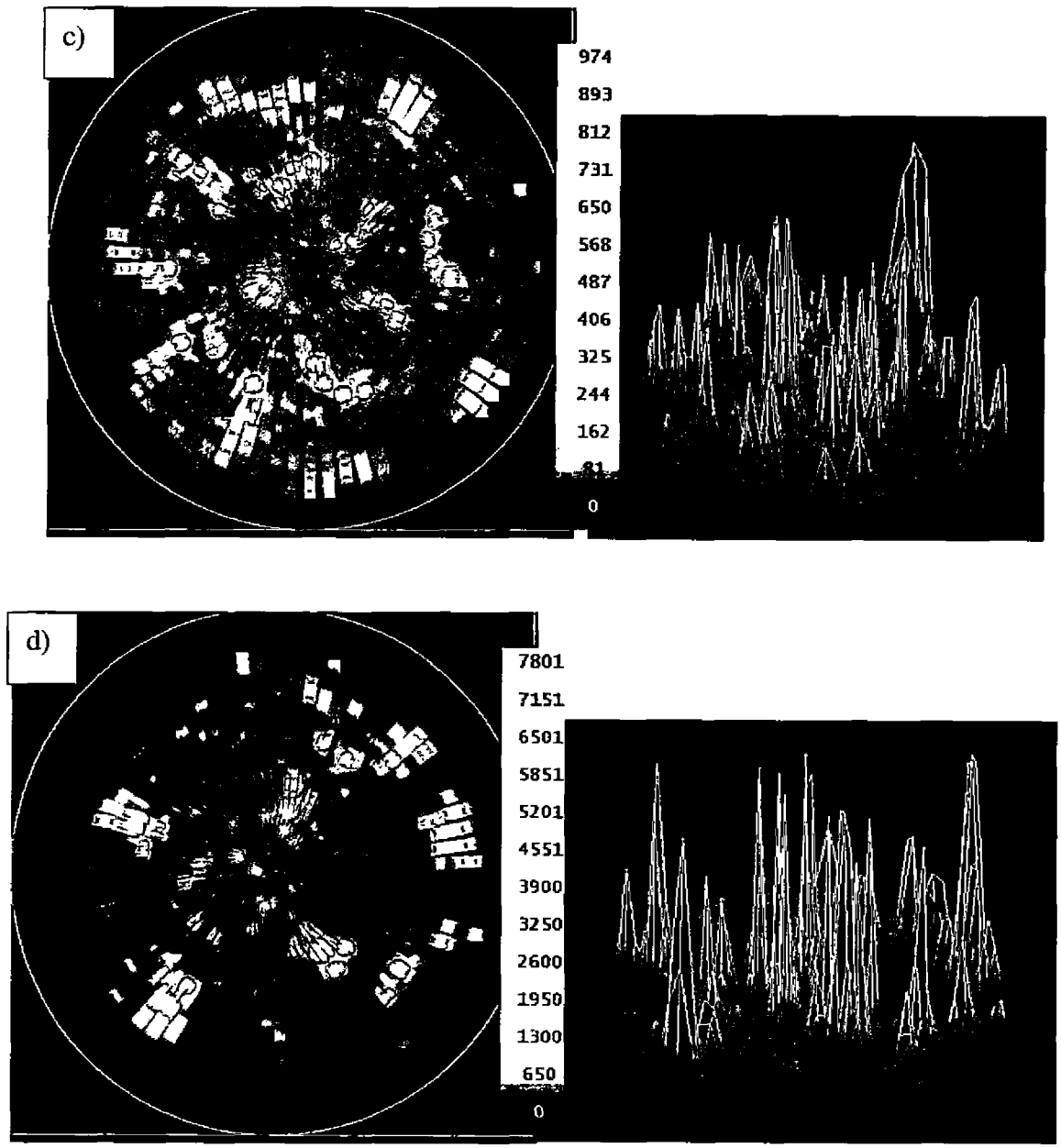

Figure 5-52: Pole figures for hot-pressed titanium, measured by X-ray diffraction, a) {002} pole figure, b) {012} pole figure, c) {011} pole figure.

Some symmetry can be observed on the (002) and (012) maps. Yet, compared to the rolled plates, the hot-pressed specimen has little texture.

XRD spectra were obtained and it was confirmed for heat-treated specimens, the phase composition did not alter, i.e. it was still single-phase α. Figures 5-53 and 5-54 are spectra from the surface of the 50-h-heated, rolled specimen and the hot-pressed plate, respectively. The strongest reflections were obtained from the (002) planes of the rolled specimen (confirming the pole-figure results) and the (101) planes in the hot-pressed material.

The Archemedes density of titanium, was 4.50 ± 0.01 g/cc, in agreement with published values (Lampman, 1990). Within experimental error the density was uninfluenced by heat treatment. Table 5-13 and 5-14 summarize the longitudinal- and shear- bulk velocities obtained with plate samples before and after stress-relief treatment. The contact-transducers used had a working-frequency of 5MHz. The longitudinal velocity, as measured through the plate thickness, significantly decreased on heat-treatment. The maximum (-0.4%) was observed for the as-received, rolled plate. The rolling-stress distribution in these plates was previously described as low tension in the surface and significant compression deeper in the material (Leon-Salamanca and Bray, 1995). The decrease of longitudinal wave velocity suggests relief of the compressive stress, initially present in the sheet thickness. The fact that this change was less for specimens B, C, and D suggests previous grain-growth-heat treatment altered the residual-stress-state in the plates.

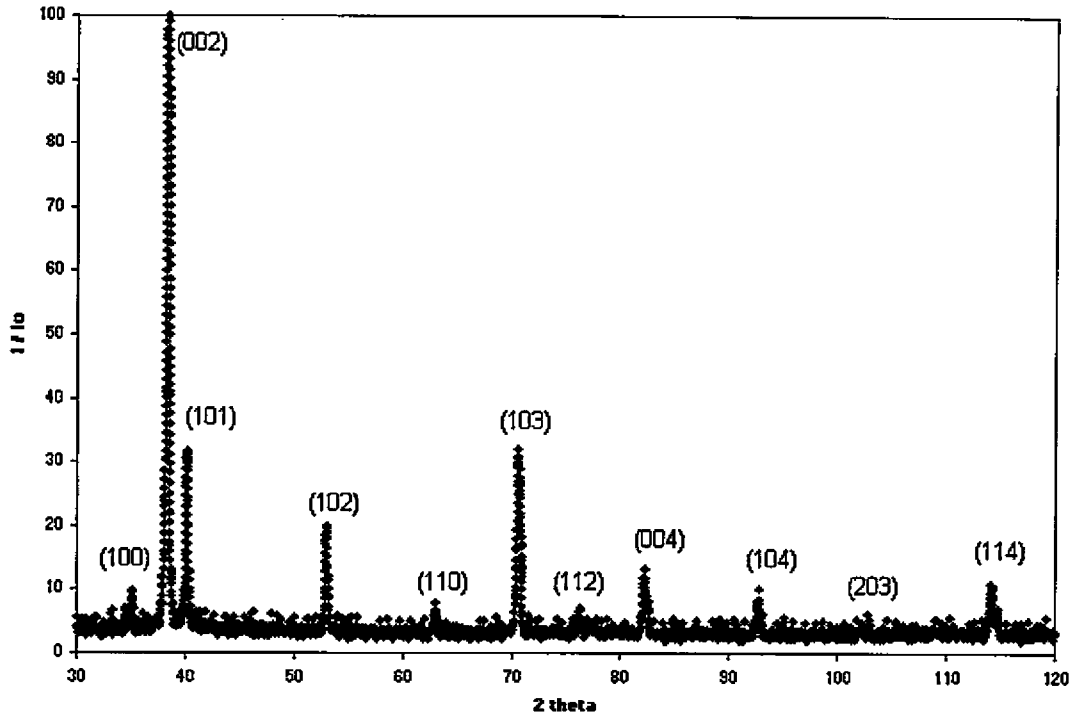

Figure 5-53: XRD spectrum from the CP4 Titanium plate surface. α - reflections identified.

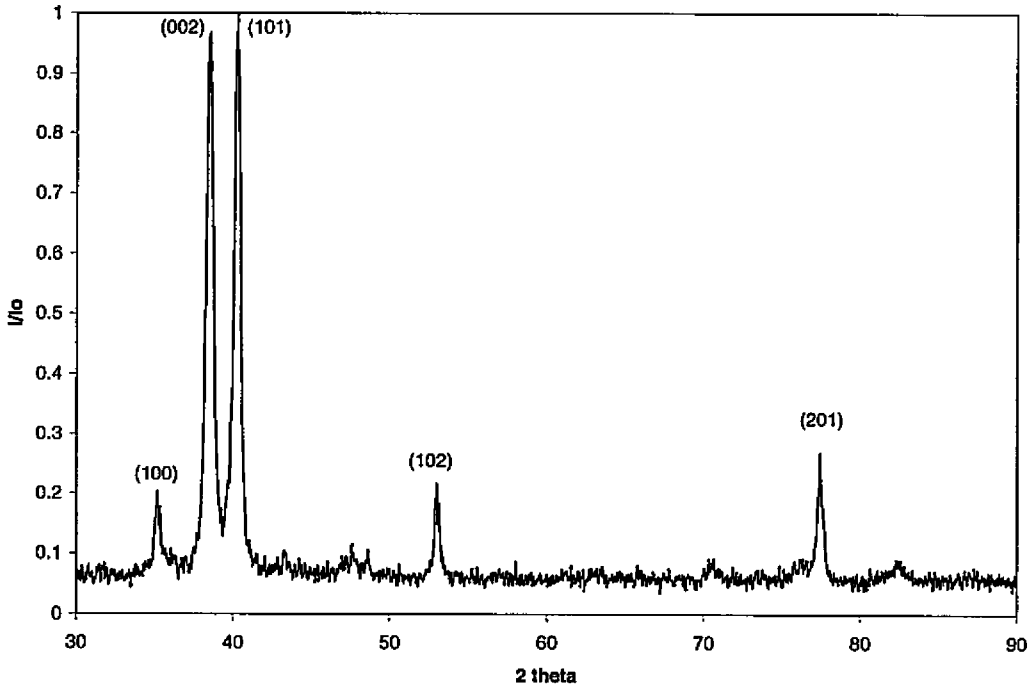

Figure 5-54: XRD spectrum from the hot-pressed Titanium plate surface. α - reflections identified.

The longitudinal wave velocity through the thickness of the hot-pressed plate was not significantly affected by the annealing process, implying minimal residual stress was present. Before annealing, the hot-pressed plate was ground and polished, which must

Table 5-13: Bulk velocities measured in Titanium before annealing.

Sample	Grain Size µm	Density g/cc +/- 0.01	Longitudinal Velocity m/s	Polarizatio Direction Vs. Rolling	Shear Velocity m/s
Titanium CP4 as-received	15 +/- 3	4.49	6221 +/- 6	0 deg	3146+/-4
				90 deg	3262+/-3
Titanium CP4 **B**	27 +/- 2	4.50	6201 +/- 5	0 deg	3144+/-3
				90 deg	3249+/-4
Titanium CP4 **C**	35+/- 3	4.50	6177 +/- 6	0 deg	3118+/-3
				90 deg	3247+/-3
Titanium CP4 **D**	45+/- 3	4.50	6157 +/- 6	0 deg	3090+/-3
				90 deg	3224+/-3
Titanium hot-pressed	75+/- 14	4.49	6136 +/- 6	0 deg	3191+/-4
				90 deg	3184+/-3

have introduced surface stress (Pineault et al, 2001). The bulk longitudinal wave is insensitive to these stresses.

Shear wave velocities were measured with particle polarization in the rolling and transverse directions. An average difference of 4.1% confirmed the presence of texture. The results can be related to the pole figures and magnesium study presented earlier. The

pole figures show the rolling plane consists of the basal planes, some of which have normals tilted towards the transverse direction. The single crystal magnesium study on the other hand showed that the shear velocities along the c-axis are independent of the sound polarization direction. Titanium can be assumed to behave similarly since its structure has the same space group ($P6_3$ / mmc). If all the grains were oriented such that the c-axis was normal is the rolling plane, and there is no grain anisotropy and texture, no change would have been observed in the shear velocity with polarization. The fact the basal planes are distributed around the rolling plane normal and some are tilted (up to ~40°) from this normal, indicates the shear-wave through the plate-thickness propagates in other directions as well as <001>. The magnesium crystal measurements show the shear velocity is significantly different along the [100] direction so will vary in other directions. Texture in the rolled titanium awarded the highest velocity to the texture (transverse) direction.

Pole figures showed very little texture in the hot-pressed plate. Consequently the shear velocity was approximately independent of polarization direction (0.2% maximum difference). The hot pressed plate was cold-rolled to 20% reduction which resulted in a change of shear wave velocity in the rolling (3088m/s) and transverse (3119m/s) directions (a 1% change).

Upon annealing, a trend was observed in the change of shear velocities, although the error was large. Velocities in the rolling direction increased slightly, suggesting relief of the surface tensile residual stresses. Velocities in the transverse direction decreased, implying existence of initial compressive stresses. A 0.33 - 0.4% anisotropy of

Table 5-14: Bulk velocities measured in Titanium after annealing.

Sample	Density +/- 0.01 g/cc	Longitudinal Velocity m/s	% change from before stress-relief	Polarizatio Direction Vs. Rolling	Shear Velocity m/s	% change from stress-relief
Titanium CP4 as-received	4.49	6196 +/- 6	-0.4 +/- 0.1	0 deg	3148+/-3	0.1 +/- 0.1
				90 deg	3258+/-3	-0.1+/- 0.1
Titanium CP4 **B**	4.50	6182 +/- 6	-0.3+/- 0.1	0 deg	3147+/-3	0.1 +/- 0.1
				90 deg	3247+/-3	-0.1 +/- 0.1
Titanium CP4 **C**	4.50	6157+/- 6	-0.3+/- 0.1	0 deg	3118+/-3	0
				90 deg	3245+/-3	-0.1 +/- 0.1
Titanium CP4 **D**	4.50	6148 +/- 6	-0.2+/- 0.1	0 deg	3093+/-3	0.1 +/- 0.1
				90 deg	3223+/-3	0
Titanium hot-pressed	4.49	6137+/- 5	0.0+/- 0.1	0 deg	3191+/-3	0
				90 deg	3184+/-3	0

velocity between the directions, remained. This is attributable to the texture induced by the rolling process and the incomplete removal of the associated stresses upon anneal.

Longitudinal and shear velocities were plotted .vs. the grain size and an inverse relationship was observed (Figures 5-55 and 5-56). This phenomenon has also been noted by others. Saiie et al (1987) proposed it is due to a dispersion effect. The ratio of grain- diameter to ultrasound-wavelength varies between 0.012 and 0.03, i.e. in the Rayleigh-wave scattering region. Saiie et al (1987) suggest grain scattering increases rapidly with grain diameter 'D' ($\cong D^3$ in the Rayleigh region) and concurrently, dispersion of the ultrasonic pulse increases,

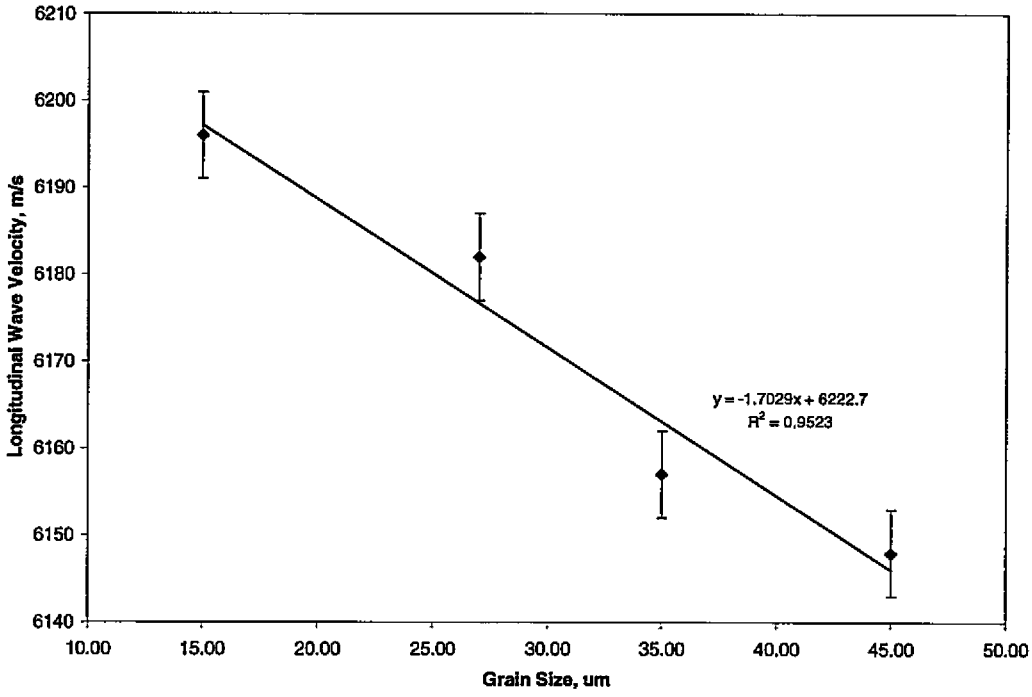

Figure 5-55: Longitudinal wave velocities in CP4 Titanium

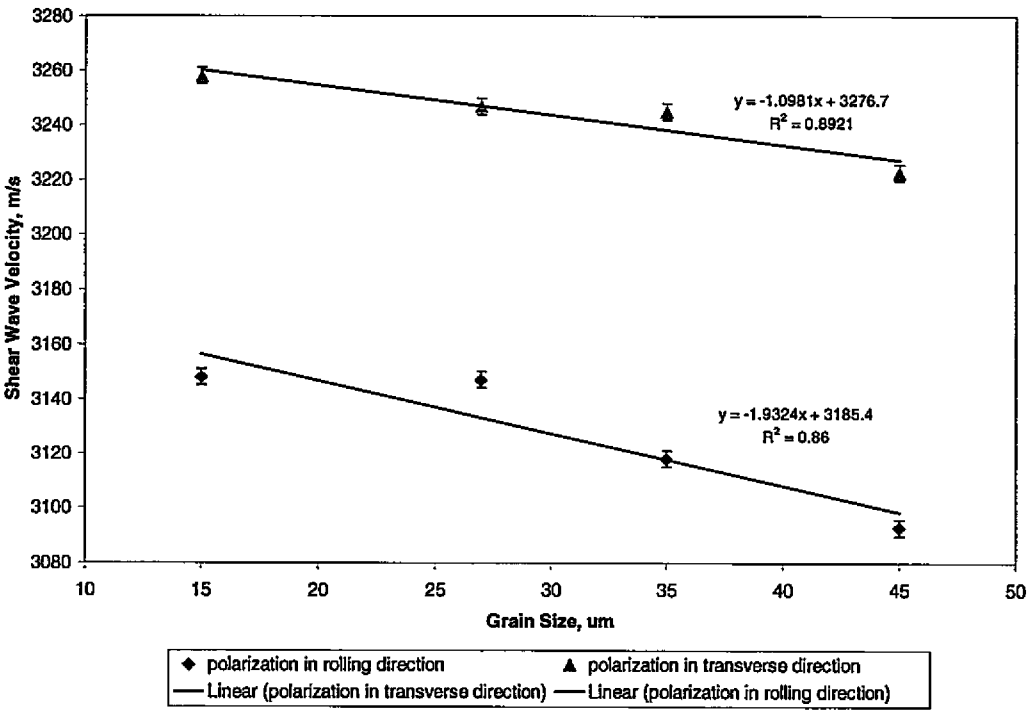

Figure 5-56: Shear wave velocities in CP4 Titanium

i.e. higher frequency signals are scattered along the sound path, so velocities decrease. Palanichamy et al (1995) suggested an inverse relationship between grain-size and ultrasonic longitudinal-, and shear-, velocities for AISI 316 stainless steel. They found shear waves are more sensitive to change of grain size. This is not so in the present work. Palanichamy et al did not however, consider the influence of texture. Present results confirm the polarized, shear-wave-velocity is significantly influenced by the texture. Murthy (2000) observed the same for ultrasonic velocities in polycrystalline YIG.

The elastic properties of titanium samples were calculated via Equations 34-36 (Chapter 2) and the resulting values are listed in Table 5-15. Also included are the calculated rms (root mean square) errors. The Bulk Modulus and Poisson's Ratio are close to published values for CP4 titanium (0.34 and 110 GPa, respectively) (Lampman, 1990). However, the Young's Modulus determined is higher (the book value is 104GPa). These properties do however depend closely on exact composition and heat treatment (Graft et al, 1956). The literature values quoted are for CP4 Ti containing 0.4 wt% oxygen, annealed for two hours at 700°C. Also, on occasion, there are differences between the elastic moduli measured by the dynamic method .vs. the static method. These differences reflect grain boundary elastic behavior, which plays no role in the dynamic method but may in the static one (Graft et al, 1956).

Table 5-15: Elastic Properties of the stress-relieved CP4 and hot-pressed titanium, determined by ultrasonics.

Sample	Polarization Direction	Bulk Modulus GPa	Young's Modulus GPa	Poisson's Ratio v
Titanium CP4 as-received	Rolling	113.1 +/- 0.2	118.1 +/- 0.3	0.326 +/- 0.007
	Transverse	108.9 +/- 0.2	124.8 +/- 0.3	0.309 +/- 0.007
Titanium CP4 **B**	Rolling	112.5 +/- 0.2	118 +/- 0.3	0.325 +/- 0.007
	Transverse	108.7 +/- 0.2	124.1 +/- 0.3	0.31 +/- 0.007
Titanium CP4 **C**	Rolling	113.1 +/- 0.2	116 +/- 0.3	0.329 +/- 0.007
	Transverse	108.2 +/- 0.2	124.2 +/- 0.3	0.309 +/- 0.007
Titanium CP4 **D**	Rolling	112.6 +/- 0.2	114.5 +/- 0.3	0.332 +/- 0.007
	Transverse	107.7 +/- 0.2	122.4 +/- 0.3	0.311 +/- 0.007
Titanium hot-pressed	0degrees	108.1 +/- 0.2	120.2 +/- 0.3	0.315 +/- 0.007
	90 degrees	108.4 +/- 0.2	119.8 +/- 0.3	0.316 +/- 0.007

The rolled specimens exhibited elastic property anisotropy i.e. Bulk Modulus and Poisson's Ratio were higher in the rolling direction whereas the Young's Modulus was higher in the transverse direction. Elastic moduli reflect the bond strength in the material and this varies with crystallographic direction. Thus it is to be expected that, in a rolled metal where preferred crystallographic orientations exist, the elastic moduli will change

with direction. The hot-pressed titanium, being isotropic, exhibited uniform elastic properties i.e. independent of measurement direction.

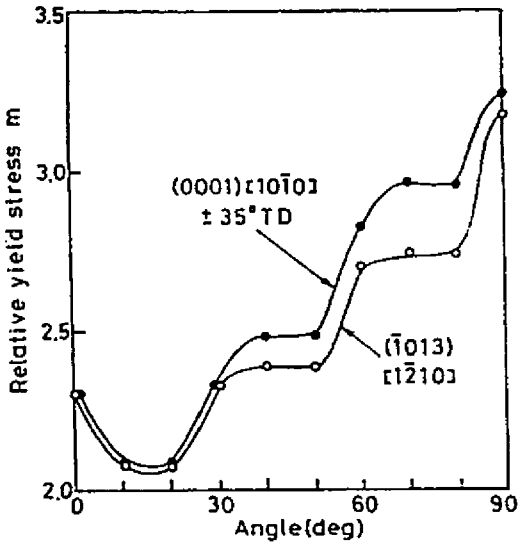

Figure 5-57: Change of the relative yield stress with the angle from the rolling direction, calculated for the ($\bar{1}$03) [1$\bar{2}$0] and (001) [10$\bar{1}$] +/- 35° TD orientations (Inagaki, 1992)

A number of studies have shown in cold rolled and annealed pure titanium that, the yield stress is minimum in the rolling direction and increases appreciably with increasing angle to the rolling direction (Inagaki, 1992). Accordingly, the Young's Modulus will be highest in the transverse direction. Thus the results presented in Table 5-15 agree with those of previous investigations. Figure 5-57 presents the relative yield stress versus the angle from the rolling direction as plotted by Inagaki (1992), for the (001)[100]Angle γ = +/- 35° TD and the (-103)[120] main orientations (the former the 'cold-rolling texture, the latter the 'grain-growth' texture). The ratio of the yield stress in the transverse to that in

the rolling direction was shown to be ~1.4, which compares well with the ratio of the transverse direction E_T, (Young's Modulus) to the rolling direction, E_R, observed in this work ($E_T / E_{R=} \sim 1.1$). The actual ratio will depend on the % rolling reduction as well as the magnitude of tilt of the (001) plane towards the transverse axis (Inagaki 1992). It is important to note, the anisotropies of yield strength in Figure 5-57 are quite similar for both orientations. This suggests little change would occur in the anisotropies of the yield-stress (and the Young's Modulus) during the grain-growth process. This is also found herein (Table 5-15).

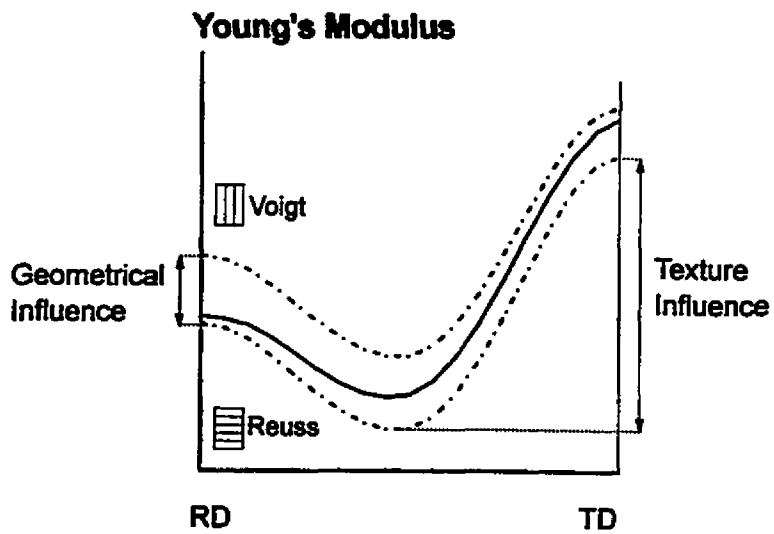

Figure 5-58: Influence of texture and geometrical factors on elastic properties in the sheet plane – schematic (Bunge et al, 1997)

It must be emphasized that, not only texture, but also the shape and mutual arrangement of the grains dictate the macroscopic averages of crystallographically anisotropic properties in polycrystalline materials (Bunge et al, 1997). The most well known example of this 'geometrical,' influence are the Voigt and Reuss bounds of the

elastic properties (side-by-side or on-top arrangement of crystallites, respectively). This effect for Young's Modulus is presented schematically in Figure 5-58. Bunge et al (1997) showed the geometrical structure parameters may influence the properties within the entire range between the Voigt and Reuss bounds. The latter may however, deviate from each other by $\leq 25\%$ the absolute value.

5.3.2 Determination of the Acoustoelastic Coefficients for Titanium

The Acoustoelastic Coefficients were obtained via the 4-point bend test utilizing the Rayleigh-wave (R_w) cylindrical transducer (15 MHz working frequency) and the critical-longitudinal-wave (L_{cr}) spherical transducer (12 MHz). The Rayleigh waves propagated along the sample so the rolled titanium was studied in the rolling and transverse directions. Figures 5-59, 5-61, 5-63 and 5-65 are plots of the surface wave velocities .vs. strain for the rolled and hot-pressed titanium. The ultrasonic velocity increases with compressive strain in all cases. The Acoustoelastic Coefficients were obtained from the slopes of plots of the percentage-change of velocity versus stress (Figures 5-60, 5-62, 5-64 and 5-66). The stress present was calculated via the strain-measured and the Young's Modulus measured earlier. The y-axis error bars account for sample deflection under load. The latter increases the transducer - sample distance which in turn influences the measured velocity. The error in the slope value was analyzed via the 'Box' method.

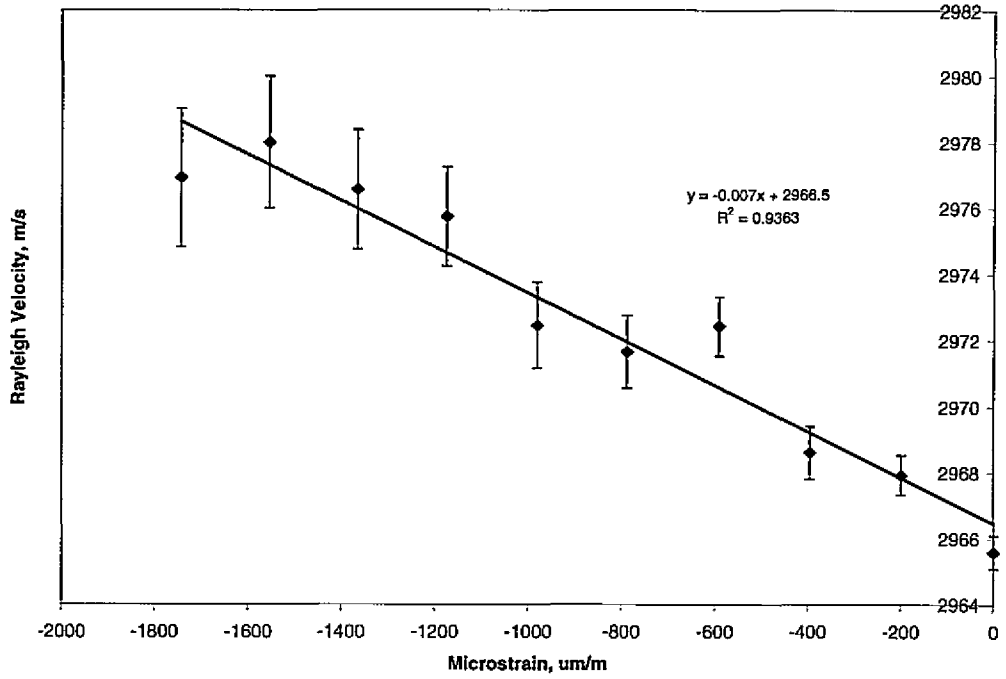

Figure 5-59: Rayleigh wave velocity dependence on the compressive strain during a 4-point bend test, in CP4 Titanium (rolling direction in sample's longitudinal direction).

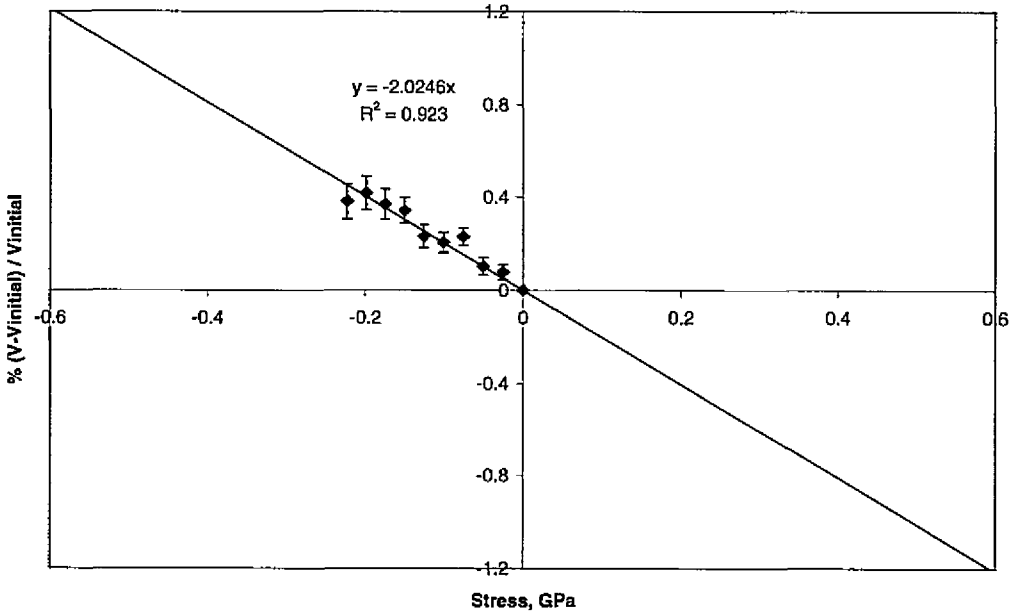

Figure 5-60: Shift in Rayleigh wave velocity and strain, induced in 4-point bend in CP4 Titanium (specimen cut with the longitudinal dimension in the rolling direction; sound propagation in the rolling direction)

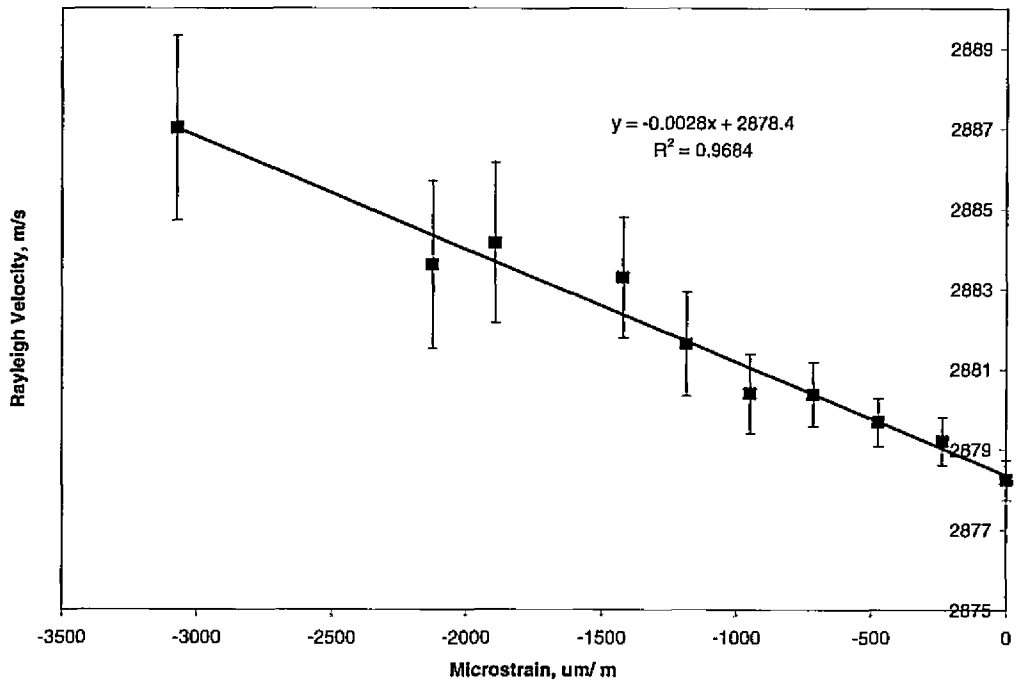

Figure 5-61: Rayleigh wave velocity dependence on the compressive strain in CP4 titanium (transverse direction in sample's longitudinal direction).

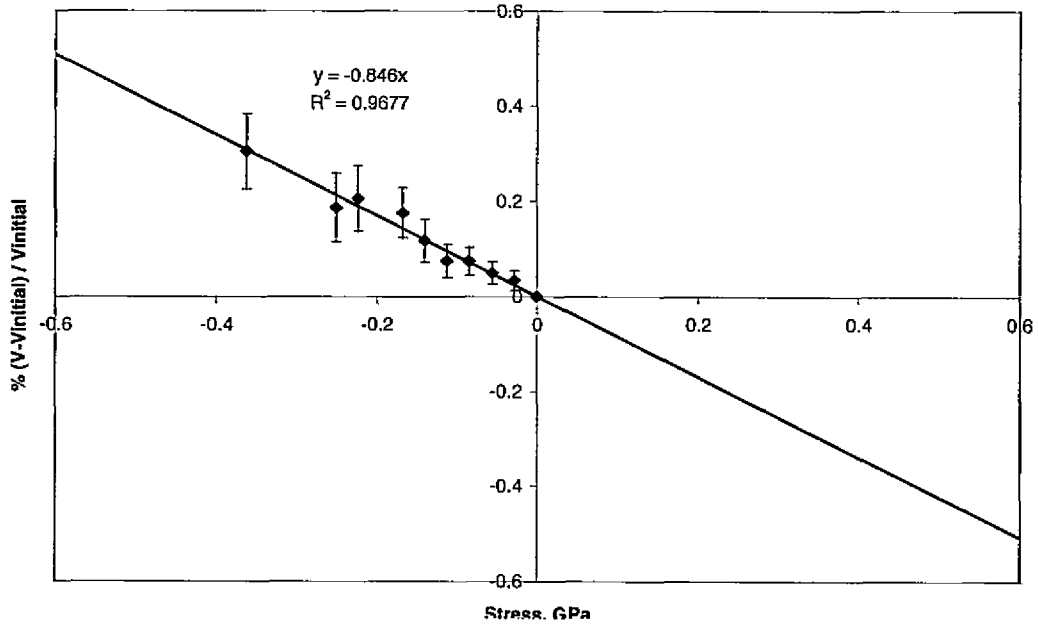

Figure 5-62: Shift in Rayleigh wave velocity and strain, induced in 4-point bend in CP4 Titanium (specimen cut with the longitudinal dimension in the transverse direction; sound propagation in the rolling direction)

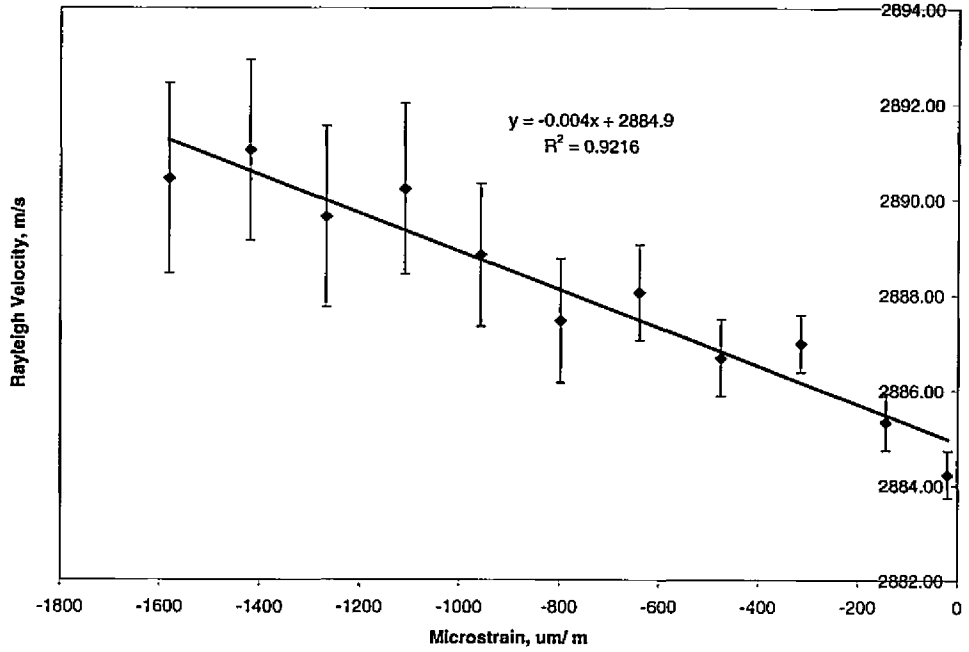

Figure 5-63: Rayleigh wave velocity dependence on the compressive strain in hot-pressed titanium

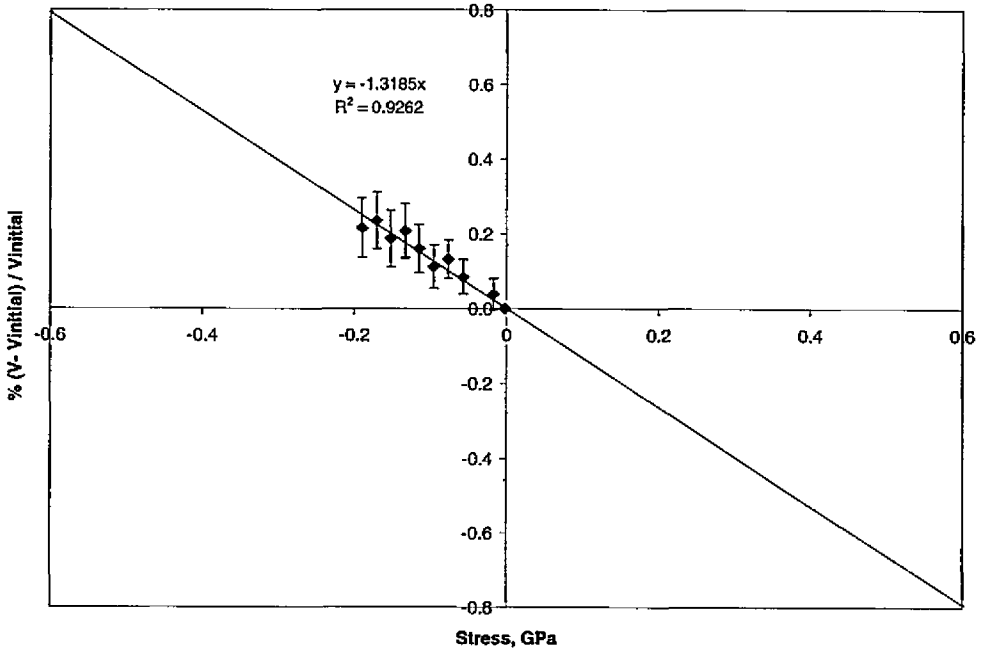

Figure 5-64: Shift in Rayleigh wave velocity and strain, induced in 4-point bend in hot-pressed Titanium (sound propagation in the rolling direction)

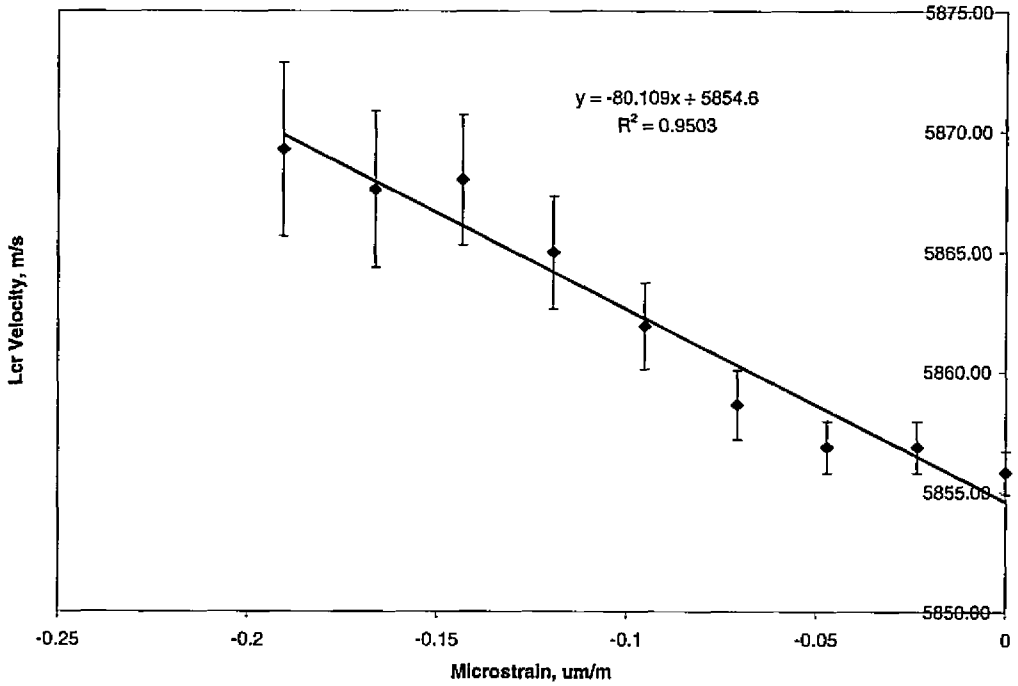

Figure 5-65: L_{cr} wave velocity dependence on the compressive strain in hot-pressed titanium (L_{cr} wave generated with a spherical transducer).

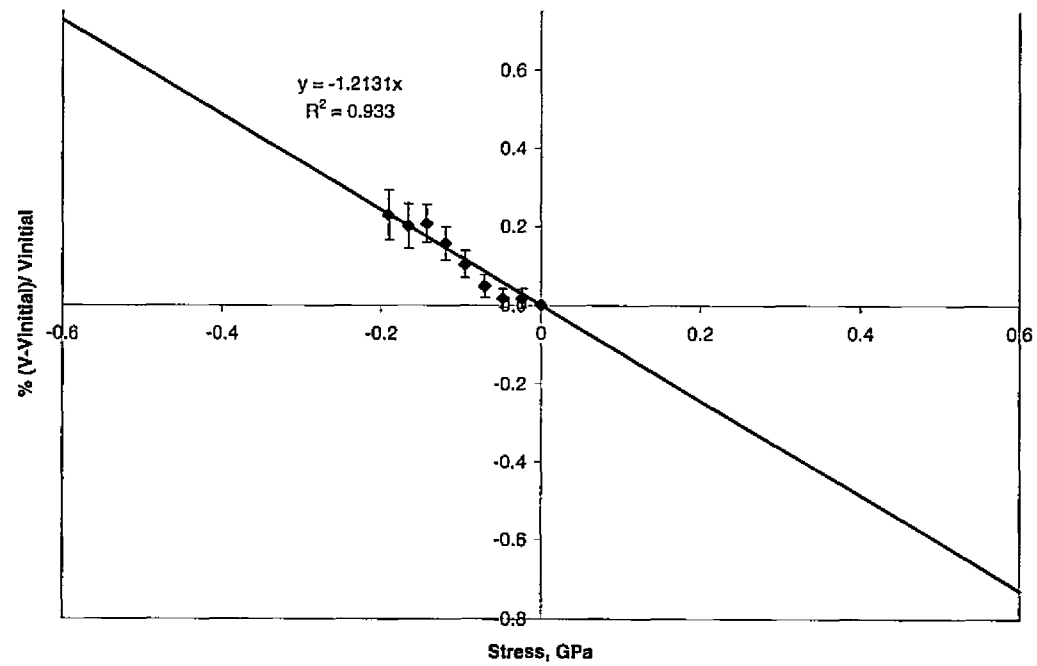

Figure 5-66: Shift in L_{cr} wave velocity and strain, induced in 4-point bend in hot-pressed titanium (sound generated with spherical transducer).

The resulting Acoustoelastic Coefficients are summarized in Table 5-16. The value for the rolling direction via the Rayleigh wave is ~2.4 times higher than the transverse direction, as previously reported by Schneider (2001), (rolled steel) and Tanala et al (1995), (rolled aluminum alloy).

The L_{cr} Acoustoelastic Coefficient was measured with the long sample side in the transverse direction. The bulk-longitudinal, and critical-longitudinal-surface (L_{cr}), waves are the most sensitive to the residual stress so their Acoustoelastic Coefficients should be higher. This was not the case in the present experiments and may be because of the different types of foci of the Rw and Lcr transducers; i.e. line (cylindrical) and point (spherical). The Rayleigh wave transducer has a line-focus and was positioned so the Rw wave propagated in the plate's longitudinal direction. Thus, during bending, this wave experiences compression and little tension from transverse direction (the Poisson Effect). The L_{cr} wave, on the other hand, with its point focus, propagates 360° from the injection point on the sample's surface so detects both the Poisson Effect, compression in the surface's longitudinal direction, and tension in the transverse direction. The latter explains the lower value of the L_{cr} Acoustoelastic Coefficient.

Table 5-16: Acoustoelastic Coefficients obtained with Rayleigh Waves propagating in the sample longitudinal direction and the spherically focused Lcr waves .

Material (Treatment Direction)	Rayleigh Wave Acoustoelastic Coefficient, %/GPa	Lcr Wave Acoustoelastic Coefficient, %/GPa
CP4 Titanium, (Rolling Direction)	**-2.02 ± 0.14**	
CP4 Titanium, (Transverse Direction	**-0.85 ±0.06**	**-1.21 +/- 0.06**
Hot Pressed Titanium	**-1.32 ± 0.07**	

5.3.3 The Machining of the Surfaces of Titanium

To introduce residual stresses into the surface, Ti samples were face-milled at varying feed rates but constant speed and depth-of-cut. The surfaces of the rolled titanium had roughness (R_a) values; 0.48 ± 0.05, 0.97 ± 0.11, and 1.4 ± 0.07 μm. The hot-pressed titanium had Ra values: 0.97 ± 0.08, 1.46 ± 0.09, and 2.03 ± 0.09 μm. Three rolled samples were machined as follows: the as-received and the 'D' CP4 sample so machining lines are ~ parallel to the rolling direction; the 'B' sample such that the lines run ~ parallel to the transverse direction. Optical micrographs and surface topography plots of these surfaces are shown in Figures 5-67 and 5-68

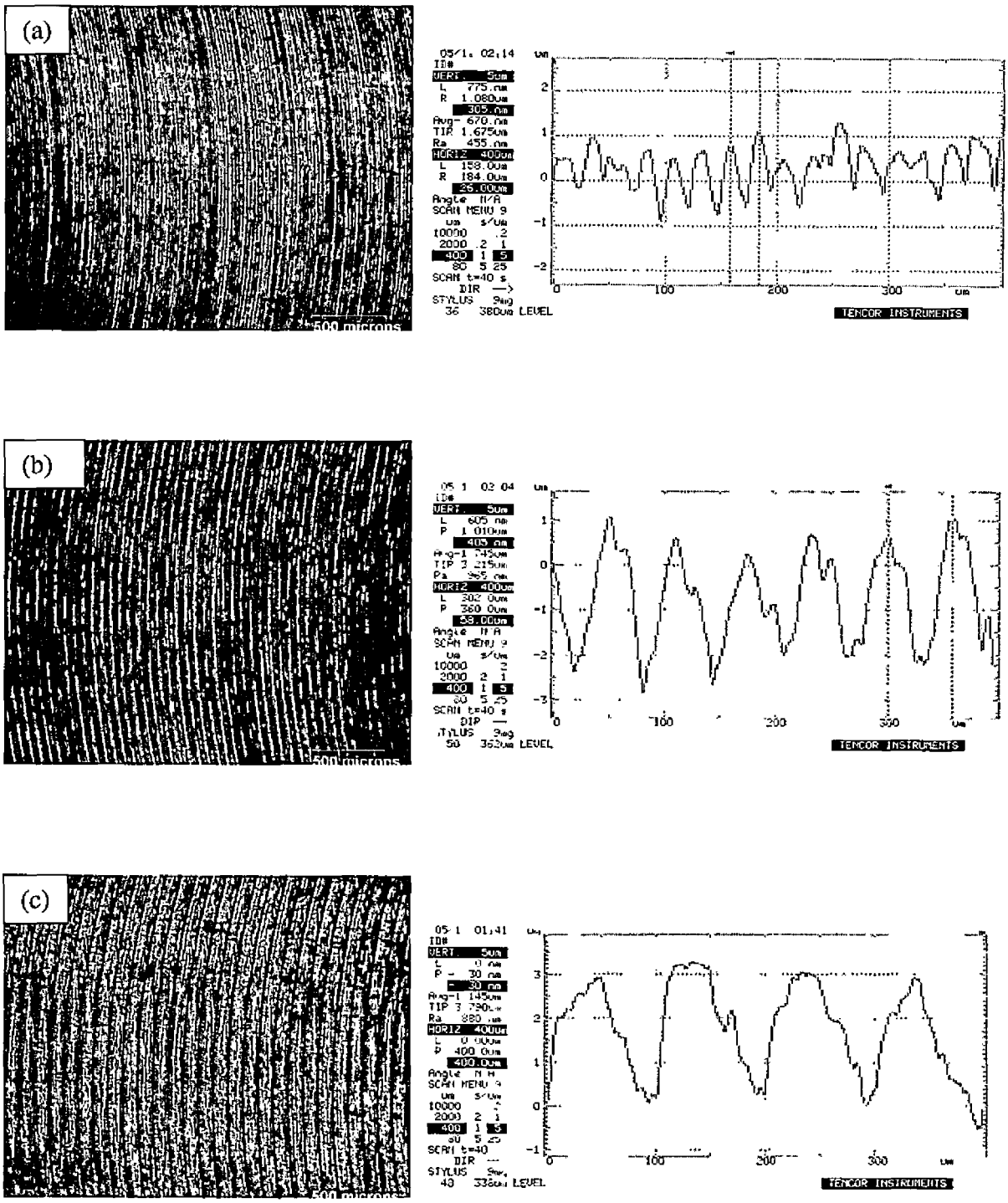

Figure 5-67: Optical photographs of the machined CP4 Titanium surfaces with the corresponding surface profiles obtained via Alpha Step; (a) Ra = 0.48μm, (b) Ra = 0.97μm, (c) Ra = 1.4μm.

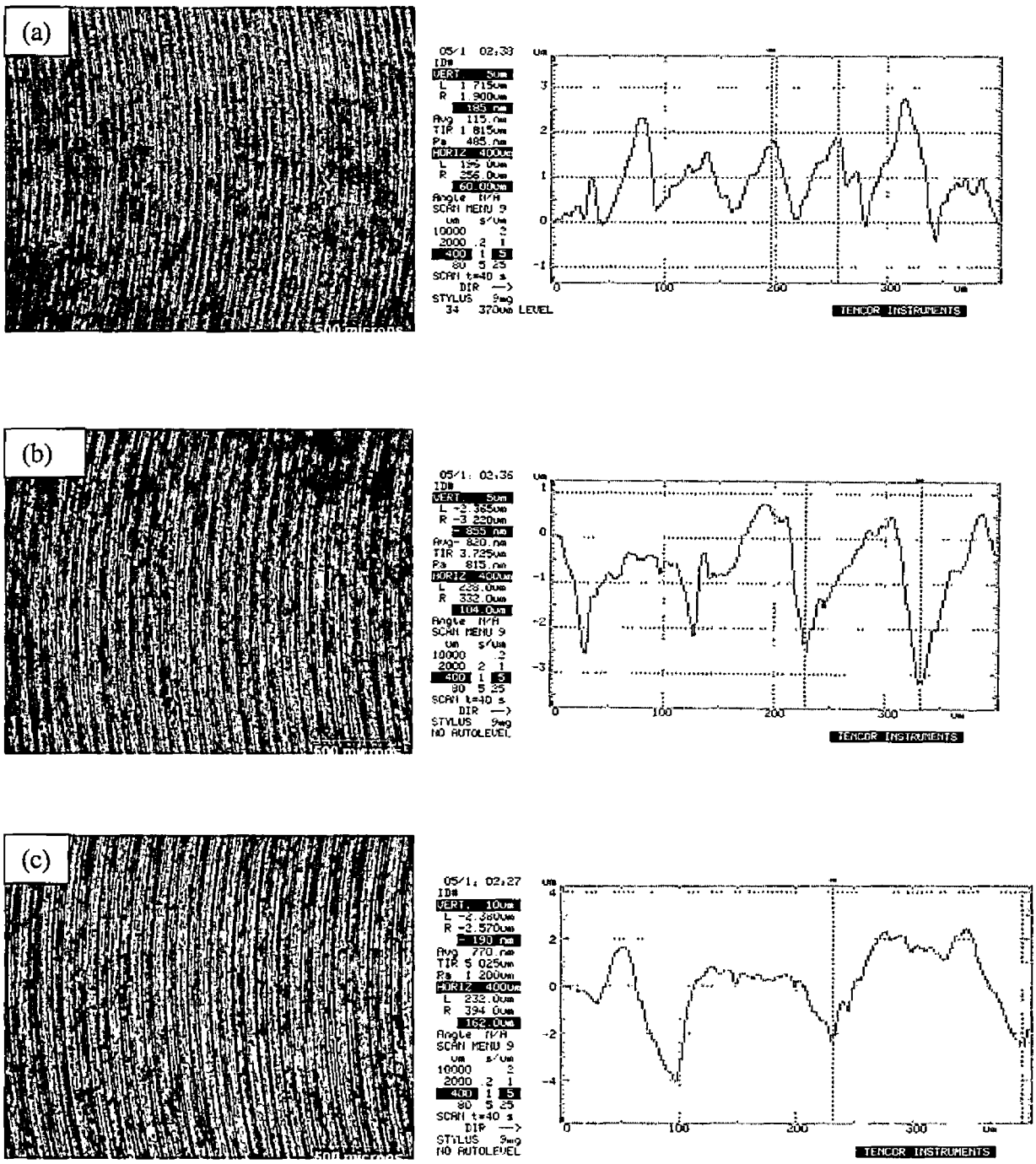

Figure 5-68: Optical photographs of the hot-pressed Titanium surfaces with the corresponding surface profiles obtained via Alpha Step; (a) Ra = 0.97μm, (b) Ra = 1.46μm, (c) Ra = 2.03μm.

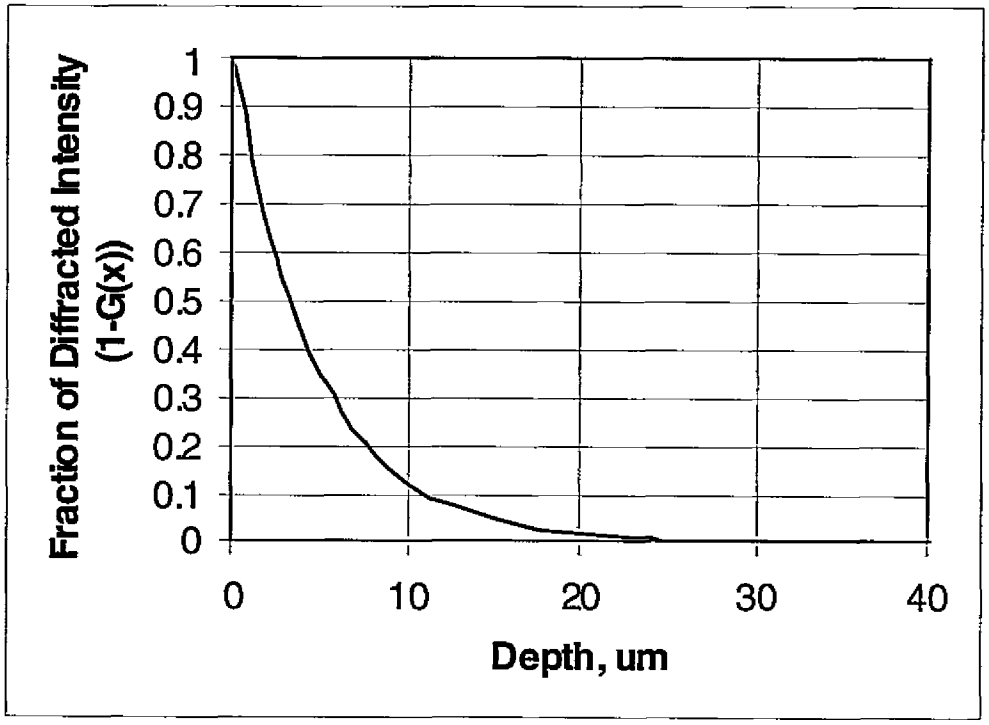

Figure 5-69: Effective penetration depth of Cu radiation into titanium

5.3.4 X-ray-determination of Residual Stresses in Titanium

The residual stresses in the machined rolled-, and hot-pressed,- Ti, were measured by X-ray diffraction from machined and smooth surfaces. Copper radiation was used with K_α $\lambda = 1.5418$A. Figure 5-69 shows the X-ray penetration depth into titanium as calculated via:

$$G_x = \left[1 - e^{-\mu x(1+1/\sin\beta)}\right] \quad (70)$$

where $\beta = 2\theta - 90°$ and μ the (mass absorption coefficient x the titanium density). Clearly ~80% of the X-rays are diffracted within a layer 8μm thick and no radiation penetrates > 25μm. Thus stress information by this method is an average value over a 8

μm deep layer. Stresses were measured in the machined locations, transverse to the grooves using an aperture- size 1 mm x 5 mm. Measurements were conducted on high-angle (213) plane with d-spacing ~0.821 Å at $2\theta = 140°$.

Stresses in the Ti plates were measured before and after stress-relief and the values are plotted versus R_a in Figures 5-70 and 5-71. The rolled sample contains a large compressive stress within its smooth surface (250 MPa) due to sample preparation (grinding and polishing). The hot-pressed sample, although ground and polished the same way as the rolled plates, had a low value of tensile residual stress within its smooth surface. These values indicate the stress in a shallow surface layer. An example of the stress profile developed on grinding, hardened-steel is shown in Figure 5-72 (Hilley, 1971).

The stresses measured were compressive in both Ti samples, highest values being associated with the finest surface finish (lowest feed rate). The compressive stresses were relieved completely by annealing, and some tensile strain left. The stress was measured in the rolled sample after annealing parallel and perpendicular to the machining lines. Values were very close considering the error bars.

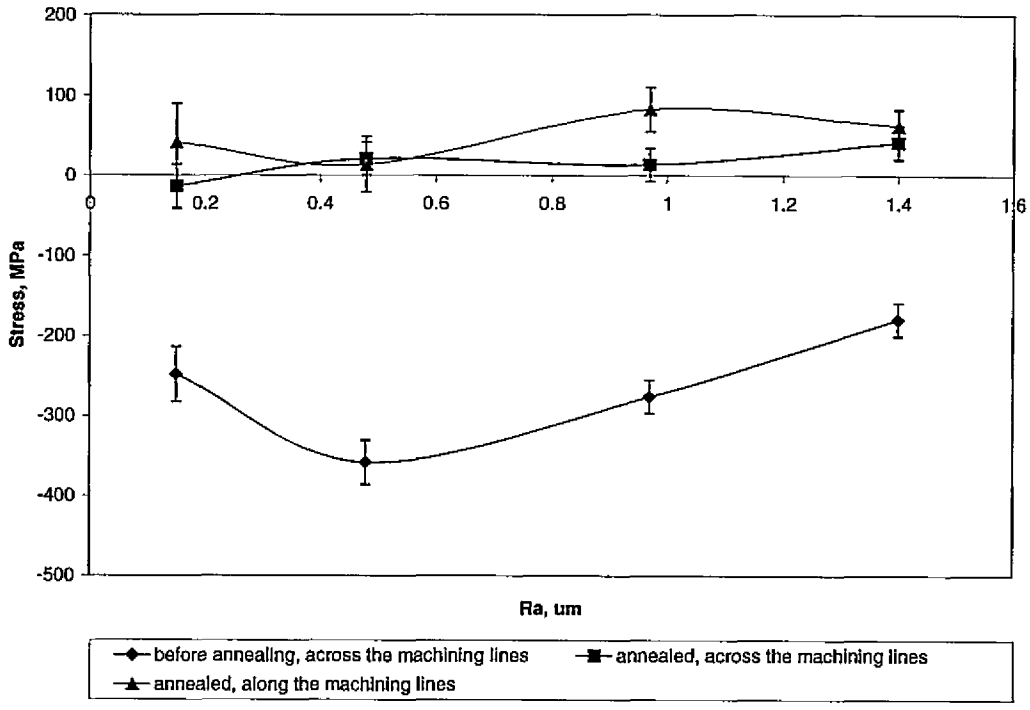

Figure 5-70: X-ray determined stresses in as-received CP4 Titanium, before and after stress-relief

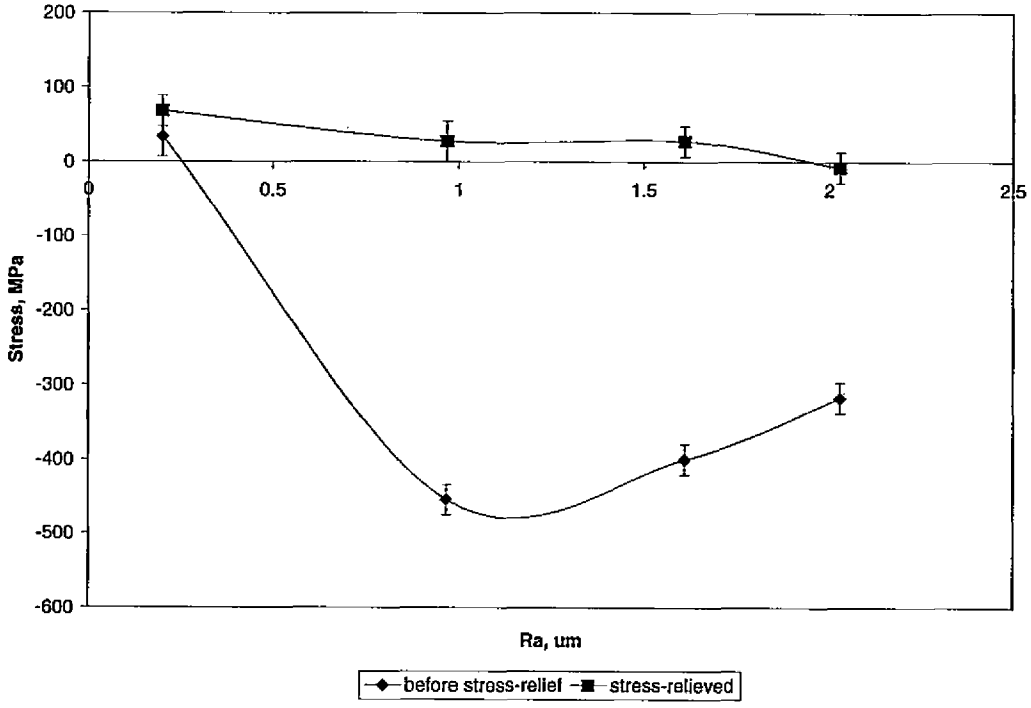

Figure 5-71: X-ray determined stresses in hot-pressed CP Titanium, before and after stress-relief

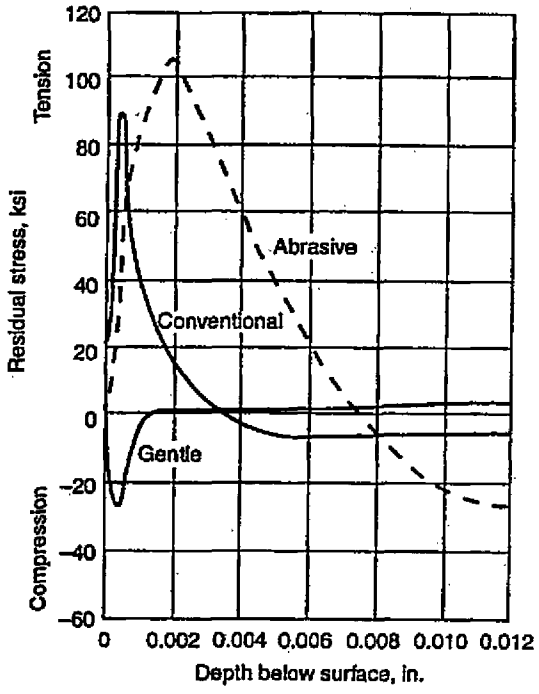

Figure 5-72: Subsurface residual stress distribution after grinding hardened steel (Hilley et al, 1971)

5.3.5 Ultrasonic Examination of the Surfaces of Rolled and Hot-Pressed Titanium Plates with Rayleigh Waves

The R_w wave (15-20 MHz) and L_{cr} wave (10-12 MHz) velocities were measured before and after stress relief at each location on the titanium samples. After alignment to produce optimum surface and specular signals, the transducers were fixed permanently. Care was taken to position the samples at the same transducer location each time. A reference, stress-free, Zeodar-glass was used to correct for temperature change.

The stress gradient was examined over a range of frequencies thus, depth into the specimen. Annealed specimens are supposed to provide information on the effect of exclusively grain scattering (polished surface) and combined grain scattering and surface-roughness (machined, annealed surfaces).

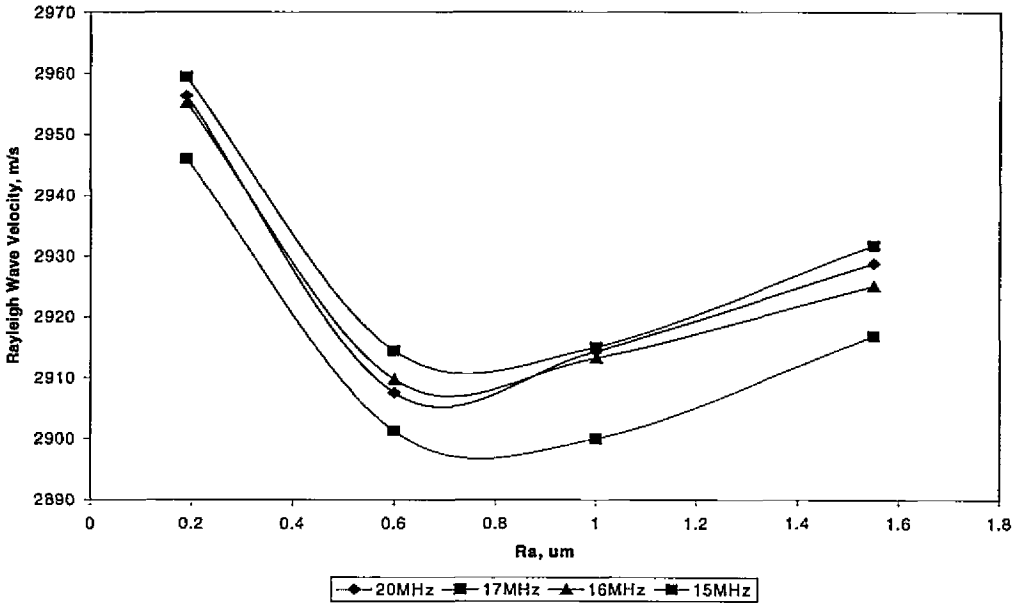

Figure 5-73: Rayleigh wave velocities measured in stress-relieved CP4 Ti (measurements along the rolling direction. Avg. Error = 0.9 m/s)

Literature reports the surface wave velocity decreases with increasing frequency for both these conditions (Pecorari (2000), Ruiz et al (2002), Tardy et al (1996)). This was not observed. To illustrate this problem Figure 5-73 shows the Rayleigh wave velocities measured in stress-relieved CP4, 27μm grain-size plate. The 15MHz (lowest frequency) Rw sound traveled at the lowest velocity. Closer examination of the sound signals, showed the output frequency (surface-wave-signal-frequency) was lower than the input-frequency (specular signal frequency). The output frequency from 15 16, 17, and 20 MHz input, ranged between 15 and 17 MHz, depending on the surface. As the output frequencies overlapped and changed, no specific information could be extracted from frequency dependence. However, it is concluded that, when working with titanium, useful frequency is limited to 15 MHz for a given travel length (≥ 1.2 mm). Further

frequency increase results in output values close to those for 15MHz. Thus, figures from this point on, only contain the 15 MHz information.

The Rw velocities measured before and after stress-relief of the as-received titanium plate (15 μm grain size), Plate 'B' (27 μm grain size), Plate 'D' (45 μm grain size) and hot-pressed plate, are plotted .vs. surface roughness in Figures 5-74 to 5-77. Clearly, velocities in the annealed samples are lower than the unannealed ones. Suggesting relief of compressive stresses. These results compare well with the bulk-velocity measurements listed in Table 5-14. When the results for the three rolled plates are compared, the change of velocity is higher for sample 'B', wherein measurements were taken in the rolling direction even though the same level of stress is expected in all three plates. This observation agrees with the Acoustoelastic Constant values, (measured earlier), i.e. higher in the rolling direction.

As the surface roughness increases from smooth to machined, the sonic velocity significantly decreases. However, with further increase of surface roughness, phenomena other than dispersion therefrom play a role and the sonic velocity value levels or slightly increases. This observation will be discussed later.

Grain size changes these plots. In the hot-pressed plate, (R_a =2.03 μm) the velocity increases significantly. This observation implies a limiting value of the (Ra/sound-

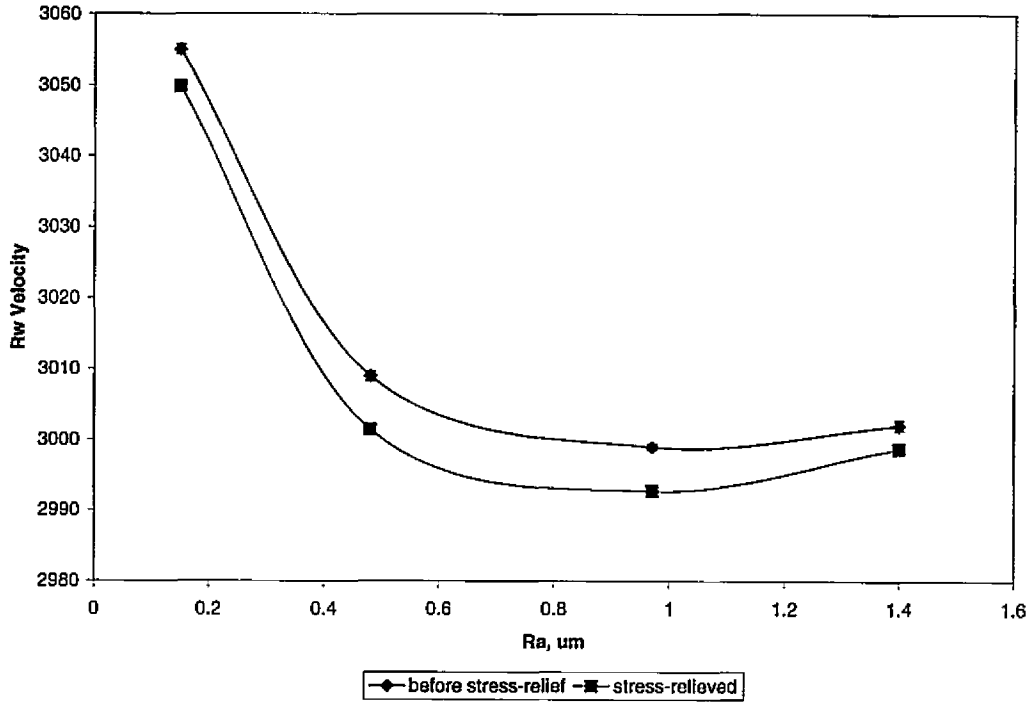

Figure 5-74: A comparison of R_w velocity measured at 15 MHz in as-received Ti, before and after stress-relief (measurements in the transverse direction, Avg. Error on velocity = 0.9 m/s).

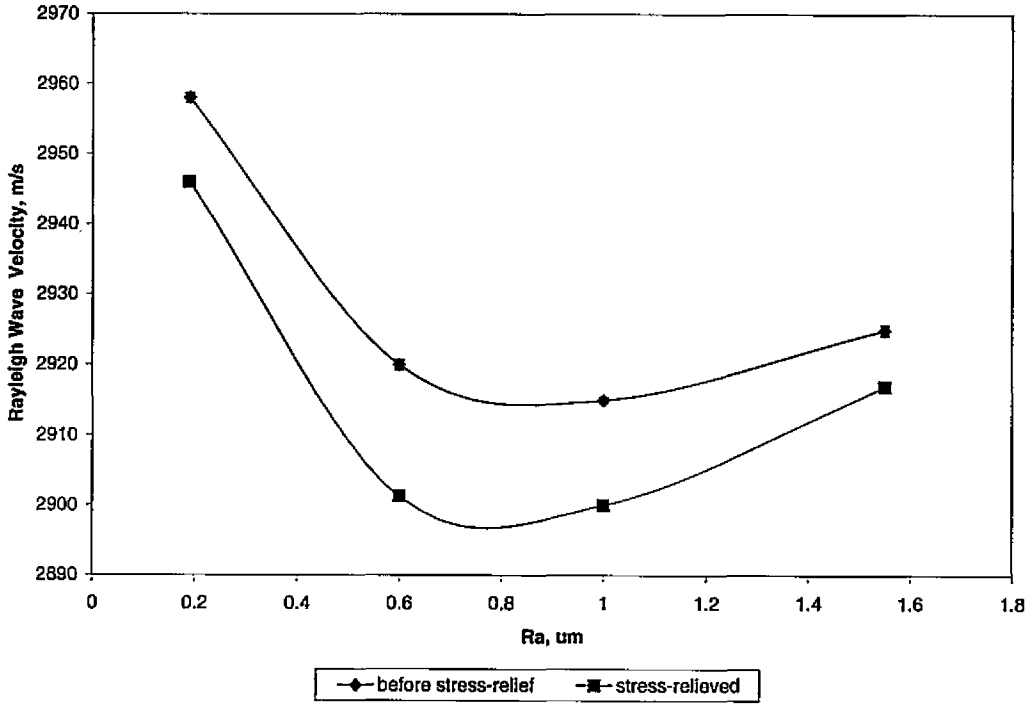

Figure 5-75: A comparison of R_w velocity measured at 15 MHz, before and after stress-relief in the Ti plate B (27μm grains, measurements along the rolling direction, Avg. Error = 0.8 m/s).

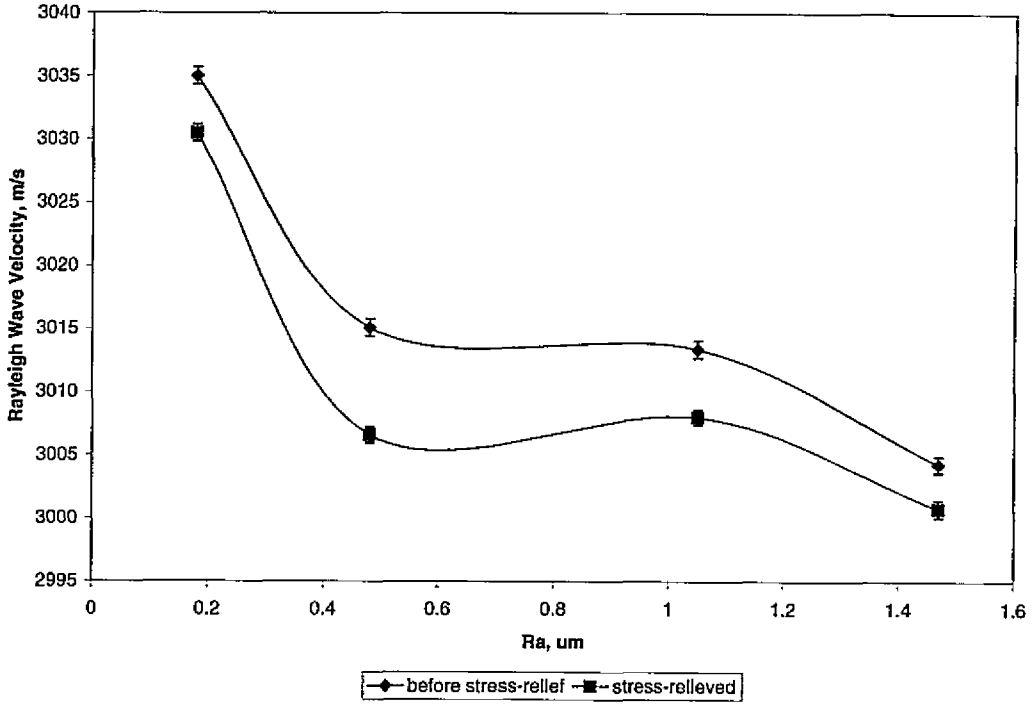

Figure 5-76: A comparison of R_w velocity measured at 15 MHz, before and after stress-relief in the Ti plate D (45 μm grains, measurements along the transverse direction, Avg. Error = 0.9 m/s).

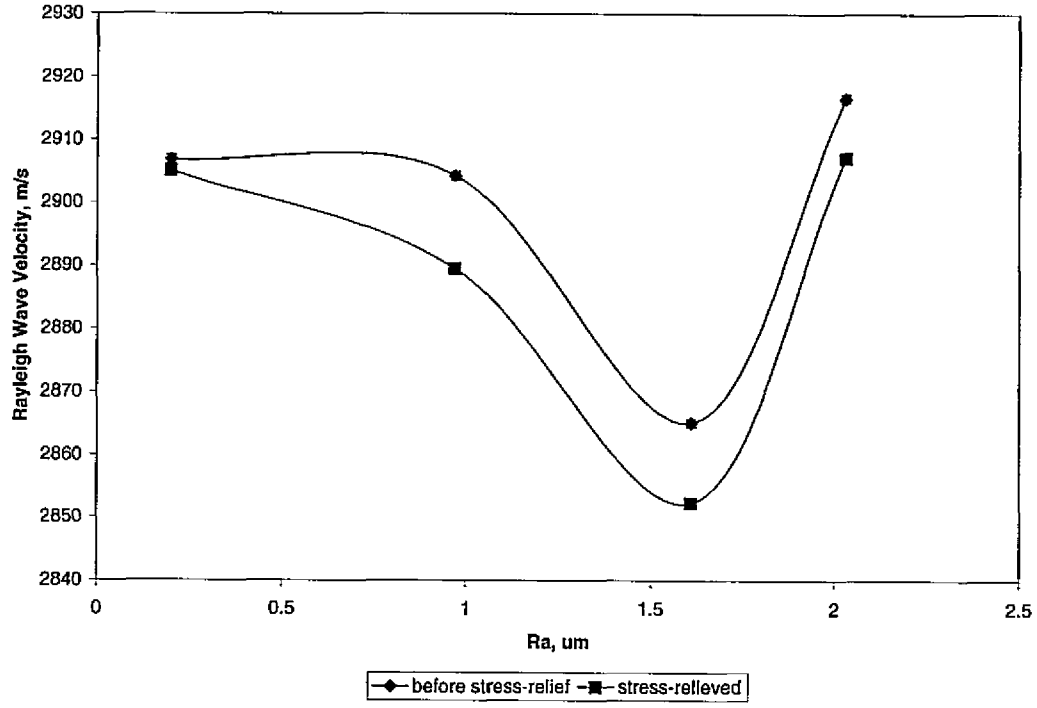

Figure 5-77: A comparison of R_w velocity measured at 15 MHz, before and after stress-relief in the hot-pressed-CP4-Titanium (Avg. Error = 0.8 m/s)

wavelength) ratio, above which decreasing velocity with increasing surface roughness no longer exists (~ 0.85% in this case). Possible reasons for this will be discussed later. The decrease of Rw velocity with surface roughness agrees with observations for glass and glass ceramic.

The percentage change of velocity upon annealing was calculated and converted to stress using the Acoustoelastic Constants (Table 5-16). The results are plotted in Figures 5-78 to 5-80. Graphs for the as-received and hot-pressed plates include the X-ray-determined relieved-stress. The ultrasonic results agree well with the X-ray data but values are lower. This may be because ultrasonic waves examine a greater depth than X-rays (~ 250 μm versus ~ 8 μm) and consequently are subject to a different average stress (a stress gradient from the surface is expected.)

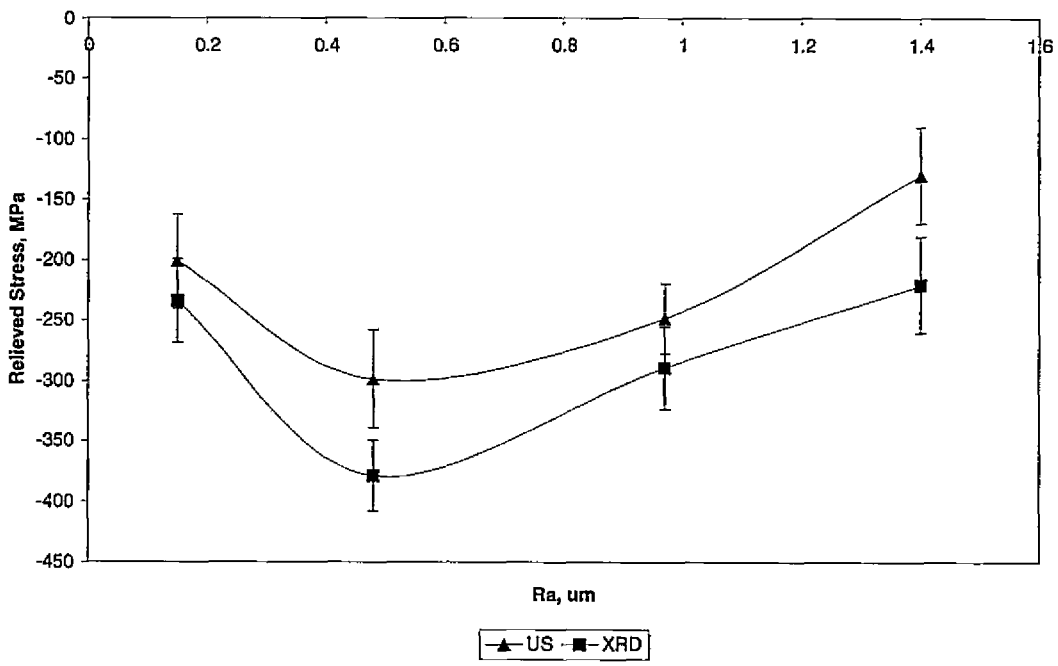

Figure 5-78: Comparison of XRD and ultrasonically (US) determined relieved stress in as-received Ti (measurements along the transverse direction)

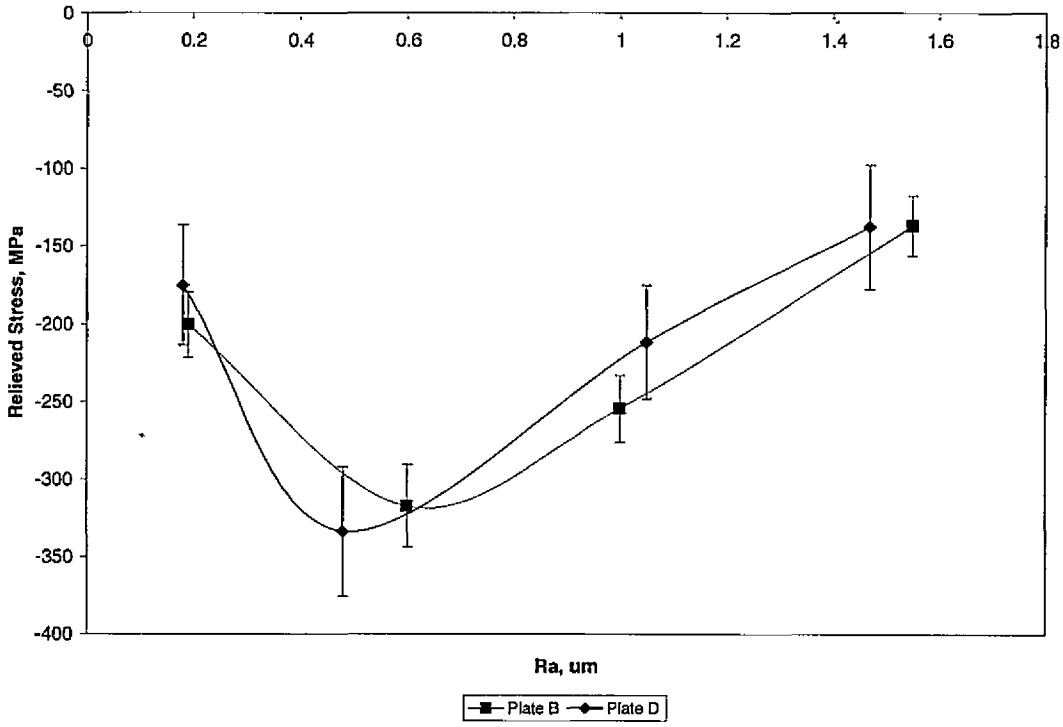

Figure 5-79: Ultrasonically-determined stress in titanium: plate B (measurements along the rolling direction), plate D (measurements along the transversal direction)

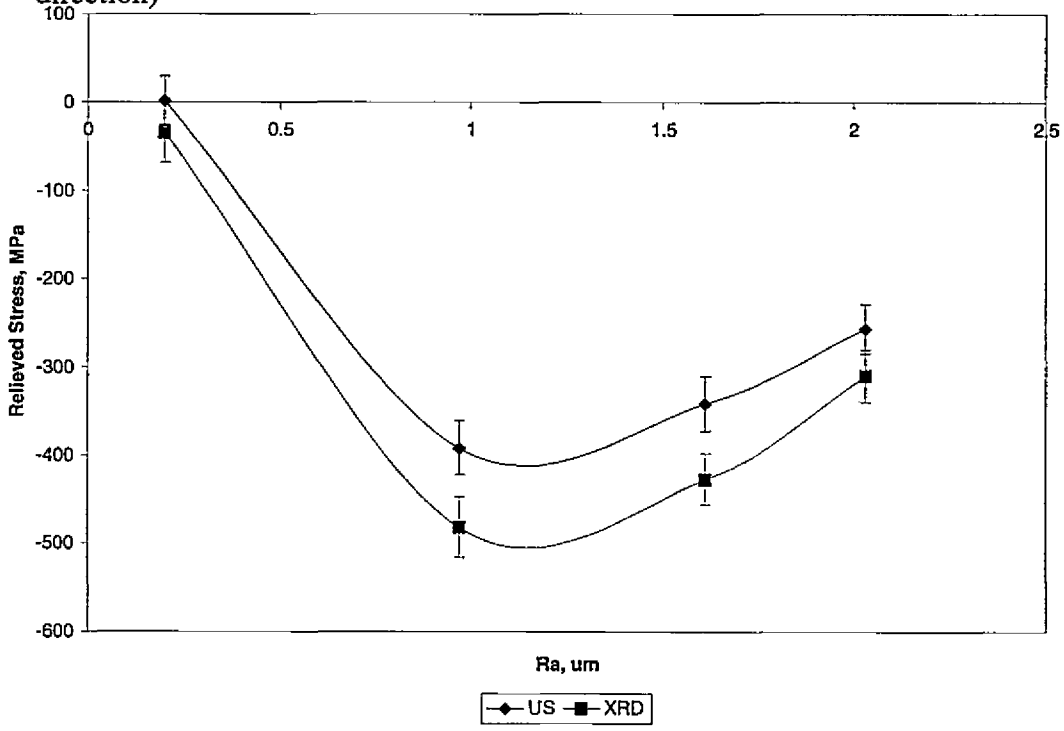

Figure 5-80: Comparison of XRD and ultrasonically (US, 15MHz) determined relieved stress in hot-pressed Ti

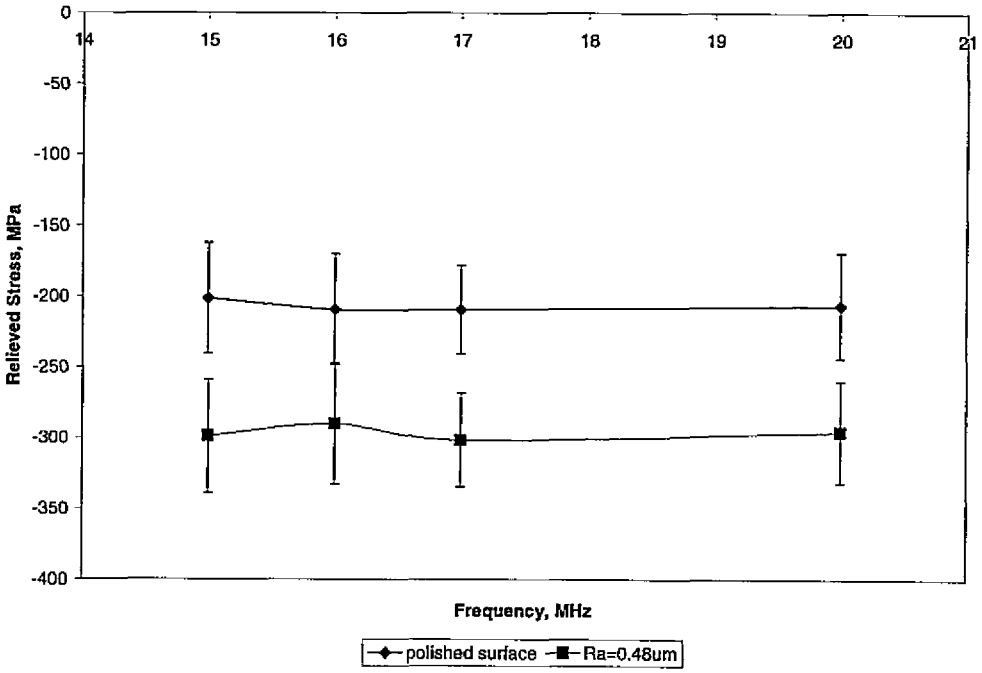

Figure 5-81: Relieved residual stress measured with different frequencies in rolled Ti

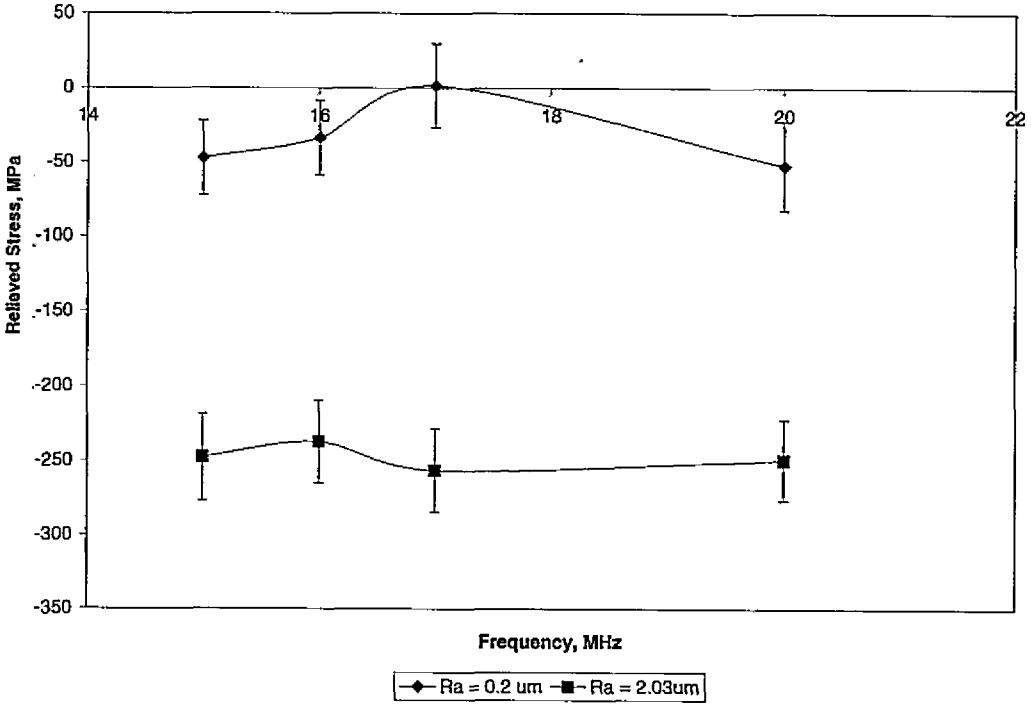

Figure 5-82: Relieved residual Stress measured with different frequencies in the hot-pressed titanium.

Different input frequencies of ultrasound gave the same residual stress values, (within error limits). Figures 5-81 and 5-82 show this for the as-received and hot-pressed Ti. This must be the result of the output frequencies being ~ equal (see earlier).

The Rw velocities were measured and compared along annealed, rolled-titanium specimens of differing grain size. Figure 5-83 shows the results in the rolling direction and Figure 5-84, the transverse direction. Behavior similar to that of bulk waves was found. This even though plots of grain-size are measured in the plates' cross-sections and Rw velocity values along the plates' surfaces. Surface-wave velocity also decreased with grain-size. The velocity of a Rayleigh wave in JRQ steel was identified as influenced by grain-size by Pecorari et al (2000).

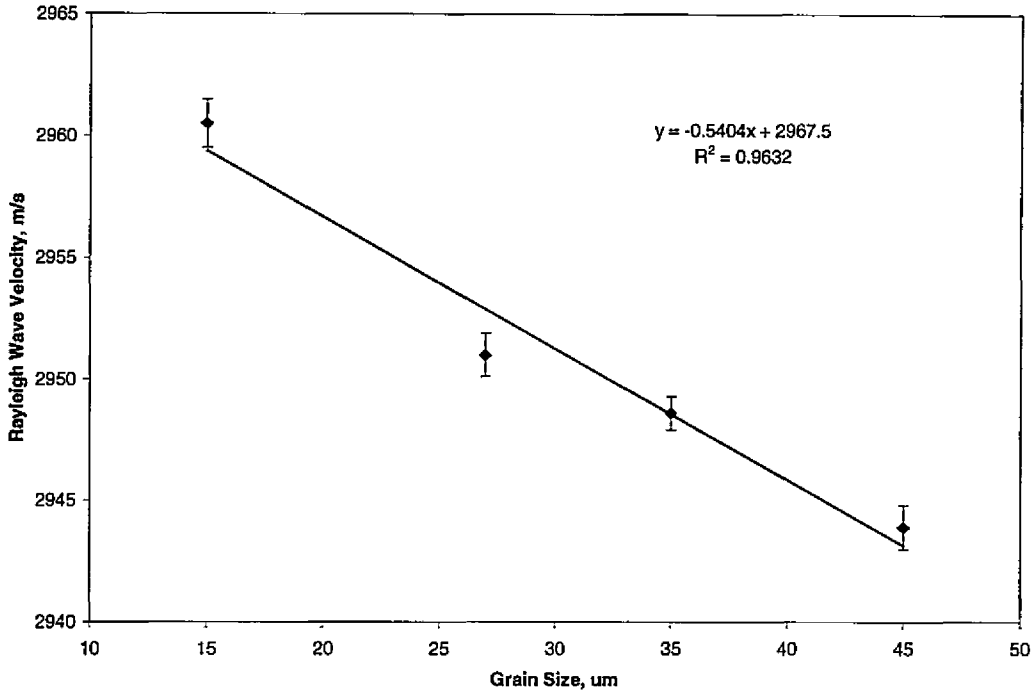

Figure 5-83: Rayleigh Wave Velocity dependence on grain size; rolling direction.

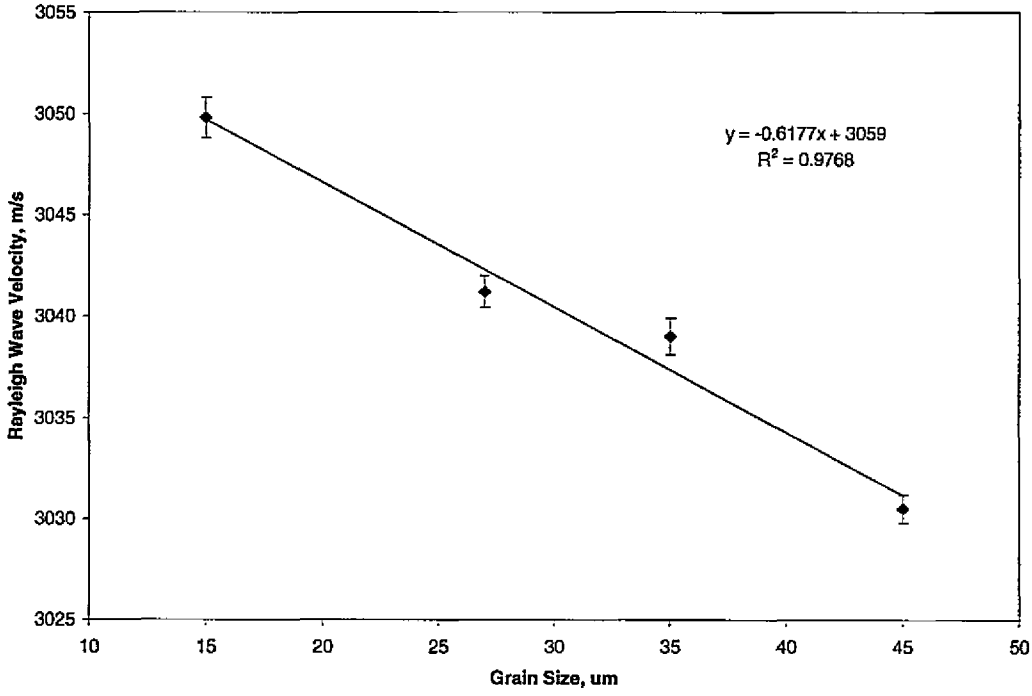

Figure 5-84: Rayleigh Wave Velocity dependence on grain size; transverse direction.

5.3.6 Lcr Examination of Titanium Plates

L_{cr} velocities were measured on cold-rolled, and hot-pressed- titanium. Figures 5-85 and 5-87 show the results before and after stress-relief. Clearly, velocities significantly decrease on stress-relief, illustrating the L_{cr} wave's capability to detect compressive stress. Considering the stress-relieved plots, surface roughness has the same effect on L_{cr} (spherical-focus) waves as on R_w (cylindrical focus) waves i.e. velocity decreases with increasing surface roughness, although it does not level at a certain R_a as per the R_w velocity. However, when the Acoustoelastic Constant is used to convert the percentage velocity change to stress, values higher than the yield stress were obtained (570 MPa) (Figures 5-86 and 5-88). A possible reason for this anomaly is an incorrect value of Acoustoelastic Constant. During bending, the sample top surface longitudinal direction is under compression and tension in the transverse direction. The spherical focus transducer monitors both, so the associated Acoustoelastic Constant is significantly lower than if exclusively monitoring compression. The stresses in machined Ti surfaces measured by X-ray diffraction are across the machining lines so the state of stress parallel to the machining lines, is unknown. The average plane stress in the machined surfaces obtained using the low Acoustoelastic Constant was unusually high, suggesting the stress parallel to the machining lines may be compressive. Thus, the Acoustoelastic Constant measured with the Lcr spherical transducer in the bend test is probably invalid.

The 'relieved stress' graphs include predicted plots, calculated from the changes of Lcr-velocity measured and the Acoustoelastic Constant quoted by Maxfield (2003) for the directional wave, (-2.6 %/GPa). The values of stress thus obtained are more

reasonable and closer to those measured with the Rayleigh waves. It is thus concluded that the directional L_{cr} Acoustoelastic Constant can be used to give an estimate of stress when the velocity of sound from the spherically focused L_{cr} wave is measured. However, this may not be the case if the spherically-focused L_{cr}-wave detects highly anisotropic stresses in a surface.

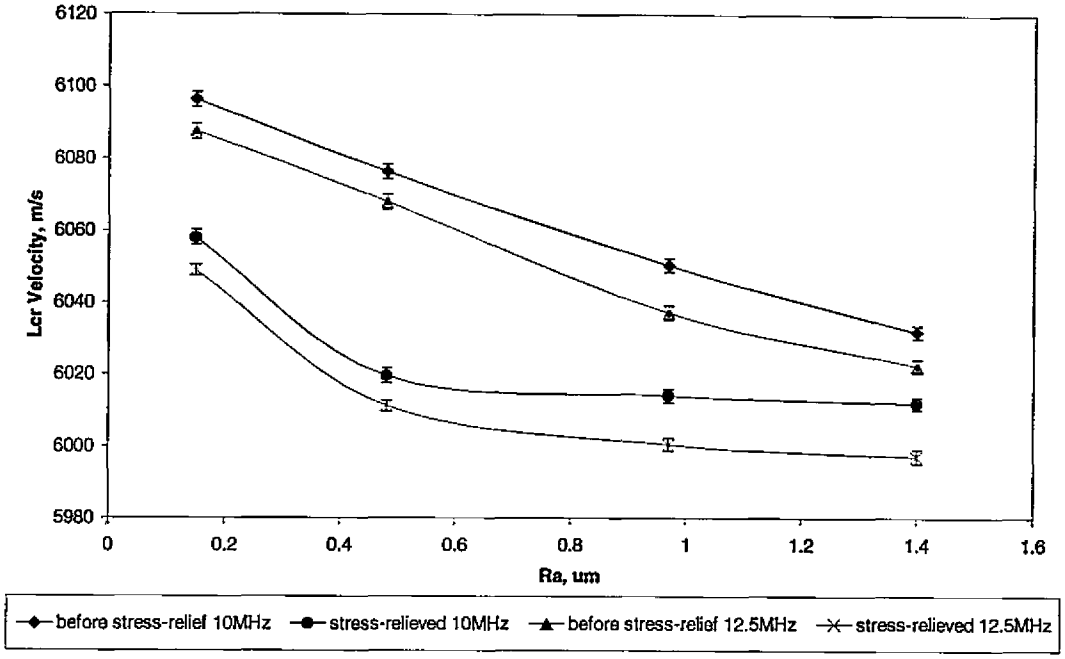

Figure 5-85: L_{cr} velocities in as-received CP4 Titanium, before and after stress relief (spherical transducer).

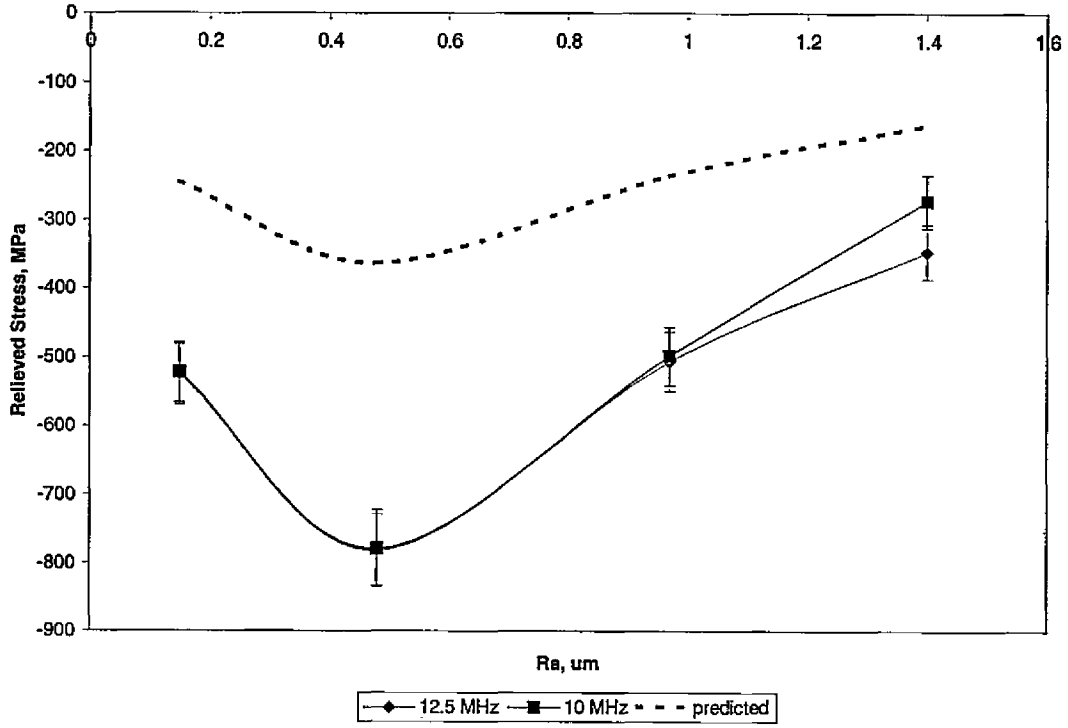

Figure 5-86: Stress relieved in the as-received CP4 Titanium, as determined with L_{cr} waves.

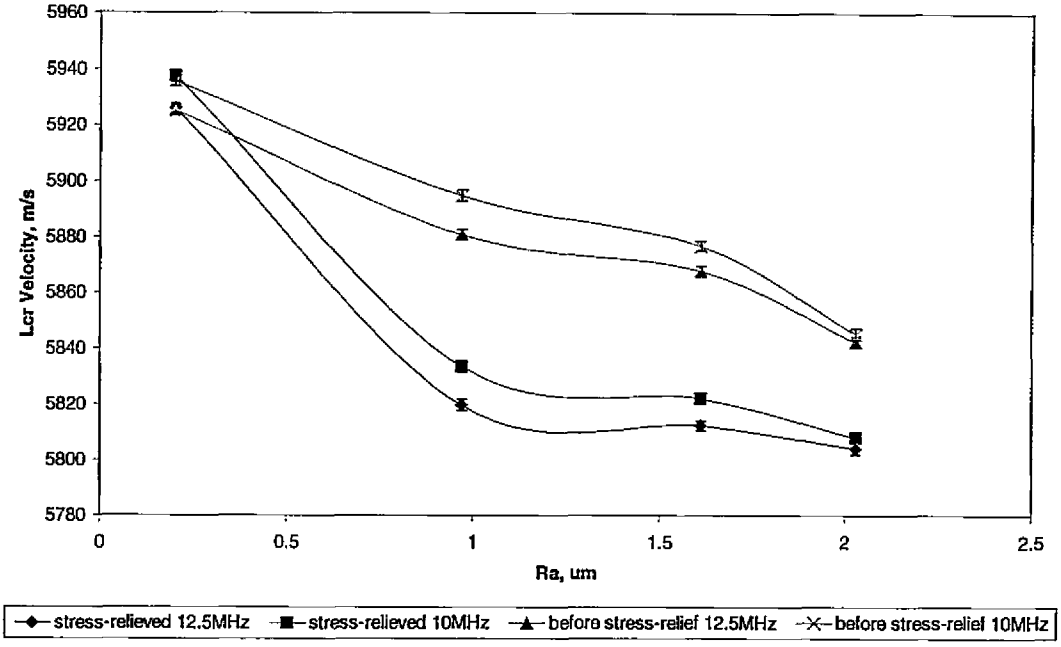

Figure 5-87: L_{cr} velocities in hot-pressed CP Titanium, before and after stress relief (spherical transducer).

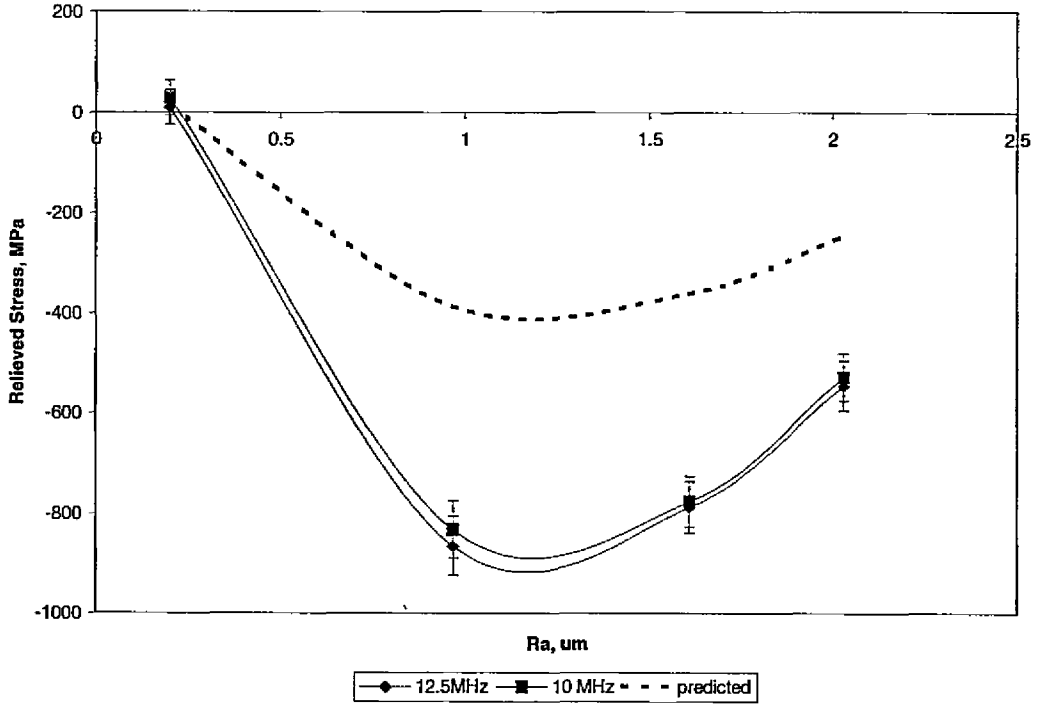

Figure 5-88: Stress relieved in the hot-pressed CP Titanium, as determined with L_{cr} waves.

5.4 Ultrasonic Signatures of Titanium, Corning 9604 glass and Corning 9606 Glass-Ceramic

The complexity of the problem has been systematically built from amorphous isotropic material (Corning 9604) to isotropic but partially crystalline Corning 9606 and eventually textured, polycrystalline titanium. In this section an attempt is made to generalise the results i.e. distinguish the contribution to the change in velocity of grain scattering, texturing and the surface roughness

Figures 5-89, 5-90, and 5-91 are plots of Rw velocity vs. surface roughness R_a vs. frequency, for glass, glass-ceramic and textured titanium (measurements in the transverse direction); a) before stress-relief, and b) after stress-relief. Machining introduced compressive stresses in each case. Interestingly stress-relief by annealing caused plot shift to lower velocities, yet the pre-anneal plot-shape remained illustrating the change of velocity due to stress (maximum observed ~0.52%) is small, relative to the other contributions: surface roughness ($\leq$ 8%), texture ($\leq$ 2.4%), and grain scatter ($\leq$ 0.6%). These values underscore the ease with which results may be misinterpreted unless all sonic-velocity influences are considered. Plots for the stress-annealed specimens (Figures 5-89 b), 5-90 b), 5-91 b)) convey the effect of surface roughness and grain scatter on Rayleigh wave velocity.

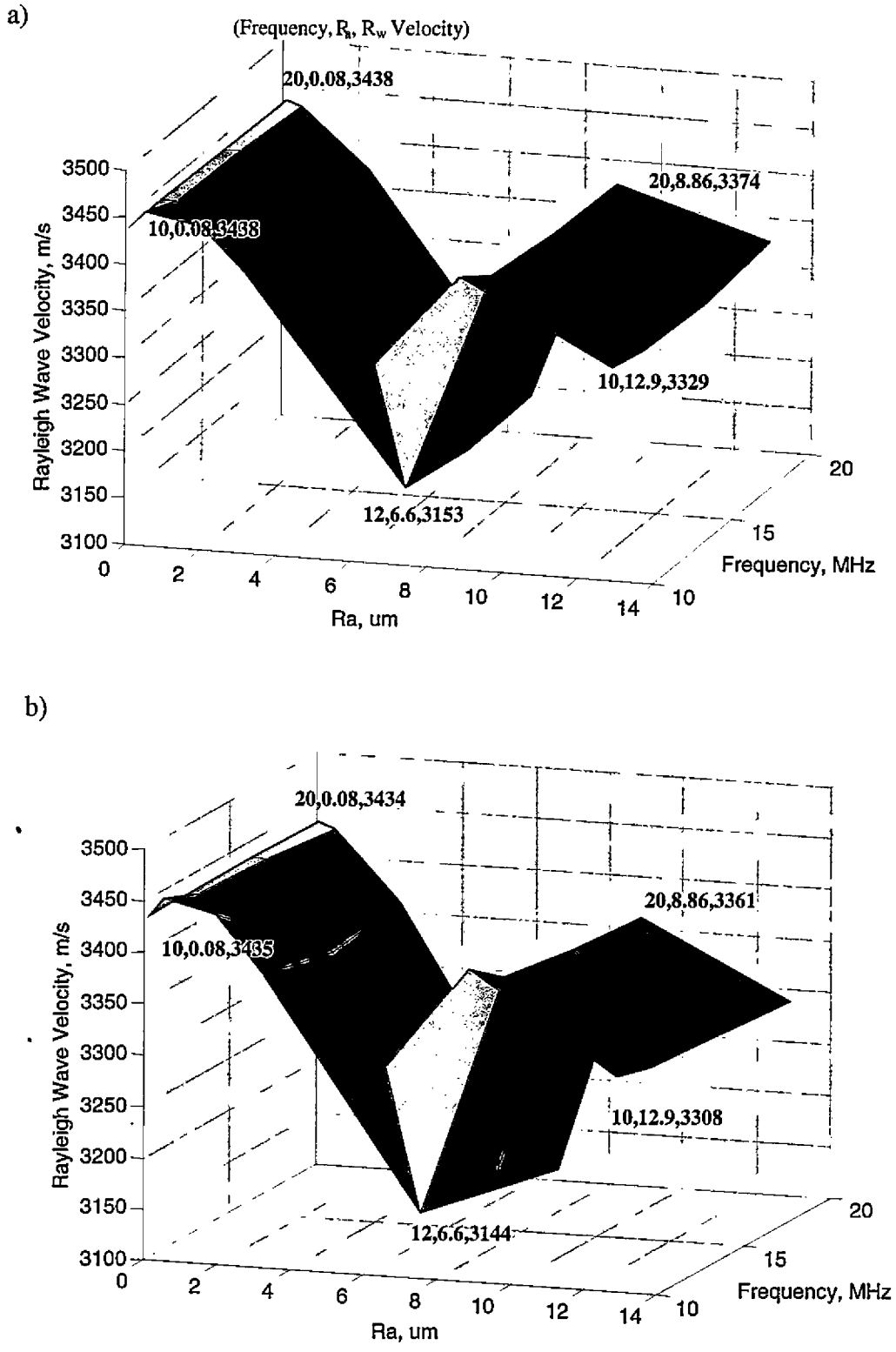

Figure 5-89: Rayleigh wave velocity dependence on surface roughness and frequency in Corning 9604 glass, a) before and b) after stress-relief.

a)

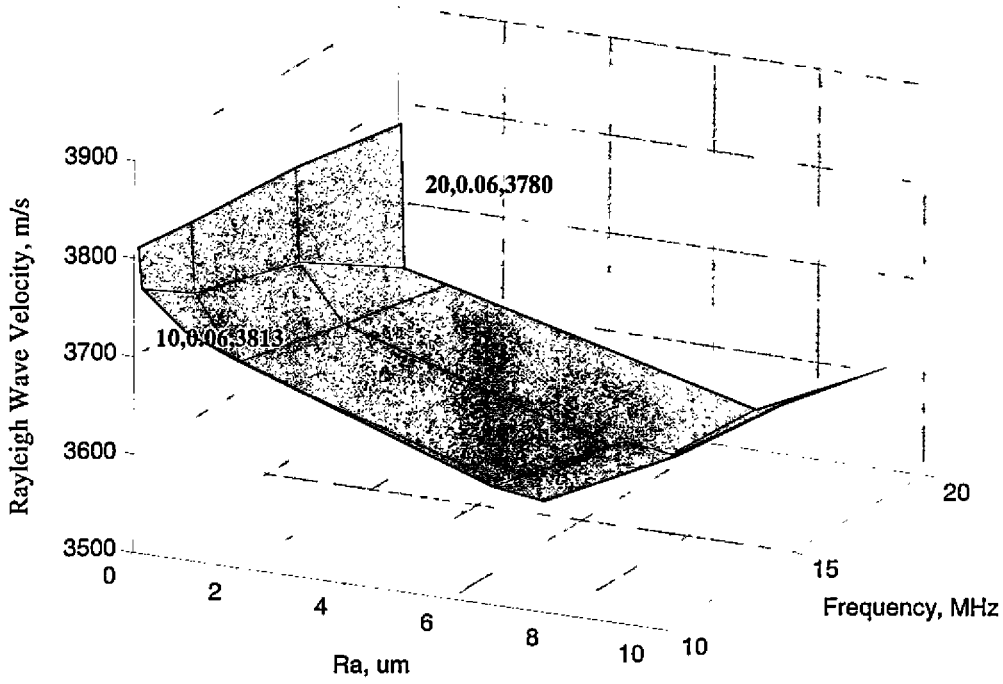

b)

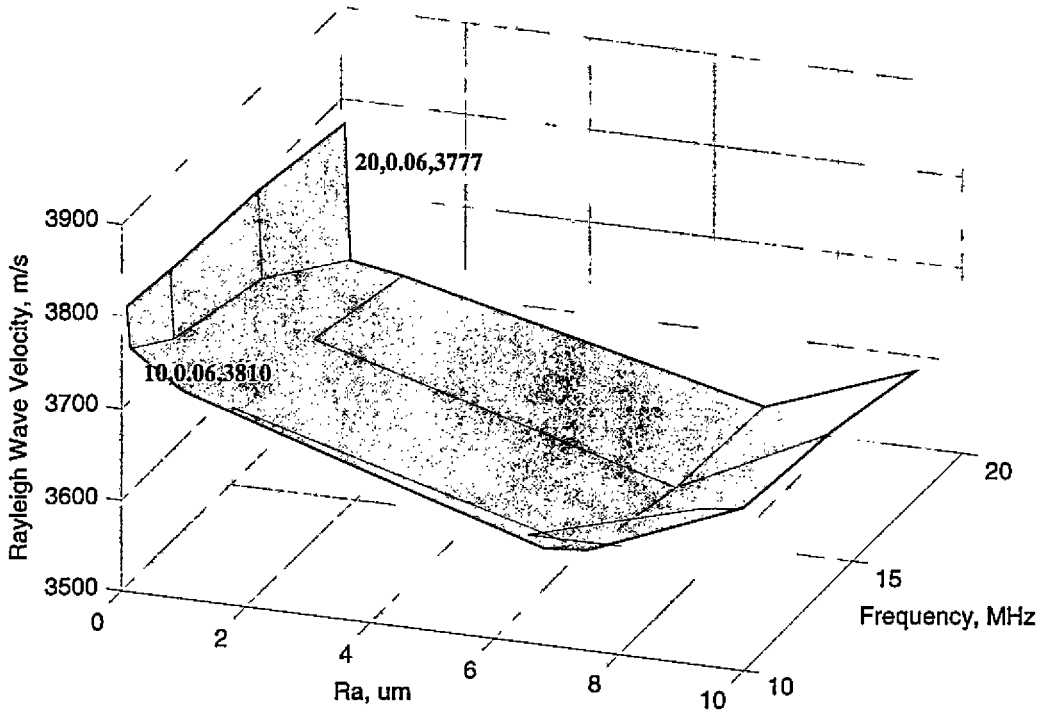

Figure 5-90: Rayleigh wave velocity dependence on surface roughness and frequency Corning 9606 glass-ceramic, a) before and b) after stress-relief.

a)

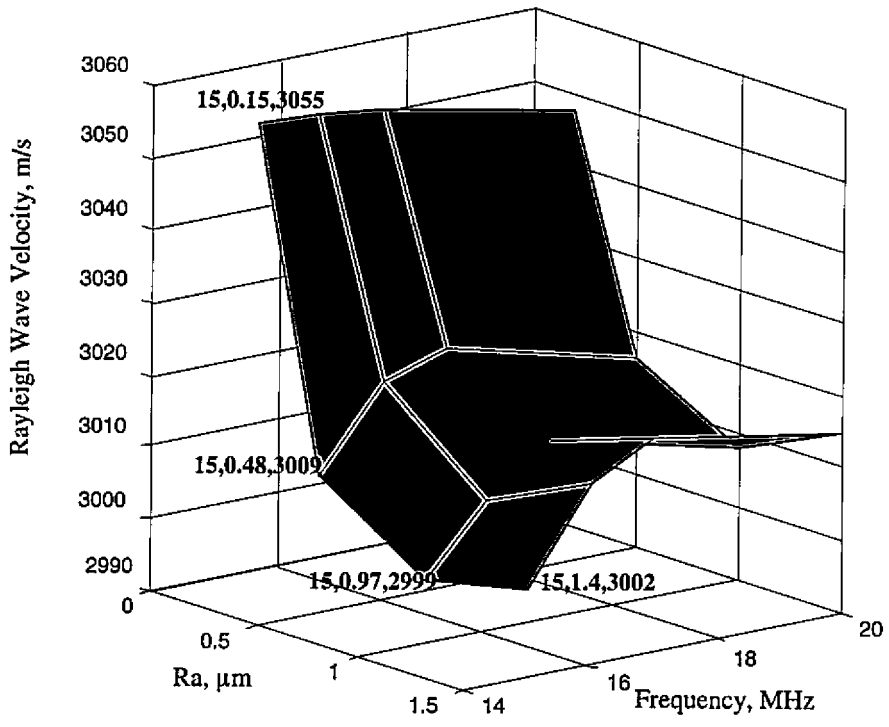

b)

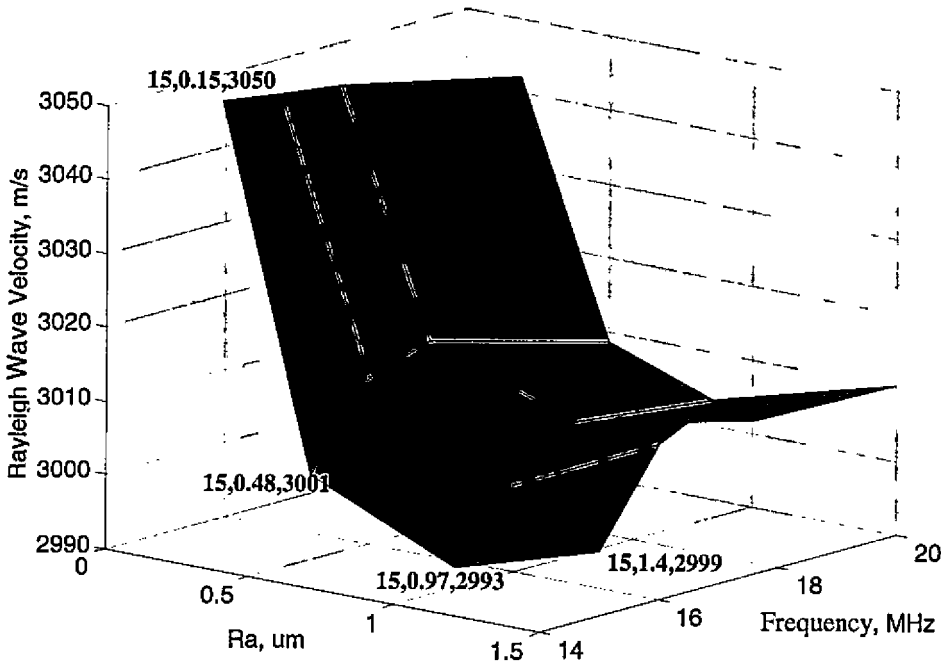

Figure 5-91: Rayleigh wave velocity dependence on surface roughness and frequency in rolled CP Titanium (measurements in transverse direction), a) before and b) after stress-relief.

In every machined material studied, the initial increase of surface roughness caused increased time-of-flight of the Rayleigh wave and decreased velocity. The velocities increased at a certain R_a value. The reason for the velocity drop with roughness was explained in literature as roughness-induced scattering dispersing the ultrasonic pulse (Tardy et al (1996), Ruiz et al (2002)). However, the dispersion effect is difficult to predict as it depends on the type of scatterer involved with different roughness profiles. Maxfield (2003) suggests a 'mass loading effect', where surface inhomogeneities cause an apparent change of density, or specifically, surface volume. From this and the present results it is argued, as the size of the micro-inhomogeneities approach the Rayleigh wavelength , the surface-wave path is no longer straight but rather follows the surface topography, i.e. the distance traveled is effectively longer so the time-of-propagation increases. Surface wave formulae do not take this into account, just the travel time. Consequently, the measured velocity is "lower." (Patel, 2003). An important factor is the specific groove spacing and depth versus the sound wavelength. The transducers used herein are broad band, with frequency range ± 120% of centre frequency. Thus 30 MHz is the highest frequency with wavelength ~115 μm in glass and ~125 μm in glass-ceramic. The spacing between the grooves on the rough surfaces is 20 μm to 100 μm in the rolled Ti and 500 μm in the glass and glass-ceramic. Thus the roughness "wavelength" is comparable with the sound wavelength.

Table 5-17: Comparison between Estimated and Measured Velocities in Titanium (15MHz Rayleigh Waves)

Ra µm	Roughness Wavelength / Sound Wavelength Ratio	Roughness Depth µm	Roughness Wavelength µm	Estimated Travel Path mm +/- 0.003	Measured Rw Velocity m/s	Rw Velocity Estimated from changing Travel Path
polished				1.269	3042.2	3042+/-2
0.48	0.115	1 +/- 0.3	24 +/- 3	1.284	3008.8	3006+/-2
0.97	0.335	3 +/- 0.5	60 +/- 5	1.290	3001.8	2992+/-2
1.4	0.5	3 +/- .5	100 +/- 8	1.280	3010.2	3016+/-2

To examine the influence of increasing sound path length on the results, an Alpha-step surface profile (Figure 5-67) was used to estimate the path length along inhomogeneities in rolled titanium. The results are tabulated in Table 5-17. Even though the grooves are shallow, their spacing (roughness wavelength) in Ti is comparable with sound wavelength (for the 15 MHz Rayleigh waves). The path increases by ~1.7% in the low R_a surfaces which explains the drop of measured sound velocity. However, the ultrasonic travel path along the surface topography decreased for the 1.4 µm R_a surface, (increased roughness wavelength, but an insignificant change of damage depth). Consequently, a shorter sound-travel-time is measured and a velocity increase. The above suggests when the $\lambda_{roughness} / \lambda_{Rayleigh\ wave} \geq \sim 0.1$, in machined titanium surface, the sound follows the surface topography, provided the groove depth is constant. The percentage increase of the travel path can be assumed equal to the percentage drop of velocity due to

surface roughness and the resulting estimated velocities agree well with those measured (Table 5-17).

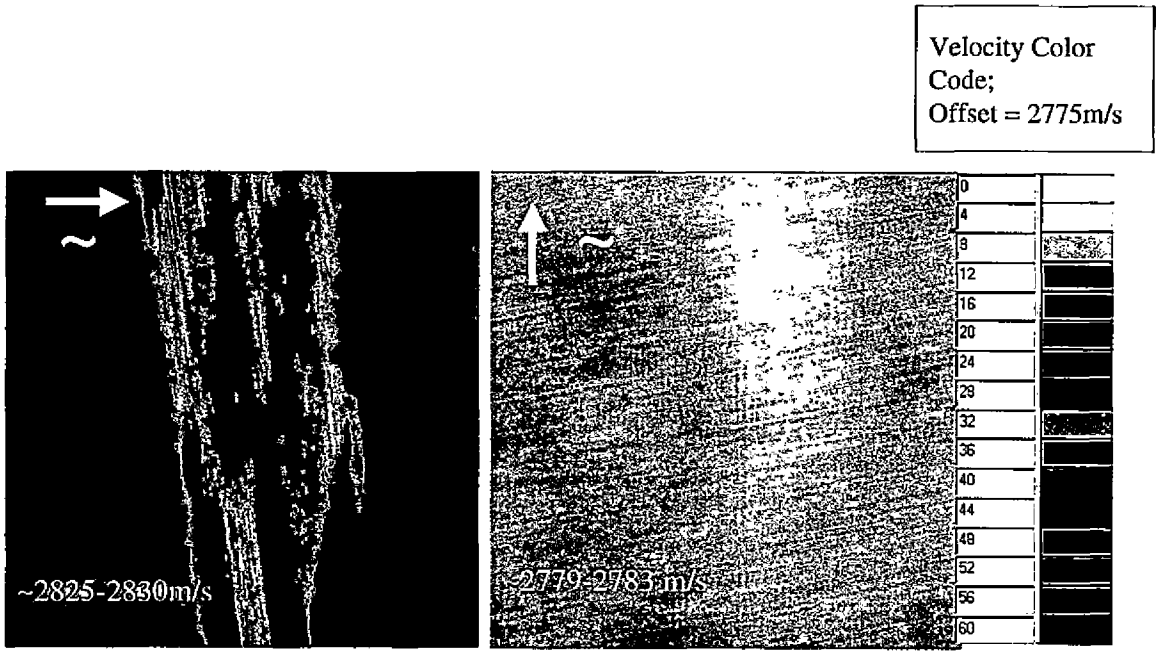

Figure 5-92: Rayleigh wave velocity acoustic image for a Ti specimen surface obtained with sound propagating across and along the grooves (the arrows indicate the sound propagation direction).

Since machined surface-grooves are directional and cylindrical Rayleigh wave transducers are also, the orientation of the transducer over the grooves will influence the velocity measured. The machining conditions were simulated on Ti via a series of closely spaced grooves. The R_w velocity mapping was performed parallel and perpendicular to them. Figure 5-92 clearly shows the velocity is more influenced when sound propagates across the grooves due to travel-path-change and scattering. The difference of velocity between the two scans must be due to grain texture and anisotropic stresses in the surface.

To illustrate whether a machined surface influences residual stress measurement, the grooved specimen was bent beyond its yield strength (600 MPa). The compressive stresses involved therein caused an increase of velocity along the smooth surface and the

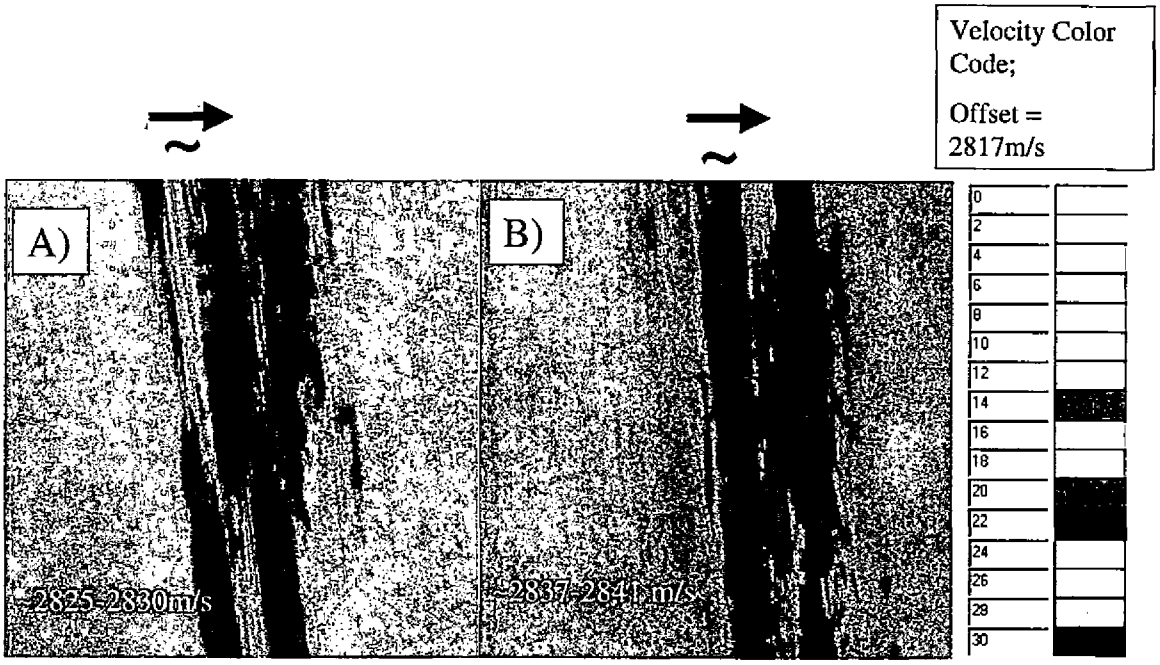

Figure 5-93: Rayleigh wave velocity acoustic image for a Ti plate surface (a) before and (b) after application of compressive stress.

grooved area (Figure 5-93). The measurement direction versus groove direction is very important from this study, as the residual stress distribution in the surface may not be isotropic.

The increased 'sound-travel-path' explanation should also hold for glass and the glass-ceramic with low R_a surfaces. For $R_a \leq 6.6$ μm (glass) and ≤ 6.8 μm (glass-ceramic), Figures 5-89 (b) and 5-90 (b), the velocities decreased, then increased again for

$R_a \geq 9.3$ μm, where the surface nature was different from titanium i.e., grooves were narrow, deep (up to 60 μm), had sharper edges, and importantly, were further apart than for the lower R_a surfaces (separation distance was 200 - 300 μm). The increase in velocity in the glass and glass-ceramic is explained by the surface appearing flat/ polished to the propagating sound. The travel path along a flat surface ≈ 1.2 mm. The grooves are narrow and far apart, hence sound propagating along the surface encounters 4 - 6 grooves. Much of the surface is flat and therefore the sound velocity is higher. However, the grooves cause scattering and sound velocity is lower than along the polished surface.

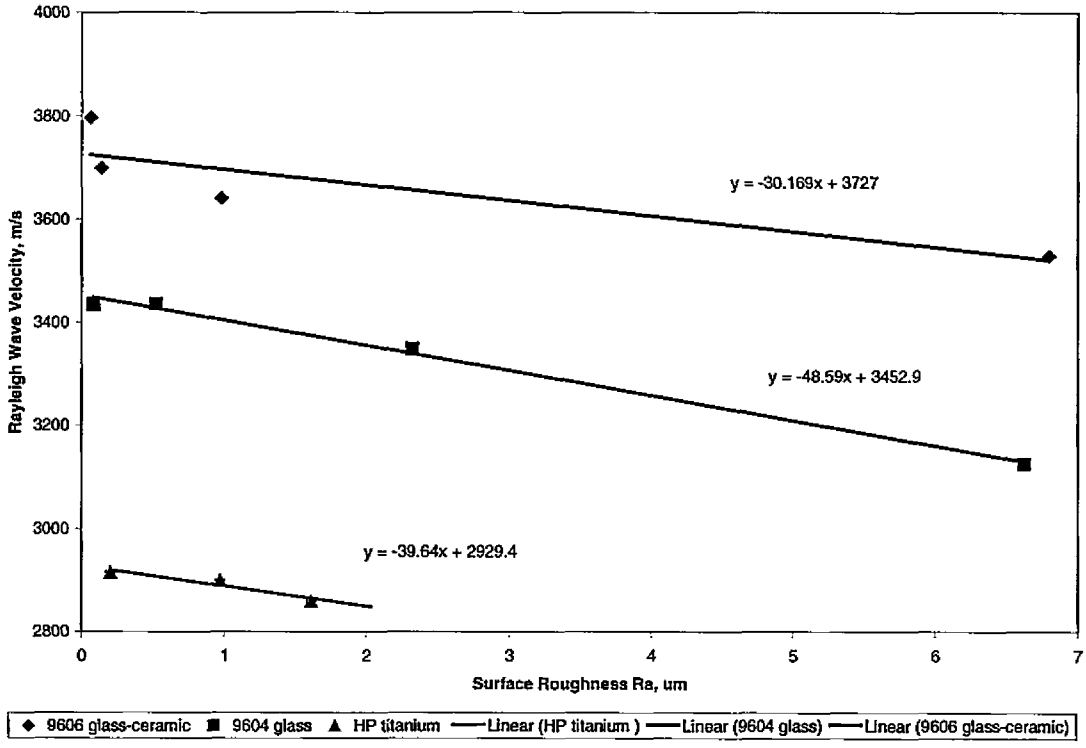

Figure 5-94: Comparison of the surface-roughness dependence of Rayleigh wave velocity for titanium (15 MHz), glass (16 MHz), and glass-ceramic (16 MHz).

The 15 MHz Rw velocity behavior in the low-R_a-surfaces for glass, glass-ceramic and titanium are compared in Figure 5-94. Best fit lines are drawn through the points. Clearly, the velocities drop rapidly with increasing glass roughness. Velocities are affected differently by the surface topography due to grains and grain boundary scattering in the polycrystalline material. When measuring stress the slopes of these lines can be used to estimate the change in Rayleigh velocity due to roughness.

There is an important difference in the behavior of Rayleigh wave velocity between annealed glass and glass ceramic with increasing frequency (even though the stress is not completely removed), (Figures 5-89 (b) and 5-90 (b)). Sonic velocities in polished and low-roughness surfaces are independent of frequency in the glass, whereas an inverse relationship exists in the glass-ceramic. Clearly this must be due to grain presence. High frequencies are more highly attenuated. As the surface roughness increases in the glass material, roughness-induced dispersion causes the velocity to drop. These results agree with other studies (as discussed earlier). Quantitative information cannot be extracted vis a vis the influence of surface roughness exclusively for Corning 9604 (glass) and for both surface-roughness and grain scattering for 9606 (glass-ceramic), as X-rays indicate stress is still present after annealing in the latter.

The influence of grain scattering on the Rayleigh velocity along titanium with rough surfaces is tracked in Figure 5-95. The velocity is inversely proportional to grain size for a smooth surface. As it was presented earlier, the slopes of the best-fit lines are different for the rolling and transverse direction (-0.54 ± 0.05 and -0.62 ± 0.6, respectively). This

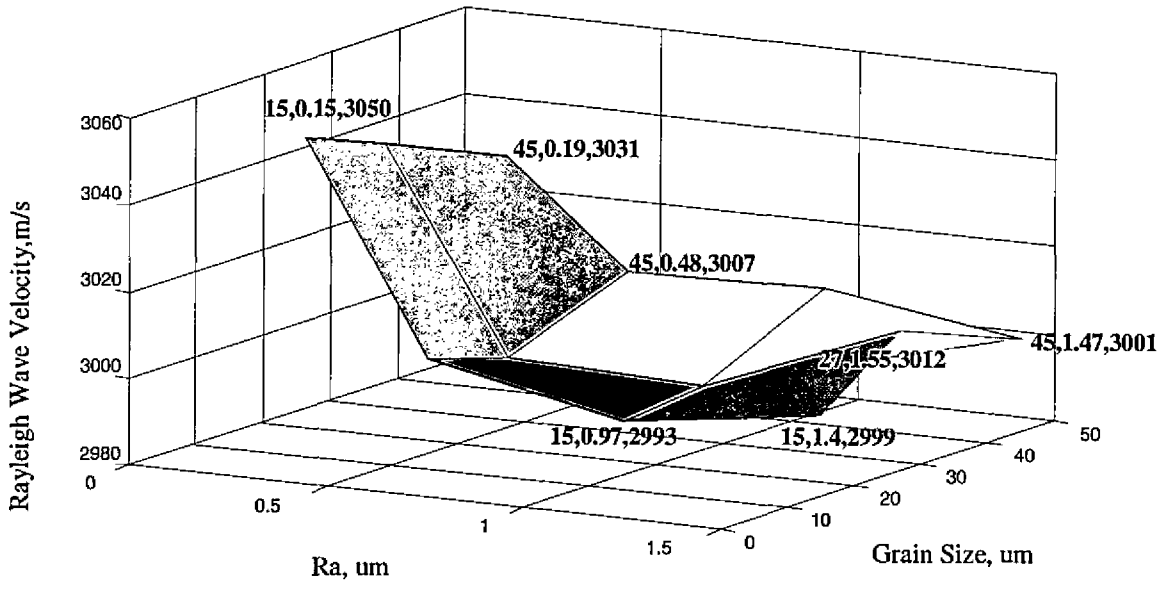

Figure 5-95: Dependence of the Rayleigh wave velocity on surface roughness, (R_a) and grain size in as-received, cold-rolled titanium (measurements in the transverse

trend is not followed when the surface roughness increases (Figure 5-95), indicating the combined effect of roughness-scattering and grain-scattering is not easy to predict. To obtain a better understanding of this phenomena the frequency dependence of velocity should be studied. However, as discussed earlier, the useful frequency range for titanium is limited to 15 MHz maximum for distance travel (≥ 1.2mm). In turn, on lowering the frequency, the influence of surface roughness and stress is less profound.

The cold-rolled titanium results show texture influences the velocity of both surface and bulk waves. The difference in R_w velocity between the rolling and transverse direction in the sheets used in the present work, was 2.6%. Figure 5-96 is a plot of the

R_w, "slowness," curve (inverse velocity), 360° around the rolling direction, for as-received, cold-rolled titanium (Patel, 2001). This data can be used to predict Rayleigh wave velocities in all directions, if the rolling or transverse direction velocity is known. However, such a prediction is a rough one as different % rolling reduction and heat treatment will change the proportion of this plot. This slowness curve may also contain the contribution of surface residual stresses if anisotropic. The approximately elliptical shape of this curve emphasises that, when using directional ultrasonic surface waves to study stress, the orientation of stress measurement versus rolling direction, must be known.

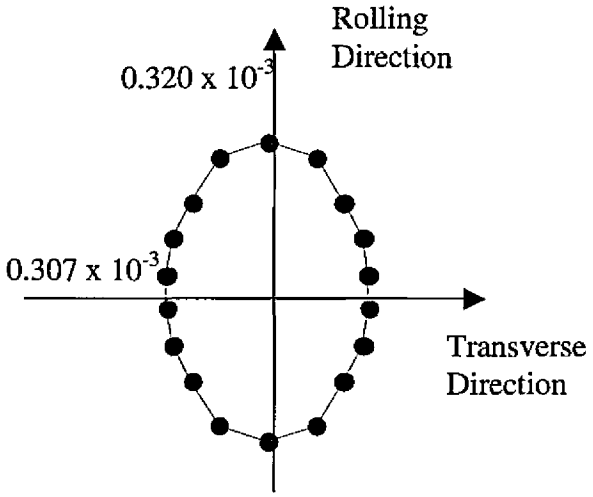

Figure 5-96: The "slowness" (inverse velocity) curve for rolled titanium (Patel, 2001).

It is constructive at this point to summarize the data collected in different parts of this project (Table 5-18). The experimental results are compared with reference states, i.e. glass-ceramic with annealed, smooth-surface glass and rolled titanium with hot-pressed (no texture). The total change in velocity following machining can be divided into contributions from the factors influencing the ultrasonic velocity (V), according to the following empirical equation:

$$V_{MEASURED} = V_{REFERENCE} + \Delta V_{GRAINS} + \Delta V_{SURFACE\ ROUGHNESS} + \Delta V_{TEXTURE} + \Delta V_{STRESS} \quad (70)$$

All measurements in Table 5-18 are for Rayleigh waves of frequency 15 MHz and 16 MHz for titanium and glass/ glass-ceramic, respectively. Only results for machined surfaces of 1μm-R_a are included.

For glass and glass-ceramic Equation 70 simplifies, as no texture is present. Corning 9604 glass surface is assumed as the reference for Corning 9606 glass-ceramic, since it is the precursor of 9606. When the glass is machined, the total change of velocity comprises that due to surface roughness and due to induced stress. The surface roughness change can be corrected via the wave travel path estimation (discussed earlier), thus the approximate velocity change due to stress is estimated.

The total change of velocity in the glass-ceramic contains an additional factor due to the grains present. The large change in velocity between the glass and glass-ceramic is not as much due to grain scattering (grains size only ~0.6 μm) rather to phase change. The difference between 9606 and 9604 in the measured influence of surface roughness on

Table5-18: Summary of the experimental results for glass, glass-ceramic and titanium; RD – rolling direction, TD – transverse direction.

Material	V measured m/s +/- 0.9 m/s	V_{REF} m/s	ΔV_{TOTAL} m/s	ΔV_{GRAIN} m/s +/- 7 m/s	$\Delta V_{TEXTURE}$ m/s +/- 7 m/s	$\Delta V_{SURFACE\ ROUGHNESS}$ m/s, +/- 1.4 m/s	ΔV_{STRESS} m/s +/- 1.4m/s	ΔStress UT MPa	ΔStress XRD MPa
CORNING 9604 GLASS (smooth, annealed)	3435	3435	X	X	X	X	X	X	X
MACHINED GLASS	3417.2	3435	-17.8	X	X	-22.3	4.5	-22 +/- 6	X
ANNEALED, MACHINED GLASS	3412.7	3435	-22.3	X	X	-22.3	X	X	X
CORNING 9606 GLASS-CERAMIC (smooth, annealed)	3797	3435	362	362	X	X	X	X	X
MACHINED GLASS-CERAMIC	3646.3	3435	211.3	362	X	-156.2	5.5	-22 +/- 7	-44 +/- 20
ANNEALED, MACHINED GLASS-CERAMIC	3640.8	3435	205.8	362	X	-156.2	X	X	X

HOT-PRESSED (HP) TITANIUM, 75μm grains	2905	2905	X	X	X	X	X	X	X
MACHINED	2904.2	2905	96.2	X	X	-15.5	14.7	-386 +/- 34	-482.3 +/- 35
ANNEALED, MACHINED	2889.5	2905	81.5	X	X	-15.5	X	X	X
ROLLED TI (TD), 15μm	3049.8	2905	144.8	37.2	107.6	X	X	X	X
MACHINED	2999	2905	94	37.2	107.6	-57.1	6.3	-248 +/- 29	-289 +/- 34
ANNEALED, MACHINED	2992.7	2905	87.7	37.2	107.6	-57.1	X	X	X
ROLLED TITANIUM (RD), 27μm	2946	2905	41	25.9	15.1	X	X	X	X
MACHINED	2915	2905	10	25.9	15.1	-46	15	-255 +/- 22	-290 +/- 35
ANNEALED, MACHINED	2900	2905	-5	25.9	15.1	-46	X	X	X
ROLLED TITANIUM (TD), 45μm	3030.5	2905	125.5	18.6	106.9	X	X	X	X
MACHINED	3013.4	2905	108.4	18.6	106.9	-22.5	5.4	-212 +/- 33	-290 +/- 35

ANNEALED MACHINED	3008	2905	103	18.6	106.9	-22.5	X	X	X

MAGNESIUM SINGLE CRYSTAL	SOUND PROPAGATION DIRECTION	POLARIZATION DIRECTION	SHEAR VELOCITY, m/s +/- 2 m/s
	[010]	[001]	3092
		[110]	3107
	[001]	[010]	3060
		[110]	3063

the R_w velocity illustrates the phenomenon previously discussed in detail. Even though the R_a value is the same for both glass and glass-ceramic, the influence of roughness on the Rw velocity is significantly different (-22.3 vs. –156 m/s). This suggest the type of roughness is more important than the R_a value (groove-depth, groove-spacing, sharpness of the groove edges). Also, as the difference is so large, laser-etching may have changed the material properties of the surface.

The change in residual stress on annealing, measured in the glass and glass-ceramic was similar, -22 +/- 6 MPa. For the glass ceramic this is ~1/2 the value measured with XRD. This difference is expected as the penetration depth of ultrasound is ~10 times that of X-rays.

Hot-pressed titanium (75μm grain size) was chosen as reference for the rolled Ti as it has minimum texture. It is assumed the hot-pressed material's chemical-composition, purity, density and mechanical properties are the same as the rolled material. The stress developed in machined hot-pressed Ti is lower than the value via XRD (~20 times penetration depth). The difference between the velocities measured in HP and rolled Ti is due to different grain size and texture in the smooth annealed surfaces and due to the same two, plus different type of surface roughness and different level of stress in the machined surfaces. The grain contribution can be estimated from graphs of R_w velocity vs. grain size (Figures 5-83 and 5-84). In terms of texture, the change of velocity is much smaller in the rolling direction, than the transverse (15 m/s vs. 107 m/s). The magnitude of the change of velocity due to stress, reflects, not only the level of stress, but also the higher Acoustoelastic Constant in the rolling direction (-2.02 vs. -0.85 %/GPa,

respectively). Also, the quoted change of velocity due to the residual stress assumes complete removal thereof after annealing. Even though this may not be completely true, XRD shows the after-anneal stress in the surface is 13 MPa for the hot-pressed and 18 MPa for the rolled samples. Thus, since the samples received identical stress-relief treatment, the 'after-anneal' stress-level in each type may be assumed the same.

The results for the Mg single crystal are included at the end of the table to illustrate the role of texture (direction) on sound velocity. Bulk, (and consequently surface) ultrasonic velocities differ significantly with crystallographic direction.

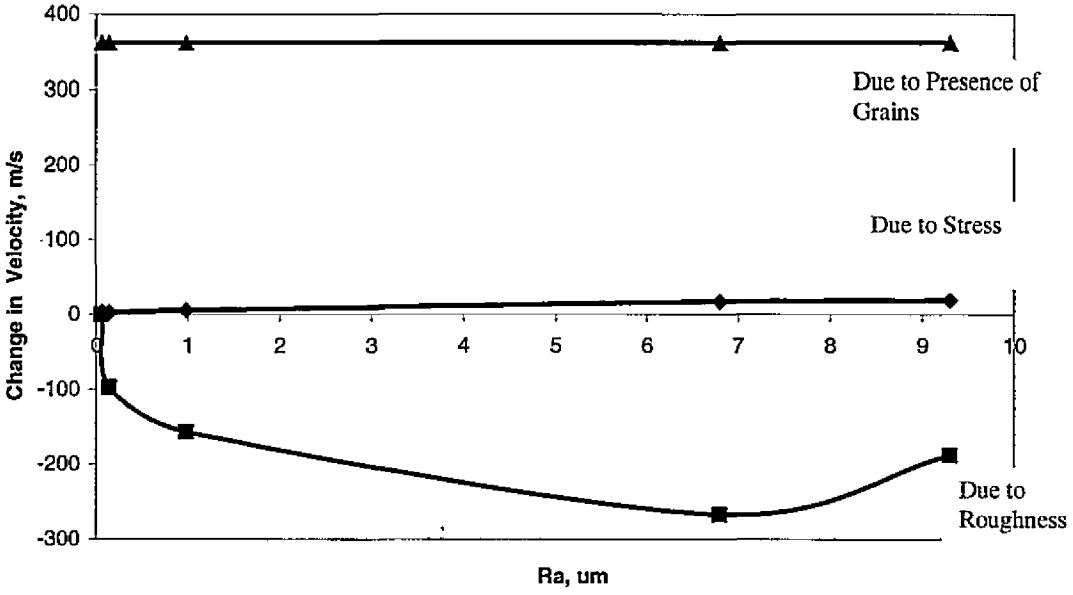

Figure 5-97: Comparison of changes of velocity in Corning 9606 glass-ceramic upon machining.

There is a very important point in Table 5-18 which, though discussed earlier, cannot be stressed enough. The influence of surface roughness, texture and grains on the

Rayleigh wave velocity is much larger than stress. Just how much larger is dramatically illustrated for machined glass-ceramic (Figure 5-97) and machined-rolled-titanium (Figure 5-98).

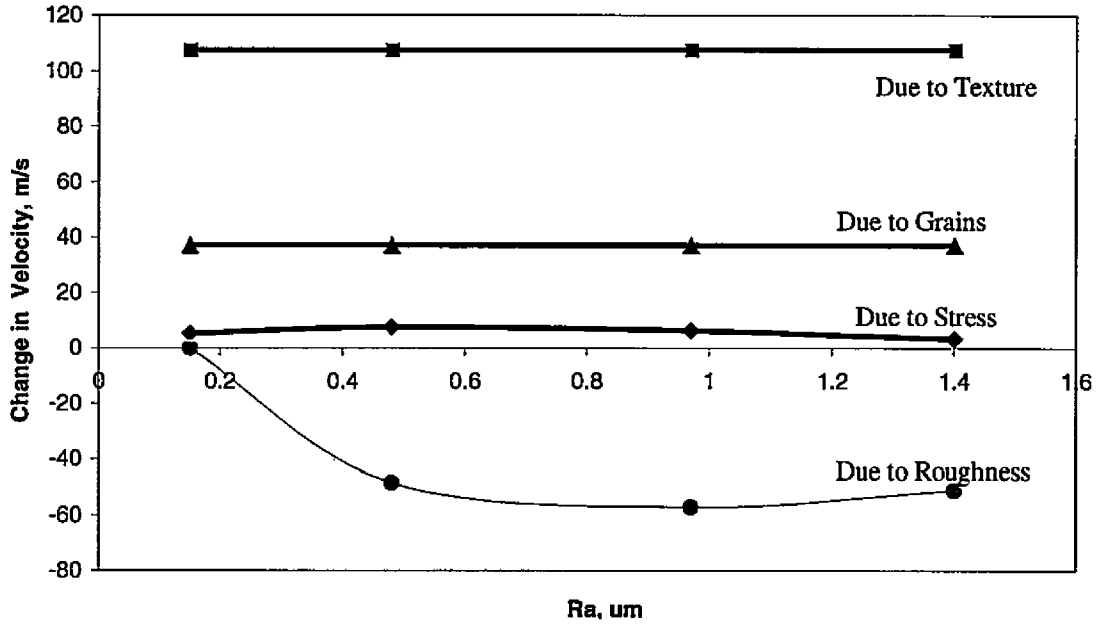

Figure 5-98: Comparison of changes in velocity in rolled titanium upon machining (measurements in the transverse direction)

Thus it has been demonstrated that, given careful attention is paid to determining and correcting-out other contributions to the ultrasonic-velocity change, the residual surface stress can be determined in both sign and value. The latter agrees well with XRD data however the massive establishment of XRD equipment is replaced by the small, mobile and much cheaper transducer/ electronic-processing ultrasonic system.

Chapter 6

CONCLUSIONS

The results of this work, lead to conclusions vis a vis the measurement of residual stress in machined components with surface-acoustic ultrasonic waves.

The influence of grains on surface wave velocity can be corrected for if a single frequency is used and velocity .vs. grain-size is known at that frequency (see Figures 5-83 and 5-84). Varying the frequency to identify the stress profile below the surface produces velocities influenced not only by stress, but also by grain and roughness scattering. Both increase with increasing frequency.

The difference of velocity of surface waves propagating in the rolling, and transverse, directions cannot be assumed purely due to texture. If a principal-stress direction exists in the surface residual-stress distribution, it reflects in surface wave velocity. Orthogonally-polarized, shear-waves are better to identify the texture effect, as they are less sensitive to surface stress, provided the specimen thickness > 6mm. The latter, however, assumes minimum or isotropic bulk stresses. It is not clear how the texture/ bulk wave interaction is related to that of surface waves, as surface waves are generally less sensitive to texture. The distribution of texture through the thickness, however, should be considered. A complete examination of this phenomenon should be undertaken.

If machining produces anisotropic roughness (i.e., lines/ grooves from milling), one way of isolating the effect thereof on the R_w velocity is via 'Surface Wave Velocity' versus Roughness (R_a) plots. These must be used with caution, as it is not necessarily R_a that determines the velocity, but the ratio of groove spacing to sound wavelength plays an important role, as well as the groove depth. Another approach to identify the roughness effect on surface-wave velocity is to measure the difference of velocity along and across, the machining lines. The velocity along the latter is less affected by the roughness. However, this assumes the stress is isotropic in the surface. This may not be the case. To identify stress parallel to the machining lines, the surface roughness contribution may be ignored. The situation becomes more complicated when the surface roughness is isotropic (i.e., shot-peened surfaces) as identification of the roughness effect on surface wave velocity requires changing frequency (as roughness scattering increases with frequency). Sound velocity at different frequencies is influenced by the change of residual stress with depth. There is also the contribution of increased grain scatter. As shown earlier, if a single frequency is used, the travel path can be estimated and stress values (without a scattering factor) can be calculated.

The above identifies the importance of grain size, texture, and surface roughness in the measurement of residual surface stresses via ultrasound. Qualitative information was thus obtained herein. The maps and relations generated for material conditions in the present experiments should enable future work to more closely predict the magnitude of different factors contribution to ultrasonic velocity measurement.

Chapter 7

FUTURE WORK

Further examination of titanium requires development of transducers with frequencies 5 - 15 MHz. A residual-stress-free reference should be obtained. To correct for grain scatter, maps of surface wave velocity .vs. grain size .vs. frequency should be generated. Such will provide the reference velocity state for obtaining residual stress as a function of surface condition. Shot-peening (which gives an isotropic surface-residual-stress distribution) would help with understanding the stress depth-profile as a function of frequency. The surface roughness contribution can be estimated provided the travel path is known (as discussed). Slowness graphs should also be developed for reference samples. Results for different frequencies should be compared with X-ray depth profile results.

References

Adler, L., Cook, K.V., Dewey, B.R., King, R.T., The Relationship Between Ultrasonic Rayleigh Waves and Surface Residual Stress, Materials Evaluation, 1977, pp. 93-96

Ambardar, R., Jayakumar, T., Pathak, S.D., Prabhakar, O., Ultrasonic Velocity Measurement to Assess Casting Quality, Insight: Non-Destructive Testing and Condition Monitoring, Vol. 38, No. 7, Jul. 1996, pp. 502-508

Badidi Bouda, A., Lebaili, S., Benchaala, A., Grain Size Influence on Ultrasonic Velocites and Attenuation, NDT&E International, Vol. 36, 2003, pp. 1-5

Bar-Cohen, Y., Birks, A.S., Chang, F.H., Ultrasonic Pulse Echo Techniques, Nondestructive Testing Handbook, 2nd ed., vol. 10, 1996

Bar-Cohen, Y., Xue, T., Lih, S., Polymer Piezoelectric Transducers for Ultrasonic NDE, NDTnet, Vol. 1, No. 09, September 1996

Barrett, C.S., Massalski, T.D., Structure of Metals, 3rd ed., Oxford: Pergamon, 1980

Belahcene, F., Lu, J., Determination of Residual Stress in Z8CDWV12 Steel Using Critically Refracted Longitudinal Waves, JSME International Journal, Series A, Vol. 43, No. 4, 2000, pp. 367-373

Birks, A.S., Golis, M.J., Green Jr., R.E., "Introduction to Ultrasonic Testing", *Nondestructive Testing Handbook*, vol. 10, 2nd edition, ed. Moore, P.O., McIntire, P., American Society of Nondestructive Testing, 1996

Blessing, G.V., Slotwinski, J.A., Eitzen, D.G., Ryan, H.M., Ultrasonic Measurements of Surface Roughness, Applied Optics, Vol. 32, No. 19, 1 July 1993, pp. 3433-3437

Bray, D.E., Ultrasonic Stress Measurement with the Lcr Technique, 1998, http://brayengr.com/lcrproc2.html

Bray, D.E., Current Directions of Ultrasonic Stress Measurement Techniques, Proceedings of the 15th World Conference on Non-Destructive Testing, 15-21 Oct, 2000, Rome

Bray, D.E., Ultrasonic Stress Measurement in Pressure Vessels, PVP-Vol. 429, Residual Stress Measurement and General Nondestructive Evaluation, ASME 2001, pp. 15-23

Bray, D.E., Egle, D.M., Ultrasonic Studies of Anisotropy in Cold-Worked Layer of Used Rail, Metallurgical Science, Vol. 15, 1981, pp. 574-582

Bray, D.E., Junghans, P., Application of the Lcr Ultrasonic Technique for Evaluation of Post-Weld Heat Treatment in Steel Plates, NDT&E International, Vol. 28, No. 4, 1995, pp. 235-242

Bray, D.E., Kim, S.J., Fernandes, M., Ultrasonic Evaluation of Residual Stresses in Rolled Aluminum Plates, Proceedings of the 9th International Symposium on Nondestructive Characterization of Matreials, Ed. Green, R.E., Sydney, Australia, June28-July 2, American Institute of Physics, NY, 1999, pp. 443-448

Bray, D.E., Pathak, N., Srinivasan, M.N., Residual Stress Distributions in the Rim of a Steam Turbine Disk Using the Lcr Ultrasonic Technique, Materials Science Forum, Vols. 210-213, 1996, pp. 317-324

Bray, D.E., Stanley, R.K., Nondestructive Evaluation, McGraw-Hill Series in Mechanical Engineering, 1989

Bray, D.E., Stanley, R.K., Nondestructive Evaluation, CRC Press, Boca Raton, FL, revised edition, 1997

Bray, D.E., Tang, W., Subsurface Stress Evaluation in Steel Plates and Bars Using the L_{cr} Ultrasonic Wave, Nuclear Engineering and Design, Vol. 207, pp. 231-240, 2001

Bray, D.E., Tang, W., Grewal, D., Ultrasonic Stress Evaluation I a Turbine/Compressor Rotor, Journal of Testing and Evaluation, Vol. 25, No. 5, Sept. 1997, pp. 503-509

Bunge, H.J., Kiewel, H., Fritsche, L., Reinert, T., Influence of Grain Shape and Orientation Correlation on the Elastic Properties of Polycrystalline Materials, Thermec' 97, International Conference on Thermomechanical Processing of Steels and Other Materials, Volume 2, Ed. Chandra, T., Sakai, T., pp. 2365-2371.

Chance, B.H., Bray, D.E., Ultrasonic Measurement of Residual Stress Relaxation in Welded Steel Plates Using Critically Refracted Longitudinal Waves, PVP-Vol. 429, Residual Stress Measurement and General Nondestructive Evaluation, ASME 2001, pp. 71-78

Cracknell, A.P., Ultrasonics, Wykeham Publications, Crane Russak & Company, Inc., New York, 1980

Crecraft, D.I., The Measurement of Applied and Residual Stresses in Metals Using Ultrasonic Waves, Journal of Sound and Vibrations, Vol. 51, 1967, pp. 173-192

Cullity, B.D., Elements of X-Ray Diffraction, Addison-Wesley Publishing Company, Inc., 1967

Doyle, P.J., Glass-Making Today: an Iintroduction to Current Practice in Glass Manufacture, Redhill: Portcullis Press, New York, 1979, pp. 254-256.

Duquennoy, M., Ouaftouh, M., Ourak, M., Determination of Stresses in Aluminum Alloy Using Optical Detection of Rayleigh Waves, Ultrasonics, Vol. 37, 1999, pp. 365-372

Duquennoy, M., Ouaftouh, M., Ourak, M., Ultrasonic Evaluation of Stresses in Orthotropic Materials Using Rayleigh Waves, NDT&E International, Vol. 32, 1999, pp. 189-199

Duquennoy, M., Ouaftouh, M., Qian, M.L., Jenot, F., Ourak, M., Ultrasonic Characterization of Residual Stresses in Steel Rods Using a Laser Line Source and Piezoelectric Transducers, NDT&E International, Vol. 34, 2001, pp. 355-362

Duquennoy, M., Ouaftouh, M., Ourak, M., Jenot, F., Theoretical Determination of Rayleigh Wave Acoustoelastic Coefficients: Comparison with Experimental Values, Ultrasonics, Vol. 39, 2002, pp. 575-583

Egle, D.M., Bray, D.E., Measurement of Acoustoelastic and Third-Order Elastic Constants for Rail Steel, J. Acoust. Soc. Am. Vol. 60, 1976, pp.741-744

Egle, D.M., Bray, D.E., Application of the Acousto-Elastic Effect to Rail Stress Measurement, Materials Evaluation, Vol. 37, No. 4, 1979, pp. 41-46

Filipczynski, L., Pawlowski, Z., Wehr, J., Ultrasonic Methods of Testing Materials, Butterworths, London, 1966

Fitting, D.W., Adler, L., Ultrasonic Spectral analysis for NDE, Plenum Press, New York, NY, 1981

Fukada, E., Yasuda, J., Japanese Journal of Applied Physics, No. 3, 1964, p. 117

Gericke, O.R., The Future of Ultrasonic Spectroscopy, Reynolds, P.M., ed., British Non-Ferrous Metals Research Association, London, 1971

Gilbert, R., Shannon, R.C., Heat Treating of Titanium and Titanium Alloys, ASM Metals Handbook, vol. 5, 19 , pp. 913-923

Gilmore, R.S., Industrial Ultrasonic Imaging/ Microscopy, Ultrasonic Instruments and Devices II, Academic Press, 1999;

Gmyrin, S.Ya., The Problem of the Interference of Ultrasonic Waves on Traversing a Plane Layer of Contact Liquid, Defektoskopiya, No. 3, 1992, pp. 59-67

Gmyrin, S.Ya., Propagation of Ultrasonic Waves Through a Layer of Contact Liquid Taking the Article Surface Roughness into Account, Russian Journal of Nondestructive Testing, Vol. 29, No. 4, 1993, pp. 242-249

Graft, W.H., Rostoker, W., The Measurement of Elastic Modulus of Titanium Alloys, Symposium on Titanium, Los Angeles, California, Spet. 17 and 18, 1956, pp. 131-144.

Hayes, M., Rivlin, R.S., Surface Waves in Deformed Elastic Materials, Archive of Rational Mechanics and Analysis 8, 1961, pp. 359-380

Heyman, J.S., Allison, S.G., Salama, K., Chu, S.I., Symposium on NDE, applications to materials processing, Metals Park, OH, American Society of Metals, 1983, pp. 177-184

Hickernell, F.S., Surface Acoustic Wave Technology Macrosuccess through Microseisms, Physical Acoustics, Vol. 24, Ultrasonic Instruments and Devices II, Academic Press, 1999, p.p. 135-209

Hirao, M., Fukuoka, H., Hori, K., Acousto-Elastic Effect of Rayleigh Surface Wave in Isotropic Material, Journal of Applied Mechanics, 48, 1981, pp. 119-124

Hlavac, J., The Technology of Glass and Ceramics, Elsevier, Amsterdam, 1983

Hsu, H.N., Experimental Mechanics, Vol. 14, 1974, p. 169

Hueter, T.F., Bolt, R.H., Sonics, Wiley, New York, 1955

Hughes, D.S., Kelly, J.L., Physical Review, Vol. 92, p. 1145, 1953

Husson, D., Bennett, S.D., Kino, G.S., Rayleigh Wave Measurement of Surface Residual Stresses, Review of Progress in Quantitative Nondestructive Evaluation, Thompson, D.O., ed., Vol. 3, 1984, pp. 1293-1303

Inagaki, H:, Texture and Mechanical Anisotropy in Cold Rolled and Annealed Pure Ti Sheets, Zeitschrift fuer Metallkunde, Vol. 38, No. 1, Jan, 1992, pp. 40-46

Iwashimizu, Y., Kobori, O., The Rayleigh Wave in a Finitely Deformed Isotropic Elastic Material, Journal of the Acoustical Society of America, Vol. 48, No. 3, 1978, pp. 910-916

Jassby K., Saltoun, D., Use of Ultrasonic Rayleigh Waves for the Measurement of

Applied Biaxial Surface Stresses in Aluminum 2024-T351 Alloy, Materials Evaluation, Vol. 40, 1982, pp. 198-205

Junghans, P., Bray, D.E., Beam Characteristics of High Angle Longitudinal Wave Probes, NDE: Applications, Advanced Methods, and Codes and Standards, Proceedings 1991 ASME Pressure Vessels and Piping Conference, San Diego, CA, June 23-27, pp. 39-44

Kandil, F.A., Lord, J.D., Fry, A.T., Grant, P.V., A Review of Residual Stress Measurement Methods – A Guide to Technique Selection, NPL Report MATC(A)04, Feb. 2001

Kawai, H., The Piezoelectricity of Poly(vinylidene Fluoride), Japanese Journal of Applied Physics, Vol. 8, 1969, pp. 975-976

King, R.R., Birdwell, J.A., Bray, D.E., Clotfelter, W.N., Risch, E.R., Proceedings of the Ninth Symposium on Nondestructive Evaluation, San Antonio, TX, pp. 91-105, 1973;

King, R.B., Fortunko, C.M., Determination of In-Plane Residual Stress States in Plates Using Horizontally Polarized Shear Waves, Journal of Applied Physics, Vol. 56, No. 6, 1983, pp. 3027-3035

Kinsler, L.E., Frey, A.R., Coppens, A.B., Sanders, J.V., Fundamentals of Acoustics, John Wiley & Sons, Inc., New York, 2000

Kline, R., Jiang, L., Using Rayleigh Wave Dispersion to Characterize Residual Stresses, Review of Progress in Quantitative Nondestructive Evaluation, Vol. 15, 1997, pp. 1629-1636

Kramarenko, G.K., Mel'kanovich, A.F., Gringerg, O.A., The Effect of Surface Processing of Articles on Ultrasonic Testing with a Direct Probe in the Contact Version, Defektoskopiya, No. 3, 1973, pp. 16-24

Krautkramer, J., Krautkramer, H., Ultrasonic Testing of Materials, 3rd ed., Springer-Verlag, Berlin, 1983

Kumar, A., Jayakumar, T., Palanichamy, P., Raj, B.: Scripta Mater., Vol. 40, 1999, pp. 333-340

Kumar, A., Laha, K, Jayakumar, T., Bhanu Sankara Rao, Raj, B., Comprehensive Microstructural Characterization in Modified 9Cr-1Mo Ferritic Steel by Ultrasonic Measurements, Metallurgical and Materials Transactions A, Vol. 33A, June 2002, pp. 1617-1626

Lampman, S., Wrought Titanium and Titanium Alloys, ASM Handbook, Vol. 2, Properties and Selection: Nonferrous Alloys and Special-Purpose Materials, 1990, ASM International, pp. 592-633

Lee, Y.C., Kim, J.O., Achenbach, J.D., Measurement of Stress by Line-Focus Acoustic Microscopy, Ultrasonics, Vol. 32, No. 5, 1994, pp. 359-365

Leon-Salamanca, T., Bray, D.E., Residual Stress Measurement in Steel Plates and Welds using Critically Refracted Longitudinal Waves, Res. Nondestr. Eval. Vol. 6, No. 5, May/ June 1995

Leon-Salamanca, T., Reinhart, E.R., Characterization of Subsurface Stress Gradients in Metals Using Ultrasound, PVP-Vol. 276/ NDE-Vol. 12, Determining Material Characterization: Residual Stress and Integrity with NDE, ASME 1994, pp. 179-181

Leon-Salamanca, T., Reinhart, E.R., Bray, D.E., Golis, M., Field Applications of an Ultrasonic Method for stress Measurement in Structure, Nondestructive Testing (Proceedings of the 12th World Conference, ed. Boogaard, J., Van Dijk, G., Amsterdam, The Netherlands, April 1989, pp. 1484-1489

Li, V., Ji, J.L., Lebrun, G.E., The Influence of Surface Roughness on Stress Determination by the X-ray Diffraction Technique, Experimental Techniques, Vol. 19, No. 2, March/April 1995, pp. 9-11

Lindgren, E.A., Jones, T.S., Berger, H., Rosen, M., Review of Progress in Quantitative NDE, 13, Plenum Press, New York, 1994, p. 2039

Lindgren, E.A., Marting, L.P., Rosen, M., Berger, H., Nondestructive Residual Stress Measurements in Composites, 43rd International SAMPE symposium, May 31- June 4, 1998, pp. 1465-1473

Lu, W.Y., Peng, L.W., Holland, S., Measurement of Acousto-Elastic Effect of Rayleigh Surface Waves Using Laser Ultrasonics, Review of Progress in Quantitative Nondestructive Evaluation, Vol. 17, 1998, pp. 1643-1648

Martin, B.G., Materials Evaluation, Vol. 32, No. 11, Nov. 1974, pp. 229-234

Mattiat, O.E., Ultrasonic Transducer Matreials, Plenum Press, New York and London, 1971

Matzkanin, G.A., Yolken, H.T., "A Review of Techniques for Nondestructively Characterizing Residual Stress in Metals", PVP-Vol. 429, Residual Stress Measurement and General Nondestructive Evaluation, ASME 2001, pp. 1-8

Maxfield, B., Industrial Sensors & Actuators, San Leandro, CA, private communications, 2001-2003

Meek, S.W., Peter, D., Horne, D., Young, K., Novotny, V., Microscopic Imaging of Residual Stress Using a Scanned Phase Measurement Acoustic Microscope, Applied Physics Letters, Vol. 55, 1989, pp. 1835-1837

Meeker, T.R., ANSI/IEEE Standard on Piezoelectricity. IEEE Trans. UFFC Vol. 43 No.5, 1996

Mogil'ner, L.E., Sakhranov, A.V., Urman, N.S., The Transmission of a Bounded Ultrasonic Wave Through a Layer of Contacting Liquid in the Case of Inclined Incidence and a Pulsed Mode of Radiation, Defektoskopiya, No. 1, 1986, pp. 70-80;

Murthy, S.R., A Study of Ultrasonic Velocity and Attenuation on Polycrystalline YIG, Journal of Magnetism and Magnetic Materials, Vol 222, 2000, pp. 121-127

Murthy, S.R., A Study of Ultrasonic Velocity and Attenuation on Polycrystalline Ni-Zn Ferrites, Bulletin of Materials Science, Vol. 24, No. 6, Dec. 2001, pp. 611-616

Nishiwaki, N., Hori, S., Yoshida, K., Mineo, K., Measurement of Injection Molding and Machining Process Using Ultrasonic Technique, 1988 IEEE Ultrasonic Symposium, pp. 755-758

Okade, M., Mizuno, K., Kawashima, K., Measurement of Acoustoelastic Coefficient of Surface Waves with Scanning Acoustic Microscope, Review of Progress in Quantitative Nondestructive Evaluation, Vol. 14, 1995, pp. 1883-1889

Palanichamy, P., Bharat, P., Subramanian, C.V., Bhattacharya, D.K., Baldev, R., A NDT Method for Grain Size Determination in Austenitic Stainles Steel, Transactions of IIM, Vol. 51, No. 5, 1988, pp. 485-488

Palanichamy, P.,J., A., Jayakumar T., Bhattacharya, D.K., Ultrasonic Velocity Measuerments for Estimation of Grain Size in Austenitic Stainless Steel, Journal of Non-Destructive Ecaluation, Vol. 14, 1994, pp. 1-4

Palanichamy, P., Joseph, A., Jayakumar, T., Raj, B., Ultrasonic Velocity Measurements for Estimation of Grain Size in Austenitic Stainless Steel, NDT&E International, Vol. 28, No. 3, 1995, pp. 179-185

Pao, Y.H., Sachse, W., Fukuoka, H., Acoustoelasticity and Ultrasonic Measurements of Residual Stress, Physical acoustics, Vol. 17, 1984, pp. 61-143

Papadakis, E.P., Ultrasonic Attenuation Caused by Scattering in Polycrystalline Metals,

Journal of Acoustics Society Amer., Vol. 37, 1965, pp. 711-717

Papadakis, E.P., Inverse Problem in Materials Characterization Through Ultrasonic Attenuation and Velocity Measurements, Nondestructive Methods for Material property Determination, Hershey, PA, USA, Plenum Press, 1984, pp. 151-160

Papadakis, E.P., Physical Acoustics and Microstructure of Iron Alloys, International Metals Reviews, Vol. 1, 1984, pp. 1-24

Papadakis, E.P., Oakley, C.G., Selfridge, A.R., Maxfield, B., Fabrication and Characterization of Transducers, Ultrasonic Instruments and Devices II, Academic Press, San Diego, 1999

Patel, N.D., An Ultrasonic Study of the Vitreous Systems $MoO_3 - P_2O_5$ and $H_2O - P_2O_5$, Ph.D. Thesis, 1982

Patel, N.D., Fallon Ultrasonics Inc., private communications, 2000-2003

Payne, P.A., Ultrasonic Transducers: design, construction and applications, Int. J. of Materials and Product Technology, Vol. 9, Nos 4/5/6, 1994, pp. 403 - 427

Pecorari, C., Attenuation and Dispersion of Rayleigh Waves Propagating on a Cracked Surface: an Effective Field Approach, Ultrasonics, Vol. 38, 2000, pp. 754-760

Pecorari, C., Gros, X., Acosta, B., Debarberis, L., Beers, M., Manna, G., Assessment of Steels Ageing by Rayleigh Wave Velocity Measurements, Proceedings of the 15th World Conference on Non-Destructive Testing, 15-21 October, 2000, Rome

Pecorari, C., Scattering of a Rayleigh Wave by a Surface-Breaking Crack with Faces in Partial Contact, Wave Motion, Vol. 33, 2001, pp. 259-270

Pineault, J.A., Belassel, M., Brauss, M.E., Proto Manufacturing Ltd., X-Ray Diffraction Residual Stress Measurement in Failure Analysis, ASM Handbook, Vol. 11: Failure Analysis and Prevention and Practical Failure Analysis, 2001, pp. 484-497

Pineault, J.A., Brauss, M.E., Stress Mapping – A New Way of Tackling the Characterization of Residual Stress, Experimental Techniques, 1995, Vol. 19, No. 2, pp. 17-18

Posakony. G.J., Influence of the Pulser on the Ultrasonic Spectrum: The Reslts of an Experiment, Materials Evaluation, Vol. 43, No. 4, March 1985, pp. 413-419

Pritchard, S.E., Use of Ultrasonics for Residual Stress Analysis, NDT International, Vol. 20, No. 1, Feb. 1987, pp. 57-60

Qian, M.L., Duquennoy, M., Ouaftouh, M., Jenot, F., Ourak, M., Laser Ultrasonic s Characterization of Surface Residual Stresses in Steel Rods, Review of Progress in Quantitative Nondestructive Evaluation, July 2000

Rabinovich, Ceramics Produced by Sintering, Nucleation and Crystallization in Glasses, ed. Simmons, J.H., et al, American Ceramic Society, 1982

Rakhimov, V.F., The Effect of Roughness of the Contact Surfaces on the Transmission of Ultrasonic Oscillations, Defektoskopiya, No. 11, 1988, pp. 50-56

Razvi, S., Li, P., Salama, K., Cantrell, J.H., Yost, W.T., Review of Progress in Quantitative Non-Destructive Evaluation, Vol. 6B, Plenum Press, 1987, p. 1403

Rice, R., Microstructure Dependence of Mechanical Behaviour of Ceramics, Treatise on Materials Science and Technology, Vol. 11, Academic Press, New York, 1977, pp. 199-381

Ruiz, A.M., Nagy, P.B., Diffraction Correction for Precision Surface Acoustic Wave Velocity Measurements, Journal of Acoustical Society of America, Vol. 112, No. 3, Pt. 1, Sep. 2002, pp. 835-842

Ruud, C.O., A Review of Selected Non-Destructive Methods for Residual Stress Measurement, NDT International, Vol. 15, No. 1, Feb. 1982, pp. 15-23

Saiie, J., Wang, T., Bilgutay, N.M., Spectra Evaluation of Ultrasonic Grain Signals, IEEE Ultrasonic Proceedings, 1987, pp. 1015-1020

Santos, A.A., Bray, D.E., Ultrasonic Stress Measurement using PC based and Commercial Flaw Detectors, Review of Scientific Instruments, Vol. 71, No. 9, pp. 3464-3469, September 2000

Sayers, C.M., Texture Independent Determination of Residual Stress in Polycrystalline Aggregates using Rayleigh Waves, J. Phys. D: Appl. Phys., Vol. 17, 1984, pp. L179-L184

Schneider, E., Nondestructive Evaluation of Stress States in Components Using Ultrasonic and Electromagnetic Techniques, PVP-Vol. 429, Residual Stress Measurement and General Nondestructive Evaluation, ASME 2001, pp. 41-48

Schneider, E., Goebbels, K., Determination of Residual Stress by Linearly Polarized Ultrasonic Waves, Inst. Mech. Eng., London, Paper C147/82, 1982, pp. 103-107

Schramm, R.E., Szelazek, J., Van Clark, Jr.A., Ultrasonic Measurement of Residual

Stress in the Rims of Inductively Heated Railroad Wheels, Materials Evaluation,Vol. 54, No. 8, Aug. 1996, pp. 929-934

Selfridge, A.R., Approximate Material Properties in Isotropic Material, IEEE Transactions on Sonics and Ultrasonics, Vol. SU-32, No. 3, 1985, p.p.

Shcherbinskii, V.G., A New Technique for Surface Roughness Assessment and Correctin in Ultrasonic Testing, European Journal of NDT, Vol. 3, No. 1, 1993, pp. 10-16

Shung, K.K., Zipparo, M., Ultrasonic Transducers and Arrays, IEEE Engineering in Medicine and Biology, pp. 20-30, Nov./ Dec. 1996

Silk, M.G., Ultrasonic Transducers for Nondestructive Testing, Adam Hilger Ltd., Bristol, 1984;

Smith, J.F., Thompson, R.B., Simultaneous Ultrasonic Evaluation with Differentiation of Stress and Texture, Journal of Materials Engineering and Perfomance, Vol. 3, No. 2, Apr. 1994, pp. 273-281

Stephens, R.W.B., Ultrasonics International 1975 Conference Proceedings, IPC Science and Technology Press, Guildford, 1975, p. 9

Strnad, Z., Glass-Ceramic Materials, Glass Science and Technology 8, Elsevier, 1986

Szelazek, J., Monitoring of Thermal Stresses in Continuously Welded Rails with Ultrasonic Technique, ECNDT '98, Copenhagen, Vol. 3, No. 6, NDTnet, June 1998

Tanala, E., Bourse, G., Fremiot, M., De Belleval, J.F., Determination of Near Surface Residual Stresses on Welded Joints Using Ultrasonic Methods, NDT&E International, Vol. 28, No. 2, 1995, pp. 83-88

Tang, W., Bray, D.E., Stress and Yielding Studies Using Critically Refracted Longitudinal Wave, NDE Engineering Codes and Standards and Material Characterization, Proceedings of 1996 Pressure Vessel & Piping Conference, Montreal, PVP-Vol. 322, NDE-Vol. 15, pp. 41-48

Tardy, F., Noroy, M.H., Paradis, L., Baboux, J.C., Material Surface Characterization by a Rayleigh Velocity Measurement, NDTnet, Vol. 1, No. 11, Nov. 1996

Thompson, R.B., Lu, W.Y., Clark, Jr., A.V., Ultrasonic Methods, Handbook of Measurement of Residual Stresses, Fairmont Press, 1995

Thompson, R.B., Smith, J.F., Lee, S.S., Effects of Microstructure on the Acoustoelastic Measurements of Stress, Nondestructive Evaluation: Application to Materials

Processing, ed. Buck, O., Wolf, S., The American Society for Metals, Metals Park, OH, 1984, pp. 137-145

Thompson, R.B., Wormley, S.J., Experience in Stress Measurement with the SH-Wave Technique, PVP-Vol. 276, Determining Material Characterization: Residual Stress and Integrity With NDE. ASME, pp. 163-167, 1994;

Tolstoy, I., Clay, C.S., Ocean Acoustics: Theory and Experiment in Underwater Acoustics, American Institute of Physics, New York, 1987

Truell, R., Elbaum, C., Chick, B.B., Ultrasonic Methods in Solid State Physics, Acandemic Press, New York and London, 1969

Vary, A., Ultrasonic Measurement of Material Propeties, Research Techniques in Non-Destructive Testing, Ed. R. Sharpe, Academic Press, London, England, 1980, Part 4, pp. 159-204

Vasil'ev, A.G., Murav'ev, V.V., Smirnov, A.N., Ultrasonic Method of Testing Surface Roughness, Defektoskopiya, No. 2, 1994, pp. 71-72

Warren, P.D., Pecorari, C., Kolosov, O.V., Roberts, S.G., Briggs, G.A.D., Characterization of Surface Damage Via Surface Acoustic Waves, Nanotechnology, Vol. 7, 1996, pp. 295-301

Wells, P.N.T., Biomedical Ultrasonics, Academic Press Inc., London, UK, 1977

Yoshimi, K., Ishiyama, S., Hanada, S., Murayama, Y., Measurement of Recrystallization Texture in H.C.P. Structures by the Selected Area Channeling Pattern Method, Physica Status Solidi (A) Applied Research, Vol. 124, No. 1, Mar, 1991, pp. 81-94

Zhang, C., Achenbach, J.D., Dispersion and Attenuation of Surface Waves Due to Distributed Surface-Breaking Cracks, J. Acoust. Soc. Am., Vol. 88, 1990, pp. 1986-1992